Performance and Design of Extruded Fiber-Reinforced Mortar with Preferentially Aligned Fibers

Rashed Alarrak

Dissertation submitted to the faculty of the Virginia Polytechnic Institute and State University in partial fulfillment of the requirements for the degree of

Doctor of Philosophy
in
Civil Engineering

Alexander S. Brand, Chair
Carin L. Roberts-Wollmann
Nathan King
Bilel Aidi

April 19th, 2024
Blacksburg, VA

Keywords: Fiber-reinforced concrete, Mortar, Fracture, Flexural, Fiber alignment, Extrusion, Digital image correlation, X-ray computed tomography, Crack propagation, Strain localization, Injection, Flexural model

Copyright © 2024, Rashed Alarrak

Performance and Design of Extruded Fiber-Reinforced Mortar with Preferentially Aligned Fibers

Rashed Alarrak

ABSTRACT

This dissertation presents a comprehensive investigation into the mechanical properties of fiber-reinforced concrete (FRC), focusing on fracture and flexural toughness properties, the impact of fiber orientation and distribution, and the evaluation of flexural models for predicting the behavior of functionally graded FRC. It embarks on a critical investigation aimed at bridging a significant gap in the understanding of FRC materials' behavior, particularly in terms of fracture and flexural performance.

Across five distinct manuscripts, this work employs a variety of experimental methodologies, including three-point bend tests, four-point bend tests, digital image correlation, X-ray computed tomography, and the implementation of the two parameter fracture model and then size effect fracture method to explore the effects of different casting techniques – namely, conventional casting and pump-driven extrusion – on the performance of FRC. The core hypothesis tested throughout these studies suggests that the extrusion process, by aligning fibers parallel to tensile stresses, significantly enhances the concrete's ductility, post-peak behavior, and overall fracture and flexural properties. This hypothesis was corroborated across various experiments, which demonstrated that fiber alignment *via* extrusion not only enhances the concrete's mechanical properties but also leads to more effective crack propagation control, increased toughness, and enhanced residual strengths.

The research encompasses a series of systematic investigations into the effects of fiber alignment on the mechanical properties of FRC, revealing that the extrusion process significantly enhances fracture and flexural properties and maintains residual strength after peak stress. Utilizing both extrusion-based and conventional casting methods with varying dosages of polyvinyl alcohol fibers, the study demonstrates notable improvements in fracture properties, deflection at failure, and equivalent flexural strength ratio for extrusion-based specimens compared to their conventionally cast counterparts.

Moreover, the dissertation explores the impact of casting methods and fiber orientation on fracture energy, offering a size-dependent improvement in extrusion-based methods. The strategic distribution of steel fibers, employing an innovative targeted fiber injection for creating Functionally Graded FRC (FG-FRC), is shown to significantly enhance the structural integrity and resilience of the material. The analysis of flexural models applied to FG-FRC specimens, proposing a novel functionally graded factor to improve model predictability, further advances the understanding of the predictability and reliability of these models in assessing FRC's structural behavior.

This dissertation advances academic knowledge in the field of FRC casting and offers significant implications for the construction industry, demonstrating a profound understanding of the challenges and opportunities in extrusion-based FRC casting. Through its innovative approach and detailed investigations, this work contributes significantly to the advancement of the FRC casting field, paving the way for the development of more resilient and efficient construction materials.

Performance and Design of Extruded Fiber-Reinforced Mortar with Preferentially Aligned Fibers

Rashed Alarrak

GENERAL AUDIENCE ABSTRACT

This research explores the enhancement of concrete's strength and flexibility through the incorporation of individual fibers, with a special focus on the integration and alignment of these fibers. The study examines how concrete can be made more resilient by mixing in fibers in specific ways. A variety of tests, including bending beams and employing advanced imaging techniques, were conducted to observe the effects of mixing fibers using traditional methods versus a novel extrusion-based technique that aligns the fibers in the desired direction in the concrete. The research hypothesized that this innovative alignment method would improve the concrete's ductility and enhance its ability to resist crack propagation. The findings confirmed this hypothesis, revealing that aligned fibers significantly improve concrete's bending capacity, reduce sensitivity to cracking, and retain residual strength even after cracking.

Further investigation into varying methods of fiber addition, such as a targeted approach for placing fibers in strategic locations, demonstrated a marked enhancement in the material's ductility. Additionally, the study evaluated mathematical models for predicting the behavior of fiber-reinforced concrete, aiming to improve the understanding and reliability of these models for practical construction applications. In short, the research underscores that adjusting the method of fiber integration into concrete can lead to the development of structures that are both stronger and more durable. This advancement holds promising implications for the future of construction, offering pathways to create more resilient and efficient building materials.

Dedication

To my parents, Samar Alomani and Mohammad Alarrak.

Acknowledgements

I am deeply thankful for the extensive support and guidance I have received on my path to completing this dissertation. First and foremost, I must express my profound gratitude to Allah, whose blessings have opened the door for my academic pursuits at Virginia Tech. I also wish to convey my heartfelt appreciation to the government of Kuwait, represented by Kuwait University, for their continuous support throughout my educational journey.

My academic mentors, especially my committee chair, Dr. Alexander Brand, deserve special recognition. Dr. Brand's vast knowledge and guidance have significantly influenced the direction and quality of my research. Under his mentorship, I have gained invaluable insights and encouragement, which have fostered a rich learning environment. Furthermore, I am grateful to my committee members, Dr. Wollmann, Dr. Aidi, and Dr. King, for their critical contributions that have augmented my research experience and pushed me to expand my understanding.

Above all, my heartfelt appreciation goes to my family. To my mother, Samar, and my father, Mohammad, your support has been the cornerstone of my success. Striving to make you proud has been my driving force, and standing here today, as a PhD holder, is a testament to your belief in my abilities. I must also extend a special thank you to my friend Abdullah Al Rufaydah, who has been like a brother throughout my PhD journey. His kindness and support have been invaluable during challenging times. Likewise, my gratitude goes to Byeonguk Jeon for his essential assistance in the early stages of my PhD. His support has been crucial to my success.

Completing this dissertation is not only an academic achievement but also a personal milestone, realized through the collective support and guidance of many individuals. To everyone involved in this journey, I extend my heartfelt gratitude.

Table of Contents

ABSTRACT ..... **ii**

GENERAL AUDIENCE ABSTRACT ..... **iv**

Dedication ..... **v**

Acknowledgements ..... **vi**

List of Figures ..... **xv**

List of Tables ..... **xxii**

Chapter 1. Introduction **1**

1.1. Background and Motivation **1**

1.2. Previous Research on Fiber Alignment **3**

1.3. Additive Manufacturing Techniques **3**

1.4. Nozzle Design for Pump Extrusion-Based FRC **4**

1.5. Problem Statement **4**

1.6. Research Objectives **6**

1.7. Dissertation Organization and Contribution **7**

1.7.1. Chapter 1: Introduction ***8***

1.7.2. Chapter 2: Research Preparation ***8***

1.7.3. Chapter 3: Fracture Properties of Extruded Fiber-Reinforced Mortar with Preferentially Aligned Fibers ***8***

1.7.3.1. Intellectual merit *9*

1.7.3.2. Broader impacts *9*

1.7.4. Chapter 4: Flexural Toughness of Extruded Fiber-Reinforced Mortar with Preferentially Aligned Fibers ***10***

1.7.4.1. Intellectual merit *10*

1.7.4.2. Broader impacts *10*

1.7.5. Chapter 5: Size Effect of Fracture Properties of Extruded Fiber-Reinforced Mortar with Preferentially Aligned Fibers *11*

1.7.5.1. Intellectual merit *11*

1.7.5.2. Broader impacts *12*

1.7.6. Chapter 6: Mechanical Performance of Extruded Functionally Graded Fiber-Reinforced Mortar with Targeted Fiber Injection *12*

1.7.6.1. Intellectual merit *13*

1.7.6.2. Broader impacts *13*

1.7.7. Chapter 7: Flexural Models Exploration for Functionally Graded Steel Fiber-Reinforced Mortar Considering Fiber Dosage and Orientation *14*

1.7.7.1. Intellectual merit *14*

1.7.7.2. Broader impacts *14*

1.7.8. Chapter 8: Conclusions and Recommendations *15*

1.8. References **15**

Chapter 2. Research Preparation **20**

2.1. Mix Design Selection **20**

2.1.1. Fiber Type Selection *20*

2.2. Extrusion System **23**

2.2.1. Nozzle Design and Fabrication *23*

2.3. Mixing Procedure and Sample Preparations **26**

2.3.1. Conventional Cast Mix Method *27*

2.3.2. Pump Extrusion Based Method *28*

2.4. Experiment Setup **28**

2.4.1. Three-point Bending Fracture Test *30*

2.4.2. Four-point Bending Flexural Test *31*

2.4.3. Digital Image Correlation Setup *32*

2.5. Experimental Testing Template's Development 33

2.5.1. Fracture Test Template 34

2.5.2. Flexural Test Template 36

2.6. References 37

Chapter 3. Fracture Properties of Extruded Fiber-Reinforced Mortar with Preferentially Aligned Fibers 38

3.1. Introduction 39

3.1.1. Research Objective 41

3.2. Experimental Methodology 42

3.2.1. Theoretical Background 42

3.2.2. Mix Design and Properties 45

3.2.3. Testing Program and Sample Preparation 46

3.2.4. Digital Image Correlation 49

3.3. Test Results and Discussion 52

3.3.1. Fiber Orientation of Fractured Specimens 52

3.3.2. Fracture Properties 53

3.3.3. Total Fracture Energy 59

3.3.4. Crack Propagation and Strain Localization 60

3.4. Conclusion 64

3.5. Authorship Contribution Statement 66

3.6. References 66

Chapter 4. Flexural Toughness of Extruded Fiber-Reinforced Mortar with Preferentially Aligned Fibers 71

4.1. Introduction 72

4.1.1. Background and Motivation 72

4.1.2. Previous Research on Fiber Alignment *72*

4.1.3. Additive Manufacturing Techniques *73*

4.1.4. Nozzle Design for Pump Extrusion-Based FRC *74*

4.1.5. Improvement of Flexural Toughness *75*

4.1.6. Digital Image Correlation Technique *76*

4.1.7. Research Objective *77*

4.2. Experimental Methodology **78**

4.2.1. Theoretical Background *78*

4.2.2. Mix Design and Properties *80*

4.2.3. Testing Program and Sample Preparation *82*

4.2.4. Digital Image Correlation *84*

4.3. Test Results and Discussion **87**

4.3.1. Fiber Orientation of Fractured Specimens *87*

4.3.2. Flexural Properties *88*

4.3.3. Flexural Toughness *93*

4.3.4. Crack Propagation and Strain Localization *96*

4.4. Conclusion **103**

4.4.1. Limitation and Future Work *104*

4.5. Authorship Contribution Statement **104**

4.6. References **105**

Chapter 5. Size Effect of Fracture Properties of Extruded Fiber-Reinforced Mortar with Preferentially Aligned Fibers **110**

5.1. Introduction **111**

5.1.1. Background and Motivation *111*

5.1.2. Previous Research on Fiber Alignment *111*

5.1.3. Nozzle Design for Pump Extrusion-Based FRC *112*

5.1.4. Size Effect Method *113*

5.1.5. Size Effect for Fracture in FRC *115*

5.1.6. Research Objective *116*

5.2. Experimental Methodology **117**

5.2.1. Theoretical Background *117*

5.2.2. Mix Design and Properties *120*

5.2.3. Testing Program and Sample Preparation *122*

5.3. Test Results and Discussion **125**

5.3.1. Peak Load and Total Fracture Energy *125*

5.3.2. SEM Fracture Properties *130*

5.4. Conclusion **133**

5.4.1. Limitation and Future Work *134*

5.5. Authorship Contribution Statement **135**

5.6. References **136**

Chapter 6. Mechanical Performance of Extruded Functionally Graded Fiber-Reinforced Mortar with Targeted Fiber Injection **141**

6.1. Introduction **142**

6.1.1. Mechanical Performance of FG-FRC *142*

6.1.2. Fiber Injection Techniques *143*

6.1.3. Fiber Alignment *144*

6.1.4. Additive Manufacturing Techniques *144*

6.1.5. X-ray Computed Tomography *145*

6.1.6. Digital Image Correlation *145*

6.1.7. Research Objective *146*

6.2. Experimental Methodology 147

6.2.1. Theoretical Background 147

6.2.1.1. Flexural Properties 147

6.2.1.2. Fracture Properties 150

6.2.2. Mix Design and Properties 152

6.2.3. Testing Program and Sample Preparation 154

6.2.4. Digital Image Correlation 159

6.2.5. X-ray Computed Tomography 162

6.3. Test Results and Discussion 165

6.3.1. Fiber Dosage and Orientation 165

6.3.2. Flexural Properties 171

6.3.3. Fracture Properties 183

6.3.4. Crack Propagation and Strain Localization 192

6.4. Conclusion 199

6.4.1. Limitation and Future Work 200

6.5. Authorship Contribution Statement 201

6.6. References 202

Chapter 7. Flexural Models Exploration for Functionally Graded Steel Fiber-Reinforced Mortar Considering Fiber Dosage and Orientation 210

7.1. Introduction 211

7.1.1. Innovation of Functionally Graded FRC 212

7.1.2. Fiber Injection Techniques and Alignment 212

7.1.3. Flexural Models in FRC 213

7.1.3.1. fib Rigid-Plastic Model 214

7.1.3.2. fib Linear Model 215

7.1.3.3. ER-465 Model *215*

7.1.4. Prediction of FRC's Flexural Strength ***216***

7.1.5. Research Objective ***217***

7.2. Experimental Methodology **218**

7.2.1. Flexural Properties ***218***

7.2.2. Theoretical Background of Flexural Models ***220***

7.2.2.1. ER-465 Model *221*

7.2.2.2. fib Linear Model *225*

7.2.2.3. fib Rigid Plastic Model *228*

7.2.3. Theoretical Background of Flexural Models FRC Classifications ***230***

7.2.4. Mix Design and Properties ***232***

7.2.5. Testing Program and Sample Preparation ***235***

7.2.6. X-ray Computed Tomography ***236***

7.3. Test Results and Discussion **237**

7.3.1. Fiber Orientation Factor ***237***

7.3.2. Flexural Properties ***239***

7.3.3. Flexural Models for FRC ***244***

7.3.3.1. ER-465 Flexural Model III Refinement *249*

7.3.4. Development of Functionally Graded Factor ***252***

7.3.5. FG-FRC Classification ***257***

7.4. Conclusion **259**

7.4.1. Limitation and Future Work ***260***

7.5. Authorship Contribution Statement **262**

7.6. References **263**

Chapter 8. Conclusions and Recommendations **267**

8.1. Research Overview **267**

8.2. Major Findings 268

8.3. Limitations 270

8.4. Recommendations for Future Work 270

List of Figures

Figure 2.1: P-25 Pump Extrusion System 23

Figure 2.2: Initial Nozzle Head Design 25

Figure 2.3: Nozzle Design Attached to PVC Hose 25

Figure 2.4: Extrusion-based Method's Nozzle Design 26

Figure 2.5: Specimen's Support Used in Testing (Used in All Studies) 29

Figure 2.6: Small Specimen's Support Used in Testing (Used in Chapter 5) 29

Figure 2.7: Large Specimen's Support Used in Testing (Used in Chapter 5) 29

Figure 2.8: Test Setup of Three-point Bending Beam Specimen 30

Figure 2.9: Notched Beam's Specimens 30

Figure 2.10: Clip Gauge Attached to the Knife Edges 31

Figure 2.11: Test Setup of Four-Point Bending Beam Specimen 31

Figure 2.12: LVDT Placement in the Four-Point Bending Test 32

Figure 2.13: Beam Specimen Prepared for DIC Analysis 33

Figure 2.14: Two Digital Cameras Used in DIC 33

Figure 2.15: Loading Command in the Fracture Test Template 35

Figure 2.16: Unloading Command in the Fracture Test Template 35

Figure 2.17: Loading Command in the Flexural Test Template 36

Figure 3.1: Theoretical Basics of: a) TPFM and b) MTPM in Determining the Critical Crack Length 44

Figure 3.2: Test Setup of Three-point Bending Beam Specimen 47

Figure 3.3: Extrusion-based Method's Nozzle Design 48

Figure 3.4: Beam Specimen Used for Fracture Test 50

Figure 3.5: Two Digital Cameras Used in DIC 50
Figure 3.6: Load-CMOD Curves for DIC and Clip Gauge 51
Figure 3.7: Experimental Technique for Determining the Critical Crack Length Using DIC 52
Figure 3.8: Front View of Fractured Specimens of: a) EB and b) CV 53
Figure 3.9: Load-CMOD Curve for 0.5% FRC Specimens 56
Figure 3.10: Load-CMOD Curve for 1% FRC Specimens 57
Figure 3.11: Fracture Toughness Comparison for all FRC Specimens 58
Figure 3.12: Effective Critical Crack Length Comparison for all FRC Specimens 58
Figure 3.13: Full Strain Field at the Critical Stage for 0.5% Fiber Content Specimens 61
Figure 3.14: Full Strain Field at the Critical Stage for 1% Fiber Content Specimens 61
Figure 3.15: Full Strain Field (x-axis) When the Crack Reached the Top for 1% Fiber Content Specimens 62
Figure 3.16: Full Strain Field (y-axis) When the Crack Reached the Top for 1% Fiber Content Specimens 63
Figure 4.1: Five Stages of Load-deflection Curve (adapted from ASTM C1609) 79
Figure 4.2: PVA Fibers 81
Figure 4.3: Test Setup of Third-point Bending Beam Specimen 82
Figure 4.4: Extrusion-based Method's Nozzle Design 83
Figure 4.5: LVDT Installation on Beam Specimen 84
Figure 4.6: Beam Specimen Used for Flexural Test 86
Figure 4.7: Two Digital Cameras Used in DIC 86
Figure 4.8: Load-deflection Curves for DIC and LVDT 87
Figure 4.9: Front View of Fractured Specimens of: a) EB and b) CV 88

Figure 4.10: Load-deflection Curve for PC Specimens 91
Figure 4.11: Load-deflection Curve for 0.5% FRC Specimens 91
Figure 4.12: Load-deflection Curve for 1% FRC Specimens 92
Figure 4.13: Flexural Residual Strength Comparison for all FRC Specimens 93
Figure 4.14: Equivalent Flexural Strength Ratio Comparison for all FRC Specimens 96
Figure 4.15: Full Strain Field (x-axis) at the 1st Stage for 0.5% Fiber Content Specimens (the contour legend indicates the concentration of each strain level) 98
Figure 4.16: Full Strain Field (x-axis) at the 1st Stage for 1% Fiber Content Specimens (the contour legend indicates the concentration of each strain level) 99
Figure 4.17: Full Strain Field (x-axis) at the 4th Stage for 0.5% Fiber Content Specimens (the contour legend indicates the concentration of each strain level) 100
Figure 4.18: Full Strain Field (x-axis) at the 4th Stage for 1% Fiber Content Specimens (the contour legend indicates the concentration of each strain level) 100
Figure 4.19: Full Strain Field (y-axis) at the 4th Stage for 0.5% Fiber Content Specimens (the contour legend indicates the concentration of each strain level) 102
Figure 4.20: Full Strain Field (y-axis) at the 4th Stage for 1% Fiber Content Specimens (the contour legend indicates the concentration of each strain level) 102
Figure 5.1: Test Setup of Three-point Bending Beam Specimen 118
Figure 5.2: PVA Fibers 122
Figure 5.3: Extrusion-based Method's Nozzle Design 124
Figure 5.4: Relative Fracture Energy Comparison 128
Figure 5.5: Load-deflection Curve for Small-Size Specimens 129
Figure 5.6: Load-deflection Curve for Medium-Size Specimens 129

Figure 5.7: Load-deflection Curve for Large-Size Specimens 130
Figure 5.8: Size-effect Regression for Variables X and Y for PC Specimens 132
Figure 5.9: Size-effect Regression for Variables X and Y for CV1% Specimens 132
Figure 5.10: Size-effect Regression for Variables X and Y for EB1% Specimens 133
Figure 6.1: Five Stages of Load-deflection Curve for Softening Behavior (adapted from ASTM C1609) 148
Figure 6.2: Five Stages of Load-deflection Curve for Hardening Behavior (adapted from ASTM C1609) 149
Figure 6.3: Steel Fibers 153
Figure 6.4: Test Setup of Four-point Bending Beam Specimen 155
Figure 6.5: Test Setup of Three-point Bending Beam Specimen 155
Figure 6.6: Targeted Fiber Injection Method's Setup 156
Figure 6.7: Extrusion-based Method's Nozzle Design 156
Figure 6.8: Schematic of Extrusion-based Fiber Injection Process 157
Figure 6.9: FG-FRC Mix Designs 158
Figure 6.10: LVDT Installation on Beam Specimen 159
Figure 6.11: Clip Gauge Attached to the Knife Edges 159
Figure 6.12: Beam Specimen Painted for DIC 160
Figure 6.13: Two Digital Cameras Used in DIC 160
Figure 6.14: Load-deflection Curves for DIC and LVDT 162
Figure 6.15: Load-CMOD Curves for DIC and Clip Gauge 162
Figure 6.16: XCT Analysis Views: a) Top, b) Front, and c) Cross-sectional 164
Figure 6.17: XCT Layer Analysis Sections 164

Figure 6.18: Fiber Orientation Angle for M1 Specimen..... 167
Figure 6.19: Fiber Orientation Angle for M2 Specimen..... 168
Figure 6.20: Fiber Orientation Angle for M3 Specimen..... 169
Figure 6.21: Fiber Orientation Angle for M4 Specimen..... 170
Figure 6.22: Fiber Orientation Angle for M5 Specimen..... 171
Figure 6.23: Load-deflection Curve for M1 and M5 Specimens..... 174
Figure 6.24: Equivalent Flexural Strength Ratio Comparison for M1 and M5 Specimens..... 175
Figure 6.25: Load-deflection Curve for M1 and M4 Specimens..... 176
Figure 6.26: Equivalent Flexural Strength Ratio Comparison for M1 and M4 Specimens..... 177
Figure 6.27: Load-deflection Curve for M2 and M4 Specimens..... 178
Figure 6.28: Equivalent Flexural Strength Ratio Comparison for M2 and M4 Specimens..... 179
Figure 6.29: Load-deflection Curve for M3 and M5 Specimens..... 180
Figure 6.30: Equivalent Flexural Strength Ratio Comparison for M3 and M5 Specimens..... 181
Figure 6.31: Load-deflection Curve for M2 and M3 Specimens..... 182
Figure 6.32: Equivalent Flexural Strength Ratio Comparison for M2 and M3 Specimens..... 183
Figure 6.33: Load-CMOD Curve for M1 and M4 Specimens..... 186
Figure 6.34: Total Fracture Energy Comparison for M1 and M4 Specimens 187
Figure 6.35: Load-CMOD Curve for M2 and M4 Specimens..... 188
Figure 6.36: Total Fracture Energy Comparison for M2 and M4 Specimens 189
Figure 6.37: Load-CMOD Curve for M3 and M5 Specimens..... 189
Figure 6.38: Total Fracture Energy Comparison for M3 and M5 Specimens 190
Figure 6.39: Load-CMOD Curve for M2 and M3 Specimens..... 191
Figure 6.40: Total Fracture Energy Comparison for M2 and M3 Specimens 192

Figure 6.41: Full Strain Field (x-axis) at the 1st Stage FG-FRC Specimens (the contour legend indicates the concentration of each strain level) 194
Figure 6.42: Full Strain Field (x-axis) at the 4th Stage for FG-FRC Specimens (the contour legend indicates the concentration of each strain level) 196
Figure 6.43: Full Strain Field (y-axis) at the 4th Stage for FG-FRC Specimens (the contour legend indicates the concentration of each strain level) 198
Figure 6.44: Full Strain Field (y-axis) at the 4th Stage for FG-FRC (the contour legend indicates the concentration of each strain level) 198
Figure 7.1: Test Setup of Three-point Bending Beam Specimen [17] 219
Figure 7.2: Five Stages of Load-CMOD Curve (adapted from EN 14651)..... 219
Figure 7.3: Stress-strain Relationship for Concrete in Compression (adapted from ER-465) ... 222
Figure 7.4: Stress-strain Relationship for FRC in Tension (adapted from ER 465)..... 223
Figure 7.5: ER-465 Flexural Model III (adapted from ER 465)..... 224
Figure 7.6: fib Linear Model (adapted from MC 2010)..... 228
Figure 7.7: Residual Tensile Strength Computation in fib Rigid-plastic Model (adapted from MC 2010) 229
Figure 7.8: fib Rigid-plastic Model (adapted from MC 2010) 230
Figure 7.9: FG-FRC Mix Designs 234
Figure 7.10: Steel Fibers [17] 234
Figure 7.11: Schematic of Extrusion-based Fiber Injection Method [17] 236
Figure 7.12: XCT Analysis Views: a) Top, b) Front, and c) Cross-sectional [17]..... 237
Figure 7.13: Load-CMOD Curve for M1 Specimens 242
Figure 7.14: Load-CMOD Curve for M2 Specimens 243

Figure 7.15: Load-CMOD Curve for M3 Specimens 243

Figure 7.16: Load-CMOD Curve for M4 Specimens 244

Figure 7.17: Load-CMOD Curve for M5 Specimens 244

Figure 7.18: Percentage of Error Comparison for Flexural Models 249

Figure 7.19: Prediction Comparison of ER 465 Model Using Different Values of K_s 252

Figure 7.20: Percentage of Error Comparison for ER 465 Flexural Models 255

Figure 7.21: Percentage of Error Comparison for fib Rigid-Plastic Flexural Models 256

Figure 7.22: Percentage of Error Comparison for fib Linear Flexural Models 256

Figure 7.23: FG-FRC Material Classification 259

List of Tables

Table 2.1: Properties of Materials 20

Table 2.2: Fiber Trial Result 22

Table 2.3: Properties of PVA Fibers 22

Table 2.4: Properties of Steel Fibers 22

Table 3.1: Composite Mixture Proportions 45

Table 3.2: Properties of PVA Fibers 46

Table 3.3: Compressive Strength Results 46

Table 3.4: Fracture Properties of 0.5% FRC Specimens Using TPFM 54

Table 3.5: Fracture Properties of 1% FRC Specimens Using TPFM 55

Table 3.6: Fracture Toughness Modes Comparison of 0.5% FRC Specimens 55

Table 3.7: Fracture Toughness Modes Comparison of 1% FRC Specimens 56

Table 3.8: Total Fracture Energy Results for 1% FRC Specimens 59

Table 4.1: Concrete Mixture Proportions 81

Table 4.2: Properties of PVA Fibers 81

Table 4.3: Compressive Strength Results 81

Table 4.4: Final Net Deflection for All Beam Specimens 89

Table 4.5: Flexural Properties of PC Specimens 90

Table 4.6: Flexural Properties of 0.5% FRC Specimens 90

Table 4.7: Flexural Properties of 1% FRC Specimens 90

Table 4.8: Flexural Toughness Properties of 0.5% FRC Specimens 94

Table 4.9: Flexural Toughness Properties of 1% FRC Specimens 94

Table 5.1: Dimensions of the Beam Specimens Used for the Size Effect Model 118

Table 5.2: Concrete Mixture Proportions 121

Table 5.3: Properties of PVA Fibers 121

Table 5.4: Compressive Strength Results 122

Table 5.5: Peak Load and Relative Fracture Energy Values for All Specimens 126

Table 5.6: Fracture Parameters of PC and FRC Specimens Using Size-Effect Method 131

Table 6.1: Concrete Mixture Proportions 153

Table 6.2: Properties of Steel Fibers 153

Table 6.3: Compressive Strength Results 154

Table 6.4: Fiber Count and Orientation of FG-FRC Specimens* 166

Table 6.5: Flexural Properties of FG-FRC Specimens 172

Table 6.6: Flexural Toughness Properties of FG-FRC Specimens 173

Table 6.7: Fracture Properties of FG-FRC Specimens 184

Table 6.8: Total Fracture Energy Results of FG-FRC Specimens 185

Table 7.1: Conversion Factor (αc) 223

Table 7.2: FRC Material Classification 232

Table 7.3: Concrete Mixture Proportions [17] 233

Table 7.4: Properties of Steel Fibers [17] 233

Table 7.5: Compressive Strength Results [17] 235

Table 7.6: Fiber Count and Orientation of FG-FRC Specimens* [17] 238

Table 7.7: Flexural Properties of FG-FRC Specimens 240

Table 7.8: Flexural Toughness Properties of FG-FRC Specimens 241

Table 7.9: Parameter of Flexural Models 246

Table 7.10:Predictability of Flexural Models 248

Table 7.11:Predictability of ER-465 Model Using Different Values of K_s 251

Table 7.12: FG-FRC Material Classification Results 258

Chapter 1. Introduction

1.1. Background and Motivation

Conventional concrete, being inherently brittle, offers limited resistance to applied loads, whether dynamic or static, due to its weakness in the tensile and flexural properties. This limitation has historically been mitigated through the use of reinforcement rebar. This method has provided essential support, enhancing its load-bearing capacity. Nevertheless, a more advanced solution is emerging in the form of Fiber-Reinforced Concrete (FRC). FRC, a cementitious composite material comprising of Portland cement concrete with the discrete fibers, FRC has gained significant attention in recent years, predominantly due to its distinctive potential for strain-hardening behavior and the arrest of crack propagation [1−4]. Depending on the fiber type and fiber dosage, the fibers can enhance the mechanical performance, load-bearing capacity, and pseudo-ductility of the concrete [5−18]. Typically, FRCs incorporate a fiber volume of less than 1 %, which is introduced during the mixing phase [18,19]. In this dissertation, the volume range of ≤1 % was chosen since it represents a practical level that engineers could feasibly use in the field, allowing for significant improvements in the concrete's deformation capacity and tensile strength by effectively managing crack propagation through fiber bridging [20].

Despite its advantages, FRC faces a critical challenge in fiber distribution due to the limitations of conventional mixing techniques, which often result in fibers orienting randomly [5,6,11,13,14,21−25]. Fibers are maximally effective when they are aligned parallel to the induced tensile stress, so randomly oriented fibers in three-dimensional space is an extreme reduction in performance relative to preferential alignment [26]. The efficacy of fiber reinforcement is

quantified through the fiber efficiency factor, which varies with orientation, highlighting the importance of aligning fibers with principal tensile stresses for optimal performance [27].

Within the scope of this dissertation, the mechanical benefits offered by fiber alignment in FRC have been explored. This was achieved by comparing samples with aligned fibers against those with a random dispersion. The methodological approach leaned on a pump extrusion-based casting technique to orient fibers in the desired direction within cementitious mixtures. This method employs a pump extruder complemented by a nozzle delivery system, and this configuration ensured that the fresh mixture was channeled into the casting mold, aligning the fibers parallel to the principal tensile stresses. The effectiveness of this method was validated through extensive testing, including three-point fracture and four-point toughness bending tests, demonstrating its superiority over traditional casting methods.

The research further introduces an innovative approach for incorporating stiffer, longer fibers through a semi-automated post-extrusion injection process, aiming to produce functionally graded FRCs. This method holds the potential to revolutionize the construction industry by allowing for the tailored engineering of FRC properties. The hypothesis that fiber alignment, achieved through extrusion, could significantly enhance the concrete's mechanical properties was thoroughly tested. Techniques such as Digital Image Correlation (DIC) and X-ray Computed Tomography (XCT) were employed to examine crack propagation, strain localization, and verify fiber dosage and orientation. The findings of this study not only underscore the importance of fiber orientation in enhancing the mechanical properties of FRC but also open new avenues for additive manufacturing technologies, enabling the construction of FRC structures with customized engineering properties.

1.2. Previous Research on Fiber Alignment

The orientation of fibers in FRC has been a subject of extensive research since the early 1970s [28–30]. A fiber is considered completely aligned if its position falls within a range of ±20° in relation to the extrusion direction [31]. Understanding and controlling fiber alignment can significantly impact the mechanical performance of FRC, making it a critical aspect to explore [32–35]. To achieve the advantages of fiber alignment, researchers have explored various methods to orient the fibers in the desired direction. Magnetic fields have been utilized to align steel fibers [7,22,25,33,36], and modified casting methods have been developed to orient fibers during the consolidation process as fresh concrete flows [12–14,32,37,38]. Among these, extrusion-based methods stand out for their ability to precisely align fibers, leveraging additive manufacturing to maximize tensile resistance [31,39–51]. Early research on extruded FRC, in the 1990s and early 2000s, suggested that extrusion methods, such as ram or plunger extrusion, could lead to beneficial strain-hardening behaviors [28,40,41,47,52], though research specifically focusing on the effect of extrusion on fiber alignment within cementitious composites has been limited [49,46,51].

1.3. Additive Manufacturing Techniques

Recent studies have delved further into extrusion-based additive manufacturing techniques for FRC. Ma *et al*. [31] used a 3D printer to extrude basalt fiber-reinforced cementitious material, achieving fiber alignment in the print direction by using a nozzle with a diameter smaller than the fiber length. While the extrusion-based printing process showed well-oriented structures, there were issues with weak interfaces and voids between circular bead layers [31,45,48]. Ye *et al*. [45] attempted to mitigate these issues with a rectangular nozzle for polyethylene fiber FRC, but increased fiber content led to twisted orientations and reduced tensile strength.

To overcome these challenges, the integration of flow-induced casting methods with a pump extruder via a nozzle conveyor system shows potential. This approach can provide rheological benefits by aligning fibers in the desired direction after extrusion, thus enhancing mechanical properties in the target direction of FRC structures [13,23,53]. Using a nozzle conveyor system, from pump pressure to extrusion, can prevent fiber twisting, caused by the pump shaft's rotation, ensuring efficient fiber alignment [32,45,54].

1.4. Nozzle Design for Pump Extrusion-Based FRC

Innovations in nozzle design have been crucial for improving FRC extrusion techniques, aiming to optimize fiber alignment and the mechanical properties of printed structures. Ma *et al.* [31] utilized an oval-shaped nozzle to align basalt fibers, achieving significantly higher flexural strength in printed samples, despite challenges with inter-layer voids. Ye *et al*. [45] used rectangular nozzle which improved upon this by addressing void issues, although fiber twisting during extrusion emerged as a new problem, affecting tensile strength. Zhou *et al.* [53] observed that high extrusion pressure could disrupt fiber alignment, while Huang *et al.* [55] introduced an L-shaped vertical nozzle, yielding increased flexural strength and toughness in printed specimens. This nozzle achieved a 33 % improvement in fiber orientation compared to conventional casting, showcasing the potential of specialized nozzle designs in enhancing FRC printing outcomes.

1.5. Problem Statement

The construction industry's continuous evolution has brought forward the innovative use of FRC in various applications, ranging from structural components to intricate architectural elements. Among the advancements, extrusion-based FRC casting techniques, such as additive manufacturing, have emerged as a promising avenue for fabricating complex shapes and structures

with enhanced mechanical properties. Despite these advancements, significant knowledge gaps remain regarding the fundamental understanding of the mechanical behavior of FRC materials, particularly in relation to the role of fiber alignment and distribution achieved through extrusion processes. This gap not only hinders the optimization of FRC materials for specific applications but also limits the potential for these materials to revolutionize construction practices.

The complexity of fiber alignment within FRC significantly influence the material's mechanical properties, including fracture, flexural, and toughness. Yet, comprehensive data and insights into how these factors interplay during the extrusion process are scarce. Current methodologies and understanding largely overlook the dynamic effects of fiber orientation and distribution, leading to a lack of predictive accuracy in the performance of extruded FRC structures. Furthermore, the industry lacks a systematic approach to integrating high-stiffness fibers during the extrusion process, which could enhance the mechanical performance of FRC materials. The absence of a comprehensive model that incorporates fiber orientation for the structural design of extruded FRC further aggravate this issue, leaving a critical gap in the field.

This dissertation addresses these challenges by embarking on a thorough investigation aimed at fundamentally altering the understanding of FRC materials' mechanical behaviors, with a specific focus on the impact of fiber alignment and distribution. The research is structured around several key objectives, including exploring the effects of fiber alignment on FRC's mechanical properties, understanding the dynamics of crack propagation and strain localization, developing a novel fiber injection method during the extrusion process, and creating a comprehensive structural design model that incorporates fiber dosage and orientation. Through a series of methodical research tasks, this study aims to bridge the existing knowledge gap, offering valuable contributions to the field of extrusion-based FRC casting.

1.6. Research Objectives

This dissertation is dedicated to bridging the notable gap within the extrusion-based FRC casting field by delivering essential data and insights. These contributions aim to improve the understanding of the mechanical behaviors of FRC materials, focusing on the significant roles of fiber alignment and distribution. The research sets out to achieve several ambitious goals. Firstly, it will explore the impact of fiber alignment on the mechanical properties, including fracture and flexural behaviors of FRC materials. Following this, the study will delve into the dynamics of crack propagation and strain localization within FRC specimens, providing a deeper understanding of the material's behavior under stress. Additionally, the research intends to develop a novel method for injecting fibers during the extrusion process of FRC, a technique that promises to have substantial applicability in the construction industry. Lastly, the dissertation aims to develop a comprehensive model for the structural design of extruded FRC, incorporating the crucial aspect of fiber orientation. Through a series of targeted research activities, this work will methodically address each of these objectives, paving the way for significant advancements in the field. These objectives will be met by specifically achieving research tasks:

- **Task 1** involves understanding the mechanism of the pump, selecting the most appropriate mix design and fiber type, and developing an experimental software template to be used in performing mechanical testing.
- **Task 2** involves an investigation of the fracture properties of the extruded FRC with polyvinyl alcohol (PVA) fibers compared to the conventional cast FRC to show the effect of fiber alignment achieved *via* pump extrusion. Further investigation needed for the crack propagation process and strain localization is performed in the layer's interfaces using DIC.

- **Task 3** involves an investigation of the flexural toughness properties of the extruded FRC with PVA fibers compared to the conventional cast FRC to show the effect of fiber alignment achieved *via* pump extrusion. Further investigation for the crack propagation process and strain localization is performed in the layer's interfaces using DIC.

- **Task 4** delves into examining the influence of specimen size on the fracture properties of extruded FRC with PVA fibers, in comparison to traditional cast FRC. This investigation aims to highlight the benefits of fiber alignment, achieved through pump extrusion, across various scales of specimens.

- **Task 5** involves a development of a novel targeted fiber injection technique, which employs a conveyor system designed for integrating high-stiffness steel fibers into mortar directly at the nozzle just before extrusion. It delves into examining the mechanical performance, including the flexural and fracture properties, of functionally graded steel FRC. Further investigation assessed the fiber dosage and orientation within each of the functionally-graded FRC specimens using XCT.

- **Task 6** advances design opportunities in using the flexural models provided in ER-465 specifications and fib Model Code 2010 (MC 2010) to predict the flexural strength of FRC sections. It involves developing a constitutive model using the data from tests performed in the notched beams.

1.7. Dissertation Organization and Contribution

The dissertation consists of five manuscripts, within eight chapters, each contributing novel contributions and advancements to the field of FRC. These manuscripts collectively address the tasks outlined previously, weaving a comprehensive narrative that spans from theoretical

frameworks to practical applications. The intellectual merit and broader impacts of the research are thoroughly discussed for each chapter, underscoring the dissertation's contribution to both the academic community and the industry. The outline of the dissertation is presented as follows:

1.7.1. Chapter 1: Introduction

This chapter discusses the knowledge gaps and problems in extrusion-based FRC and provides the general background knowledge employed in this dissertation. This also entails the problem statement, objectives, and the organization of the dissertation.

1.7.2. Chapter 2: Research Preparation

This chapter outlines the foundational steps required before initiating the research. These steps include Task 1 which encompass understanding the pump's mechanism, selecting the optimal mix design and fiber type, and creating a specialized software template for subsequent mechanical testing.

1.7.3. Chapter 3: Fracture Properties of Extruded Fiber-Reinforced Mortar with Preferentially Aligned Fibers

This chapter corresponds to Task 2, which focuses on exploring the fracture properties of extruded FRC using PVA fibers. This is contrasted with conventional cast fiber reinforced concrete to highlight the impact of fiber alignment achieved through pump extrusion. The unique aspect of this study is the quantification of the fracture properties of extruded FRC utilizing DIC, the two-parameter fracture model (TPFM), and the modified two parameter model (MTPM). This manuscript was published in *Construction and Building Materials.*

1.7.3.1. Intellectual merit

The novel approach of this chapter lies in the comparison of extruded FRC with conventional cast FRC, offering a new dimension to understand the influence of fiber alignment achieved through pump extrusion. The quantification of the fracture properties of extruded FRC sets this research apart, as it brings into play advanced techniques such as DIC, TPFM, and MTPM. By assessing crack propagation and strain localization, especially at layer interfaces using DIC, this chapter contributes valuable data and findings that could reshape the understanding of the mechanical behavior of FRC materials, specifically the role of fiber alignment and distribution.

1.7.3.2. Broader impacts

From an infrastructure and civil engineering perspective, understanding fracture properties and strain behaviors in construction materials is vital for designing safer and more resilient structures. As urban centers grapple with aging infrastructure, the implications of this research become even more pressing. Enhanced knowledge of the mechanical properties of extruded FRC can guide engineers in making informed decisions about material selection for future infrastructure projects. The findings could potentially lead to the development of stronger, longer-lasting, and more sustainable construction materials, thereby reducing maintenance costs, minimizing environmental impacts, and increasing public safety. Furthermore, insights from this chapter may stimulate innovations in other fields where FRC materials are employed, ensuring more durable and efficient applications across a multitude of industries.

1.7.4. Chapter 4: Flexural Toughness of Extruded Fiber-Reinforced Mortar with Preferentially Aligned Fibers

This chapter addresses Task 3, focusing on examining the flexural toughness properties of the extruded FRC using PVA fibers by establishing a modified ASTM C1609 test. This examination is compared against the conventional cast fiber reinforced concrete to underscore the influence of fiber alignment attained through pump extrusion. The novelty of this study is the quantification of the flexural properties of extruded FRC using the DIC technique. This manuscript was published in *Construction and Building Materials.*

1.7.4.1. Intellectual merit

This chapter promises a pioneering exploration into the flexural toughness properties of extruded FRC, especially when contrasted with conventional cast FRC. Currently, no standardized test method exists to quantify the toughness of extruded or 3D printed FRC, so this study innovated a modification of the existing ASTM C1609 test method. The emphasis on understanding the nuances of fiber alignment, as influenced by pump extrusion, extends the comprehension of how material fabrication methods can significantly influence mechanical properties. The standout feature of this research is the added strain quantification concurrently with flexural properties using DIC. This methodological approach is set to offer new insights into crack propagation and strain behaviors, especially in layer interfaces, providing a more detailed and nuanced perspective on material behavior than was previously available.

1.7.4.2. Broader impacts

The revelations regarding the flexural toughness properties of extruded FRC have profound implications for the world of construction and civil engineering. An enhanced understanding of

these properties can drive the creation of infrastructures that not only last longer but also better withstand environmental stresses, such extreme weather conditions. By introducing the potential for stronger and more resilient materials, this research can significantly reduce infrastructure repair and replacement costs in the long run, leading to sustainable urban development. Furthermore, the broader adoption of materials with superior flexural toughness could play a critical role in ensuring public safety, as structures become less susceptible to catastrophic failures. Given the ubiquity of FRC materials in various industries, the findings from this chapter might also stimulate advances in sectors beyond construction, promoting a wider societal impact.

1.7.5. Chapter 5: Size Effect of Fracture Properties of Extruded Fiber-Reinforced Mortar with Preferentially Aligned Fibers

This chapter tackles Task 4 by scrutinizing the size effects on fracture properties, specifically fracture energy and process zone size, of extruded FRC utilizing PVA fibers. It contrasts these properties with those of conventional cast FRC to highlight the impact of fiber alignment achieved *via* pump extrusion. The innovative aspect of this research lies in the detailed quantification of fracture properties of extruded FRC across different specimen sizes, offering valuable insights for industrial applications where larger specimens are utilized. The manuscript is in preparation for submission to a journal publication.

1.7.5.1. Intellectual merit

This chapter undertakes a critical examination of size effects on the fracture properties of extruded FRC using PVA, setting a new precedent in the study of fiber-reinforced concretes. The comparative analysis against conventional cast FRC brings to light the significant impact of fiber alignment, a feature that is enhanced through pump extrusion techniques. The innovative aspect

of this research lies in its methodical quantification of fracture properties, particularly fracture energy and process zone size, across varying scales of specimen sizes. This approach not only addresses a gap in existing literature but also contributes to the nuanced understanding of how specimen size influences the mechanical behavior of FRCs, thereby refining predictive models and design principles.

1.7.5.2. Broader impacts

The findings from this chapter hold substantial potential for broad applications in the construction industry, especially in the design and implementation of large-scale infrastructure projects. By providing concrete data on how the fracture properties of extruded FRC change with specimen size, this research enables engineers and designers to make more informed decisions, optimizing the durability and resilience of structures. This could lead to the development of buildings and infrastructures that are better suited to withstand environmental stresses and loading conditions over time, significantly reducing maintenance and repair costs.

1.7.6. Chapter 6: Mechanical Performance of Extruded Functionally Graded Fiber-Reinforced Mortar with Targeted Fiber Injection

In alignment with Task 5, this chapter delves into the creation of a targeted fiber injection technique, which employs a conveyor system designed for integrating high-stiffness steel fibers into mortar directly at the nozzle just before extrusion. A thorough exploration of mechanical properties, encompassing both flexural and fracture characteristics of functionally graded FRC, is undertaken. XCT is also utilized to confirm the fiber dosage and fiber alignment in each extruded layer. This manuscript is under review for publication in *Cement and Concrete Composites.*

1.7.6.1. Intellectual merit

This chapter represents an innovative step forward in the domain of FRC fabrication techniques. By introducing a semi-automated targeted fiber injection method for integrating high-stiffness steel fibers, it challenges conventional practices and expands the opportunities in construction of functionally graded FRC, which has previously met significant limitations. This research's distinction lies in its various exploration, utilizing both DIC and the XCT to delve into the flexural and fracture properties of the extruded functionally graded FRC. The employment of XCT for assessing fiber dosage and orientation brings a novel level of detail and accuracy to the understanding of FRC, bridging the microscopic and macroscopic views of the material.

1.7.6.2. Broader impacts

The development of a new fabrication method that can potentially revolutionize the way FRC structures are constructed can garner significant societal implications. Structures made with such functionally graded FRCs could showcase enhanced durability and resilience, catering to the growing global need for sustainable infrastructure. The targeted fiber dosage and orientation in FRC specimens can lead to optimized designs, ultimately translating to cost savings for construction projects and reduced environmental footprints. As urbanization continues to accelerate worldwide, the benefits of such advancements in FRC technology could have far-reaching implications, not only in constructing safer urban landscapes but also in promoting a more sustainable approach to infrastructure development. This work can also serve as a precedent for other industries, encouraging them to rethink material fabrication techniques for enhanced performance and sustainability.

1.7.7. Chapter 7: Flexural Models Exploration for Functionally Graded Steel Fiber-Reinforced Mortar Considering Fiber Dosage and Orientation

As planned in Task 6, this chapter delves into the potential design opportunities afforded by utilizing the flexural models presented in the ER-465 and MC 2010 specifications to predict the flexural strength of FRC sections. Additionally, there is an emphasis on the formulation of a constitutive model, drawing from the data obtained from tests conducted on the notched beams as highlighted in Chapter 5. Given that the flexural models take into account the fiber's orientation factor, this chapter will explore this factor through the casting methodology used in Chapter 5 which involves using a targeted fiber injection technique in an extrusion-based system. This manuscript is in preparation for submission to a journal publication.

1.7.7.1. Intellectual merit

In the domain of FRC research, this chapter introduces a notable exploration by offering the potential of the flexural models to extruded concrete. The core merit lies in its attempt to predict the flexural strength of FRC sections using established specifications but in a novel application. The endeavor to formulate a constitutive model, rooted in empirical data from notched beam tests (as covered in Chapter 5), is a prove to this research's ambition to bridge theoretical knowledge with practical applications. The novel aspect of examining the fiber's orientation factor, especially when viewed through the lens of a distinct casting methodology, further amplifies this chapter's contribution to the field.

1.7.7.2. Broader impacts

Predicting the flexural strength of FRC sections with heightened accuracy can profoundly reshape the construction industry. Buildings, bridges, and various other infrastructure can be

designed with better reliability, leading to structures that are both safer and more cost-efficient. Through better understanding of the impact of fiber orientation through different casting methodologies, construction professionals can make more informed choices, resulting in optimized material utilization and, consequently, reduced waste. On a societal level, this can translate to more resilient infrastructure, thereby ensuring public safety and reducing the environmental impact linked with frequent repairs or replacements. Moreover, a clear understanding of the design opportunities offering from established models can be instrumental for educators, policymakers, and industry practitioners, boosting an environment of knowledge sharing and informed decision-making.

1.7.8. Chapter 8: Conclusions and Recommendations

This chapter offers a comprehensive overview of the five manuscripts covered in this dissertation. It outlines the significant points from each manuscript, presents recommendations for subsequent research endeavors, and underscores the practical implications derived from the research findings.

1.8. References

[1] Y. Akkaya, J. Picka, S.P. Shah, Spatial distribution of aligned short fibers in cement composites, Journal of Materials in Civil Engineering 12 (2000) 272–279.

[2] Y. Shao, S. Marikunte, S.P. Shah, Extruded fiber-reinforced composites, Concrete International 17 (1995) 48–53.

[3] Z. Li, B. Mu, T.P. Chang, C.-T. Hsu, Prediction of overall tension behavior of short fiber-reinforced composites, International Journal of Solids and Structures 36 (1999) 4071–4087. https://doi.org/10.1016/S0020-7683(98)00191-7.

[4] H. Stang, V.C. Li, Extrusion of ECC-material, in: Proc. of High Performance Fiber Reinforced Cement Composites, 1999: pp. 203–212.

[5] I. da Silva Brito, D. Alan Strauss Rambo, S. Martini, R. Pícolo Salvador, M. Fabrízio de Menezes Freitas, Flexural behavior of HPFRCC: Enhancing post-crack strength and

toughness by magnetic alignment of the reinforcement, Construction and Building Materials 269 (2021) 121265. https://doi.org/10.1016/j.conbuildmat.2020.121265.

[6] A. Abrishambaf, M. Pimentel, S. Nunes, Influence of fibre orientation on the tensile behaviour of ultra-high performance fibre reinforced cementitious composites, Cement and Concrete Research 97 (2017) 28–40. https://doi.org/10.1016/j.cemconres.2017.03.007.

[7] R. Mu, Y. Xue, L. Qing, H. Li, Y. Zhao, J. Zhou, J. Su, Preparation and mechanical performance of annularly aligned steel fiber reinforced cement-based composite pipes, Construction and Building Materials 211 (2019) 167–173. https://doi.org/10.1016/j.conbuildmat.2019.03.146.

[8] S. Xu, Y. Lyu, S. Xu, Q. Li, Enhancing the initial cracking fracture toughness of steel-polyvinyl alcohol hybrid fibers ultra high toughness cementitious composites by incorporating multi-walled carbon nanotubes, Construction and Building Materials 195 (2019) 269–282. https://doi.org/10.1016/j.conbuildmat.2018.10.133.

[9] A. Enfedaque, M.G. Alberti, J.C. Gálvez, Influence of Fiber Distribution and Orientation in the Fracture Behavior of Polyolefin Fiber-Reinforced Concrete, Materials 12 (2019) 220. https://doi.org/10.3390/ma12020220.

[10] C. Xie, M. Cao, M. Khan, H. Yin, J. Guan, Review on different testing methods and factors affecting fracture properties of fiber reinforced cementitious composites, Construction and Building Materials 273 (2021) 121766. https://doi.org/10.1016/j.conbuildmat.2020.121766.

[11] L. Ferrara, M. Di Prisco, M.G.L. Lamperti, Identification of the stress-crack opening behavior of HPFRCC: the role of flow-induced fiber orientation, in: Proceedings FraMCoS, 2010: pp. 1541–1550.

[12] S.-T. Kang, J.-K. Kim, Investigation on the flexural behavior of UHPCC considering the effect of fiber orientation distribution, Construction and Building Materials 28 (2012) 57–65. https://doi.org/10.1016/j.conbuildmat.2011.07.003.

[13] S.-T. Kang, J.-K. Kim, Numerical simulation of the variation of fiber orientation distribution during flow molding of Ultra High Performance Cementitious Composites (UHPCC), Cement and Concrete Composites 34 (2012) 208–217. https://doi.org/10.1016/j.cemconcomp.2011.09.015.

[14] L. Ferrara, N. Tregger, S.P. Shah, Flow-induced fiber orientation in SCSFRC: monitoring and prediction, in: Design, Production and Placement of Self-Consolidating Concrete, Springer, 2010: pp. 417–428.

[15] A. Noushini, M. Hastings, A. Castel, F. Aslani, Mechanical and flexural performance of synthetic fibre reinforced geopolymer concrete, Construction and Building Materials 186 (2018) 454–475. https://doi.org/10.1016/j.conbuildmat.2018.07.110.

[16] M. Maalej, V.C. Li, Flexural/tensile-strength ratio in engineered cementitious composites, Journal of Materials in Civil Engineering 6 (1994) 513–528. https://doi.org/10.1061/(ASCE)0899-1561(1994)6:4(513).

[17] S.P. Yap, C.H. Bu, U.J. Alengaram, K.H. Mo, M.Z. Jumaat, Flexural toughness characteristics of steel–polypropylene hybrid fibre-reinforced oil palm shell concrete, Materials & Design 57 (2014) 652–659. https://doi.org/10.1016/j.matdes.2014.01.004.

[18] J. Li, J. Chen, C. Wan, J. Niu, Flexural toughness and evaluation method of steel fiber reinforced self-compacting lightweight aggregate concrete, Construction and Building Materials 277 (2021) 122297. https://doi.org/10.1016/j.conbuildmat.2021.122297.

[19] Y. Zhang, F. Aslani, Development of fibre reinforced engineered cementitious composite using polyvinyl alcohol fibre and activated carbon powder for 3D concrete printing, Construction and Building Materials 303 (2021) 124453. https://doi.org/10.1016/j.conbuildmat.2021.124453.

[20] J. Roesler, G. Paulino, C. Gaedicke, A. Bordelon, K. Park, Fracture Behavior of Functionally Graded Concrete Materials for Rigid Pavements, Transportation Research Record 2037 (2007) 40–49. https://doi.org/10.3141/2037-04.

[21] R. Mu, H. Li, L. Qing, J. Lin, Q. Zhao, Aligning steel fibers in cement mortar using electro-magnetic field, Construction and Building Materials 131 (2017) 309–316. https://doi.org/10.1016/j.conbuildmat.2016.11.081.

[22] L. Liu, J. Xu, Y. Wang, T. Yin, H. Chu, Electrical and piezoresistive properties of steel fiber cement-based composites aligned by a magnetic field, J. Wuhan Univ. Technol.-Mat. Sci. Edit. 37 (2022) 229–240. https://doi.org/10.1007/s11595-022-2522-2.

[23] L. Ferrara, N. Ozyurt, M. di Prisco, High mechanical performance of fibre reinforced cementitious composites: the role of "casting-flow induced" fibre orientation, Mater Struct 44 (2011) 109–128. https://doi.org/10.1617/s11527-010-9613-9.

[24] H. Huang, X. Gao, L. Li, H. Wang, Improvement effect of steel fiber orientation control on mechanical performance of UHPC, Construction and Building Materials 188 (2018) 709–721. https://doi.org/10.1016/j.conbuildmat.2018.08.146.

[25] P. Kheml, K. Carrera, K. Künzel, V. Papež, R. Sovják, Summary of findings on magnetic orientation of fibers in cement composites, Materials Today: Proceedings 58 (2022) 1104–1107. https://doi.org/10.1016/j.matpr.2022.01.201.

[26] B. Mobasher, Mechanics of Fiber and Textile Reinforced Cement Composites, Release Date: Sept, 2011, 480 pp, 2011.

[27] W.D. Callister, D.G. Rethwisch, Callister's Materials science and engineering, 10th edition, Wiley, Hoboken, NJ, 2019.

[28] Y. Akkaya, J. Picka, S.P. Shah, Spatial distribution of aligned short fibers in cement composites, Journal of Materials in Civil Engineering 12 (2000) 272–279.

[29] A.E. Naaman, H.W. Reinhardt, Characterization of high performance fiber reinforced cement composites—HPFRCC, in: High Performance Fiber Reinforced Cement Composites, 1996: pp. 1–24.

[30] S.P. Shah, C. Ouyang, Mechanical behavior of fiber-reinforced cement-based composites, Journal of the American Ceramic Society 74 (1991) 2727–2953.

[31] G. Ma, Z. Li, L. Wang, F. Wang, J. Sanjayan, Mechanical anisotropy of aligned fiber reinforced composite for extrusion-based 3D printing, Construction and Building Materials 202 (2019) 770–783. https://doi.org/10.1016/j.conbuildmat.2019.01.008.

[32] L. Ferrara, N. Ozyurt, M. di Prisco, High mechanical performance of fibre reinforced cementitious composites: the role of "casting-flow induced" fibre orientation, Mater Struct 44 (2011) 109–128. https://doi.org/10.1617/s11527-010-9613-9.

[33] A. Abrishambaf, M. Pimentel, S. Nunes, Influence of fibre orientation on the tensile behaviour of ultra-high performance fibre reinforced cementitious composites, Cement and Concrete Research 97 (2017) 28–40. https://doi.org/10.1016/j.cemconres.2017.03.007.

[34] A. Enfedaque, M.G. Alberti, J.C. Gálvez, Influence of Fiber Distribution and Orientation in the Fracture Behavior of Polyolefin Fiber-Reinforced Concrete, Materials 12 (2019) 220. https://doi.org/10.3390/ma12020220.

[35] C. Xie, M. Cao, M. Khan, H. Yin, J. Guan, Review on different testing methods and factors affecting fracture properties of fiber reinforced cementitious composites, Construction and Building Materials 273 (2021) 121766. https://doi.org/10.1016/j.conbuildmat.2020.121766.

[36] R. Mu, H. Li, L. Qing, J. Lin, Q. Zhao, Aligning steel fibers in cement mortar using electro-magnetic field, Construction and Building Materials 131 (2017) 309–316. https://doi.org/10.1016/j.conbuildmat.2016.11.081.

[37] L. Ferrara, M. Di Prisco, M.G.L. Lamperti, Identification of the stress-crack opening behavior of HPFRCC: the role of flow-induced fiber orientation, in: Proceedings FraMCoS, 2010: pp. 1541–1550.

[38] A.C. Bordelon, J.R. Roesler, Spatial distribution of synthetic fibers in concrete with X-ray computed tomography, Cement and Concrete Composites 53 (2014) 35–43. https://doi.org/10.1016/j.cemconcomp.2014.04.007.

[39] X. Sun, J. Zhou, Q. Wang, J. Shi, H. Wang, PVA fibre reinforced high-strength cementitious composite for 3D printing: Mechanical properties and durability, Additive Manufacturing 49 (2022) 102500. https://doi.org/10.1016/j.addma.2021.102500.

[40] Y. Shao, S. Marikunte, S.P. Shah, Extruded fiber-reinforced composites, Concrete International 17 (1995) 48–53.

[41] Z. Li, B. Mu, T.P. Chang, C.-T. Hsu, Prediction of overall tension behavior of short fiber-reinforced composites, International Journal of Solids and Structures 36 (1999) 4071–4087.

[42] H. Takashima, K. Miyagai, T. Hashida, V.C. Li, A design approach for the mechanical properties of polypropylene discontinuous fiber reinforced cementitious composites by extrusion molding, Engineering Fracture Mechanics 70 (2003) 853–870. https://doi.org/10.1016/S0013-7944(02)00154-6.

[43] X. Zhou, Z. Li, Characterizing rheology of fresh short fiber reinforced cementitious composite through capillary extrusion, Journal of Materials in Civil Engineering 17 (2005) 28–35.

[44] Y. Zhang, F. Aslani, Development of fibre reinforced engineered cementitious composite using polyvinyl alcohol fibre and activated carbon powder for 3D concrete printing, Construction and Building Materials 303 (2021) 124453. https://doi.org/10.1016/j.conbuildmat.2021.124453.

[45] J. Ye, C. Cui, J. Yu, K. Yu, F. Dong, Effect of polyethylene fiber content on workability and mechanical-anisotropic properties of 3D printed ultra-high ductile concrete, Construction and Building Materials 281 (2021) 122586. https://doi.org/10.1016/j.conbuildmat.2021.122586.

[46] M. Sugavaneswaran, G. Arumaikkannu, Modelling for randomly oriented multi material additive manufacturing component and its fabrication, Materials & Design (1980-2015) 54 (2014) 779–785. https://doi.org/10.1016/j.matdes.2013.08.102.

[47] H. Stang, V.C. Li, Extrusion of ECC-material, in: Proc. of High Performance Fiber Reinforced Cement Composites, 1999: pp. 203–212.

[48] S.C. Paul, Y.W.D. Tay, B. Panda, M.J. Tan, Fresh and hardened properties of 3D printable cementitious materials for building and construction, Archives of Civil and Mechanical Engineering 18 (2018) 311–319. https://doi.org/10.1016/j.acme.2017.02.008.

[49] X. Qian, X. Zhou, B. Mu, Z. Li, Fiber alignment and property direction dependency of FRC extrudate, Cement and Concrete Research 33 (2003) 1575–1581.

[50] Z. Li, B. Mu, Innovations forum: Application of extrusion for manufacture of short fiber reinforced cementitious composite, Journal of Materials in Civil Engineering 10 (1998) 2–4. https://doi.org/10.1061/(ASCE)0899-1561(1998)10:1(2).

[51] Z. Hou, X. Tian, J. Zhang, D. Li, 3D printed continuous fibre reinforced composite corrugated structure, Composite Structures 184 (2018) 1005–1010. https://doi.org/10.1016/j.compstruct.2017.10.080.

[52] S.P. Shah, Y. Shao, Extrusion processing of fiber-reinforced cement-matrix composites, Processing, Design, and Performance of Composite Materials 52 (1994) 205–210.

[53] X. Zhou, Z. Li, Characterization of rheology of fresh fiber reinforced cementitious composites through ram extrusion, Materials and Structures 38 (2005) 17–24. https://doi.org/10.1061/(ASCE)0899-1561(2005)17:1(28).

[54] S.-T. Kang, J.-K. Kim, Numerical simulation of the variation of fiber orientation distribution during flow molding of ultra high performance cementitious composites (UHPCC), Cement and Concrete Composites 34 (2012) 208–217.

[55] H. Huang, X. Gao, L. Li, H. Wang, Improvement effect of steel fiber orientation control on mechanical performance of UHPC, Construction and Building Materials 188 (2018) 709–721. https://doi.org/10.1016/j.conbuildmat.2018.08.146.

Chapter 2. Research Preparation

2.1. Mix Design Selection

Material selection is principal for the success of the pump extrusion-based method in Fiber-Reinforced Concrete (FRC). The inherent properties of the chosen materials have a reflective influence on the overall extrusion process. In this study, a fiber-reinforced mortar was selected, primarily because of the challenges associated with processing coarse aggregates through the pump. This mortar mix consists of Type I Portland cement, fine aggregates, water, and fibers. The specific material properties are detailed in Table 2.1. The moisture content of the fine aggregate was maintained at 0 % by drying it prior to use.

Table 2.1: Properties of Materials

Component	Specific Gravity	Absorption Capacity (%)	Moisture Content (%)	Fineness Modulus
Portland Cement	3.15	-	-	-
Fine Aggregate	2.57	3.6	0	2.6

2.1.1. Fiber Type Selection

To determine the optimal extrusion FRC, a series of trials were performed. Fabrication and mix designs were evaluated based on previous investigations, and additional mixed trials were carried out to identify the most suitable fiber type and volume fraction, ensuring seamless pumpability through the delivery systems. Although fibers generally enhance the tensile strength of the material, some studies indicate that excessive fiber content can adversely affect the printability of the mix [1–7]. For instance, previous research reveals that volume percentages of polyvinyl alcohol (PVA) fibers exceeding 1.5 % can lead to frequent blockages of the extrusion

nozzle [1,3,5,6]. Therefore, the fiber contents were selected considering a practical and realistic level that engineers could really employ in the field [8].

Given the significance of fiber types and their properties for fiber alignment in FRC using the pump extrusion-based method, this study evaluated 10 distinct types of fibers in terms of length, diameter, and materials. The findings are presented in Table 2.2. The optimal fiber properties for the FRC mix composition, detailed in Table 2.3, were derived through a series of optimization processes. The selection of PVA fibers with a length of 19 mm was based on their being the longest fibers that did not present issues during the mixing and pumping stages.

However, as the study progressed, an innovative approach was introduced, allowing for the post-extrusion injection of fibers into the mortar, a technique detailed in Chapter 6. This method accommodates the use of stiffer and longer fibers. Consequently, steel fibers, whose properties are listed in Table 2.4, were incorporated later in the research.

Table 2.2: Fiber Trial Result

Type	Length (mm)	Diameter (mm)	Aspect ratio	Mix Observation	Pumping Issues
Steel	30	0.38	80	Mix is separated in masses (balls)	- Stuck in the pumper - Stuck in the nozzle
Polypropylene	45	0.89	50	Acceptable mix	- Stuck in the pumper - Stuck in the nozzle
Carbon	13	-	-	Mix is separated in masses (balls)	- Difficult to pump since the mix contains some fiber balls
PVA	6	0.024	250	Perfectly mixed	No issues
PVA	19	0.2	95	Perfectly mixed	No issues
PVA	30	0.66	45	Perfectly mixed	- Fiber balls stuck in the entrance of the pumper - Stuck in the nozzle
Polypropylene /polyethylene	40	0.43	90	Acceptable mix	- Fiber balls stuck in the entrance of the pumper - Stuck in the nozzle
Polypropylene /polyethylene	32	0.43	75	Acceptable mix	- Fiber balls stuck in the entrance of the pumper -Stuck in the nozzle
Polypropylene /polyethylene	37	-	-	Acceptable mix	- Stuck in the pumper - Stuck in the nozzle
Polypropylene /polyethylene	19	-	-	Acceptable mix	- Fiber balls stuck in the entrance of the pumper - Stuck in the nozzle

Table 2.3: Properties of PVA Fibers

Length (mm)	**19**
Filament diameter (mm)	0.2
Aspect ratio	95
Specific gravity	1.3
Tensile strength (MPa)	1,000
Elongation (%)	6

Table 2.4: Properties of Steel Fibers

Length (mm)	**30**
Filament diameter (mm)	0.38
Aspect ratio	80
Specific gravity	7.8
Tensile strength (MPa)	3,070
Elongation (%)	1.5

2.2. Extrusion System

The extrusion process employed an electric pump, notably the Model P-25 from Machine Technologies, capable of producing pressures up to 2.1 MPa. This pump is equipped with a drive motor that turns a driving shaft located within a material hopper, a continuous cavity rotor-stator unit, and a dispensing head. When the drive motor activates the driving shaft rotation, the mixture is channeled to the dispensing head. This head features a downward nozzle set at a 45-degree angle. A visual representation of the pump components and its overall design can be viewed in Figure 2.1.

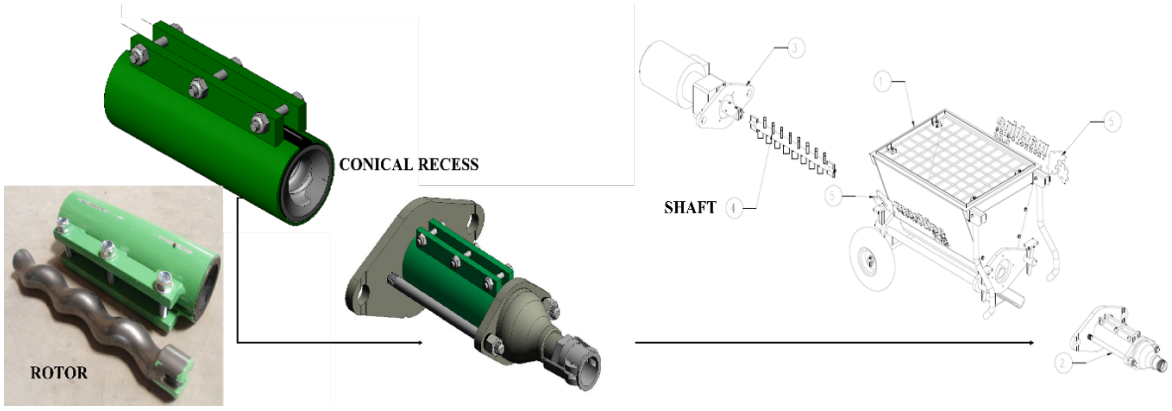

Figure 2.1: P-25 Pump Extrusion System

2.2.1. Nozzle Design and Fabrication

The design of the nozzle plays a crucial role in ensuring the effective delivery of both the fresh mixture and fibers, while preventing the random dispersion of fibers at the nozzle's end. Several factors were considered in the development of the end-effector nozzle:

i. The nozzle must be compatible with the adapter fixed to the pump.

ii. The design must incorporate a slope, from the top to the bottom, steep enough to ensure the fresh mixture flows efficiently into the mold. However, it should prevent sudden drops that could disrupt the alignment of the fibers by flow.

iii. The inner diameter of the pump extruder should not be reduced throughout the flow tunnel.

iv. Obstacles, such as bars or bumpers, that might cause fibers to become blocked should be absent.

v. The nozzle's material should be robust enough to withstand pressure build-up while remaining lightweight.

To be deemed effective, the nozzle had to meet the aforementioned criteria. During the design phase, several iterations of the nozzle were tested. In the initial attempt, only the nozzle head, depicted in Figure 2.2, was constructed and attached to the pump die. Though the head was fitted with a cast mold, manipulating the pump for nozzle insertion into the mold proved challenging. Moreover, the mixture extruded from the nozzle's end led to misaligned fibers. A subsequent design incorporated a plastic hose, commonly available in tool markets. This 3 ft hose, linking the pump and nozzle head, enhanced control over sliding and movement. Yet, the heat generated by the shaft and rotor's rapid rotation caused the plastic hose to degrade quickly once extrusion began. Seeking a more durable solution, a thicker and sturdier PVC hose replaced the plastic one, as shown in Figure 2.3. However, this PVC hose's rigidity hindered the bending of the nozzle head into the mold, rendering this adaptation unsatisfactory.

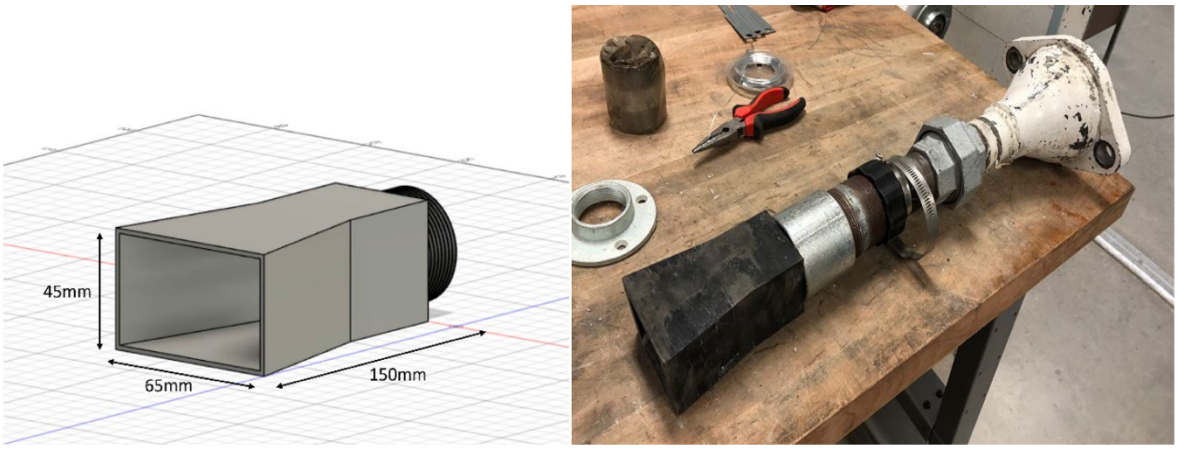

Figure 2.2: Initial Nozzle Head Design

Figure 2.3: Nozzle Design Attached to PVC Hose

The definitive nozzle design, illustrated in Figure 2.4, features a rectangular-shaped exit and seamlessly integrates into the beam mold. This nozzle was fabricated through 3D printing, utilizing polyethylene terephthalate glycol (PETG) filament as the printing material. In order to maintain fiber alignment and prevent their dispersion beyond the surface, the nozzle die was meticulously crafted to fit within the mold frame. This innovative design drew inspiration from previous studies, notably Shakor [9], which focused on enhancing the efficiency of printing cementitious materials. Furthermore, Huang's development of the L-shaped device [10] also informed this design. Employing this method ensures fiber alignment in accordance with the concrete flow direction and parallels the tensile stresses manifesting at the beam's base during bending tests.

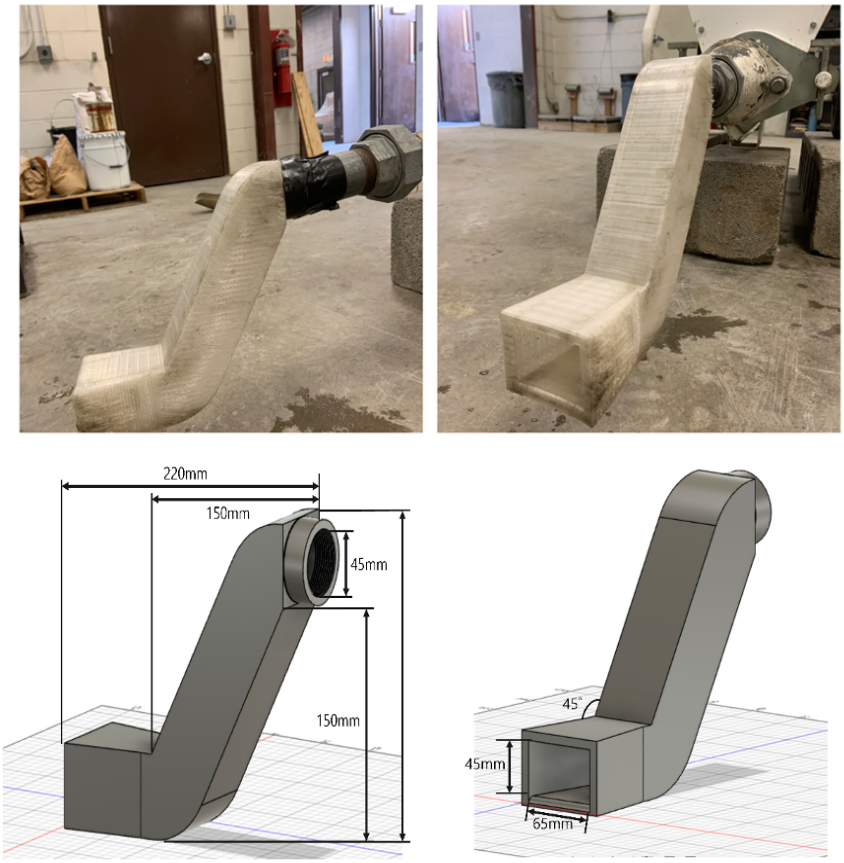

Figure 2.4: Extrusion-based Method's Nozzle Design

2.3. Mixing Procedure and Sample Preparations

Mortar mixes were prepared using two distinct methods: the conventional rodding compaction method, as detailed by ASTM C192 [11], and an extrusion-based casting approach. Pump extrusion size restrictions necessitated the use of only fine aggregate in these mixtures. Each mixture batch was designated a unique identifier to indicate the casting method used: CV for conventional cast and EB for extrusion-based cast.

For an in-depth analysis of the effects of the extrusion-based method on fiber alignment within FRCs, both the conventional cast and extrusion-based methods were conducted simultaneously using identical mix designs. The mixing materials were consistently maintained

across both casting methods, and all samples underwent storage in a single curing room with constant temperature and humidity conditions.

2.3.1. Conventional Cast Mix Method

The mixing process adhered to ASTM C192 standards but was adapted to incorporate fibers within the cementitious blend:

i. Dry Fine Aggregate Mixing: The fine aggregate was mixed dry for approximately 2 minutes or until uniformly combined. Half of the water allocation was then added.

ii. Portland Cement Integration: The Portland cement was blended into the aggregate and water mixture, with mixing continuing for 3 minutes.

iii. Water Addition: The remaining water was added gradually to reach the requisite consistency.

iv. Rest Period: The mixture was left to stand for 3 minutes, facilitating mixture settling and comprehensive ingredient incorporation.

v. PVA Fiber Addition: PVA fibers were introduced into the mixture, with an extended mixing duration of 5 minutes until achieving a smooth paste-like consistency.

Upon finalizing the mixing sequence, beam molds measuring 700 mm x 150 mm x 80 mm were prepared, a standard size utilized across all studies mentioned in this dissertation. Additionally, Chapter 5 introduced two alternative beam mold sizes: 280 mm x 60 mm x 80 mm and 1120 mm x 240 mm x 80 mm, to broaden the scope of the research. For compressive strength assessments, three cylinders specimens for each mix design, each with dimensions of 100 mm in diameter and 200 mm in height, were also prepared. All specimens were subsequently stored in a controlled environment with conditions set at 23°C and 95 % humidity. This 28-day period allowed

for optimal curing. Post-curing, the mechanical properties of the samples were thoroughly assessed.

2.3.2. Pump Extrusion Based Method

Following the preparation of the fresh mortar as detailed in Section 2.3.1, the mixture was loaded into the hopper of the P25 pump unit. This fresh mortar was then extruded through the delivery nozzle into steel molds of the dimensions previously mentioned. Subsequently, these samples underwent particular tests to assess their mechanical characteristics and confirm compliance with the set specifications and standards.

2.4. Experiment Setup

Experiments were conducted following the guidelines specified by RILEM recommendations [12] and ASTM C1609 [13]. The study utilized the digital image correlation technique to delve into the aspects of strain localization and crack progression within the beam specimens. Given that the width of the MTS Insight 150 SL electromechanical universal testing machine, used for the performing the mechanical tests, is less than the width of the beam, a custom support fixture was manufactured, as depicted in Figure 2.5, a configuration that was consistently used in all related studies within this dissertation. For the specific experiments described in Chapter 5, two additional support fixtures were designed and manufactured, showcased in Figure 2.6 and Figure 2.7, to accommodate the unique requirements of these tests.

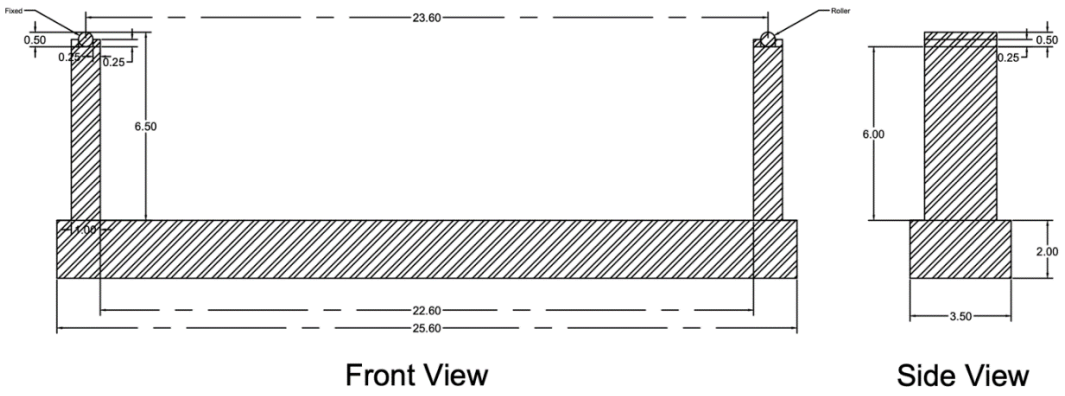

Figure 2.5: Specimen's Support Used in Testing (Used in All Studies)

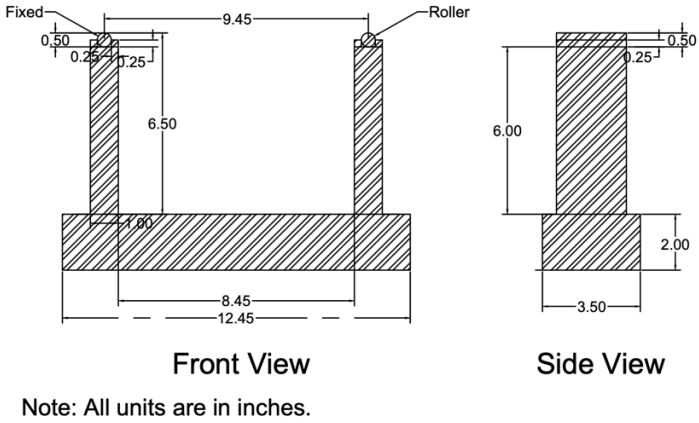

Figure 2.6: Small Specimen's Support Used in Testing (Used in Chapter 5)

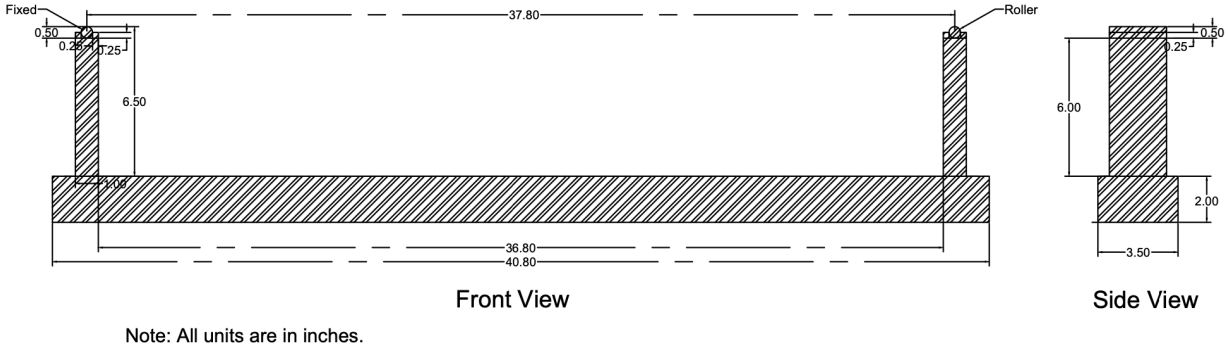

Figure 2.7: Large Specimen's Support Used in Testing (Used in Chapter 5)

2.4.1. Three-point Bending Fracture Test

Figure 2.8 illustrates the specifications of the three-point bending beam specimens. After undergoing moist curing for 27 days, a one-third notch, denoted as (a_o), was sawed into the mid-span of each beam, as represented in Figure 2.9. Fracture testing was conducted on the subsequent day. An 8 mm measurement-capacity clip-gauge was affixed to the notch's knife edges, as displayed in Figure 2.10.

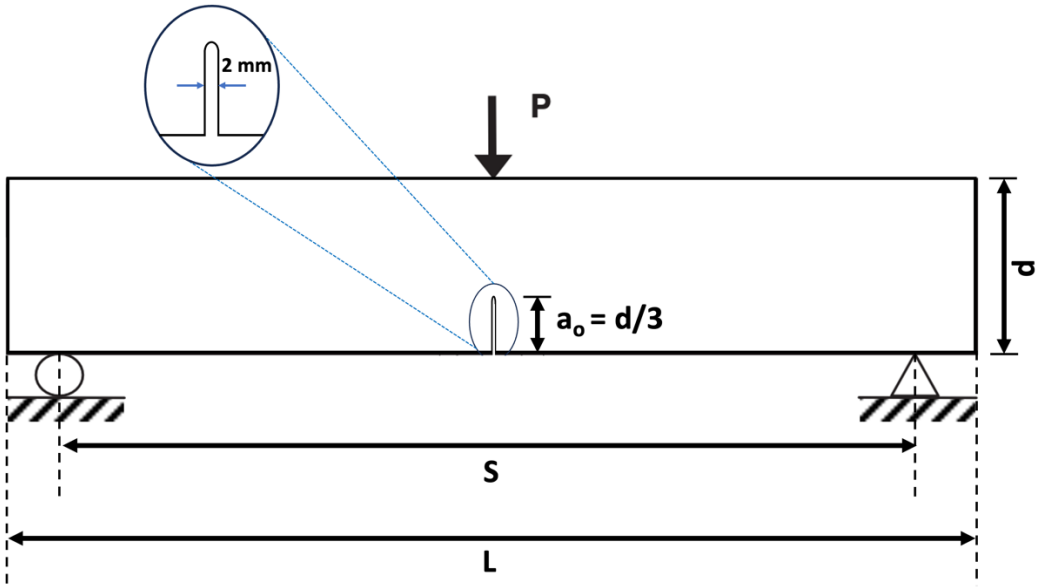

Figure 2.8: Test Setup of Three-point Bending Beam Specimen

Figure 2.9: Notched Beam's Specimens

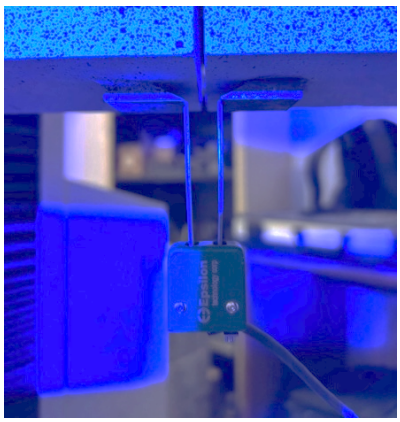

Figure 2.10: Clip Gauge Attached to the Knife Edges

2.4.2. Four-point Bending Flexural Test

Figure 2.11 shows the beam specimens used for the four-point bending test. Post 27 days of moist curing, each beam was equipped with a steel bar atop it. Flexural testing was executed the day after. A linear variable differential transducer (LVDT) device, equipped with a 6 mm measurement capacity, was positioned beneath the steel bar, as illustrated in Figure 2.12. This device was activated as the beam underwent deflection.

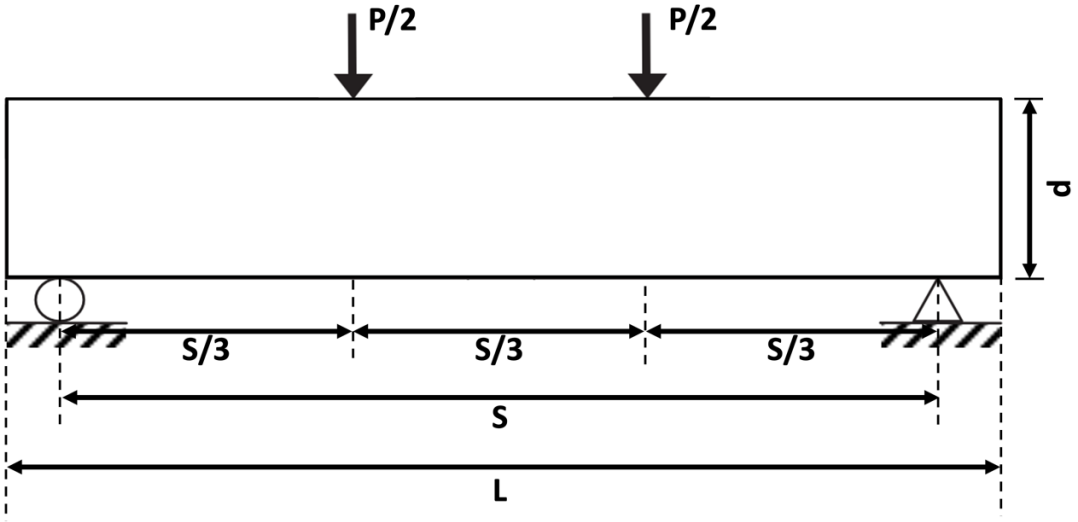

Figure 2.11: Test Setup of Four-Point Bending Beam Specimen

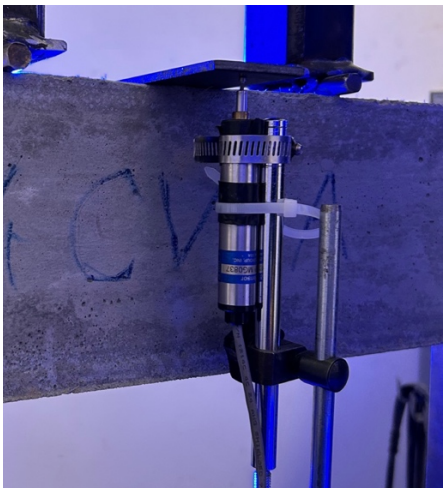

Figure 2.12: LVDT Placement in the Four-Point Bending Test

2.4.3. Digital Image Correlation Setup

For the implementation of DIC analysis, the specimen surface was sprayed with a random speckle pattern using both white and black paints, as demonstrated in Figure 2.13. Two digital cameras, depicted in Figure 2.14, were securely stationed on tripods in alignment with the testing machine, programmed to capture images at a rate of 0.1 Hz.

Subsequent 2D image correlation analyses were performed utilizing the commercial GOM™ software, which facilitated the measurement of in-plane deformations. The application of DIC provided insights into the movement of the speckle pattern, allowing for a comprehensive monitoring of the strain profile across the beam's depth. Within this research framework, DIC was employed to ascertain if the FRC specimen exhibited localized strains stemming from manufacturing inaccuracies or suboptimal bond at the layer interfaces. Moreover, this technique enabled observation of the crack propagation trajectory allowing to determine the type of fracture in the beam’s specimens.

Figure 2.13: Beam Specimen Prepared for DIC Analysis

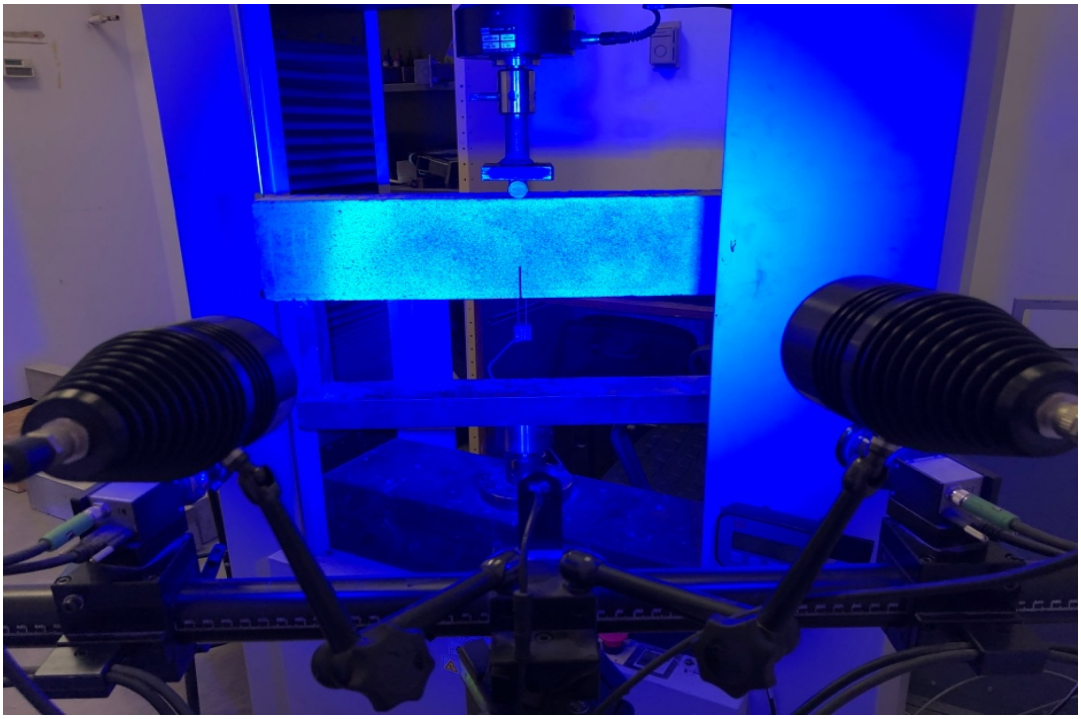

Figure 2.14: Two Digital Cameras Used in DIC

2.5. Experimental Testing Template's Development

Experimental testing templates are crucial for ensuring the accuracy and repeatability of material testing procedures. The advancements in the TW Elite software have enabled the development of more sophisticated testing templates, catering specifically to the flexural and fracture testing domains. The new templates have been enhanced to offer dynamic loading rate

adjustments in response to material behavior. With an emphasis on optimizing both insight and efficiency, these modifications allow for an improved analysis of material properties, while also expediting the overall testing duration. This section explores the details of the experimental testing template development using the TW Elite software, explaining the methodologies employed, and the advantages garnered from these advancements.

2.5.1. Fracture Test Template

The fracture test software template underwent modifications from its original form, which was primarily intended for compression testing. This template traditionally governed the crosshead to begin loading at a predetermined constant rate until failure. To add distinction to this process, additional procedures were introduced.

In the newly designed while loop structure, as represented in Figure 2.15, the crosshead initiates loading at an initial predefined rate. This continues until a manually determined unloading action is prompted. In this specific study, the decision for the initiation of this unloading action was set to occur at approximately 95 % of the peak load. Subsequent to this, the crosshead begins its unloading phase at a second predefined rate until the load reduces to a value defined as cycle_load_low (as shown in Figure 2.16). For the context of this study, the cycle_load_low value was established at 0.05 kN.

To ensure the safety and accuracy of the testing procedure, a pause interval was introduced between consecutive loading and unloading cycles. This was essential to prevent any abrupt mechanical actions which could compromise the integrity of the specimen or the test results. After this pause, the loading cycle restarts at its constant rate.

An instrumental feature of this modified template was its adaptability. Once the load-deflection curve starts to plateau post-peak, the loading rate can be incrementally increased by 0.02 mm/min. For this study, the loading rate commenced at 0.1 mm/min and culminated at 1.2 mm/min. This dynamic adaptability not only enhances the granularity of the test results but also restructures the testing process, reducing the average testing duration to a window of 40-60 minutes per specimen.

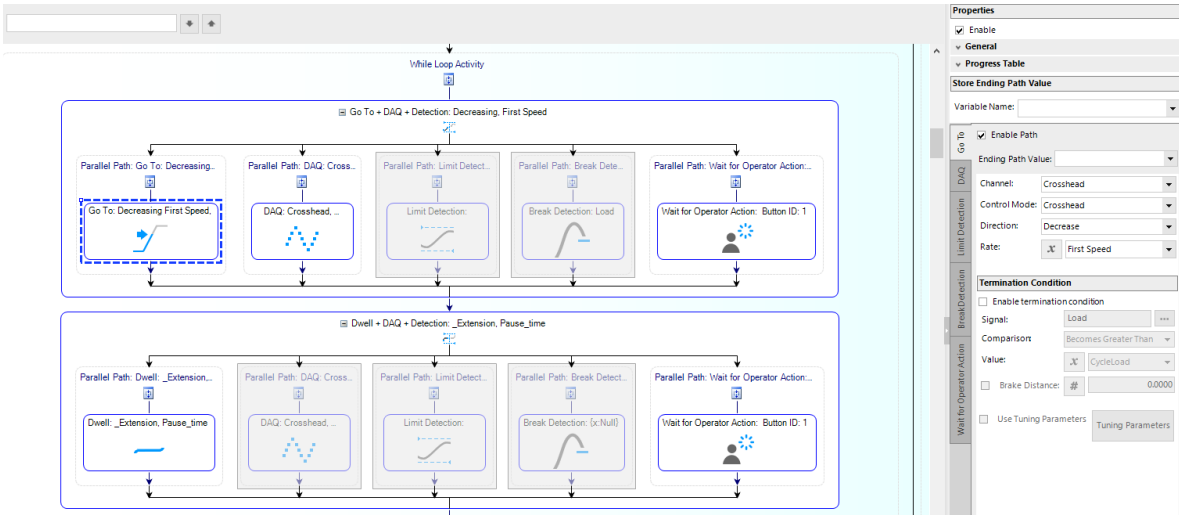

Figure 2.15: Loading Command in the Fracture Test Template

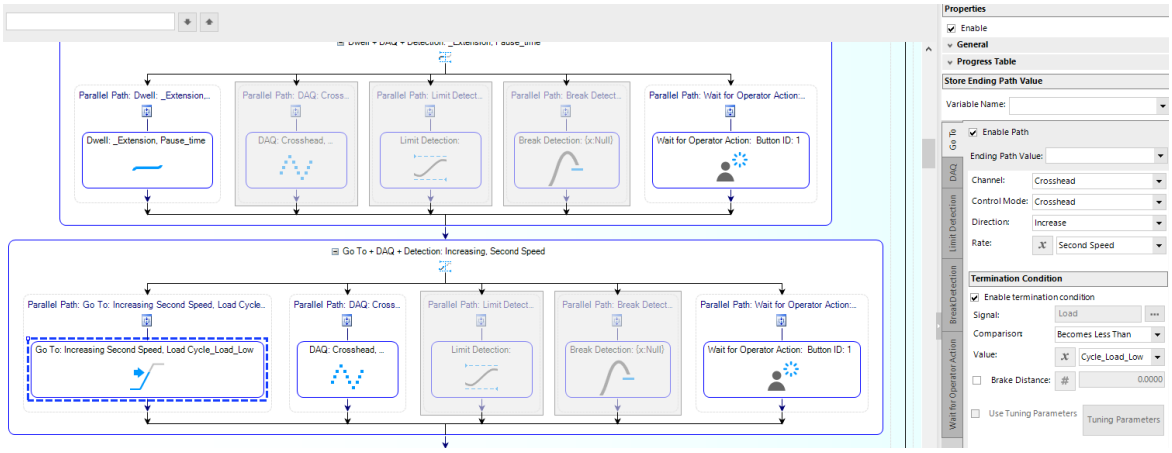

Figure 2.16: Unloading Command in the Fracture Test Template

2.5.2. Flexural Test Template

The flexural test template, originally established in the principles of a 4-point bending flexural test, has been improved to introduce advanced functionalities and precision. Traditionally, as seen in the original 4-point bending test, the crosshead would apply load at a predefined consistent rate, continuing this until the sample's point of fracture. The adapted procedure introduces more distinctions to this process.

According to the new template, outlined in Figure 2.17, the crosshead initiates the loading at a predefined rate. A distinctive feature of this revised template is its adaptability in response to the load-deflection curve behavior. When the curve starts to plateau post-peak, the system's loading rate can be dynamically augmented in increments of 0.02 mm/min. Specifically, for this study, the loading commenced at a rate of 0.1 mm/min and escalated to a maximum of 1.2 mm/min. The dynamic modification in loading rate can accelerate the test process, consolidating the typical testing duration to approximately 40 minutes to 60 minutes per specimen, hence optimizing resource utilization and time management.

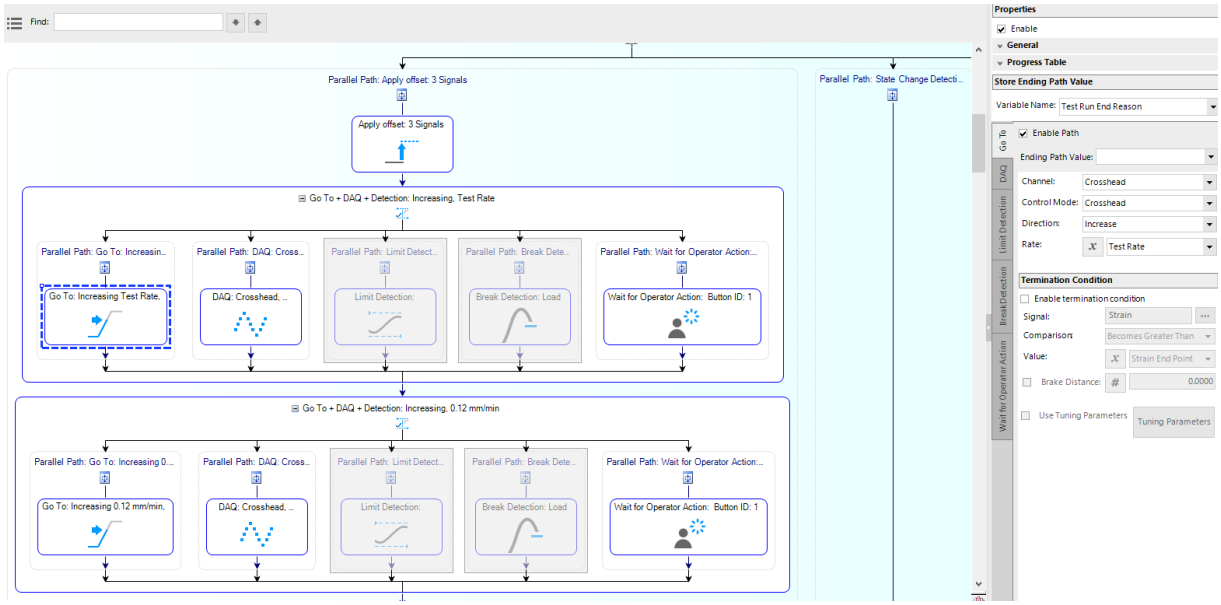

Figure 2.17: Loading Command in the Flexural Test Template

2.6. References

[1] Y. Zhang, F. Aslani, Development of fibre reinforced engineered cementitious composite using polyvinyl alcohol fibre and activated carbon powder for 3D concrete printing, Construction and Building Materials. 303 (2021) 124453. https://doi.org/10.1016/j.conbuildmat.2021.124453.

[2] X. Sun, J. Zhou, Q. Wang, J. Shi, H. Wang, PVA fibre reinforced high-strength cementitious composite for 3D printing: Mechanical properties and durability, Additive Manufacturing. 49 (2022) 102500. https://doi.org/10.1016/j.addma.2021.102500.

[3] G. Ma, Z. Li, L. Wang, F. Wang, J. Sanjayan, Mechanical anisotropy of aligned fiber reinforced composite for extrusion-based 3D printing, Construction and Building Materials. 202 (2019) 770–783. https://doi.org/10.1016/j.conbuildmat.2019.01.008.

[4] X. Qian, X. Zhou, B. Mu, Z. Li, Fiber alignment and property direction dependency of FRC extrudate, Cement and Concrete Research. 33 (2003) 1575–1581.

[5] V.C. Li, H.J. Kong, Y.-W. Chan, Development of Self-Compacting Engineered Cementitious Composites, (n.d.).

[6] J. Ye, C. Cui, J. Yu, K. Yu, F. Dong, Effect of polyethylene fiber content on workability and mechanical-anisotropic properties of 3D printed ultra-high ductile concrete, Construction and Building Materials. 281 (2021) 122586. https://doi.org/10.1016/j.conbuildmat.2021.122586.

[7] X. Zhou, Z. Li, Characterization of rheology of fresh fiber reinforced cementitious composites through ram extrusion, Materials and Structures. 38 (2005) 17–24.

[8] J. Roesler, G. Paulino, C. Gaedicke, A. Bordelon, K. Park, Fracture Behavior of Functionally Graded Concrete Materials for Rigid Pavements, Transportation Research Record. 2037 (2007) 40–49. https://doi.org/10.3141/2037-04.

[9] P. Shakor, S. Nejadi, G. Paul, A Study into the Effect of Different Nozzles Shapes and Fibre-Reinforcement in 3D Printed Mortar, Materials. 12 (2019) 1708. https://doi.org/10.3390/ma12101708.

[10] H. Huang, X. Gao, L. Li, H. Wang, Improvement effect of steel fiber orientation control on mechanical performance of UHPC, Construction and Building Materials. 188 (2018) 709–721. https://doi.org/10.1016/j.conbuildmat.2018.08.146.

[11] ASTM C192 Standard Practice for Making and Curing Concrete Test Specimens in the Laboratory, (n.d.).

[12] RILEM Committee, Determination of fracture parameters (KIC and CTODC) of plain concrete using three-point bend tests, Materials and Structures. 23 (1990) 457–760. https://doi.org/10.1007/BF02472029.

[13] C1609/C1609M − 19a, Standard test method for flexural performance of fiber-reinforced concrete (Using beam with third-point loading), ASTM International, 2019. https://doi.org/10.1520/C1609_C1609M-19A.

Chapter 3. Fracture Properties of Extruded Fiber-Reinforced Mortar with Preferentially Aligned Fibers[1]

Abstract

The fracture properties of fiber-reinforced mortar were determined in this paper using three-point bend tests on notched beams and employing the two-parameter fracture model (TPFM). A comparison was made between two casting methods: conventional casting and pump-driven extrusion. The hypothesis suggested that the extrusion process would preferentially align fibers parallel to the tensile stresses, thereby enhancing the concrete's fracture properties. The results corroborated the enhancement of concrete's ductility and post-peak behavior when fibers were added, consistent with previous studies. However, this study revealed a novel insight that preferential fiber alignment achieved through extrusion could further enhance the fracture properties of concrete. Furthermore, digital image correlation was used to obtain the entire displacement field during testing. The crack propagation process and the strain localization were investigated, and the fracture toughness considering crack deflection was calculated using a modified two parameter model (MTPM). The results showed that extrusion-based specimens exhibited more deflected cracks, affirming the hypothesis that fiber alignment *via* extrusion influenced the crack propagation, thereby enhancing the fracture properties of the composite.

Keywords: Fiber-reinforced concrete, Fracture, Digital image correlation, Extrusion, Fiber alignment, Crack propagation, Strain localization.

[1] **R. Alarrak**, B. Jeon, A.S. Brand, Fracture properties of extruded fiber-reinforced mortar with preferentially aligned fibers, Constr. Build. Mater. 403 (2023) 133022. https://doi.org/10.1016/j.conbuildmat.2023.133022.

3.1. Introduction

Fiber-reinforced concrete (FRC) is a cementitious composite material comprising Portland cement concrete and discrete fibers. This composition enhances its post-cracking performance, deformation capacity, and strength depending on the fiber type and dosage [1–5]. However, conventional concrete mixing and casting methods often lead to randomly-oriented fibers and even fiber-free zones, which reduce the effectiveness of the fibers [6]. For any fiber-reinforced composite, the effectiveness of fibers is maximized for their orientation parallel to the acting principal tensile stresses [7]. Various techniques to align the fibers in FRC have been proposed, including employing a magnetic field to align steel fibers [8–13] or modifying the casting method to align the fibers as the fresh concrete consolidates [3,6,14–16]. Recently, extrusion-based methods have emerged as a particularly promising method to fiber alignment [4,17–29].

During the 1990s and early 2000s, research on theoretical modeling and physical experimentation of extruded FRC was limited. Nonetheless, studies reported that FRC manufactured by an extrusion method using a ram or plunger showed a pseudo-strain-hardening behavior [17,18,24,30]. Some researchers reported that a typical extrusion process can, to some extent, influence the orientation of fibers in the cementitious matrix [26,23,29]. Takashima *et al*. investigated the extrusion effect using a ram extruder on fiber alignment in FRC embedded with polypropylene fibers, and they found that the extruded composites had approximately 80 % of the fibers aligned with the extrusion direction, when using fiber volume fractions ranging from 0 % to 8.4 % [19]. However, a fiber volume fraction greater than 3 % is often deemed impractical or uneconomical [21,31].

Various researchers have considered fiber alignment achieved through extrusion-based additive manufacturing methods. Ma *et al*. used a 3D printer to extrude a cementitious material

reinforced with basalt fibers, inducing fiber alignment along the print direction by ensuring the nozzle diameter to be smaller than the length of the fiber [27]. This method, however, resulted in weak interfaces and inevitable voids between the circular bead layers due to the layer-by-layer stacking process [22,25,27]. To prevent this weakness, Ye *et al*. used an extruder fitted with a rectangular-shaped nozzle to print FRC with polyethylene fibers, thereby avoiding inter-layer voids. They found that the sample with 1.0 % fiber content showed slightly enhanced tensile strain capacity compared to the conventional cast specimens. However, as the fiber content increased to 1.5 % and 2.0 %, a more twisted fiber orientation was observed, resulting in reduced tensile strength compared to the conventional cast specimens [22]. This distortion was reasoned to be caused by the high extrusion pressure at the nozzle [20]. These findings suggest that there could be potential rheological benefits to integrating the flow-induced casting method, which indicates aligning fibers as the fresh concrete flows during consolidation, with a pump extruder by utilizing a nozzle conveyor system to align fibers more effectively in the desired direction post-extrusion [15,32,33]. By employing a nozzle conveyor system from the pump pressure to extrusion, twisting of fibers due to the pump shaft rolling can be prevented [6,22,34]. Therefore, the nozzle-based pump extrusion system may effectively and mechanically enhance the alignment of fibers, leading to improved fracture properties of FRC structures in the designated direction [4,19,21,22,27].

Several studies have been performed on fiber orientation or dispersion since the early 1970s [30,35,36]. Fibers can be considered “fully oriented” when they lie within ±20° of the extrusion direction [27]. If fiber alignment along the flow of mixture could be predicted, then it becomes possible to control the fiber direction of FRC resulting in improvement of its structural properties [15,32,37]. This is because fibers orientation significantly affects the mechanical performance of FRC, including peak load, fracture toughness, and fracture energy [6,13,38,39].

To investigate the fracture behavior of FRC with oriented fibers, this study employed digital image correlation (DIC) technology. DIC, a non-contact and non-interferometric optical method, measures the displacement and deformation of specimens under external load. Additionally, it provides a visual representation of crack development in fracture tests. One of the significant advantages of the DIC is its ability to provide high-resolution full-field surface displacement/strain data that are difficult to obtain using conventional strain gauge measurement [40–46,22,47]. Because DIC can clearly illustrate the progression of flexural tests, it was employed to monitor the surface strain field and its transient changes occurring post-cracking [43]. Jenkins *et al*. used DIC to monitor localized strain at layer interfaces in 3D printed beams during flexural tests, which allowed them to analyze and determine the fracture mode of their specimens [47].

Given the heterogeneity of concrete and the presence of fibers, the actual crack trajectory may deviate from the initially originated primary crack [48]. Therefore, Carpinteri *et al*. created a modified two-parameter model (MTPM) based on the two-parameter fracture model (TPFM) and investigated the effect of crack deflection on fracture toughness [49]. The mechanism of crack deflection occurs when a crack propagates through the concrete matrix and encounters a fiber. The fiber functions as a barrier that deflects the crack path, absorbing energy and preventing its propagation. This deflection leads to the formation of a secondary crack that deviates at an arbitrary angle (θ) from the primary crack, resulting in a mixed mode fracture toughness (K_{I+II}). To consider K_{I+II}, the full field surface strain data obtained via DIC was used to capture the critical crack length for the mixed mode fracture.

3.1.1. Research Objective

This study advanced the state-of-the-art in developing an effective extrusion-based method for achieving fiber alignment. The fracture properties of conventionally cast and extruded FRC

with polyvinyl alcohol (PVA) fibers were investigated. The use of DIC was also demonstrated to be effective in evaluating the TPFM and the MTPM for these composites. The novelty of this study lies in its quantification of the fracture properties of extruded FRC through the employment of DIC, TPFM, and MTPM.

3.2. Experimental Methodology

3.2.1. Theoretical Background

Single-edge notched beams (SENB) were cast for measuring fracture properties according to the two-parameter fracture model (TPFM) [50,51], and the total fracture energy was computed according to the method proposed by Hillerborg [52]. With these combined fracture tests, the Mode I critical stress intensity factor (K_{IC}), the critical crack tip opening displacement ($CTOD_C$), the strain energy release rate (G_{IC}), and the total fracture energy (G_F) were determined using three-point bending tests.

Understanding the fracture properties of a material relies heavily on the critical effective crack length (a_c), which serves as a key determinant in predicting material failure due to stress-induced cracks. The load causing the specimen's fracture is defined as the peak load, and the concurrent crack length is denoted as the critical effective crack length. In a fracture event, the critical effective crack length signifies the point where a material's stress intensity factor aligns with its fracture toughness (K_{IC}).

All beam specimens were subjected to one cycle of loading and unloading to calculate K_{IC}, $CTOD_C$, and G_{IC}, from the loading and unloading compliances. When the load reached a peak and then decreased to about 95 % of the peak load, the specimen was unloaded manually. The specimen was then reloaded until failure. The loading compliance (C_i) was calculated as the inverse of the

slope of the loading curve. The unloading compliance (C_u) was calculated as the inverse of the slope of the unloading curve. The critical effective crack length (a_c) was calculated by equating the modulus of elasticity computed with the loading compliance (E_i) and the modulus of elasticity computed with the unloading compliance (E_u), which are presented in Equation 1 and Equation 2, respectively, where S is the span length, a_o is the initial notch depth, b is the width of the specimen, d is the depth of the specimen, α_o is the initial notch depth ratio, α_c is the critical notch depth ratio, and $g_2(\alpha)$ is the geometric factor of opening displacement defined in Equation 3.

$$E_i = \frac{6Sa_o g_2(\alpha_o)}{C_i b d^2} \tag{1}$$

$$E_u = \frac{6Sa_c g_2(\alpha_c)}{C_u b d^2} \tag{2}$$

$$g_2(\alpha) = 0.76 - 2.28\alpha + 3.87\alpha^2 - 2.04\alpha^3 + \frac{0.66}{(1-\alpha)^2} \tag{3}$$

The K_{IC} was calculated using Equation 4, where P_{max} is the peak load, W_o is the self-weight of the specimen, L is the length of the specimen, and $g_1(\alpha)$ is the geometric function defined in Equation 5. Finally, $CTOD_C$ and G_{IC} were computed according to Equations 6 and 7, respectively.

$$K_{IC} = 3\left(P_{max} + \frac{0.5W_o S}{L}\right)\frac{S\sqrt{\pi a_c}}{2bd^2} g_1\left(\frac{a_c}{d}\right) \tag{4}$$

$$g_1(\alpha) = \frac{1.99 - \alpha(1-\alpha)[2.15 - 3.93(\alpha) + 2.70(\alpha)^2]}{\sqrt{\pi}[1 + 2(\alpha)][1 - (\alpha)]^{\frac{3}{2}}} \tag{5}$$

$$CTOD_C = \frac{6Sa_c g_2\left(\frac{a_c}{d}\right)}{Ebd^2}\left(P_{max} + \frac{0.5W_o S}{L}\right)\left[\left(1 - \left(\frac{a_c}{a_o}\right)\right)^2 + \left(1.081 - 1.149\left(\frac{a_c}{d}\right)\right)\left(\left(\frac{a_c}{a_o}\right) - \left(\frac{a_c}{a_o}\right)^2\right)\right]^{\frac{1}{2}} \tag{6}$$

$$G_{IC} = \frac{K_{IC}^2}{E} \tag{7}$$

The SENB beams were also used for measuring the Mixed Mode (Mode I and Mode II) critical stress intensity factor (K_{I+II}) according to MTPM [49]. In this model, the critical effective crack length (a_c) was measured by considering the crack deflection mechanism, where the crack can be deviated at a deflection angle (θ) from the primary crack. Figure 3.1 represents the theoretical basics of both TPFM and MTPM in determining a_c. Therefore, a_c in the MTPM can be calculated using Equation 8, and K_{I+II} was then computed using Equation 4.

$$a_c = a_o + a\cos(\theta) \tag{8}$$

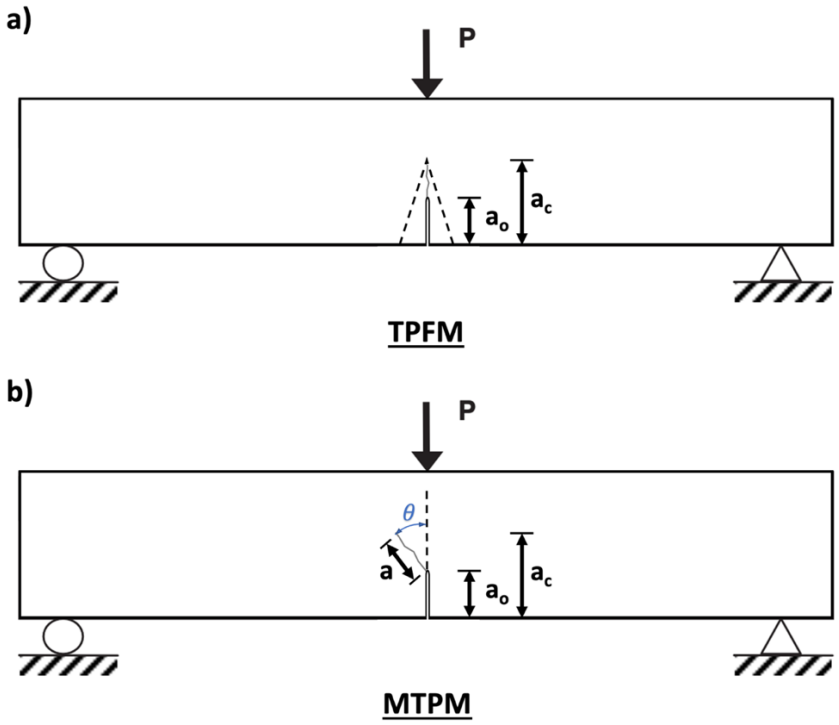

Figure 3.1: Theoretical Basics of: a) TPFM and b) MTPM in Determining the Critical Crack Length

According to the method developed by Hillerborg [52], the total fracture energy (G_F) can be defined as the ratio of the total energy (W_T) to the concrete fracture area ($(d - a_o)b$). The total

energy (W_T) is computed by adding the area under the load versus CMOD curve (W_r) to the equivalent self-weight force (P_w) multiplied by the CMOD value at failure when the load reaches zero (δ_f), as shown in Equation 9.

$$G_F = \frac{W_T}{(d - a_o)b} = \frac{W_r + 2P_w\delta_f}{(d - a_o)b} = \frac{W_r + \frac{W_o S}{L}\delta_f}{(d - a_o)b} \quad (9)$$

3.2.2. Mix Design and Properties

For this comparative study, two mortar mixtures were prepared with different PVA fiber dosages: 0.5 % and 1 % by volume. These fiber contents were selected because they are considered as a realistic level that engineers could really employ in the field [53]. Each mortar mix was cast using two methods: conventional casting according to ASTM C192 and extrusion-based casting. Only fine aggregate was used in the mixtures due to the aggregate size limitations of the pump for extrusion.

A general identification label has been assigned to each group of the mixtures. This label includes the casting method (CV = conventional cast and EB = extrusion-based cast) and the fiber volume (0.5 % or 1 %). Table 3.1 and Table 3.2 show the mixture proportions for each group and the fiber properties, respectively. The PVA fiber properties are reported by the manufacturer.

Table 3.1: Composite Mixture Proportions

Mixture ID	**CV0.5%**	**EB0.5%**	**CV1%**	**EB1%**
Type I cement (kg/m^3)	688	688	688	688
Fine aggregate (kg/m^3)	1042	1042	1042	1042
Water to cement ratio	0.40	0.40	0.40	0.40
PVA fiber volume	0.5%	0.5%	1%	1%

Table 3.2: Properties of PVA Fibers

Length (mm)	19
Filament diameter (mm)	0.2
Specific gravity	1.3
Tensile strength (MPa)	1,000
Flexural strength (MPa)	29,000

Three FRC cylinders of each fiber dosage were cast for measuring the compressive strength. Only conventionally cast mortar was used for compressive strength cylinders. Table 3.3 shows the compressive strength and statistics.

Table 3.3: Compressive Strength Results

Sample	**Compressive strength (MPa)**	**Average/ mean (MPa)**	**Standard deviation (MPa)**	**Coefficient of variation (%)**
0.5%_1	46.8	47.0	0.53	1.13
0.5%_2	46.6			
0.5%_3	47.6			
1%_1	45.2	45.7	0.60	1.31
1%_2	46.4			
1%_3	45.7			

3.2.3. Testing Program and Sample Preparation

Compressive strength was determined using ASTM C39 with only conventionally cast specimens. A total of three 4-inch (100 mm) diameter by 8-inch (200 mm) tall cylinders were tested for each mix after 28 days of moist curing.

Sixteen beams were cast, which included eight extrusion-based specimens and eight conventionally casted specimens. The eight specimens were divided into four specimens contained 0.5 % fiber content, and the other four specimens included 1 % fiber content. Figure 3.2 depicts

the test setup of three-point bending beam specimens. The beam dimensions were 700 mm by 150 mm by 80 mm, the initial notch depth (a_o) was 50 mm, and the span length was 600 mm. After 27 days of moist curing, each beam had a one-third notch saw-cut at the mid-span followed by fracture testing the next day.

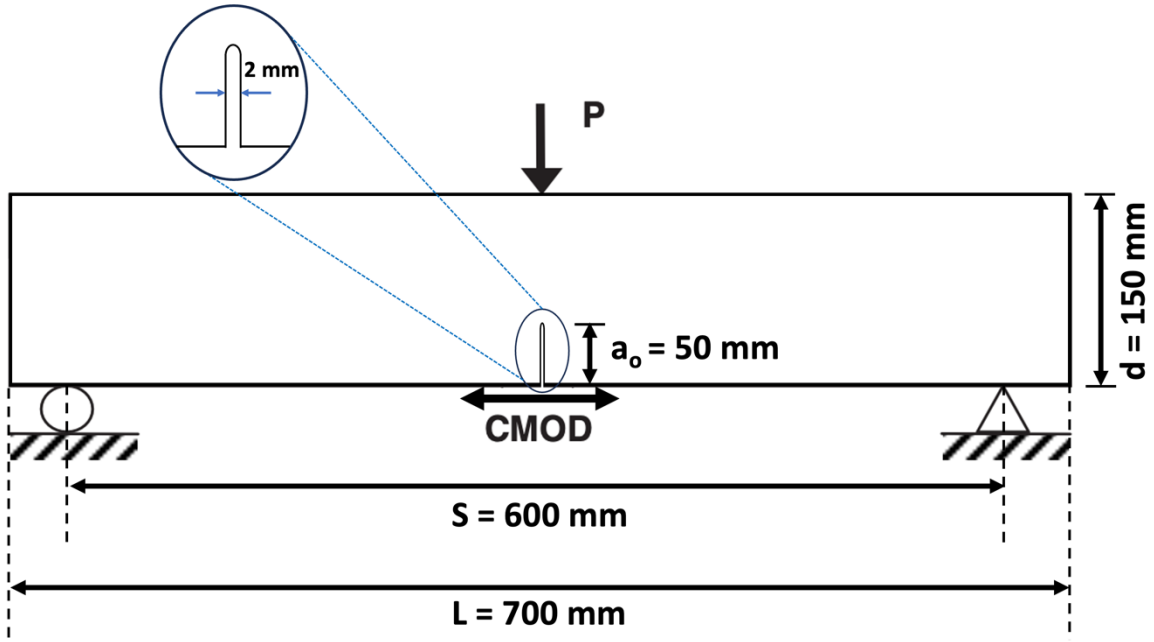

Figure 3.2: Test Setup of Three-point Bending Beam Specimen

The extrusion-based method was developed using electric pump capable of providing high pressure that can reach 2.1 MPa. A driving shaft inside a material hopper fed the mortar to a continuous cavity rotor stator pump unit, which transported the mix to the dispensing head where a custom-built nozzle was connected. The nozzle was 3D printed from polyethylene terephthalate and included a 45^o angle that was intended to force fiber alignment (Figure 3.3). Additionally, the nozzle was sized to fit the mold frame to prevent fibers from extending beyond the free surface.

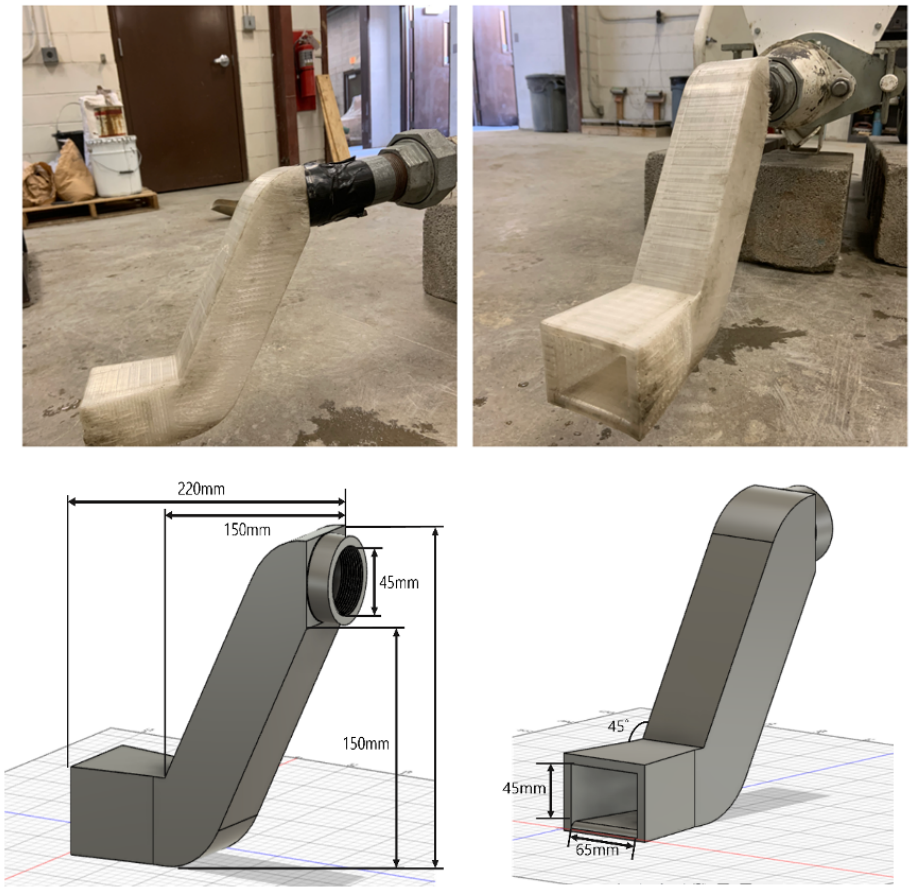

Figure 3.3: Extrusion-based Method's Nozzle Design

The EB and CV batches were mixed and cast at the same time. For EB specimens, the FRC was extruded into the beam mold by moving the pump along the mold's length, which resulted in having three layers of mortar placed in succession. No additional consolidation methods were used for the EB specimens. The CV specimens were cast according to ASTM C192.

The fracture tests were performed on an MTS Insight 150 SL electromechanical universal testing machine. The measurements in this study used a conventional clip gauge to measure the crack mouth opening displacement (CMOD). The clip gauge had a CMOD measurement capacity of 8 mm. Knife edges were installed under the notch to hold the clip gauge. All tests were performed at a displacement rate of 0.1 mm/min.

3.2.4. Digital Image Correlation

DIC is an optical technique that quantifies surface deformation across a specimen by analyzing sequential digital images captured during deformation. It operates by tracking pixel-level grayscale intensity changes between a reference and deformed image [54]. DIC employs a cross-correlation criterion to match pixel subsets between these images. This cross-correlation represents the similarity between two image subsets as they undergo relative displacement.

To conduct the DIC analysis, the specimen's surface was painted with a random speckle pattern using white and black spray paint as shown in Figure 3.4. This study employed a GOM ARAMIS DIC system. Two digital cameras, shown in Figure 3.5, were placed on a tripod in front of the testing machine and set to take digital images automatically at a frequency of 0.1 Hz. The working and sliding distances were 724 mm and 400 mm, respectively, which resulted in having a field of view of 420 mm by 320 mm by 320 mm and pixel size of 53 μm. 2D image correlation analyses were conducted using the commercial software GOM™ to measure the in-plane deformations. The software utilizes the normalized cross-correlation function to identify the deformed image subset that best aligns with each subset from the reference image, thereby computing displacement and strain fields.

DIC was used to monitor the deformation of the specimen’s surface, requiring several key components. A coordinate system with X, Y, and Z axes was established, and a surface component was constructed on the beam's surface facilitated data acquisition. An extensometer component, oriented in the X-direction, was installed at the notch base to collect the CMOD data.

The visualization and quantification of the FRC beam fracture characteristics were established using the DIC data coupled with the data from the MTS and clip gauge. A connection was established between the DIC computer and the MTS testing machine to read the load data

from the load cell. Additionally, the three-point bending test and DIC image capture processes were initiated concurrently to ensure that the bending test and DIC data were synchronized, thus meeting the data-correlation criteria. Using one specimen as an example, the strong correlation between the load-CMOD curves for both DIC and clip gauge data (Figure 3.6) verifies the accuracy of the DIC technique in measuring the displacement field. Even though a clip gauge was used to measure the CMOD, the post-peak CMOD extends beyond the range of the clip gauge, so DIC was used to monitor the post-peak CMOD.

Figure 3.4: Beam Specimen Used for Fracture Test

Figure 3.5: Two Digital Cameras Used in DIC

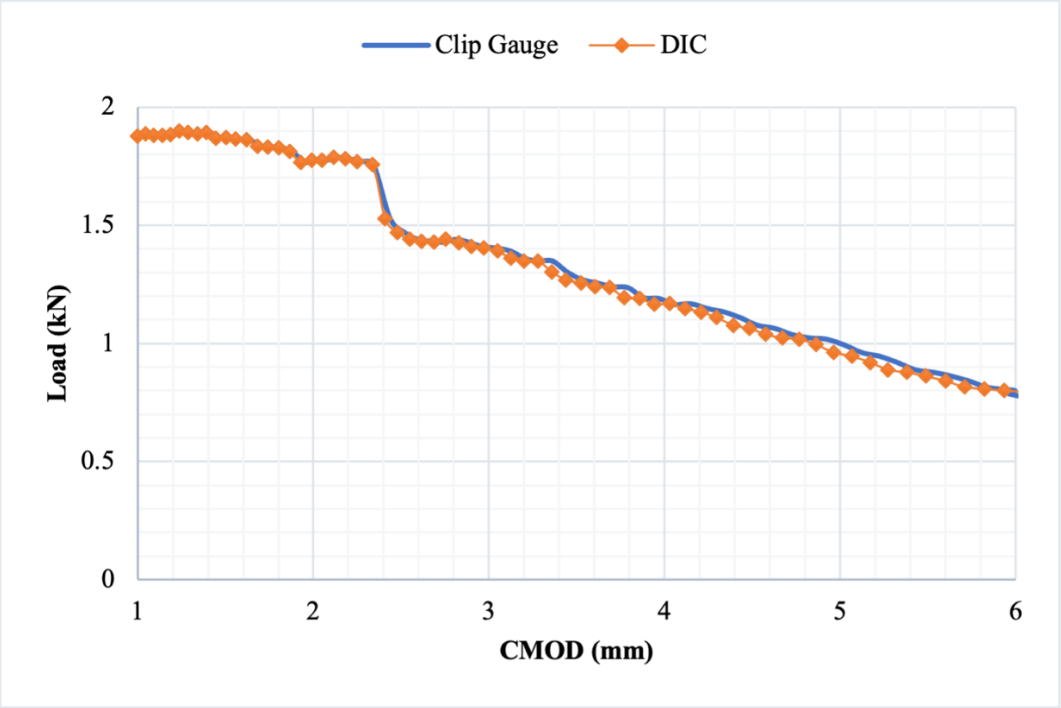

Figure 3.6: Load-CMOD Curves for DIC and Clip Gauge

The use of DIC made it possible to analyze the speckle pattern movement and monitor the strain profile along the depth of the beam and the CMOD simultaneously. In this study, the DIC was used to determine whether the FRC specimen exhibited localized strains due to manufacturing errors or poor bonding between the layer's interfaces. Through DIC, the crack propagation process was investigated, and the critical crack length was measured while taking into account the deflection angle. The crack length was measured at the point where the load-CMOD curve exhibited an abrupt decrease in load and a rapid increase in CMOD, which occurred in the region between the end of the elastic zone and the peak load [48]. As shown in Figure 3.7, the deflection angle (θ) is defined as the angle between the global axes (x and y) and the local axes of the initial crack tip (x' and y').

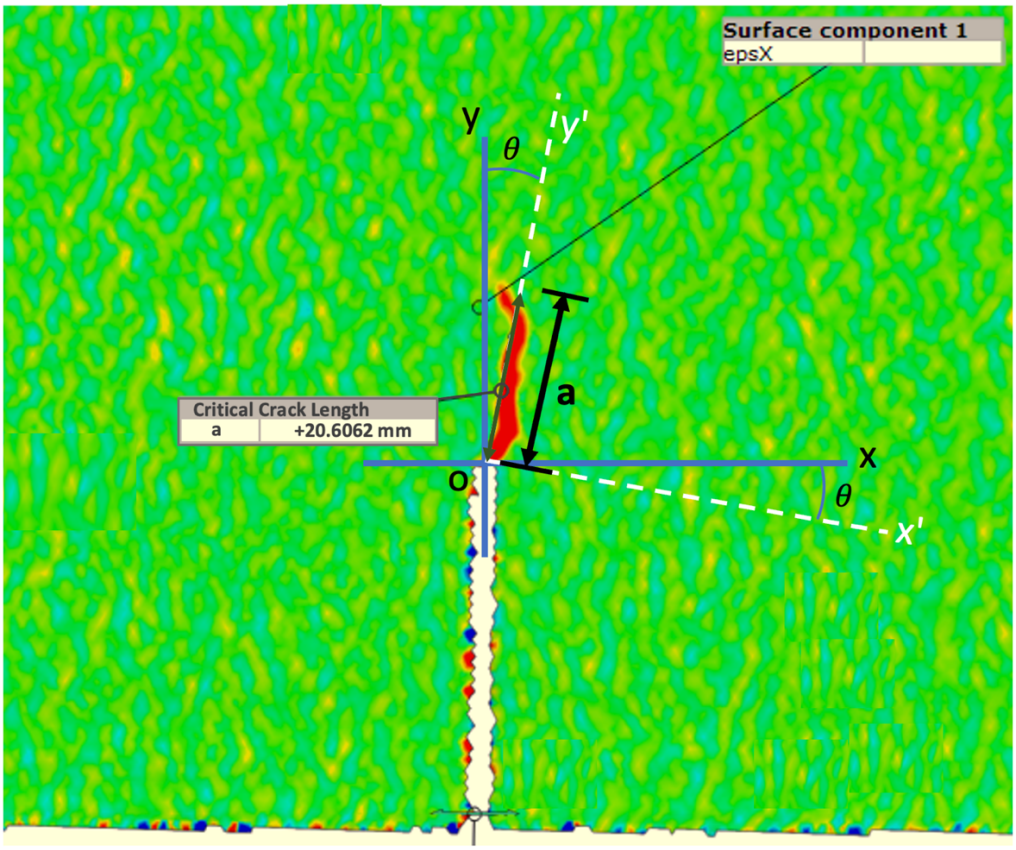

Figure 3.7: Experimental Technique for Determining the Critical Crack Length Using DIC

3.3. Test Results and Discussion

3.3.1. Fiber Orientation of Fractured Specimens

This study involved two distinct casting methods: conventional casting and pump-driven extrusion. It was hypothesized that the extrusion process would align fibers parallel to the tensile stresses, potentially enhancing the fracture properties of the concrete. To confirm this assumption, a detailed investigation of fractured specimens from both the extrusion-based (EB) and conventionally-cast (CV) methods was performed. This allowed for a rigorous assessment of the initial hypothesis. Figure 3.8 presents the front view of both a) EB and b) CV fractured specimens. In the EB specimen, it was evident that the majority of fibers were aligned along the length of the

beam. Conversely, the fibers in the CV specimen displayed a random orientation. This comparative analysis thus confirmed the initial hypothesis.

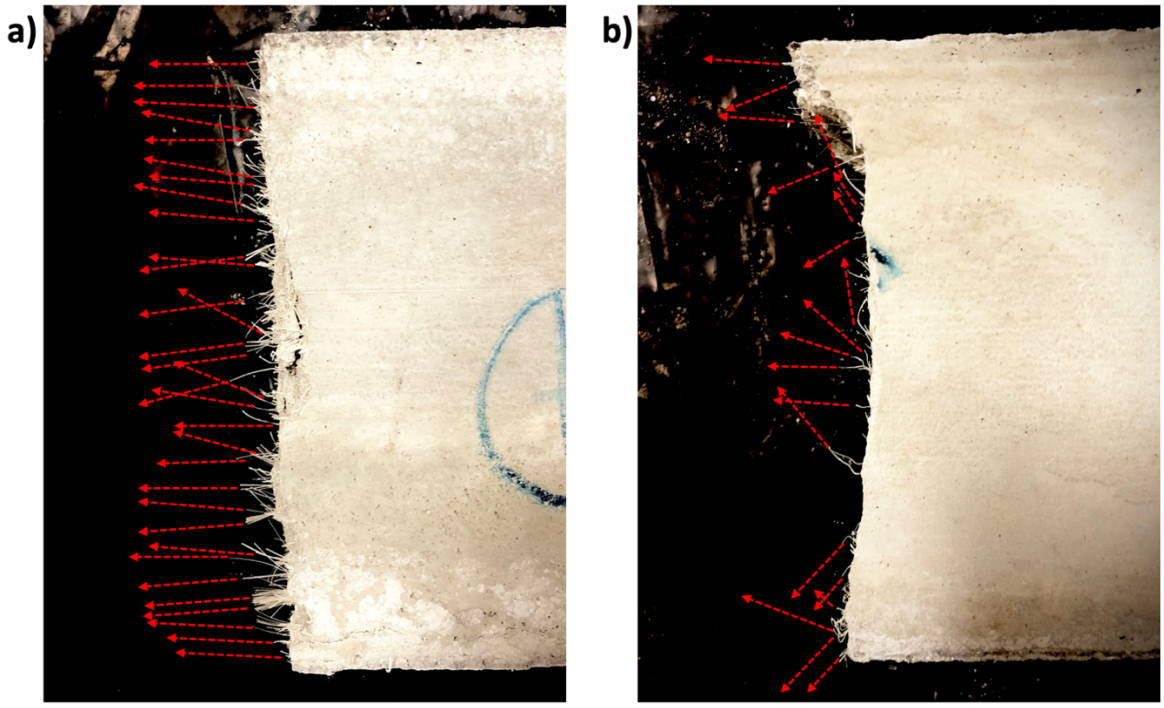

Figure 3.8: Front View of Fractured Specimens of: a) EB and b) CV

3.3.2. Fracture Properties

The results of P_{max}, K_{IC}, $CTOD_C$, and G_{IC}, using the TPFM, for both 0.5 % and 1 % fiber content specimens are presented in Table 3.4 and Table 3.5, respectively. Using a one-tailed paired t-test with a 95 % confidence interval, none of the means for the 0.5 % fiber content were statistically different between the CV and EB casting methods. However, for 1 % fiber content specimens, the K_{IC}, $CTOD_C$, and G_{IC} had greater means for the EB casting method than the CV casting method using a one-tailed paired t-test with 95 % confidence.

The values of K_{I+II}, using the MTPM, were computed and compared to the values of K_{IC} for both 0.5 % and 1 % fiber content specimens and presented in Table 3.6 and Table 3.7,

respectively. This comparison is intended to demonstrate how the crack deflection mechanism employs between CV and EB specimens. Two specimens, EB0.5%_1 and EB1%_4, exhibited two cracks, as shown in Figure 3.13 and Figure 3.14, respectively. The development of multiple cracks made it difficult to measure the critical crack length; therefore, these two specimens were ignored in the calculation of K_{I+II}. In CV0.5% and EB0.5% specimens, the increase in fracture toughness due to crack deflection mechanism were 11.8 % and 11.9 %, respectively. However, this improvement is considered insignificant based on the one-tailed paired t-test with 95 % confidence. On the other hand, when it comes to the 1 % fiber content specimens, the crack deflection mechanism showed a significant improvement in the fracture toughness of the EB specimens with an increase of 16.2 % compared to the fracture toughness without considering the crack deflection mechanism. This indicates that fibers, in EB specimens, were more effective in deflecting cracks since they were aligned perpendicular to the direction of the crack. Therefore, the extrusion-based casting method appears to be more effective at fiber alignment at higher fiber dosages. Figure 3.9 and Figure 3.10 represent the load-CMOD curve for 0.5 % and 1 % fiber content specimens, respectively.

Table 3.4: Fracture Properties of 0.5% FRC Specimens Using TPFM

Sample	$\boldsymbol{P_{max}}$ $(\boldsymbol{N})$	$\boldsymbol{K_{IC}}$ $\left(\boldsymbol{MPa\sqrt{m}}\right)$	$\boldsymbol{CTOD_C}$ $(\boldsymbol{mm})$	$\boldsymbol{G_{IC}}$ $(\boldsymbol{N/m})$
CV0.5%_1	2052	0.489	0.0129	31.26
CV0.5%_2	1844	0.713	0.0377	40.98
CV0.5%_3	2288	0.489	0.0149	32.88
CV0.5%_4	1536	0.435	0.0097	18.68
Mean	1930	0.532	0.0188	30.95
EB0.5%_1	2311	0.738	0.0209	35.22
EB0.5%_2	1687	0.495	0.0271	27.02
EB0.5%_3	2035	0.580	0.0159	25.99
EB0.5%_4	3175	1.079	0.0273	56.73
Mean	2302	0.723	0.0228	36.24

Table 3.5: Fracture Properties of 1% FRC Specimens Using TPFM

Sample	$\boldsymbol{P_{max}}$ $(\boldsymbol{N})$	$\boldsymbol{K_{IC}}$ $\left(\boldsymbol{MPa\sqrt{m}}\right)$	$\boldsymbol{CTOD_C}$ $(\boldsymbol{mm})$	$\boldsymbol{G_{IC}}$ $(\boldsymbol{N/m})$
CV1%_1	2524	0.664	0.0121	29.05
CV1%_2	2149	0.641	0.0145	21.14
CV1%_3	2263	0.633	0.0131	24.24
CV1%_4	1933	0.611	0.0122	20.85
Mean	2217	0.637	0.0130	23.82
EB1%_1	2407	0.736	0.0179	29.78
EB1%_2	2742	0.871	0.0223	48.16
EB1%_3	2570	1.018	0.0382	62.17
EB1%_4	2117	0.677	0.0222	33.04
Mean	2459	0.826	0.0252	43.29

Table 3.6: Fracture Toughness Modes Comparison of 0.5% FRC Specimens

	Mixed Mode (I+II)			**Mode I**		**Difference**
Sample	$\boldsymbol{\theta}$ (°)	$\boldsymbol{a_c}$ $(\boldsymbol{mm})$	$\boldsymbol{K_{I+II}}$ $\left(\boldsymbol{MPa\sqrt{m}}\right)$	$\boldsymbol{a_c}$ $(\boldsymbol{mm})$	$\boldsymbol{K_{IC}}$ $\left(\boldsymbol{MPa\sqrt{m}}\right)$	$\frac{\boldsymbol{K_{I+II}-K_{IC}}}{\boldsymbol{K_{IC}}}$
CV0.5%_1	31	64	0.589	54	0.489	
CV0.5%_2	21	77	0.720	76	0.713	
CV0.5%_3	42	59	0.571	53	0.489	
CV0.5%_4	40	70	0.503	63	0.435	
Mean	34	68	0.595	62	0.532	11.8%
EB0.5%_1	8	72	0.775	70	0.738	
EB0.5%_2	24	69	0.539	65	0.495	
EB0.5%_3	13	74	0.714	64	0.580	
EB0.5%_4	-	-	-	-	-	
Mean	15	72	0.676	66	0.604	11.9%

Table 3.7: Fracture Toughness Modes Comparison of 1% FRC Specimens

	Mixed Mode (I+II)			Mode I		Difference
Sample	$\boldsymbol{\theta}$ (°)	$\boldsymbol{a_c}$ $(\boldsymbol{mm})$	$\boldsymbol{K_{I+II}}$ $\left(\boldsymbol{MPa}\sqrt{\boldsymbol{m}}\right)$	$\boldsymbol{a_c}$ $(\boldsymbol{mm})$	$\boldsymbol{K_{IC}}$ $\left(\boldsymbol{MPa}\sqrt{\boldsymbol{m}}\right)$	$\frac{\boldsymbol{K_{I+II}-K_{IC}}}{\boldsymbol{K_{IC}}}$
CV1%_1	12	64	0.720	60	0.664	
CV1%_2	16	73	0.736	66	0.641	
CV1%_3	10	70	0.728	64	0.633	
CV1%_4	20	71	0.639	69	0.611	
Mean	15	70	0.706	65	0.637	10.8%
EB1%_1	-	-	-	-	-	
EB1%_2	24	81	1.109	70	0.871	
EB1%_3	6	85	1.143	80	1.018	
EB1%_4	11	73	0.726	70	0.677	
Mean	14	80	0.993	73	0.855	16.2%

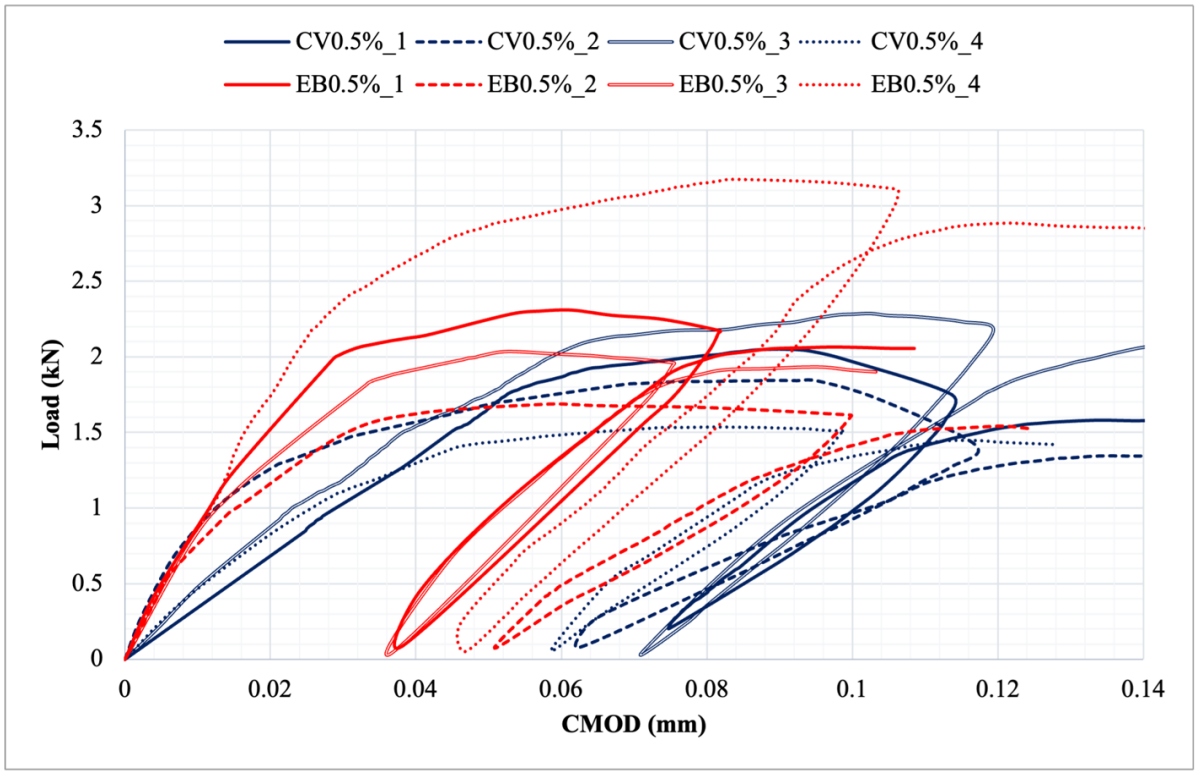

Figure 3.9: Load-CMOD Curve for 0.5% FRC Specimens

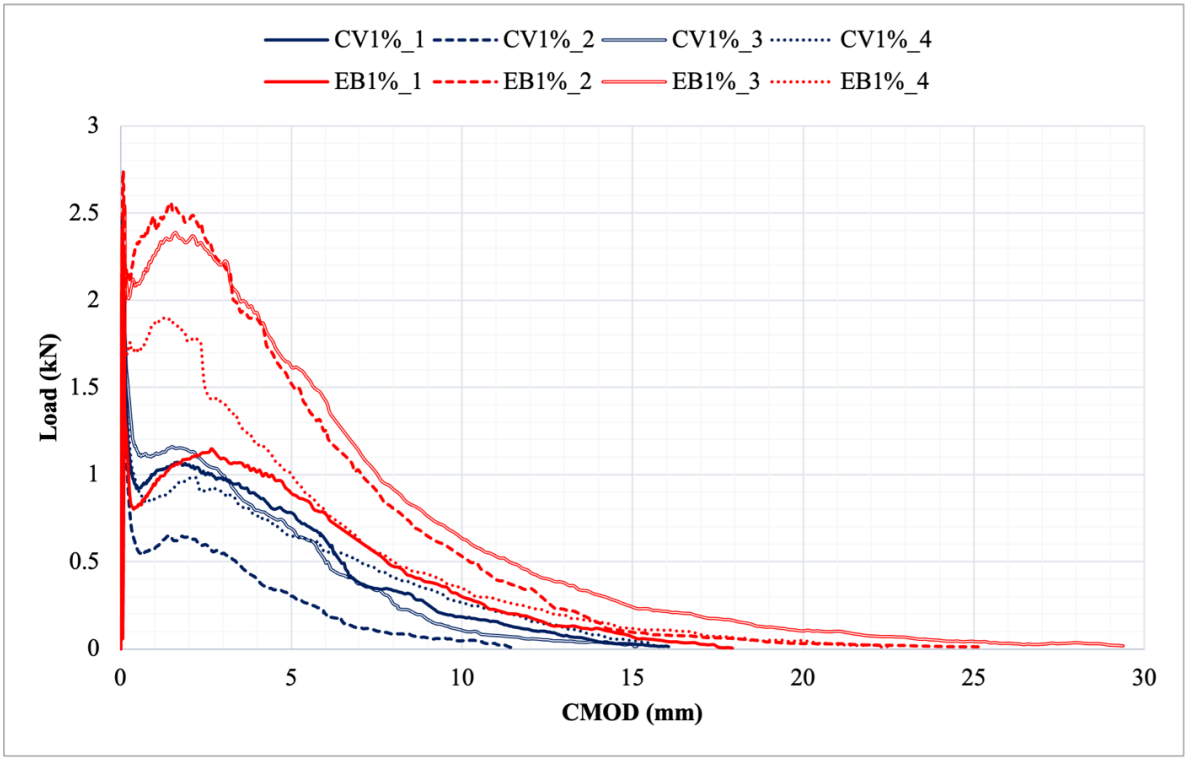

Figure 3.10: Load-CMOD Curve for 1% FRC Specimens

The fracture test results comparison of K_{IC} and K_{I+II} (Figure 3.11) demonstrates a trend contradicts the findings of a previous study [49]. The reason of this contradiction is that the previous study performed the fracture test on bone. Besides, in contrast to the current work where a_c was measured using the DIC technique, the MTPM was used in the previous study to calculate a_c theoretically. However, the current findings are consistent with other previous studies that had similar conditions [48]. Figure 3.12 represents a_c mean values for all FRC specimens considering mode I and mixed mode fracture toughness. a_c exhibited the same trend behavior in the FRC specimens for both fracture modes. In general, a_c is zero for a perfectly brittle material; however, due to the fact that fibers enhance the ductility of the material, it is natural that a_c increases with fiber content [55]. However, in this study, it seems that the extrusion-based method of casting had greater impact on increasing a_c values than the fiber content. This is presented by comparing the EB0.5% and CV1% specimens where the trend slightly increases in the EB0.5% specimens.

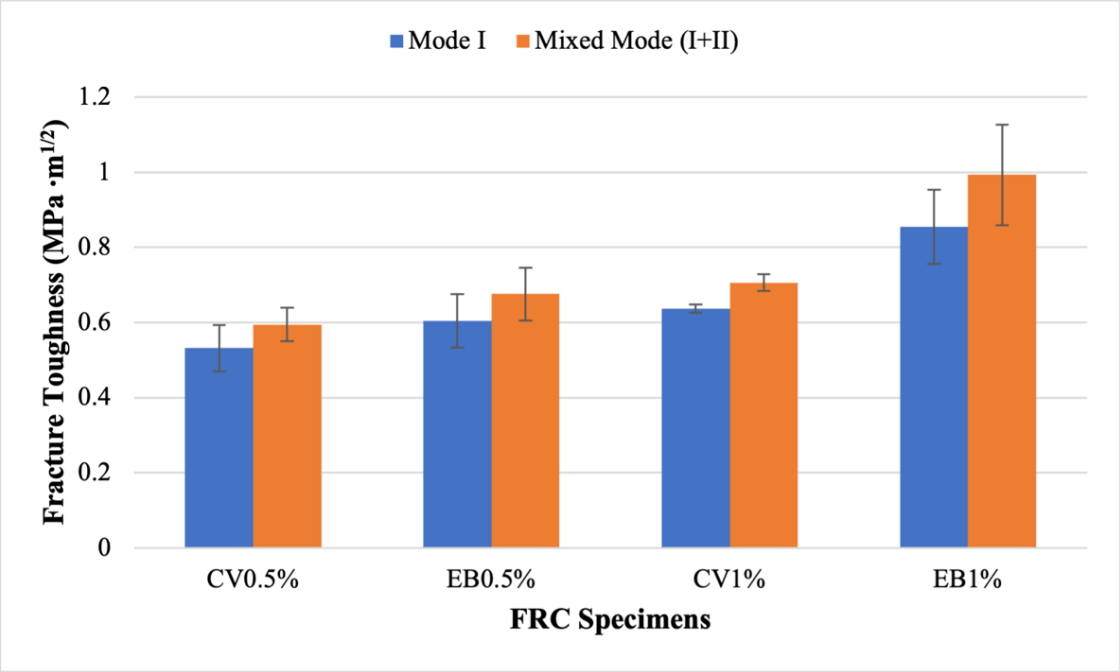

Figure 3.11: Fracture Toughness Comparison for all FRC Specimens

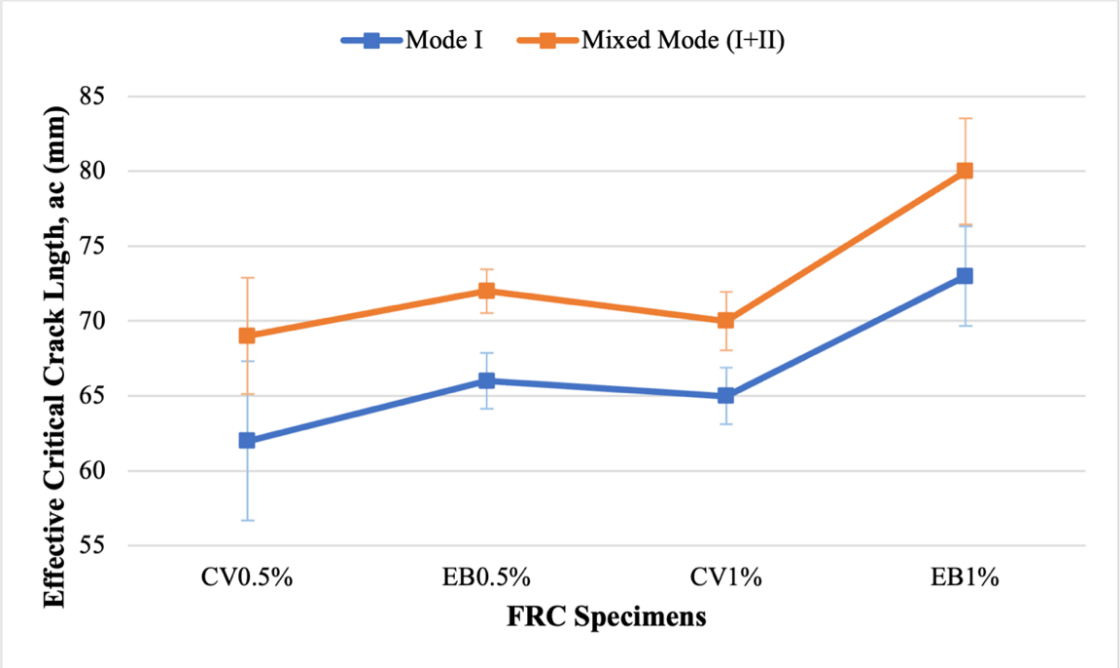

Figure 3.12: Effective Critical Crack Length Comparison for all FRC Specimens

3.3.3. Total Fracture Energy

The results of total fracture energy, shown in Table 3.8, considered only 1 % fiber content specimens. Data from a clip gauge was used to measure CMOD until the gauge's limit, after which the DIC data were used to compute CMOD. Using a one-tailed paired t-test, both δ_f and G_F had statistically greater means for the EB casting method than the CV casting method with 95 % confidence.

Table 3.8: Total Fracture Energy Results for 1% FRC Specimens

Sample	$\boldsymbol{\delta_f}$ $(\boldsymbol{mm})$	$\boldsymbol{G_F}$ $(\boldsymbol{N/m})$
CV1%_1	16.05	1323.9
CV1%_2	11.50	703.8
CV1%_3	15.13	1254.4
CV1%_4	15.74	1395.2
Mean	14.61	1169.3
EB1%_1	17.92	1544.8
EB1%_2	25.21	2890.2
EB1%_3	29.37	3211.2
EB1%_4	22.49	2017.2
Mean	23.75	2415.9

Because fibers can effectively bridge cracks, high values of CMOD at failure can be achieved. As shown in Figure 3.10, the fibers in EB1% specimens had a greater ability to bridge crack propagation compared to CV1% specimens. This is due to the fact that fibers were aligned along the direction of the concrete flow when EB method was used. Subsequently, the fibers were more efficient since they were oriented parallel to the tensile stresses. In contrast, in the CV way of casting, the fibers were randomly oriented in the beams.

There was no significant variance in the peak loads between the CV and EB ways of casting as shown in Table 3.5. However, when comparing the areas under the load–CMOD curves,

significant variances were observed. In Figure 3.10, it can be seen that the EB specimens had greater areas under the load–CMOD curves compared to the CV specimens. Also, the δ_f values were about 63 % higher in EB1% beams compared with CV1% beams. These reasons result in EB1% having a total fracture energy that is 107 % greater than CV1%. This concludes that the EB way of casting had significantly improved the fracture energy of FRC specimens.

3.3.4. Crack Propagation and Strain Localization

Critical phenomena occur during the fracture test of FRC beams, including crack propagation and strain localization. For the purpose of improving the performance of FRC structures, it is important to understand how cracks propagate and how strain localizes. In FRC, the function of fiber alignment in crack propagation is crucial. When fibers are aligned in a preferred direction, parallel to the tensile stresses, they can effectively bridge and deflect cracks, preventing their propagation. For strain localization, the layering technique used in the extrusion-based method may also introduce strain localization in the interfaces between layers, which might potentially serve as crack propagation pathways. In this section, both the crack propagation process and strain localization were investigated using the DIC technique.

The critical crack length was measured using the DIC and used to calculate the fracture toughness considering the crack deflection mechanism in the MTPM. Figure 3.13 and Figure 3.14 represent the critical crack length for 0.5 % and 1 % specimens, respectively. As it can be noticed, EB0.5%_4 and EB1%_1 specimens exhibited two cracks which made it difficult to measure the critical crack length.

Figure 3.13: Full Strain Field at the Critical Stage for 0.5% Fiber Content Specimens

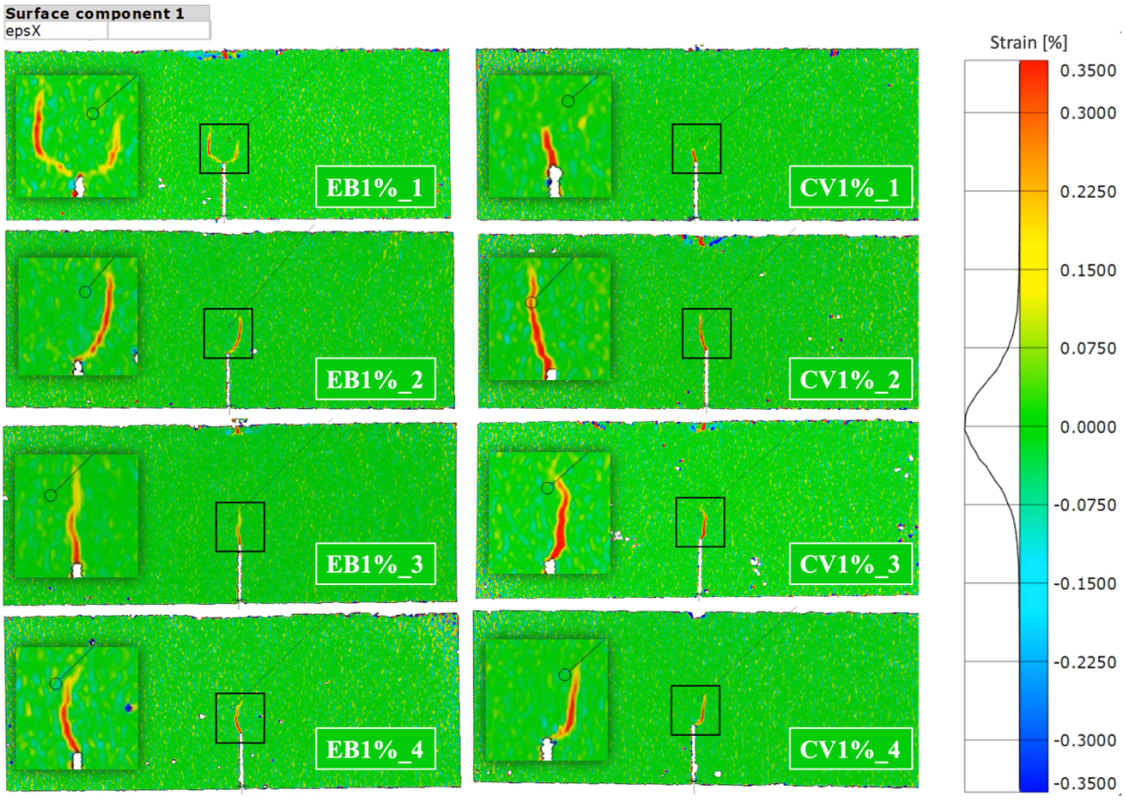

Figure 3.14: Full Strain Field at the Critical Stage for 1% Fiber Content Specimens

For a better understanding of the crack propagation process in both EB1% and CV1% specimens, Figure 3.15 represents the stage when the crack reached the top of the beam. When comparing the CV specimens with the EB specimens, it seems that there were more deflected cracks in the EB specimens, which indicated that the fibers alignment factor affected the crack propagation process. The mechanism of crack deflection expands the crack's surface area, enabling more energy absorption and increasing the material's fracture properties [56,57]. Therefore, the EB specimens had a larger increase in the mixed mode fracture toughness compared to the CV specimens.

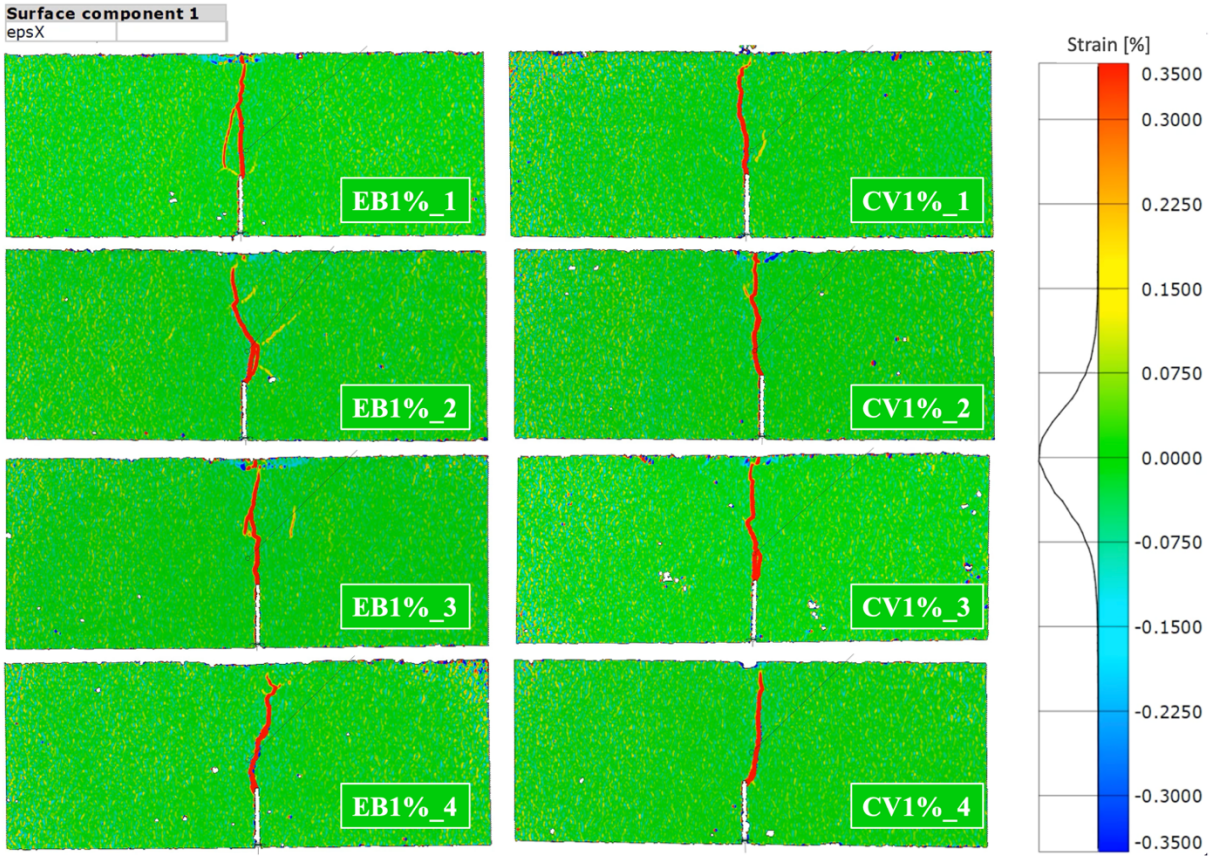

Figure 3.15: Full Strain Field (x-axis) When the Crack Reached the Top for 1% Fiber Content Specimens

When considering the strain localization between the layer interfaces, the DIC was used to capture any localized strains between the layers. Since the EB method was cast in three layers

being deposited on top of each other, the localized strains appeared between the layer interfaces for all EB specimens, as shown in Figure 3.16. However, these localized strains did not extend horizontally along the layers interface, instead, they only extended nearby the vertical crack path. This is explained by the intrinsic variations in material qualities and layer bonding strength in EB FRC. Weakness at interfaces between layers might reduce the load transfer and bonding, which could result in layer delamination and more strain localization at the interfaces [47]. Additionally, the orientation and alignment of the fibers in the layers may have an impact on how strain localization behaves at the layer interfaces. The strain localization at layer interfaces was reduced in the CV specimens since the fibers were randomly oriented which resulted in having some fibers oriented perpendicular to the horizontal crack path. These fibers resist the horizontal crack propagation between the layers and work as a bridge for load transfer and strain distribution.

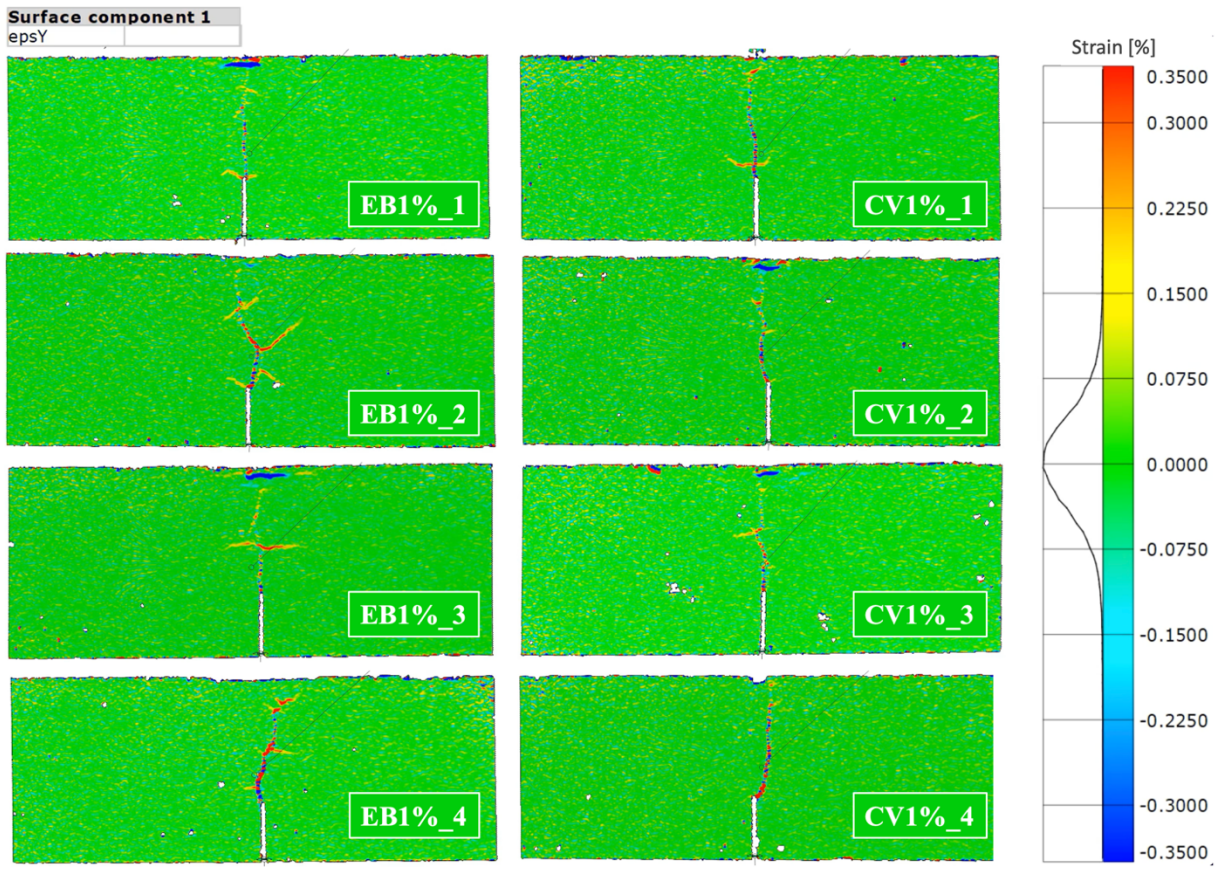

Figure 3.16: Full Strain Field (y-axis) When the Crack Reached the Top for 1% Fiber Content Specimens

3.4. Conclusion

In this study, fracture properties of fiber-reinforced mortar were evaluated and using two distinct casting methods — extrusion-based (EB) and conventional cast (CV) — and reinforced with two different PVA fiber dosages of 0.5 % and 1 % of the concrete volume. The primary findings of this study are summarized below.

1. The EB casting method enhanced the fracture properties of FRC compared to the CV casting method. However, it was found that the EB casting method demonstrated superior proficiency in fiber alignment when applied with increased fiber dosages.
2. When considering the MTPM, the fracture toughness of 1 % fiber content EB specimens improved by 16.2 % due to the crack deflection mechanism. Conversely, 0.5 % fiber content specimens showed only a slight improvement, deemed insignificant based on statistical analysis.
3. Despite the fact that a_c values typically increase as the fiber content increases, this study found that the extrusion-based method of casting had the greatest impact on increasing a_c values.
4. The DIC technique proved to be capable of measuring critical crack length and CMOD, tracking crack propagation, and observing localized strains.
5. EB specimens exhibited enhanced crack bridging capabilities and demonstrated more deflected cracks, corroborating the crucial role of fiber alignment in crack propagation and indicating superior performance of EB specimens in mixed mode fracture toughness.

6. Strain localization at layer interfaces was a distinct phenomenon in EB specimens and was influenced by fiber orientation and alignment. Conversely, in CV specimens, the random orientation of fibers mitigated this strain localization.

Overall, these results suggested that the pump extrusion-based method has great potential to improve the fracture properties of FRC, with significant implications for the construction industry. However, the application of this method in this study was limited by the use of a pump, which restricted fiber length to 20 mm and necessitated the use of synthetic fibers. The study also encountered aggregate size limitations inherent to the extrusion pump, resulting in mixtures devoid of any coarse aggregate. Although the inclusion of coarse aggregate would influence fiber orientation, the findings derived from using mortar remain relevant to the fracture properties of FRC. This relevance is emphasized by the current industry limitations of 3D printing materials, which largely confines the process to the use of mortar.

In anticipation of future research, the use of high modulus fibers such as steel fibers is proposed, along with exploring different investigative techniques for studying fiber orientation in concrete, such as X-ray computed tomography. These could offer insights into the potential enhanced performance and superior crack-bridging abilities of longer fibers. Furthermore, a detailed examination of strain localization between layer interfaces, by incorporating delay times between casting layers, could provide valuable knowledge about this crucial phenomenon.

In conclusion, while the present study has unveiled the potential of the pump extrusion-based method in enhancing FRC's fracture properties, further exploration and optimization of this technique is imperative. Future research should aim to overcome the current limitations, thereby unlocking the full potential of this innovative method for substantial advancements in the construction industry.

3.5. Authorship Contribution Statement

The authors confirm their contributions to the paper as follows: Rashed Alarrak: Writing – review & editing, Writing – original draft, Visualization, Validation, Methodology, Investigation, Formal analysis, Data curation, Conceptualization. Byeonguk Jeon: Writing – original draft, Investigation. Alexander S. Brand: Writing – review & editing, Supervision, Methodology, Conceptualization.

3.6. References

[1] A. Bentur, S. Mindess, Fibre reinforced cementitious composites, 2nd ed, Taylor & Francis, London ; New York, 2007.

[2] R.F. Zollo, Fiber-reinforced concrete: an overview after 30 years of development, Cem. Concr. Compos. 19 (1997) 107–122. https://doi.org/10.1016/S0958-9465(96)00046-7.

[3] L. Ferrara, M. Di Prisco, M.G.L. Lamperti, Identification of the stress-crack opening behavior of HPFRCC: the role of flow-induced fiber orientation, in: Proc. Fram., 2010: pp. 1541–1550.

[4] X. Sun, J. Zhou, Q. Wang, J. Shi, H. Wang, PVA fibre reinforced high-strength cementitious composite for 3D printing: Mechanical properties and durability, Addit. Manuf. 49 (2022) 102500. https://doi.org/10.1016/j.addma.2021.102500.

[5] S. Xu, Y. Lyu, S. Xu, Q. Li, Enhancing the initial cracking fracture toughness of steel-polyvinyl alcohol hybrid fibers ultra high toughness cementitious composites by incorporating multi-walled carbon nanotubes, Constr. Build. Mater. 195 (2019) 269–282. https://doi.org/10.1016/j.conbuildmat.2018.10.133.

[6] L. Ferrara, N. Ozyurt, M. di Prisco, High mechanical performance of fibre reinforced cementitious composites: the role of “casting-flow induced” fibre orientation, Mater. Struct. 44 (2011) 109–128. https://doi.org/10.1617/s11527-010-9613-9.

[7] W. Hall, Z. Javanbakht, Design and Manufacture of Fibre-Reinforced Composites, Springer International Publishing, Cham, 2021. https://doi.org/10.1007/978-3-030-78807-0.

[8] R. Mu, Y. Xue, L. Qing, H. Li, Y. Zhao, J. Zhou, J. Su, Preparation and mechanical performance of annularly aligned steel fiber reinforced cement-based composite pipes, Constr. Build. Mater. 211 (2019) 167–173. https://doi.org/10.1016/j.conbuildmat.2019.03.146.

[9] R. Mu, H. Li, L. Qing, J. Lin, Q. Zhao, Aligning steel fibers in cement mortar using electro-magnetic field, Constr. Build. Mater. 131 (2017) 309–316. https://doi.org/10.1016/j.conbuildmat.2016.11.081.

[10] L. Liu, J. Xu, Y. Wang, T. Yin, H. Chu, Electrical and Piezoresistive Properties of Steel Fiber Cement-based Composites Aligned by a Magnetic Field, J. Wuhan Univ. Technol.-Mater Sci Ed. 37 (2022) 229–240. https://doi.org/10.1007/s11595-022-2522-2.

[11] P. Kheml, K. Carrera, K. Künzel, V. Papež, R. Sovják, Summary of findings on magnetic orientation of fibers in cement composites, Mater. Today Proc. 58 (2022) 1104–1107. https://doi.org/10.1016/j.matpr.2022.01.201.

[12] I. da Silva Brito, D. Alan Strauss Rambo, S. Martini, R. Pícolo Salvador, M. Fabrízio de Menezes Freitas, Flexural behavior of HPFRCC: Enhancing post-crack strength and toughness by magnetic alignment of the reinforcement, Constr. Build. Mater. 269 (2021) 121265. https://doi.org/10.1016/j.conbuildmat.2020.121265.

[13] A. Abrishambaf, M. Pimentel, S. Nunes, Influence of fibre orientation on the tensile behaviour of ultra-high performance fibre reinforced cementitious composites, Cem. Concr. Res. 97 (2017) 28–40. https://doi.org/10.1016/j.cemconres.2017.03.007.

[14] S.-T. Kang, J.-K. Kim, Investigation on the flexural behavior of UHPCC considering the effect of fiber orientation distribution, Constr. Build. Mater. 28 (2012) 57–65. https://doi.org/10.1016/j.conbuildmat.2011.07.003.

[15] S.-T. Kang, J.-K. Kim, Numerical simulation of the variation of fiber orientation distribution during flow molding of Ultra High Performance Cementitious Composites (UHPCC), Cem. Concr. Compos. 34 (2012) 208–217. https://doi.org/10.1016/j.cemconcomp.2011.09.015.

[16] L. Ferrara, N. Tregger, S.P. Shah, Flow-induced fiber orientation in SCSFRC: monitoring and prediction, in: Des. Prod. Place. Self-Consol. Concr., Springer, 2010: pp. 417–428.

[17] Y. Shao, S. Marikunte, S.P. Shah, Extruded fiber-reinforced composites, Concr. Int. 17 (1995) 48–53.

[18] Z. Li, B. Mu, T.P. Chang, C.-T. Hsu, Prediction of overall tension behavior of short fiber-reinforced composites, Int. J. Solids Struct. 36 (1999) 4071–4087.

[19] H. Takashima, K. Miyagai, T. Hashida, V.C. Li, A design approach for the mechanical properties of polypropylene discontinuous fiber reinforced cementitious composites by extrusion molding, Eng. Fract. Mech. 70 (2003) 853–870. https://doi.org/10.1016/S0013-7944(02)00154-6.

[20] X. Zhou, Z. Li, Characterizing rheology of fresh short fiber reinforced cementitious composite through capillary extrusion, J. Mater. Civ. Eng. 17 (2005) 28–35.

[21] Y. Zhang, F. Aslani, Development of fibre reinforced engineered cementitious composite using polyvinyl alcohol fibre and activated carbon powder for 3D concrete printing, Constr. Build. Mater. 303 (2021) 124453. https://doi.org/10.1016/j.conbuildmat.2021.124453.

[22] J. Ye, C. Cui, J. Yu, K. Yu, F. Dong, Effect of polyethylene fiber content on workability and mechanical-anisotropic properties of 3D printed ultra-high ductile concrete, Constr. Build. Mater. 281 (2021) 122586. https://doi.org/10.1016/j.conbuildmat.2021.122586.

[23] M. Sugavaneswaran, G. Arumaikkannu, Modelling for randomly oriented multi material additive manufacturing component and its fabrication, Mater. Des. 1980-2015. 54 (2014) 779–785. https://doi.org/10.1016/j.matdes.2013.08.102.

[24] H. Stang, V.C. Li, Extrusion of ECC-material, in: Proc High Perform. Fiber Reinf. Cem. Compos., 1999: pp. 203–212.

[25] S.C. Paul, Y.W.D. Tay, B. Panda, M.J. Tan, Fresh and hardened properties of 3D printable cementitious materials for building and construction, Arch. Civ. Mech. Eng. 18 (2018) 311–319. https://doi.org/10.1016/j.acme.2017.02.008.

[26] X. Qian, X. Zhou, B. Mu, Z. Li, Fiber alignment and property direction dependency of FRC extrudate, Cem. Concr. Res. 33 (2003) 1575–1581.

[27] G. Ma, Z. Li, L. Wang, F. Wang, J. Sanjayan, Mechanical anisotropy of aligned fiber reinforced composite for extrusion-based 3D printing, Constr. Build. Mater. 202 (2019) 770–783. https://doi.org/10.1016/j.conbuildmat.2019.01.008.

[28] Z. Li, B. Mu, Innovations forum: Application of extrusion for manufacture of short fiber reinforced cementitious composite, J. Mater. Civ. Eng. 10 (1998) 2–4. https://doi.org/10.1061/(ASCE)0899-1561(1998)10:1(2).

[29] Z. Hou, X. Tian, J. Zhang, D. Li, 3D printed continuous fibre reinforced composite corrugated structure, Compos. Struct. 184 (2018) 1005–1010. https://doi.org/10.1016/j.compstruct.2017.10.080.

[30] Y. Akkaya, J. Picka, S.P. Shah, Spatial distribution of aligned short fibers in cement composites, J. Mater. Civ. Eng. 12 (2000) 272–279.

[31] H.-J. Kong, S.G. Bike, V.C. Li, Development of a self-consolidating engineered cementitious composite employing electrosteric dispersion/stabilization, Cem. Concr. Compos. 25 (2003) 301–309. https://doi.org/10.1016/S0958-9465(02)00057-4.

[32] L. Ferrara, N. Ozyurt, M. di Prisco, High mechanical performance of fibre reinforced cementitious composites: the role of “casting-flow induced” fibre orientation, Mater. Struct. 44 (2011) 109–128. https://doi.org/10.1617/s11527-010-9613-9.

[33] X. Zhou, Z. Li, Characterization of rheology of fresh fiber reinforced cementitious composites through ram extrusion, Mater. Struct. 38 (2005) 17–24. https://doi.org/10.1007/BF02480570.

[34] S.-T. Kang, J.-K. Kim, Numerical simulation of the variation of fiber orientation distribution during flow molding of ultra high performance cementitious composites (UHPCC), Cem. Concr. Compos. 34 (2012) 208–217.

[35] A.E. Naaman, H.W. Reinhardt, Characterization of high performance fiber reinforced cement composites—HPFRCC, in: High Perform. Fiber Reinf. Cem. Compos., 1996: pp. 1–24.

[36] S.P. Shah, C. Ouyang, Mechanical behavior of fiber-reinforced cement-based composites, J. Am. Ceram. Soc. 74 (1991) 2727–2953.

[37] A.C. Bordelon, J.R. Roesler, Spatial distribution of synthetic fibers in concrete with X-ray computed tomography, Cem. Concr. Compos. 53 (2014) 35–43. https://doi.org/10.1016/j.cemconcomp.2014.04.007.

[38] A. Enfedaque, M.G. Alberti, J.C. Gálvez, Influence of Fiber Distribution and Orientation in the Fracture Behavior of Polyolefin Fiber-Reinforced Concrete, Materials. 12 (2019) 220. https://doi.org/10.3390/ma12020220.

[39] C. Xie, M. Cao, M. Khan, H. Yin, J. Guan, Review on different testing methods and factors affecting fracture properties of fiber reinforced cementitious composites, Constr. Build. Mater. 273 (2021) 121766. https://doi.org/10.1016/j.conbuildmat.2020.121766.

[40] B. Pan, K. Qian, H. Xie, A. Asundi, Two-dimensional digital image correlation for in-plane displacement and strain measurement: a review, Meas. Sci. Technol. 20 (2009) 062001. https://doi.org/10.1088/0957-0233/20/6/062001.

[41] S. Roux, J. Réthoré, F. Hild, Digital image correlation and fracture: an advanced technique for estimating stress intensity factors of 2D and 3D cracks, J. Phys. Appl. Phys. 42 (2009) 214004. https://doi.org/10.1088/0022-3727/42/21/214004.

[42] S.G. Shah, J.M. Chandra Kishen, Fracture Properties of Concrete–Concrete Interfaces Using Digital Image Correlation, Exp. Mech. 51 (2011) 303–313. https://doi.org/10.1007/s11340-010-9358-y.

[43] D.G. Aggelis, S. Verbruggen, E. Tsangouri, T. Tysmans, D. Van Hemelrijck, Characterization of mechanical performance of concrete beams with external reinforcement by acoustic emission and digital image correlation, Constr. Build. Mater. 47 (2013) 1037–1045. https://doi.org/10.1016/j.conbuildmat.2013.06.005.

[44] S. Rouchier, G. Foray, N. Godin, M. Woloszyn, J.-J. Roux, Damage monitoring in fibre reinforced mortar by combined digital image correlation and acoustic emission, Constr. Build. Mater. 38 (2013) 371–380. https://doi.org/10.1016/j.conbuildmat.2012.07.106.

[45] S.Y. Alam, J. Saliba, A. Loukili, Fracture examination in concrete through combined digital image correlation and acoustic emission techniques, Constr. Build. Mater. 69 (2014) 232–242. https://doi.org/10.1016/j.conbuildmat.2014.07.044.

[46] K. Yu, L. Li, J. Yu, J. Xiao, J. Ye, Y. Wang, Feasibility of using ultra-high ductility cementitious composites for concrete structures without steel rebar, Eng. Struct. 170 (2018) 11–20. https://doi.org/10.1016/j.engstruct.2018.05.037.

[47] M.C. Jenkins, A.S. Brand, T.T. Painter, S.T. Sherry, A Preliminary Digital Image Correlation Study of the AnisotropicMechanical Properties of a 3D-Printed Mortar, in: 2021. https://doi.org/10.11159/iccste21.146.

[48] L. Qing, G. Cao, J. Guan, S. Li, Experimental method for determining the fracture toughness of concrete based on the modified two-parameter model and DIC technique, Fatigue Fract. Eng. Mater. Struct. 45 (2022) 400–410. https://doi.org/10.1111/ffe.13602.

[49] A. Carpinteri, F. Berto, G. Fortese, C. Ronchei, D. Scorza, S. Vantadori, Modified two-parameter fracture model for bone, Eng. Fract. Mech. 174 (2017) 44–53. https://doi.org/10.1016/j.engfracmech.2016.11.002.

[50] Y. Jenq, S.P. Shah, Two Parameter Fracture Model for Concrete, J. Eng. Mech. 111 (1985) 1227–1241. https://doi.org/10.1061/(ASCE)0733-9399(1985)111:10(1227).

[51] RILEM Committee, Determination of fracture parameters (KIC and CTODC) of plain concrete using three-point bend tests, Mater. Struct. 23 (1990) 457–760. https://doi.org/10.1007/BF02472029.

[52] A. Hillerborg, The theoretical basis of a method to determine the fracture energyG F of concrete, Mater. Struct. 18 (1985) 291–296. https://doi.org/10.1007/BF02472919.

[53] J. Roesler, G. Paulino, C. Gaedicke, A. Bordelon, K. Park, Fracture Behavior of Functionally Graded Concrete Materials for Rigid Pavements, Transp. Res. Rec. J. Transp. Res. Board. 2037 (2007) 40–49. https://doi.org/10.3141/2037-04.

[54] H. Schreier, J.-J. Orteu, M.A. Sutton, Image Correlation for Shape, Motion and Deformation Measurements: Basic Concepts,Theory and Applications, Springer US, Boston, MA, 2009. https://doi.org/10.1007/978-0-387-78747-3.

[55] B. Rehder, K. Banh, N. Neithalath, Fracture behavior of pervious concretes: The effects of pore structure and fibers, Eng. Fract. Mech. 118 (2014) 1–16. https://doi.org/10.1016/j.engfracmech.2014.01.015.

[56] E.A. Zimmermann, M.E. Launey, R.O. Ritchie, The significance of crack-resistance curves to the mixed-mode fracture toughness of human cortical bone, Biomaterials. 31 (2010) 5297–5305. https://doi.org/10.1016/j.biomaterials.2010.03.056.

[57] A. Akram, The Overview of Fracture Mechanics Models for Concrete, Archit. Civ. Eng. Environ. 14 (2021) 47–57. https://doi.org/10.21307/acee-2021-005.

Chapter 4. Flexural Toughness of Extruded Fiber-Reinforced Mortar with Preferentially Aligned Fibers[2]

Abstract

This study explored the flexural toughness properties of polyvinyl alcohol (PVA) fiber-reinforced concrete (FRC) using a modified ASTM C1609 third-point bending test, and it established a comparative study between two methods of casting: traditional casting and pump-driven extrusion. The primary hypothesis posited that the extrusion process would promote fiber alignment parallel to the tensile stresses, thereby enhancing the flexural performance of the concrete. The study corroborated previous research findings that introducing fibers enhances the ductility and post-peak performance of the concrete. Moreover, this research introduced a unique observation that strategic fiber alignment through extrusion could serve to further enhance the concrete's flexural performance. The research employed digital image correlation to capture the full displacement field during testing, facilitating an examination of the crack propagation process and strain localization. The findings showed that the extrusion-based casting method improved the residual strengths by an average of 39 % and 87 % compared to conventional cast method for the 0.5 % and 1 % fiber volume specimens, respectively. Additionally, the base of the extruded specimens exhibited a greater incidence of crack initiation and displayed enhanced energy absorption through multiple cracking events. These observations underscore the concept that fiber alignment, when facilitated by extrusion, plays a significant role in influencing crack propagation and, consequently, in improving the flexural properties of the composite material.

Keywords: Fiber-reinforced concrete, Flexural toughness, Digital image correlation, Extrusion, Fiber alignment, Crack propagation, Strain localization.

[2] **R. Alarrak**, B. Jeon, A.S. Brand, Flexural toughness of extruded fiber-reinforced mortar with preferentially aligned fibers, Constr. Build. Mater. 407 (2023) 133528. https://doi.org/10.1016/j.conbuildmat.2023.133528.

4.1. Introduction

4.1.1. Background and Motivation

Concrete is a widely used construction material, known for its compressive strength, durability, and versatility. However, its tensile and flexural properties are relatively weak, making it susceptible to cracking. Fiber-reinforced concrete (FRC) offers one solution to this limitation by incorporating dispersed fibers within the concrete matrix to improve its tensile and flexural strength. The efficacy of FRC largely depends on the type and quantity of fibers used [1,2]. Various fibers, such as those derived from steel or synthetic materials, have been demonstrated to enhance FRC's strength, ductility, stiffness, and resistance to crack propagation [3–5]. However, achieving uniform fiber orientation and alignment has proven challenging with conventional mixing and cast methods, leading to random fiber distribution and fiber-free zones [6].

4.1.2. Previous Research on Fiber Alignment

The orientation of fibers in FRC has been a subject of extensive research since the early 1970s [7–9]. A fiber is considered completely aligned if its position falls within a range of ±20° in relation to the extrusion direction [10]. Understanding and controlling fiber alignment can significantly impact the mechanical performance of FRC, making it a critical aspect to explore [6,11–13].

To achieve the advantages of fiber alignment, researchers have explored various methods to orient the fibers in the desired direction. Magnetic fields have been utilized to align steel fibers [11,14–17], and modified casting methods have been developed to orient fibers during the consolidation process as fresh concrete flows [3,6,18–21]. Among the emerging approaches, extrusion-based methods have shown promise in achieving superior fiber alignment [4,10,22–33].

These techniques leverage additive manufacturing processes to place fibers aligned to the desired direction to have most effective tensile resistance. Although early research on extruded FRC in the 1990s and early 2000s was limited, it suggested that extrusion methods, such as ram or plunger extrusion, could induce strain-hardening behavior in FRC [7,22,23,29,34]. However, only a few studies have explored the impact of extrusion on fiber alignment within the cementitious composites [31,28,33].

4.1.3. Additive Manufacturing Techniques

Recent studies have delved further into extrusion-based additive manufacturing techniques for FRC. For instance, Ma *et al*. used a 3D printer to extrude basalt fiber-reinforced cementitious material, achieving fiber alignment in the print direction by using a nozzle with a diameter smaller than the fiber length [10]. While the extrusion-based printing process showed well-oriented structures, there were issues with weak interfaces and voids between circular bead layers [10,27,30]. Ye *et al*. addressed this by using an extruder equipped with a rectangular-shaped nozzle to print FRC that incorporated polyethylene fibers. However, as the fiber content increased, a more twisted fiber orientation was observed, leading to diminished tensile strength compared to conventionally cast specimens [27].

To overcome these challenges, the integration of flow-induced casting methods with a pump extruder *via* a nozzle conveyor system shows potential. This approach offers rheological benefits by aligning fibers in the desired direction after extrusion, thus enhancing mechanical properties in the target direction of FRC structures [19,35,36]. Using a nozzle conveyor system from pump pressure to extrusion can prevent fiber twisting caused by the pump shaft's rotation, ensuring more efficient fiber alignment [6,27,37].

4.1.4. Nozzle Design for Pump Extrusion-Based FRC

As the FRC extrusion technique garners increased attention, nozzle designs have been developed for precise delivery of fresh concrete into molds. The ultimate goal has been to achieve enhanced fiber alignment and optimize the mechanical properties of printed concrete structures. Several studies have delved into the realm of nozzle-based fiber alignment, each offering unique insights and advancements. For example, Ma *et al.* [10] ventured into using an oval-shaped nozzle with a 12 mm diameter, smaller than the fiber length, to align fibers with the printing direction. In their experiments, basalt fibers were employed at a weight fraction of 0.5 % for printing. The results were promising, with fiber-aligned samples exhibiting 56 % higher flexural strength compared to conventionally cast samples. However, the challenge of inter-layer voids in the printed beams, induced by the nozzle shape, remains to be addressed. Ye *et al.* [27] designed a rectangular-shaped nozzle (10 mm by 50 mm) to address the inter-layer void issue that often arose when using circular-shaped nozzles for printing. In their study, polyethylene (PE) fibers were utilized at volume fractions of 1 %, 1.5 %, and 2 %, and a three-point bending test was performed. While the printed beams with all three different fiber volume fractions showed increased flexural toughness compared to conventional samples, the tensile strength and strain capacity of printed 1.5 % and 2 % volume fraction samples were reduced compared to conventional cast samples. Twisting of fibers during the extrusion process was identified as a potential issue, where the high pressure generated by the rotation of a screw pump caused the fresh paste to extrude out. Zhou *et al.* [36] corroborated this observation on extrusion of FRC using PVA and glass fiber, highlighting how high extrusion pressure at the nozzle die could impede fiber alignment with the extrusion direction. Without using mechanical pressure, Huang *et al.* [38] introduced an L-shaped vertical conveying nozzle to achieve an alignment of steel fibers in FRC. The device showcased promising

results, leading to increased flexural strength and toughness. Fiber orientation coefficient analysis revealed that specimens prepared using the L-shaped nozzle had an orientation average coefficient of 0.65, a significant improvement over the 0.49 average coefficient in specimens prepared by conventional cast with rodding consolidation, representing a 33 % improvement in fiber orientation. However, this L-shaped nozzle had some limitations which were improved with advanced design in this study.

4.1.5. Improvement of Flexural Toughness

Several studies have employed bending tests to investigate the effect of fiber alignment on flexural toughness of FRC. In a study conducted by Kang *et al*. [39], the researchers scrutinized the impact of fiber orientation and dispersion on the flexural strength of FRC samples. Their results emphasized that while steel fiber orientation and dispersion minimally influenced the initial cracking strength, they significantly impacted the flexural strength. The initial cracking strength was largely driven by the matrix strength, whereas the flexural strength primarily hinged on the fiber bridging strength at the crack face. Despite fiber pullout resistance during bond slip exerting little influence on initial cracking, it significantly affected the flexural strength, a relationship closely tied to fiber length and orientation. In a similar perspective, Zerbino *et al*. [40] executed three-point bending tests on self-consolidating fiber-reinforced concrete using steel and synthetic fibers. They observed that the flexural strength of the beams, cut parallel to the composite flow direction, outperformed those cut in the vertical direction. Mu *et al*. [14] carried out a study to investigate the influence of steel fiber alignment on the flexural strength of fiber-reinforced composites. The experimental design involved subjecting specimens with both aligned and randomly dispersed fibers to three-point bending tests. The results highlighted that the incorporation of fibers at varying volume fractions of 0.8 %, 1.2 %, and 2.0 % led to diverse

degrees of enhancement in the flexural strength of aligned samples compared to their randomly dispersed counterparts. Specifically, volume fractions of 0.8 %, 1.2 %, and 2.0 % resulted in flexural strength increases of 88 %, 71 %, and 57 %, respectively. Furthermore, the aligned samples displayed superior flexural toughness relative to the randomly oriented samples, with increases of 48 %, 77 %, and 39 % at the corresponding fiber volume fractions of 0.8 %, 1.2 %, and 2.0 %.

In another study, Da Silva *et al*. [41] demonstrated that steel fiber alignment yielded beneficial effects on the flexural performance, both in terms of strength and toughness, when contrasted with randomly dispersed fibers, irrespective of fiber content levels. Their study also indicated that fiber orientation brought about a reduction in the critical fiber volume for bending. Notably, their results showcased that fiber alignment considerably decreased the necessary fiber volume required to attain a certain level of toughness. For instance, when 2 % and 3 % of randomly dispersed fibers were used, toughness values of around 9.5 J and 13.2 J were realized. Conversely, specimens with aligned reinforcement achieved equivalent toughness values with merely 1.7 % and 2.2 % of fibers, respectively, which led to a reduction in the required fiber volume fraction by 15 % and 26 %, respectively.

4.1.6. Digital Image Correlation Technique

In the current research, digital image correlation (DIC) technology was employed to examine the flexural behavior of FRC with aligned fibers. DIC, a non-contact and non-interferometric optical method, is frequently used to measure deformation and displacement of materials under external loading. Additionally, this technique can graphically illustrate the initiation and progression of cracking during flexural tests. A key advantage of DIC is its ability to generate high-resolution, full-field surface displacement/strain data, which can often prove

challenging to gather using conventional strain gauge measurements [42–48,27,49]. Given DIC's capacity to provide an accurate representation of flexural test progression, Aggelis *et al*. leveraged it to observe strain distribution on the surface and its dynamic modifications following cracking [45]. Similarly, Niu *et al.* [50] analyzed the crack patterns on beam specimens and identified various fracture zones using DIC. Meanwhile, Jenkins *et al.* [49] used DIC in a flexural bending test to monitor horizontal strain distribution at the interfaces between layers in 3D printed beams that were printed in various orientation. This approach allowed them to investigate and determine the fracture mode in their specimens. However, not all printing orientations were examined in terms of their interfaces. Therefore, in this study, both vertical and horizontal strain field distributions were scrutinized to ensure that all instances of strain localization were identified.

The present study was inspired by the ASTM C1609 standard but adapted the specimen dimensions to the configuration previously developed by the authors. By applying the adjusted ASTM C1609 standard, this investigation attained uniformity in the experimental setup conditions, aligning with a prior fracture test study [51]. This congruence will facilitate subsequent analyses regarding the impact of the extrusion-based (EB) casting method. Additionally, the DIC technique was continuously employed to observe crack propagation on the surface until the beams failed. The research assessed the flexural toughness of specimens crafted through two different casting methods and incorporated two different fiber volume fractions, 0.5 % and 1 %.

4.1.7. Research Objective

This research represented a substantial advancement in the creation of a highly effective extrusion-based methodology for achieving fiber alignment. The study primarily investigated the flexural properties of fiber-reinforced concrete that included polyvinyl alcohol (PVA) fibers, fabricated using both conventional casting and extrusion techniques. Moreover, the efficiency of

DIC was demonstrated in evaluating the extended flexural toughness of these composites, utilizing a modified version of the ASTM C1609 standard. The distinguishing novelty of this study lay in its capability to quantitatively scrutinize the flexural properties of extruded FRC using DIC.

4.2. Experimental Methodology

4.2.1. Theoretical Background

The third-point bending flexural toughness test method employed in this investigation was inspired by the ASTM C1609 standard [52]. However, due to constraints in specimen fabrication, several deviations from the ASTM C1609 standard were implemented. The dimensions of the test specimen were altered to a rectangular beam that has a dimension of 700 mm by 80 mm by 150 mm tested at a span length (L) of 600 mm. This modification was implemented to ensure consistency between the three-point bending of the previous study [51], thereby facilitating further comparative data on mechanical properties influenced by the utilization of a pump extrusion-based approach.

All beam specimens were subjected to a third point monotonic loading until a net deflection of L/60. The curve of the load-deflection of the bending test was divided into five stages, as shown in Figure 4.1. The stages were defined from beginning to the first peak deflection (δ_P) and included four different net deflections of L/600, L/150, L/100, and L/60. In this study, these five stages are stated as the 1st (up to the first peak load), 2nd (up to L/600 net deflection), 3rd (up to L/150 net deflection), 4th (up to L/100 net deflection), and 5th (up to L/60 net deflection) stages, respectively. The 1st stage represents the flexural peak strength (modulus of rupture) of the material, while the 2nd stage represents the flexural residual strength after the peak which demonstrates the material's

response directly after reaching the peak load. Stages 3, 4, and 5 represent the flexural residual strength at different net deflections, which are crucial for the flexural toughness determination.

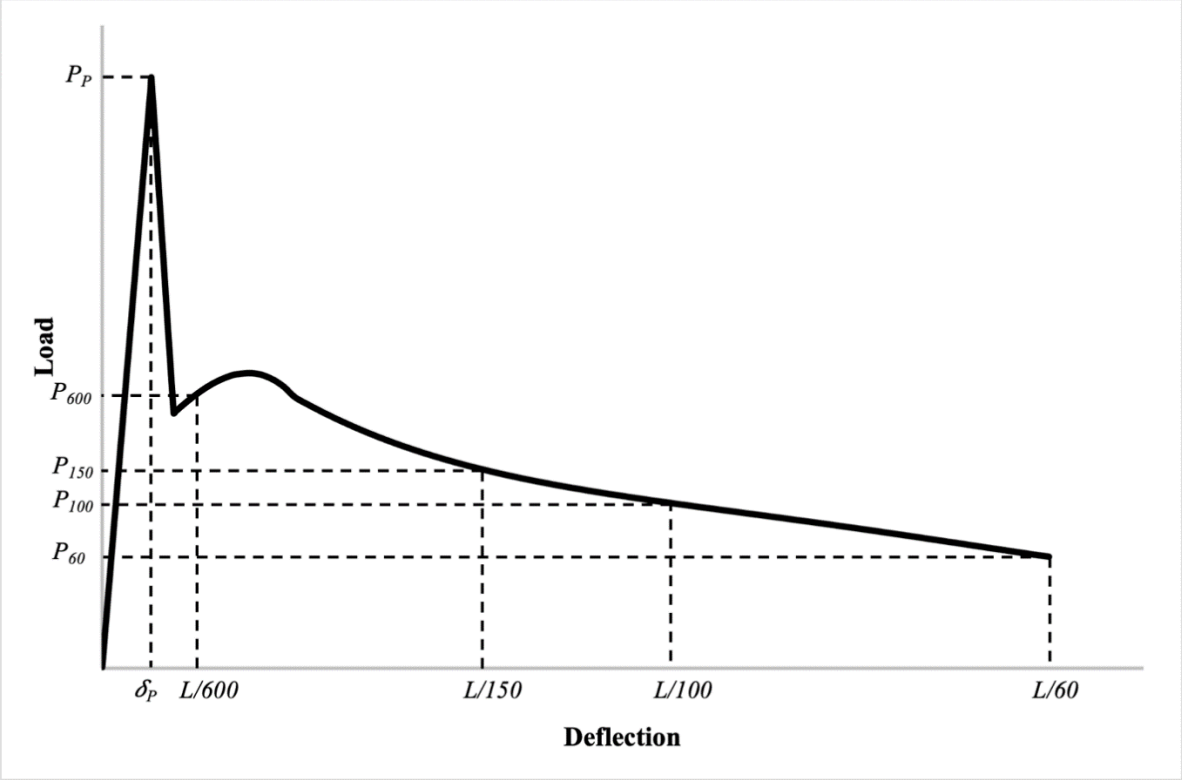

Figure 4.1: Five Stages of Load-deflection Curve (adapted from ASTM C1609)

Flexural properties including the peak strength (f_P), the residual strengths at four different net deflections ($f_{600}, f_{150}, f_{100}, f_{60}$), the flexural toughness at three different net deflections (T_{150}, T_{100}, T_{60}), and the equivalent flexural strength ratio at three different net deflections ($R_{T,150}, R_{T,100}, R_{T,60}$) were determined. The peak strength (modulus of rupture) and the residual strengths (f) were calculated according to Equation 1, where P is the corresponding load, L is the span length, b is the width of the specimen, and d is the depth of the specimen. The flexural toughness parameters (T_x) were computed as the total area under the load-deflection curve up to the corresponding net deflection. The equivalent flexural strength ratios were computed according to Equation 2, where x is the corresponding net deflection, T_x is the flexural toughness

corresponding to that net deflection, b is the width of the specimen, and d is the depth of the specimen [52].

$$f = \frac{PL}{bd^2} \tag{1}$$

$$R_{T,x} = \frac{x \cdot T_x}{f_P bd^2} \cdot 100\% \tag{2}$$

4.2.2. Mix Design and Properties

Three mortar mixtures with varied PVA fiber dosages of 0 %, 0.5 %, and 1 % by volume, were prepared for this comparative study. These fiber volumes were selected because they represent a practical level that engineers could feasibly utilize in the field [53]. Each FRC mortar mixture was cast using two distinct methods: conventional casting per ASTM C192 and extrusion-based casting. In addition, a plain concrete mixture was prepared to serve as a control specimen to study the effect of adding fibers in the mixtures. Due to the extrusion pump's limitations on aggregate size, only fine aggregate with a maximum size of 4.75 mm and a fineness modulus of 2.6 was used in the mixtures.

Each mixture group was assigned a distinct identification label, incorporating the casting method (CV = conventional cast and EB = extrusion-based cast) and the fiber volume (0.5 % or 1 %). Plain concrete specimens were denoted as PC. Table 4.1 and Table 4.2 provide the mixture proportions for each group and the fiber properties, respectively. The properties of the PVA fiber, shown in Figure 4.2, were reported by the manufacturer.

Table 4.1: Concrete Mixture Proportions

Mixture ID	PC	CV0.5%	EB0.5%	CV1%	EB1%
Type I cement (kg/m^3)	688	688	688	688	688
Fine aggregate (kg/m^3)	1042	1042	1042	1042	1042
Water to cement ratio	0.40	0.40	0.40	0.40	0.40
PVA fiber volume	0%	0.5%	0.5%	1%	1%

Table 4.2: Properties of PVA Fibers

Length (mm)	19
Filament diameter (mm)	0.2
Specific gravity	1.3
Tensile strength (MPa)	1,000
Flexural strength (MPa)	29,000

Figure 4.2: PVA Fibers

Compressive strength was determined in accordance with ASTM C39, using only conventionally cast specimens. After a moist curing period of 28 days, three cylinders from each mixture, each measuring 4 inches (100 mm) in diameter and 8 inches (200 mm) in height, were tested. The results for compressive strength, along with the corresponding statistical analysis, are provided in Table 4.3.

Table 4.3: Compressive Strength Results

	Compressive strength (MPa)	Mean (MPa)	Standard deviation	Coefficient of variation (%)
PC_1	44.9	44.8	0.90	2.01
PC_2	45.7			
PC_3	43.9			
0.5%_1	41.7	42.7	0.87	2.05
0.5%_2	43.4			
0.5%_3	42.9			
1%_1	40.4	39.5	1.13	2.88
1%_2	38.2			
1%_3	39.8			

4.2.3. Testing Program and Sample Preparation

For this study, a total of twenty beams were prepared. These included four specimens of plain concrete, eight specimens of FRC produced via extrusion-based casting, and eight specimens of conventionally casted FRC. The eight FRC specimens were further divided into two sets: four with a fiber content of 0.5 % and four with a fiber content of 1 %. Figure 4.3 illustrates the setup for the third-point bending tests conducted on the beam specimens. The dimensions of the beams were 700 mm x 150 mm x 80 mm, with a span length of 600 mm. After a moist curing period of 28 days, all beams underwent flexural testing.

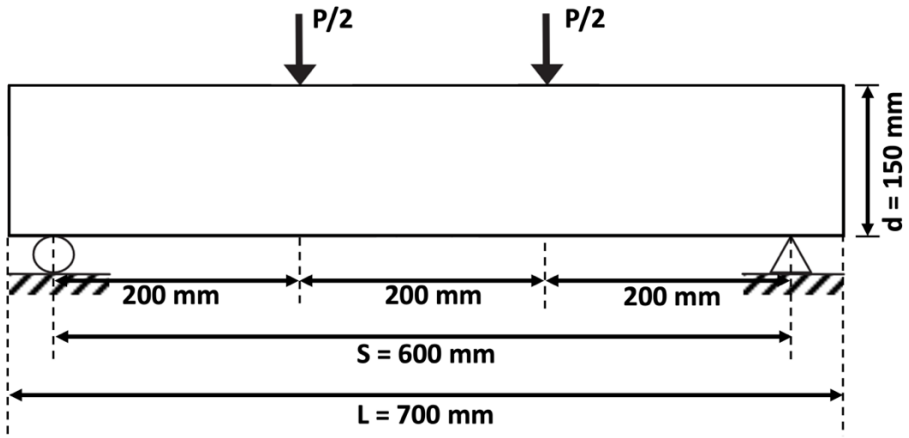

Figure 4.3: Test Setup of Third-point Bending Beam Specimen

The development of the extrusion-based method involved the use of an electric pump capable of generating pressures up to 2.1 MPa. The process initiated when the pump unit, a continuous cavity rotor stator mechanism, accepted the mortar mix from a drive shaft within a material hopper. The mixture was then transported to the dispensing head, where a custom-built nozzle was affixed. This specially designed nozzle, made from 3D printed polyethylene terephthalate, incorporated a 45-degree angle tilt to encourage fiber alignment (Figure 4.4). Additionally, the nozzle was specifically engineered to align with the mold frame, thereby preventing the fibers from exceeding the boundaries of the free surface [51].

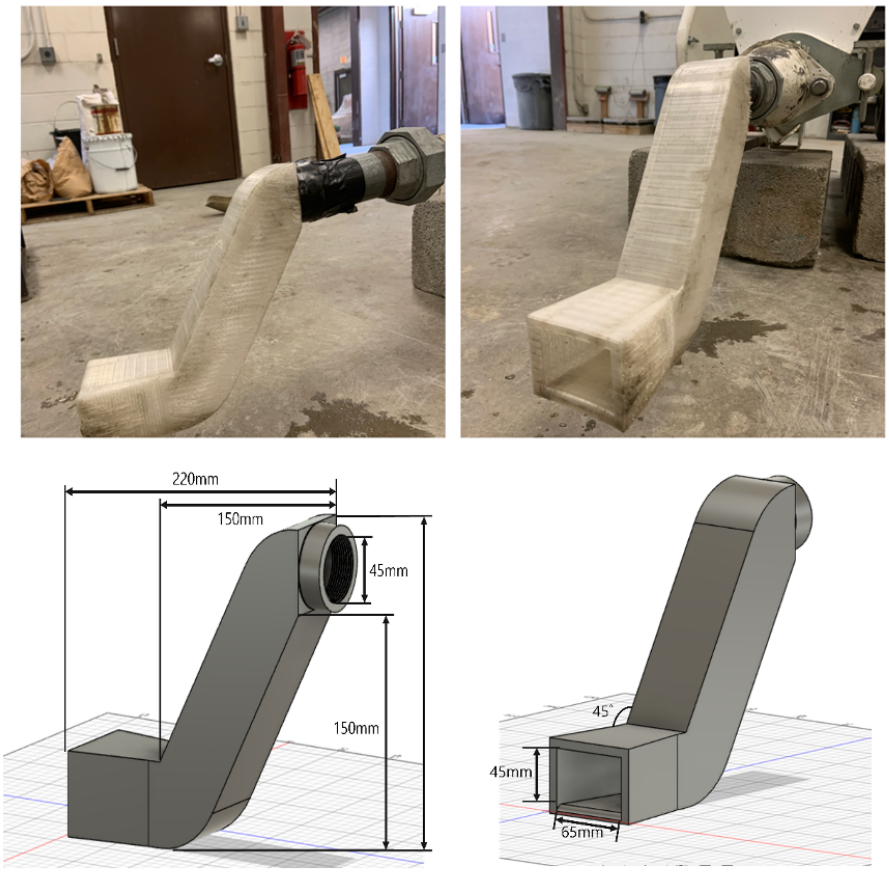

Figure 4.4: Extrusion-based Method's Nozzle Design

The EB and CV batches were mixed and cast concurrently. For the EB specimens, the FRC mixture was extruded into the beam mold by progressively moving the pump along the length of

the mold, resulting in a three-layered concrete structure. No additional consolidation methods were applied to the EB specimens. Conversely, the CV specimens were cast in accordance with the ASTM C192 standard.

The flexural tests were conducted using an MTS Insight 150 SL electromechanical universal testing machine. This study employed a linear variable differential transducer (LVDT) to capture the mid-span deflection (δ), with a deflection measurement capacity of up to 6 mm. The LVDT was positioned in a manner that allowed contact with a steel piece affixed to the top of the beam, as depicted in Figure 4.5. All tests were conducted at a displacement rate of 0.1 mm/min.

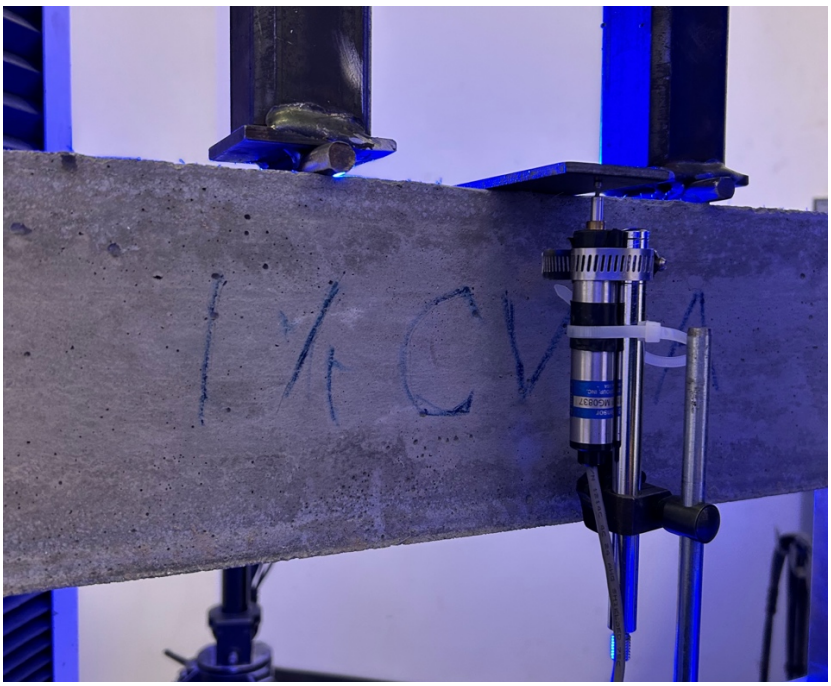

Figure 4.5: LVDT Installation on Beam Specimen

4.2.4. Digital Image Correlation

Digital image correlation (DIC) is an optical technique that enables deformation measurement at any point on a specimen's surface [54]. To conduct the DIC analysis in this study, the surface of the specimen was decorated with a random speckle pattern using black and white

spray paint, as displayed in Figure 4.6. Two digital cameras were stationed on a tripod in front of the testing machine, as shown in Figure 4.7, capturing images automatically at a frequency of 0.1 Hz. The working distance, defined as the distance between DIC system and the specimen's surface, was set at 724 mm. Meanwhile, the sliding distance, which is the separation between the two cameras, was 400 mm. This configuration resulted in a field of view measuring 420 mm x 320 mm x 320 mm, and a pixel size of 53 μm. 2D image correlation analyses were conducted using commercial GOM™ software to measure the in-plane deformations. This software utilizes the normalized cross-correlation function to identify the deformed image subset that best aligns with each subset from the reference image, thereby computing displacement and strain fields.

DIC was employed to monitor the deformation on the specimen's surface, which required several essential components. A coordinate system with X, Y, and Z axes was established. A surface component, which refers to distinct patterns or features that can be tracked across sequential images, was constructed on the beam's surface, aiding in data acquisition. Additionally, a projected point component, oriented in the Y-direction, was installed at the top-middle of the beam surface to collect deflection data.

The visualization and quantification of the FRC beam flexural characteristics were carried out using the DIC data, complemented with data from the MTS and LVDT. As demonstrated by one specimen, the close correlation between the load-deflection curves for both DIC and LVDT data (Figure 4.8) verifies the accuracy of the DIC technique in measuring the displacement field. Although LVDT was used to measure the mid-span deflection, the post-peak deflection extended beyond the range of the LVDT, necessitating the use of DIC to monitor the post-peak deflection.

The application of DIC enabled the analysis of speckle pattern movement and simultaneous monitoring of the strain profile along the depth of the beam and deflection. In this study, DIC was

used to determine if the FRC specimen exhibited localized strains due to manufacturing errors or poor bonding between the layer's interfaces. Therefore, through DIC, the crack propagation process was meticulously investigated.

Figure 4.6: Beam Specimen Used for Flexural Test

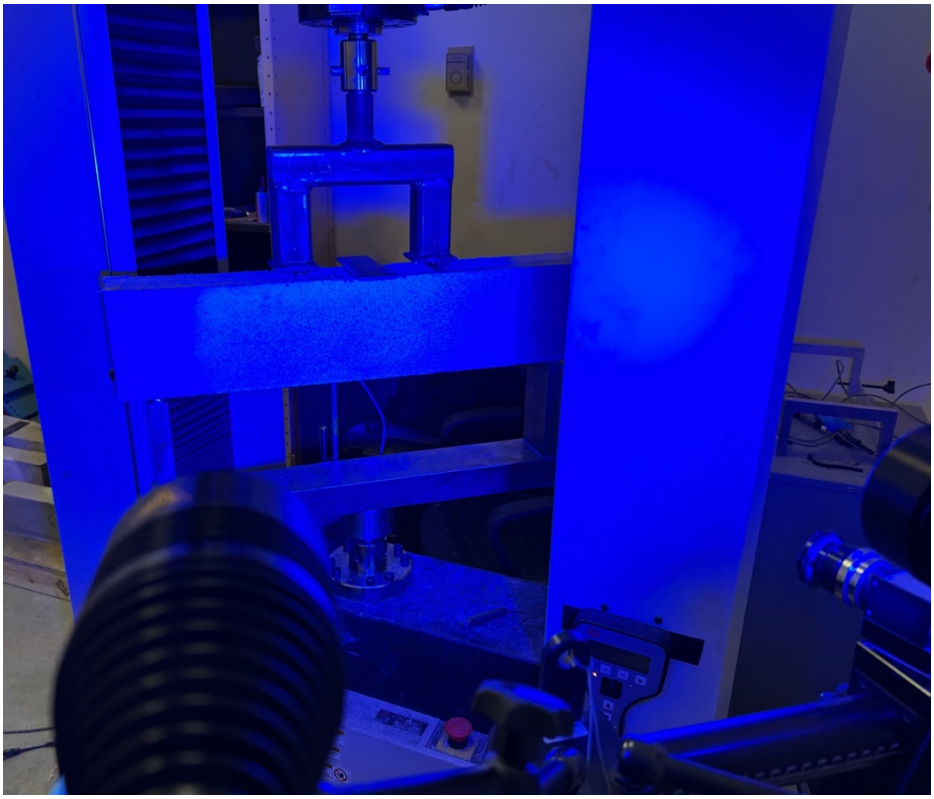

Figure 4.7: Two Digital Cameras Used in DIC

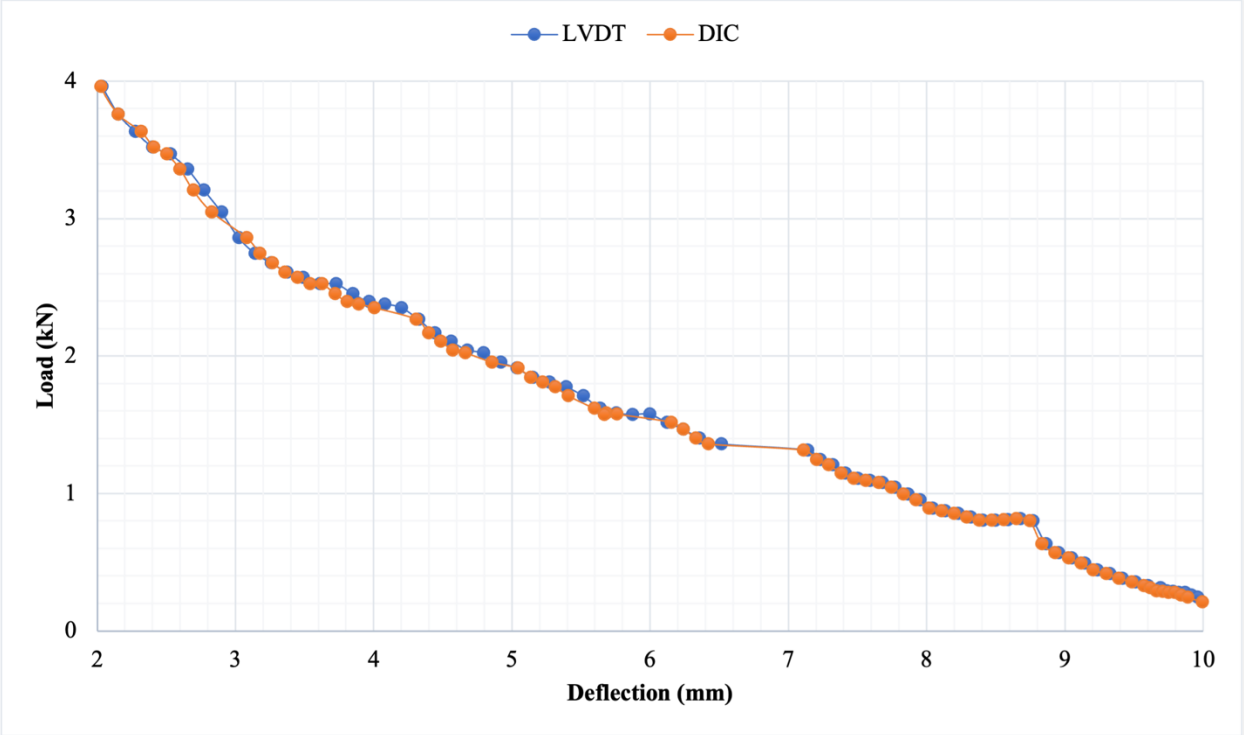

Figure 4.8: Load-deflection Curves for DIC and LVDT

4.3. Test Results and Discussion

4.3.1. Fiber Orientation of Fractured Specimens

This study utilized two unique casting methods: conventional casting and pump-driven extrusion. The hypothesis proposed that the extrusion process would align fibers parallel to the tensile stresses, possibly enhancing the flexural properties of the concrete. To verify this assumption, a comprehensive investigation of fractured specimens from both the extrusion-based (EB) and conventionally-cast (CV) methods was carried out. This provided a robust assessment of the original hypothesis.

Figure 4.9 illustrates the front view of both a) EB and b) CV fractured specimens. In the EB specimen, it became evident that the majority of fibers were aligned along the length of the beam. In contrast, the fibers in the CV specimen demonstrated a random orientation. This

comparative analysis thereby confirmed the initial hypothesis, revealing that the extrusion process indeed resulted in aligned fibers parallel to the tensile stresses, which could potentially lead to enhanced flexural properties.

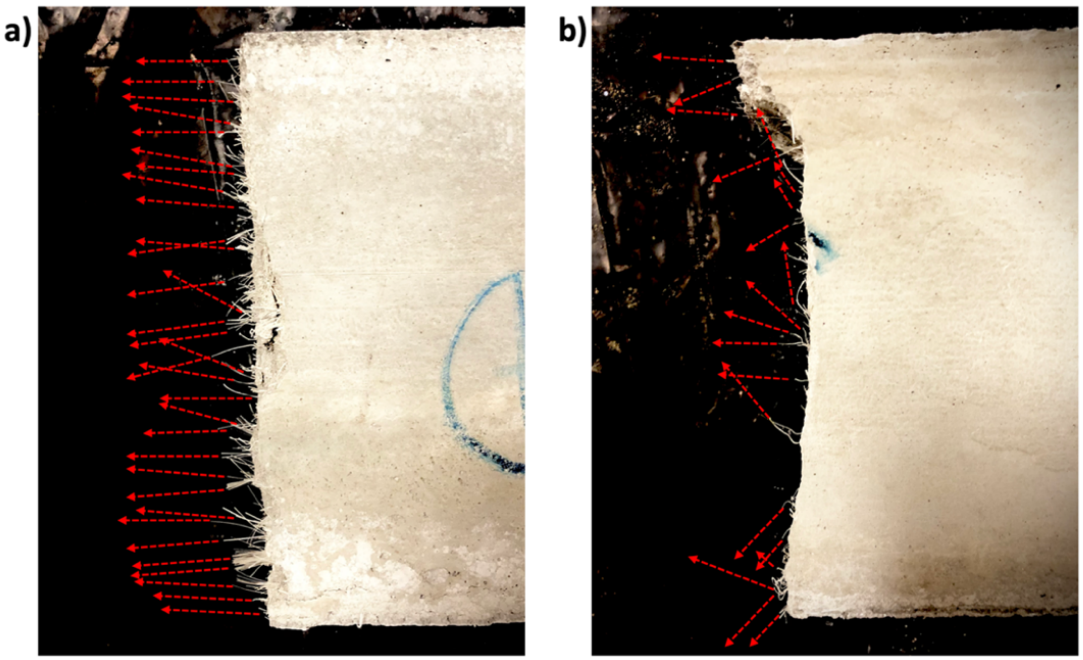

Figure 4.9: Front View of Fractured Specimens of: a) EB and b) CV

4.3.2. Flexural Properties

The final net deflections at failure were examined and reported for all beam specimens as presented in Table 4.4. For 0.5 % fiber content specimens, all the CV specimens failed before reaching a net deflection of L/60. However, two EB specimens, EB0.5%_1 and EB0.5%_4, had reached a net deflection of L/60. For 1 % fiber content specimens, two CV specimens, CV1%_2 and CV1%_4, reached a net deflection of L/60. Conversely, for EB specimens, all the four reached a net deflection of L/60. These results suggested that the EB method, which resulted in specimens with oriented fibers, increased the net deflection values at failure. This finding is consistent with previous studies [27,39,41].

Table 4.4: Final Net Deflection for All Beam Specimens

Sample	δ_f	Sample	δ_f
CV0.5%_1	L/75	CV1%_1	L/75
CV0.5%_2	L/75	CV1%_2	L/60
CV0.5%_3	L/75	CV1%_3	L/75
CV0.5%_4	L/67	CV1%_4	L/60
EB0.5%_1	L/60	EB1%_1	L/60
EB0.5%_2	L/85	EB1%_2	L/60
EB0.5%_3	L/75	EB1%_3	L/60
EB0.5%_4	L/60	EB1%_4	L/60

The results of P_{max}, f_p, f_{600}, f_{150}, f_{100}, and f_{60} for plain concrete, 0.5 %, and 1 % fiber content specimens are presented in Table 4.5, Table 4.6, and Table 4.7, respectively. Using a one-tailed paired t-test with a 95 % confidence interval, the means of P_{max} and f_p were statistically insignificant between PC, 0.5 %, and 1 % fiber content specimens. This indicates that adding PVA fibers would not result to an improvement to the peak load, which is consistent with previous studies [39,40]. However, adding PVA fibers showed to be significant in improving the post-peak behavior of concrete. This is shown in Figure 4.10, Figure 4.11, and Figure 4.12 that represent the load-deflection curve for PC, 0.5 %, and 1 % fiber content specimens, respectively.

Using a one-tailed paired t-test with a 95 % confidence interval, the mean of f_{60} for both the 0.5 % and 1 % fiber content specimens were statistically insignificant between the CV and EB casting methods. However, for both 0.5 % and 1 % fiber content specimens, the f_{600} and f_{150} had greater means for the EB casting method than the CV casting method using a one-tailed paired t-test with 95 % confidence. This enhancement in the residual strengths of EB specimens, where fibers were oriented parallel to the tensile stresses, aligned with previous research [14,27,38–40]. The values of f_{600}, which represents the residual strength after the peak, were 71 % and 50 % greater in the EB0.5% and EB1% than CV0.5% and CV1%, respectively. This shows that the EB

method had more ability to control the load drop after reaching the peak, due to fiber alignment. For the mean of f_{100}, the EB casting method proved to be significant in the 1 % fiber content specimens when compared to the CV casting method.

Table 4.5: Flexural Properties of PC Specimens

Sample	P_{max} (N)	f_P (MPa)	f_{600} (MPa)	f_{150} (MPa)	f_{100} (MPa)	f_{60} (Pa)
PC_1	10182	3.30	-	-	-	-
PC_2	9150	3.05	-	-	-	-
PC_3	8834	2.95	-	-	-	-
PC_4	9305	3.10	-	-	-	-
Mean	9368	3.10	-	-	-	-

Table 4.6: Flexural Properties of 0.5% FRC Specimens

Sample	P_{max} (N)	f_P (MPa)	f_{600} (MPa)	f_{150} (MPa)	f_{100} (MPa)	f_{60} (Pa)
CV0.5%_1	8933	3.00	0.85	0.45	0.20	0
CV0.5%_2	9805	3.25	0.65	0.50	0.25	0
CV0.5%_3	9500	3.15	0.60	0.40	0.15	0
CV0.5%_4	8289	2.75	0.70	0.40	0.25	0
Mean	9132	3.05	0.70	0.45	0.20	0
EB0.5%_1	8430	2.80	0.90	0.55	0.35	43
EB0.5%_2	9780	3.25	1.40	0.50	0.10	0
EB0.5%_3	9804	3.25	1.50	0.50	0.15	0
EB0.5%_4	8571	2.85	1.00	0.70	0.40	67
Mean	9146	3.05	1.20	0.55	0.25	27.5

Table 4.7: Flexural Properties of 1% FRC Specimens

Sample	P_{max} (N)	f_P (MPa)	f_{600} (MPa)	f_{150} (MPa)	f_{100} (MPa)	f_{60} (Pa)
CV1%_1	7984	2.65	1.25	0.45	0.20	0
CV1%_2	8926	3.00	1.30	0.80	0.55	70
CV1%_3	8698	2.90	1.40	0.75	0.40	0
CV1%_4	8905	2.95	0.80	0.75	0.55	181
Mean	8628	2.90	1.20	0.70	0.45	62.75
EB1%_1	9769	3.25	2.05	1.45	1.05	246
EB1%_2	9805	3.00	1.65	1.20	0.80	25
EB1%_3	8375	2.80	2.10	1.30	0.80	50
EB1%_4	9038	3.00	1.45	1.55	1.10	180
Mean	9247	3.00	1.80	1.40	0.95	125.25

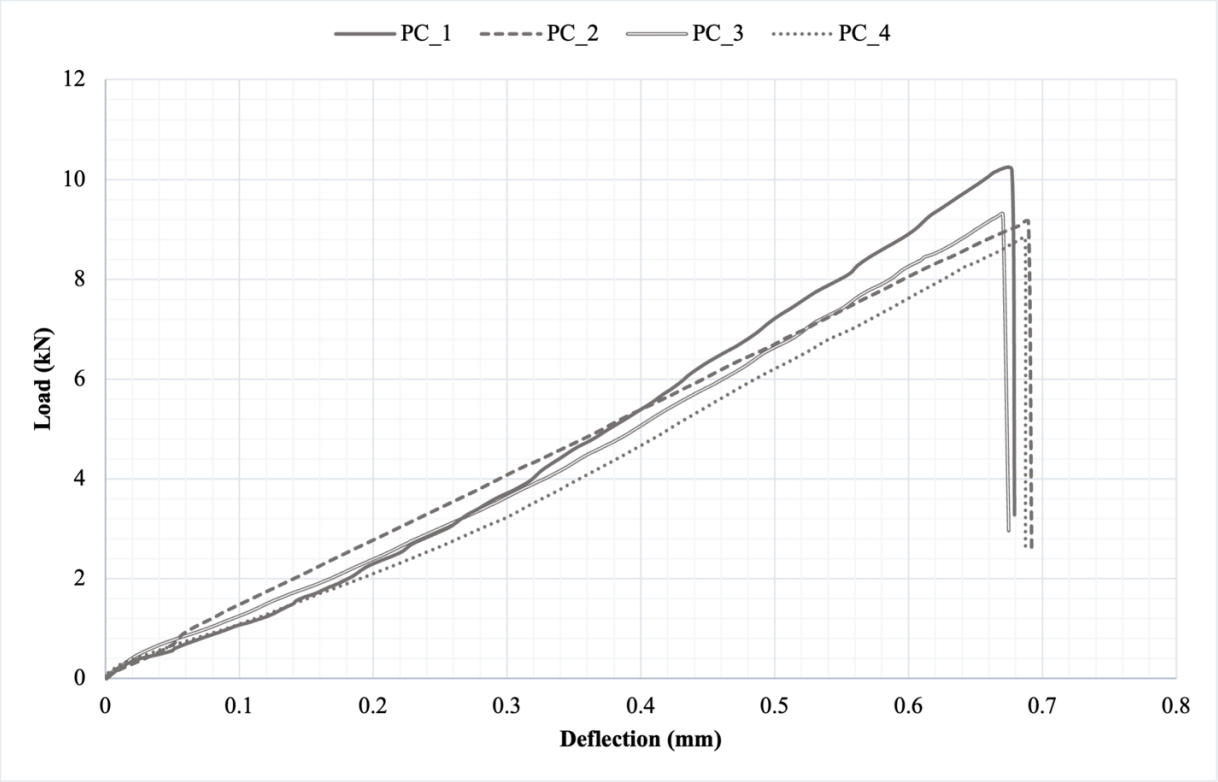

Figure 4.10: Load-deflection Curve for PC Specimens

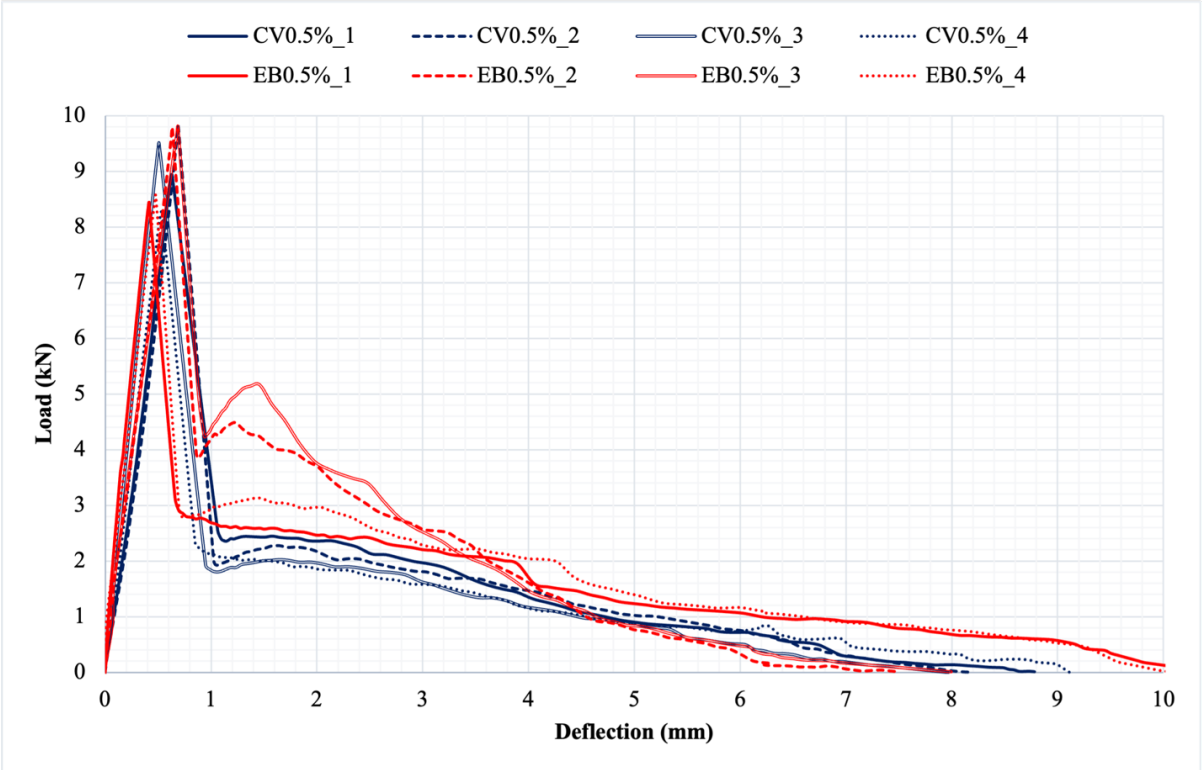

Figure 4.11: Load-deflection Curve for 0.5% FRC Specimens

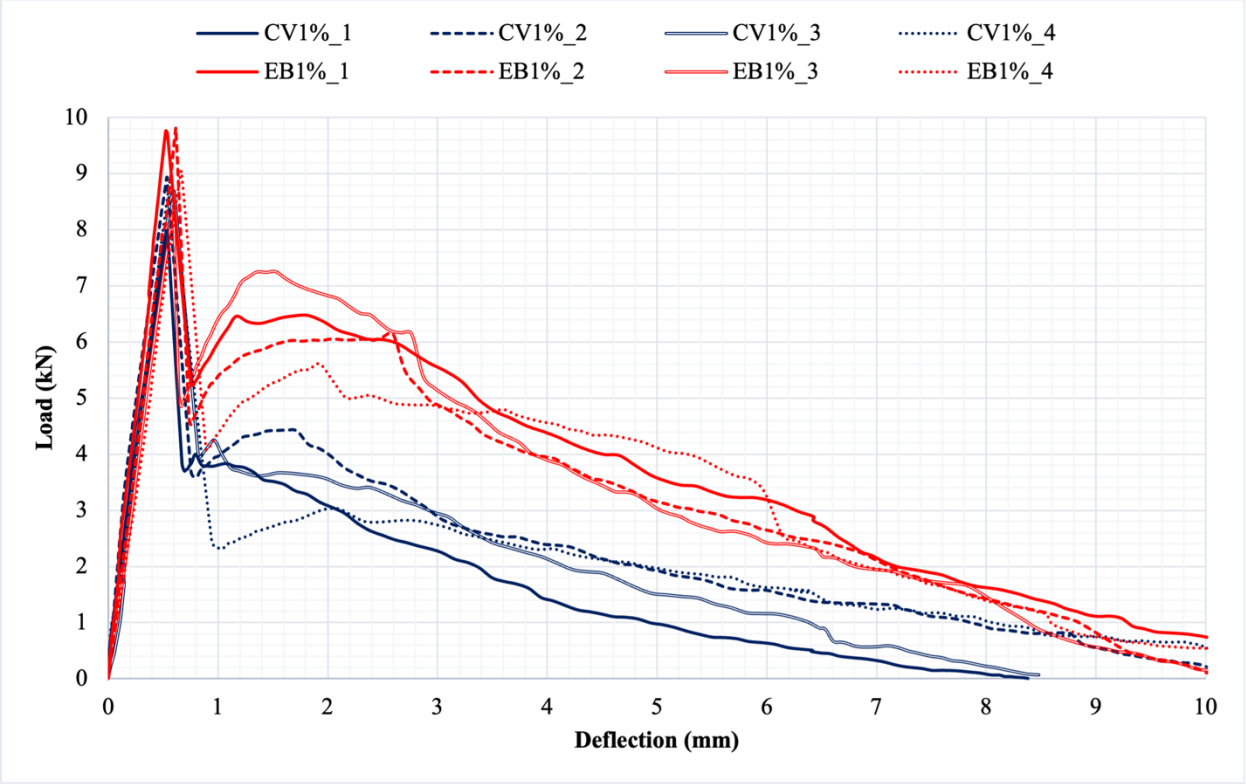

Figure 4.12: Load-deflection Curve for 1% FRC Specimens

The flexural test results comparison of the residual strengths, f_{600}, f_{150}, and f_{100} are shown in Figure 4.13. It seems that the extrusion-based method of casting had a greater impact in improving the residual strength in the 1 % fiber content specimens than on the 0.5 % fiber content specimens. This observation is quantified by the increased residual strengths of f_{600}, f_{150}, and f_{100} by 71 %, 22 %, and 25 % in the 0.5 % fiber content specimens, respectively, and by 50 %, 100 %, and 111 % in the 1 % fiber content specimens, respectively, when using the EB method. This can be attributed to the fact that increasing the fiber content, in the extrusion-based method, would result in having more aligned fibers. Such alignment significantly improved the flexural properties of the FRC specimens.

In general, due to the fact that fibers enhance the ductility of the material, it is natural that the flexural residual strengths increases with fiber content [55]. However, in this study, it appears

that the extrusion-based method of casting had greater impact on increasing f_{600} values, which represent the residual strength after the peak load, than the fiber content. This is presented by comparing the EB0.5% and CV1% specimens where the results are matched, even though the CV1% specimens included a double dosage of fibers compared to the EB0.5% specimens. Therefore, the EB method seemed to be significant in controlling the load drop after reaching the peak load. Yet, as the beam specimen approached its ultimate net deflection (at failure), increasing the fiber content in the concrete proved more beneficial than the extrusion-based casting method. Consequently, while the extrusion-based method can control immediate post-peak behavior, the fiber content eventually becomes the dominant factor in enhancing the material's flexural properties.

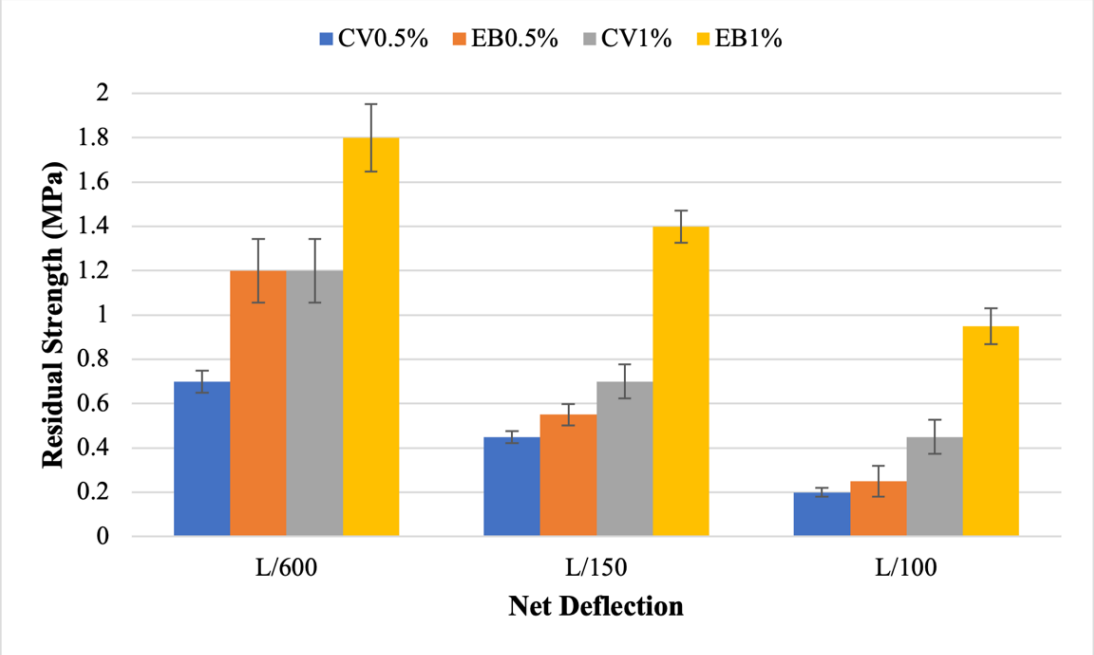

Figure 4.13: Flexural Residual Strength Comparison for all FRC Specimens

4.3.3. Flexural Toughness

The results of flexural toughness considered both 0.5 % and 1 % fiber content specimens are shown in Table 4.8 and Table 4.9, respectively. The data from the LVDT was used to measure

the mid-span deflection until the gauge's limit, after which the DIC data were used to compute the deflection at midspan. Using a one-tailed paired t-test, the flexural toughness, including T_{150}, T_{100} and T_{60}, had statistically greater means for the EB casting method than the CV casting method for both 0.5 % and 1 % specimens with 95 % confidence. This improvement aligns well with previous studies [27,38,41] and supports the idea that fiber orientation, which is more precisely controlled in the EB method, significantly enhances the flexural toughness of FRC.

Table 4.8: Flexural Toughness Properties of 0.5% FRC Specimens

Sample	$\boldsymbol{T_{150}}$ $(\boldsymbol{J})$	$\boldsymbol{T_{100}}$ $(\boldsymbol{J})$	$\boldsymbol{T_{60}}$ $(\boldsymbol{J})$	$\boldsymbol{R_{T,150}}$ (%)	$\boldsymbol{R_{T,100}}$ (%)	$\boldsymbol{R_{T,60}}$ (%)
CV0.5%_1	12	13	14	32	25	16
CV0.5%_2	11	13	14	28	22	14
CV0.5%_3	10	12	12	27	21	13
CV0.5%_4	10	11	12	29	23	15
Mean	11	12	13	29	23	15
EB0.5%_1	12	14	17	34	28	20
EB0.5%_2	15	16	16	38	28	17
EB0.5%_3	16	17	18	40	29	18
EB0.5%_4	13	15	18	36	30	21
Mean	14	16	17	37	29	19

Table 4.9: Flexural Toughness Properties of 1% FRC Specimens

Sample	$\boldsymbol{T_{150}}$ $(\boldsymbol{J})$	$\boldsymbol{T_{100}}$ $(\boldsymbol{J})$	$\boldsymbol{T_{60}}$ $(\boldsymbol{J})$	$\boldsymbol{R_{T,150}}$ (%)	$\boldsymbol{R_{T,100}}$ (%)	$\boldsymbol{R_{T,60}}$ (%)
CV1%_1	13	14	15	39	30	19
CV1%_2	15	19	23	43	36	26
CV1%_3	15	18	19	42	34	22
CV1%_4	13	17	21	37	32	24
Mean	14	17	20	40	33	23
EB1%_1	23	31	37	60	53	38
EB1%_2	21	28	33	59	51	37
EB1%_3	23	29	34	69	58	41
EB1%_4	20	28	37	56	52	37
Mean	22	29	35	61	54	38

Fibers are adept at bridging cracks, thereby facilitating increased deflection values at the point of failure. Figure 4.12 distinctly illustrates that in EB1% specimens, the fibers exhibited superior crack-bridging capabilities when compared to CV1% specimens. This enhanced performance can be attributed to the fact that the EB method aligns fibers parallel to the flow of concrete, optimizing their orientation in relation to tensile stresses. In contrast, the CV casting method results in a random distribution of fibers within the beams, potentially reducing their efficacy.

There was no significant difference in the peak load values between the CV and EB methods of casting, as shown in Table 4.7. However, a closer look at the areas beneath the load-deflection curves revealed substantial discrepancies. As depicted in Figure 4.12, the load–deflection curves for the EB specimens covered a more expansive area compared to their CV counterparts. compared to the CV specimens. Furthermore, all EB specimens achieved a net deflection of L/60. This evidence leads to the conclusion that the EB method significantly enhanced the flexural energy absorption of the FRC specimens.

The flexural test results comparison of equivalent flexural strength ratios, $R_{T,150}$, $R_{T,100}$, and $R_{T,60}$ are shown in Figure 4.14. The equivalent flexural strength ratio is a parameter used to characterize the flexural performance of FRC and provide an indication of the residual strength after first crack formation, which is a key consideration for FRC performance. It seems that using the EB method of casting resulted in higher equivalent flexural strength ratios compared to CV method, which means that the FRC specimen maintains a higher proportion of its strength after cracking, indicating that it has good ductility and toughness. However, this enhancement in the toughness was greater in the 1 % fiber content specimens than 0.5 % fiber content specimens. The EB method improved the equivalent flexural strength ratios, $R_{T,150}$, $R_{T,100}$, and $R_{T,60}$ by 28 %, 26

%, and 27 % in the 0.5 % fiber content specimens, respectively, and by 53 %, 64 %, and 65 % in the 1 % fiber content specimens, respectively. The reason is that increasing the fiber content, in the extrusion-based method, would result in having more aligned fibers. These aligned fibers contributed directly to the improvement of the FRC specimen's ductility.

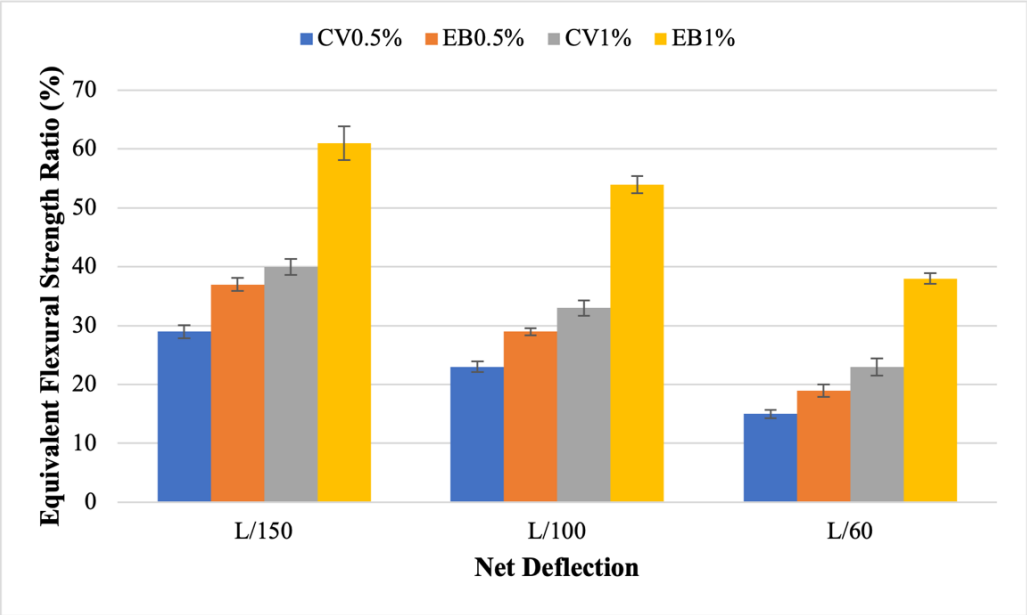

Figure 4.14: Equivalent Flexural Strength Ratio Comparison for all FRC Specimens

4.3.4. Crack Propagation and Strain Localization

There are critical phenomena that occur during the flexural test of FRC beams include crack propagation and strain localization. These phenomena play a crucial role in the performance of FRC structures, and understanding how they operate can potentially contribute to improving the performance of these structures. In the context of FRC, the alignment of fibers is vital in the process of crack propagation. If the fibers are aligned in a preferred direction, specifically parallel to the tensile stresses, they can efficiently bridge and deflect cracks, thereby inhibiting their propagation. Strain localization is another critical aspect of FRC performance. In the extrusion-based casting method, the layering technique could potentially introduce strain localization at the

interfaces between layers. This might, in turn, serve as pathways for crack propagation. In this section, the focus is on examining both the process of crack propagation and strain localization, using the DIC technique as the primary investigative tool.

The crack propagation process was investigated at different stages of the test. The 1st and 4th stages were employed for examining the crack propagation. These two stages represent the most critical stages where the 1st stage shows the crack at the peak load, while the 4th stage shows when the crack fully propagates and reaches the top of the beam. Figure 4.15 and Figure 4.16 represent the critical crack length for 0.5 % and 1 % specimens, respectively at the 1st stage.

As it can be noticed that all EB specimens, except EB0.5%_1, exhibited multiple cracks that initiated from the bottom of the beam. The initiation of multiple cracks at the bottom of a FRC beam during flexural testing can significantly influence its flexural performance [56]. In bending, the bottom of the beam experiences tension, which is where cracks are expected to initiate. The presence of multiple cracks, as opposed to a single large crack, suggested an effective distribution and alignment of fibers in the EB specimens. The embedded fibers, in the EB specimens, bridged the cracks, helping to redistribute the stress more evenly across the concrete matrix, and thereby reducing the chance of catastrophic failure [57].

For CV specimens, most of the beams exhibited one crack at the bottom of the beam. However, there were some localized strains in the middle of beam as seen in CV0.5%_1, CV0.5%_4, CV1%_2, and CV1%_4, which indicated that they might have experienced a mixed mode fracture (Mode I and II), which is a fracture condition where a material undergoes multiple forms of crack propagation modes simultaneously. The localized strains appearance at the middle of a FRC beam during a flexural test indicated an irregularity in the material properties or testing setup. This could suggest a non-uniform distribution of fibers, voids, or other imperfections within

the material. Although it seems that the specimens that exhibited localized strains in the middle of beam reached a higher value of deflection compared with the other CV specimens as seen in Figure 4.11 and Figure 4.12. Therefore, such a phenomenon necessitates further investigation to understand its implications and address potential issues in the material composition or test procedure.

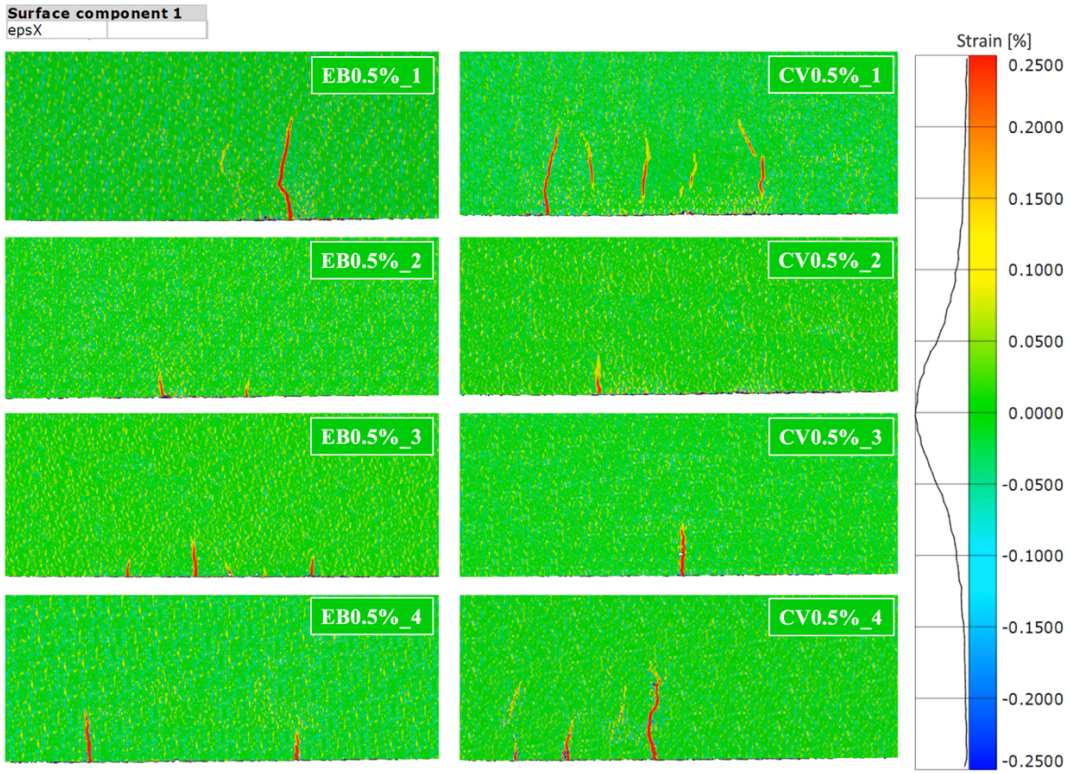

Figure 4.15: Full Strain Field (x-axis) at the 1st Stage for 0.5% Fiber Content Specimens (the contour legend indicates the concentration of each strain level)

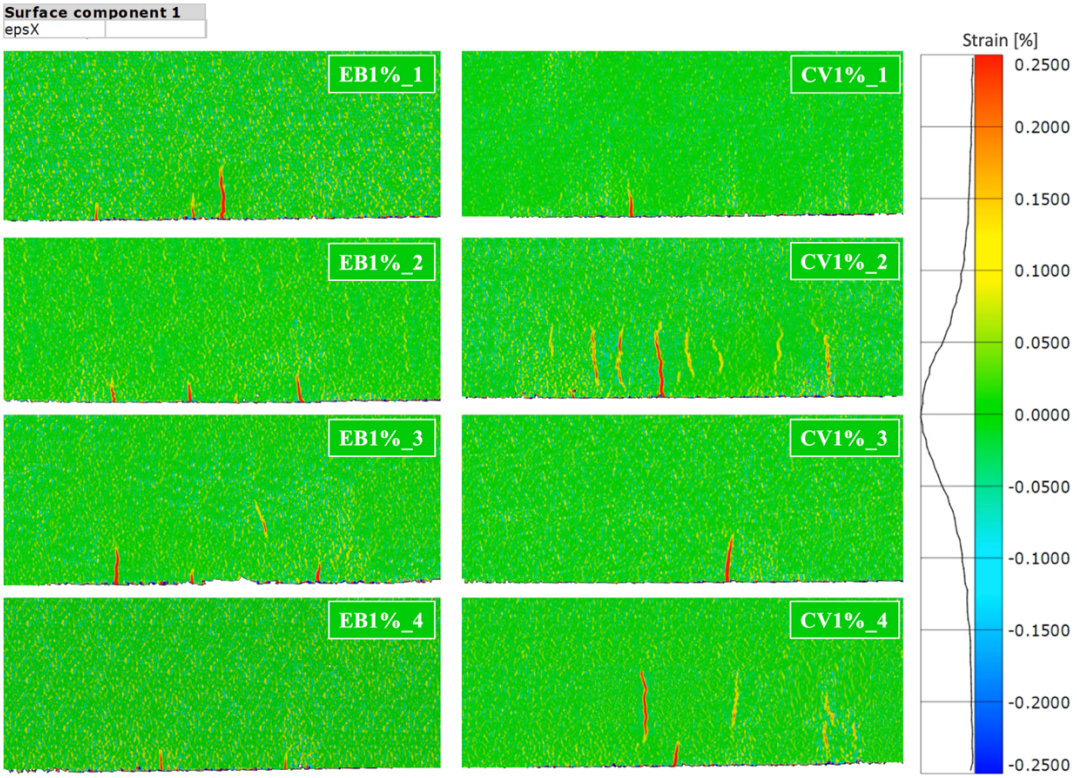

Figure 4.16: Full Strain Field (x-axis) at the 1st Stage for 1% Fiber Content Specimens (the contour legend indicates the concentration of each strain level)

For a better understanding of the crack propagation process in both EB and CV specimens, Figure 4.17 and Figure 4.18 represent the 4th stage for 0.5 % and 1 % specimens, respectively. All specimens exhibited one crack opening initiated at the bottom of the beam. However, when the crack reached the mid height of the beam, specimen EB1%_1 exhibited a secondary crack that was deflected from the primary crack as seen in Figure 4.18. Having deflected cracks in the EB specimens indicated that the fibers alignment factor affected the crack propagation process. The mechanism of crack deflection expands the crack's surface area, enabling more energy absorption and increasing the material's toughness [58,59]. Therefore, the EB1%_1 specimen had the greatest overall toughness compared with all other specimens.

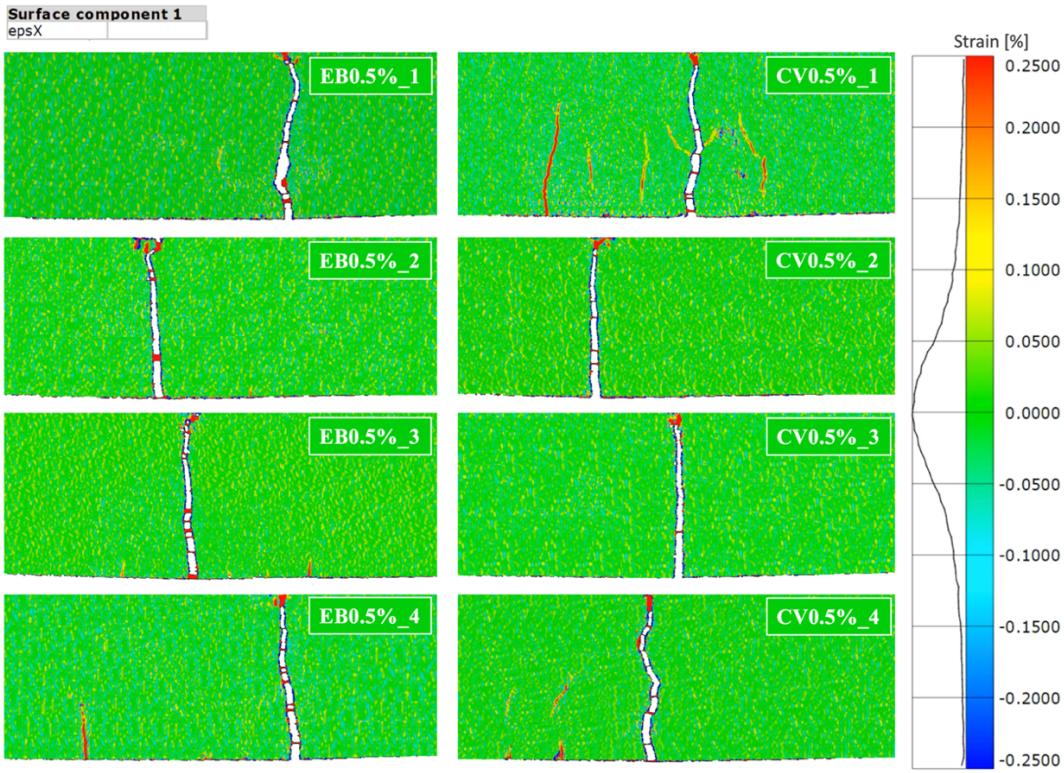

Figure 4.17: Full Strain Field (x-axis) at the 4th Stage for 0.5% Fiber Content Specimens (the contour legend indicates the concentration of each strain level)

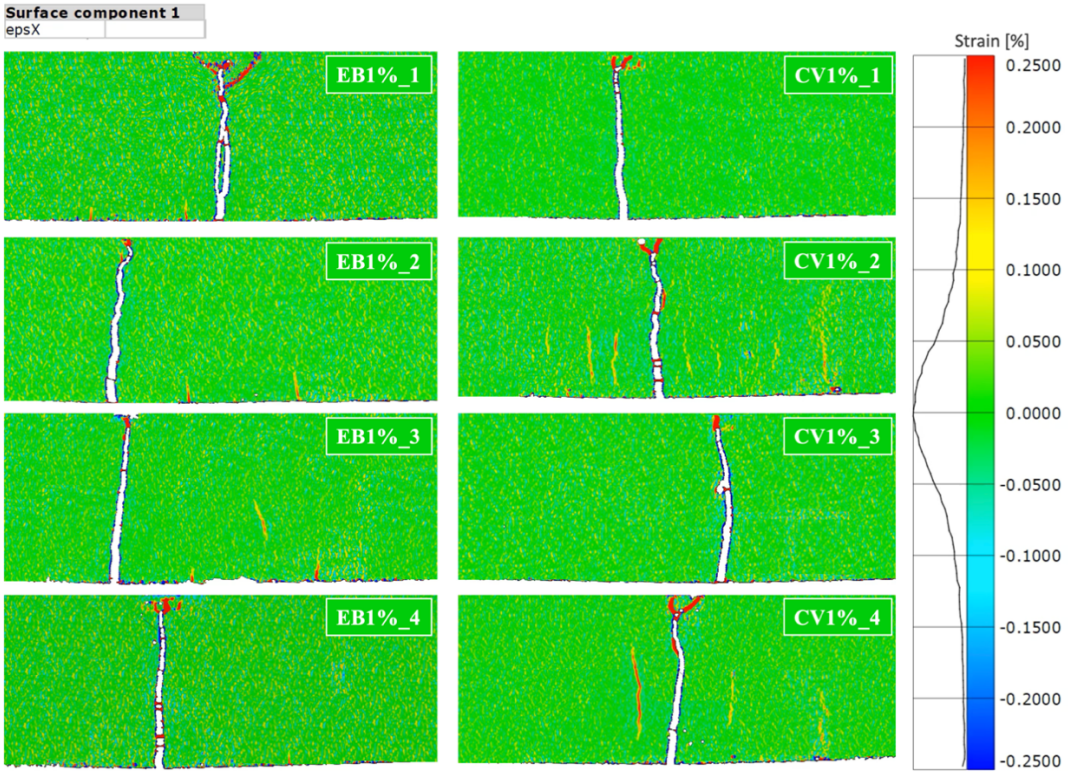

Figure 4.18: Full Strain Field (x-axis) at the 4th Stage for 1% Fiber Content Specimens (the contour legend indicates the concentration of each strain level)

Regarding the strain localization between layer interfaces, DIC was employed to detect any localized strains. Given that the EB method involved casting in three layers, with each deposited sequentially on top of the other, no localized strains were observed at the layer interfaces for both EB0.5% and EB1% specimens, as illustrated in Figure 4.19 and Figure 4.20, respectively. Even though some localized strains were confined to the vicinity of the vertical crack path of the EB specimens, such as EB0.5%_1 and EB1%_1, these localized strains did not extend horizontally along the interfaces between layers. This can be attributed to inherent variations in material qualities and layer bonding strength in the EB FRC. Insufficient strength at interfaces between layers might compromise the load transfer and bonding, which could lead to layer delamination and increased strain localization at the interfaces [49]. Moreover, the orientation and alignment of the fibers in the layers could also influence the behavior of strain localization at layer interfaces. In the CV specimens, the strain localization at layer interfaces was diminished due to the random orientation of fibers, resulting in some fibers being positioned perpendicular to the horizontal crack path. These fibers impede the horizontal propagation of cracks between layers and function as a bridge for load transfer and strain distribution.

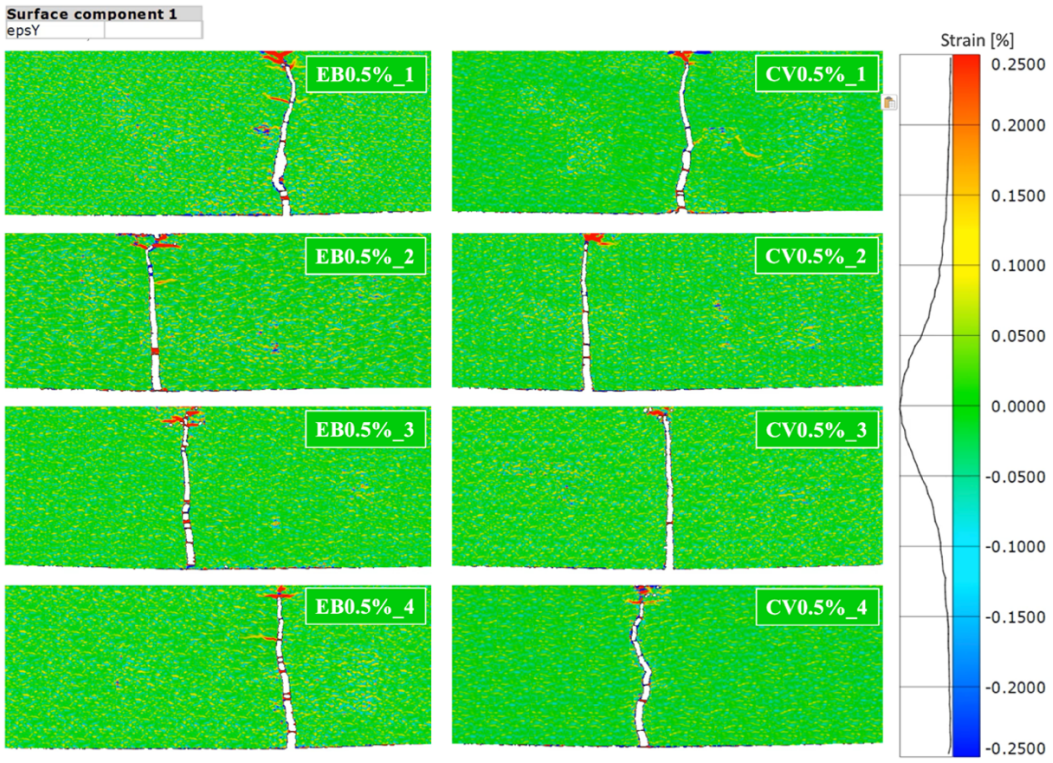

Figure 4.19: Full Strain Field (y-axis) at the 4th Stage for 0.5% Fiber Content Specimens (the contour legend indicates the concentration of each strain level)

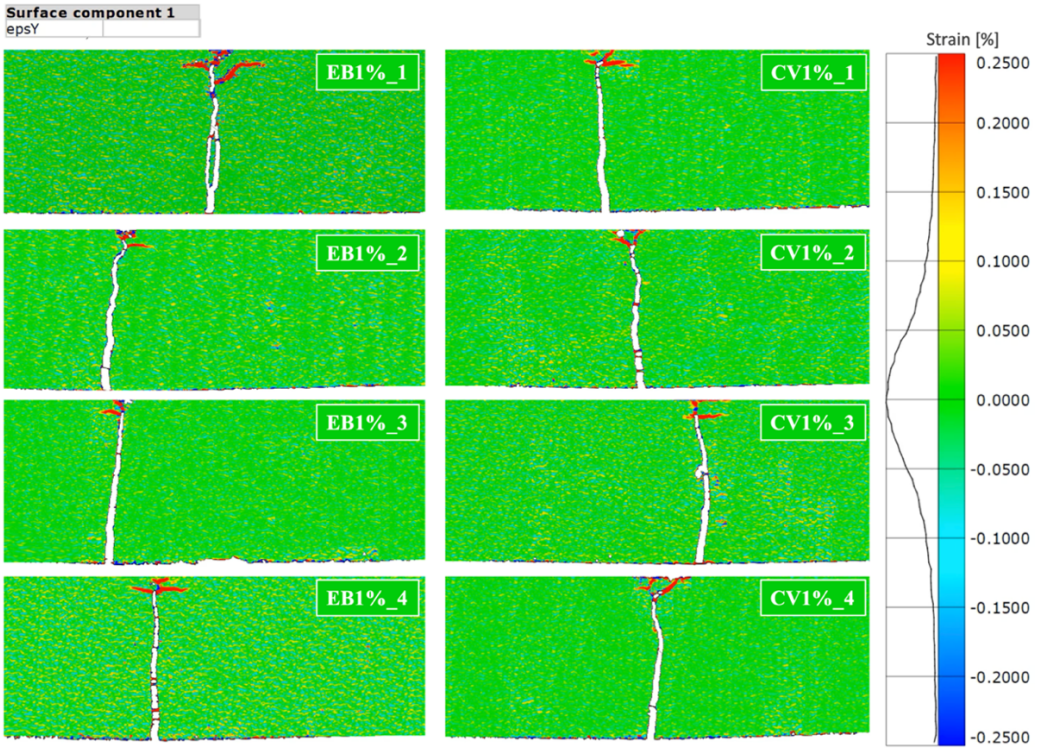

Figure 4.20: Full Strain Field (y-axis) at the 4th Stage for 1% Fiber Content Specimens (the contour legend indicates the concentration of each strain level)

4.4. Conclusion

This research assessed the flexural properties of FRC, comparing the performance of two casting methods – extrusion-based (EB) and conventional (CV) – using two PVA fiber dosages: 0.5 % and 1 % by volume. The key findings of the study are as follows:

1. While the inclusion of PVA fibers did not enhance the peak load in the third-point bending tests, the fibers did improve the post-peak behavior of the concrete.
2. The EB casting method effectively controlled the load drop immediately after reaching the peak, due to the fiber alignment. This consequently improved the residual strength at L/600 net deflection by 71 % and 50 % for the 0.5 % and 1 % fiber volume specimens, respectively.
3. Compared to the CV specimens, the EB specimens demonstrated higher deflection values at complete failure, which can be attributed to the superior crack-bridging capabilities resulting from fiber alignment.
4. The EB specimens exhibited improved ductility and toughness, retaining a significant post-peak load-carrying capacity. This led to higher equivalent flexural strength ratios compared to the CV specimens.
5. DIC was instrumental in measuring displacements under load, tracking crack propagation, and identifying localized strains between the layer interfaces.
6. The presence of multiple cracks in EB specimens, compared to a single large crack in CV specimens, highlighted the effective distribution and alignment of fibers in EB samples, facilitating stress redistribution across the concrete matrix.

7. Localized strains, observed near the vertical crack path in some of the EB specimens, did not propagate horizontally across the layer interfaces. Conversely, the random fiber orientation in the CV specimens counteracted such strain localization.

These findings underscore the potential of the extrusion-based method to enhance the flexural properties of FRC, promising significant benefits for the construction industry.

4.4.1. Limitation and Future Work

Despite the promising results, the application of the extrusion-based technique was confined to a pump that limited fiber length to 20 mm, necessitating the use of 19 mm synthetic fibers. The study also faced challenges regarding the aggregate size, as the extrusion pump required mixtures without coarse aggregate. Even though the inclusion of coarse aggregate would likely influence fiber orientation, insights derived from the mortar-based experiments are still applicable to the flexural properties of FRC. This relevance is accentuated by the current industry limitations on 3D printing materials, which typically restrict the process to using mortar.

The findings of this study shed light on the potential of the pump extrusion-based method to enhance the flexural properties of FRC. However, further exploration and optimization of this method are crucial to overcome the current limitations and fully exploit this innovative technique, ultimately paving the way for substantial advancements in the construction industry.

4.5. Authorship Contribution Statement

The authors confirm their contributions to the paper as follows: Rashed Alarrak: Writing – review & editing, Writing – original draft, Visualization, Validation, Methodology, Investigation, Formal analysis, Data curation, Conceptualization. Byeonguk Jeon: Writing – original draft,

Investigation. Alexander S. Brand: Writing – review & editing, Supervision, Methodology, Conceptualization.

4.6. References

[1] A. Bentur, S. Mindess, Fibre reinforced cementitious composites, 2nd ed, Taylor & Francis, London ; New York, 2007.

[2] R.F. Zollo, Fiber-reinforced concrete: an overview after 30 years of development, Cem. Concr. Compos. 19 (1997) 107–122. https://doi.org/10.1016/S0958-9465(96)00046-7.

[3] L. Ferrara, M. Di Prisco, M.G.L. Lamperti, Identification of the stress-crack opening behavior of HPFRCC: the role of flow-induced fiber orientation, in: Proc. Fram., 2010: pp. 1541–1550.

[4] X. Sun, J. Zhou, Q. Wang, J. Shi, H. Wang, PVA fibre reinforced high-strength cementitious composite for 3D printing: Mechanical properties and durability, Addit. Manuf. 49 (2022) 102500. https://doi.org/10.1016/j.addma.2021.102500.

[5] S. Xu, Y. Lyu, S. Xu, Q. Li, Enhancing the initial cracking fracture toughness of steel-polyvinyl alcohol hybrid fibers ultra high toughness cementitious composites by incorporating multi-walled carbon nanotubes, Constr. Build. Mater. 195 (2019) 269–282. https://doi.org/10.1016/j.conbuildmat.2018.10.133.

[6] L. Ferrara, N. Ozyurt, M. di Prisco, High mechanical performance of fibre reinforced cementitious composites: the role of "casting-flow induced" fibre orientation, Mater. Struct. 44 (2011) 109–128. https://doi.org/10.1617/s11527-010-9613-9.

[7] Y. Akkaya, J. Picka, S.P. Shah, Spatial distribution of aligned short fibers in cement composites, J. Mater. Civ. Eng. 12 (2000) 272–279.

[8] A.E. Naaman, H.W. Reinhardt, Characterization of high performance fiber reinforced cement composites—HPFRCC, in: High Perform. Fiber Reinf. Cem. Compos., 1996: pp. 1–24.

[9] S.P. Shah, C. Ouyang, Mechanical behavior of fiber-reinforced cement-based composites, J. Am. Ceram. Soc. 74 (1991) 2727–2953.

[10] G. Ma, Z. Li, L. Wang, F. Wang, J. Sanjayan, Mechanical anisotropy of aligned fiber reinforced composite for extrusion-based 3D printing, Constr. Build. Mater. 202 (2019) 770–783. https://doi.org/10.1016/j.conbuildmat.2019.01.008.

[11] A. Abrishambaf, M. Pimentel, S. Nunes, Influence of fibre orientation on the tensile behaviour of ultra-high performance fibre reinforced cementitious composites, Cem. Concr. Res. 97 (2017) 28–40. https://doi.org/10.1016/j.cemconres.2017.03.007.

[12] A. Enfedaque, M.G. Alberti, J.C. Gálvez, Influence of Fiber Distribution and Orientation in the Fracture Behavior of Polyolefin Fiber-Reinforced Concrete, Materials. 12 (2019) 220. https://doi.org/10.3390/ma12020220.

[13] C. Xie, M. Cao, M. Khan, H. Yin, J. Guan, Review on different testing methods and factors affecting fracture properties of fiber reinforced cementitious composites, Constr. Build. Mater. 273 (2021) 121766. https://doi.org/10.1016/j.conbuildmat.2020.121766.

[14] R. Mu, Y. Xue, L. Qing, H. Li, Y. Zhao, J. Zhou, J. Su, Preparation and mechanical performance of annularly aligned steel fiber reinforced cement-based composite pipes, Constr. Build. Mater. 211 (2019) 167–173. https://doi.org/10.1016/j.conbuildmat.2019.03.146.

[15] R. Mu, H. Li, L. Qing, J. Lin, Q. Zhao, Aligning steel fibers in cement mortar using electro-magnetic field, Constr. Build. Mater. 131 (2017) 309–316. https://doi.org/10.1016/j.conbuildmat.2016.11.081.

[16] L. Liu, J. Xu, Y. Wang, T. Yin, H. Chu, Electrical and Piezoresistive Properties of Steel Fiber Cement-based Composites Aligned by a Magnetic Field, J. Wuhan Univ. Technol.-Mater Sci Ed. 37 (2022) 229–240. https://doi.org/10.1007/s11595-022-2522-2.

[17] P. Kheml, K. Carrera, K. Künzel, V. Papež, R. Sovják, Summary of findings on magnetic orientation of fibers in cement composites, Mater. Today Proc. 58 (2022) 1104–1107. https://doi.org/10.1016/j.matpr.2022.01.201.

[18] S.-T. Kang, J.-K. Kim, Investigation on the flexural behavior of UHPCC considering the effect of fiber orientation distribution, Constr. Build. Mater. 28 (2012) 57–65. https://doi.org/10.1016/j.conbuildmat.2011.07.003.

[19] S.-T. Kang, J.-K. Kim, Numerical simulation of the variation of fiber orientation distribution during flow molding of Ultra High Performance Cementitious Composites (UHPCC), Cem. Concr. Compos. 34 (2012) 208–217. https://doi.org/10.1016/j.cemconcomp.2011.09.015.

[20] L. Ferrara, N. Tregger, S.P. Shah, Flow-induced fiber orientation in SCSFRC: monitoring and prediction, in: Des. Prod. Place. Self-Consol. Concr., Springer, 2010: pp. 417–428.

[21] A.C. Bordelon, J.R. Roesler, Spatial distribution of synthetic fibers in concrete with X-ray computed tomography, Cem. Concr. Compos. 53 (2014) 35–43. https://doi.org/10.1016/j.cemconcomp.2014.04.007.

[22] Y. Shao, S. Marikunte, S.P. Shah, Extruded fiber-reinforced composites, Concr. Int. 17 (1995) 48–53.

[23] Z. Li, B. Mu, T.P. Chang, C.-T. Hsu, Prediction of overall tension behavior of short fiber-reinforced composites, Int. J. Solids Struct. 36 (1999) 4071–4087.

[24] H. Takashima, K. Miyagai, T. Hashida, V.C. Li, A design approach for the mechanical properties of polypropylene discontinuous fiber reinforced cementitious composites by extrusion molding, Eng. Fract. Mech. 70 (2003) 853–870. https://doi.org/10.1016/S0013-7944(02)00154-6.

[25] X. Zhou, Z. Li, Characterizing rheology of fresh short fiber reinforced cementitious composite through capillary extrusion, J. Mater. Civ. Eng. 17 (2005) 28–35.

[26] Y. Zhang, F. Aslani, Development of fibre reinforced engineered cementitious composite using polyvinyl alcohol fibre and activated carbon powder for 3D concrete printing, Constr. Build. Mater. 303 (2021) 124453. https://doi.org/10.1016/j.conbuildmat.2021.124453.

[27] J. Ye, C. Cui, J. Yu, K. Yu, F. Dong, Effect of polyethylene fiber content on workability and mechanical-anisotropic properties of 3D printed ultra-high ductile concrete, Constr. Build. Mater. 281 (2021) 122586. https://doi.org/10.1016/j.conbuildmat.2021.122586.

[28] M. Sugavaneswaran, G. Arumaikkannu, Modelling for randomly oriented multi material additive manufacturing component and its fabrication, Mater. Des. 1980-2015. 54 (2014) 779–785. https://doi.org/10.1016/j.matdes.2013.08.102.

[29] H. Stang, V.C. Li, Extrusion of ECC-material, in: Proc High Perform. Fiber Reinf. Cem. Compos., 1999: pp. 203–212.

[30] S.C. Paul, Y.W.D. Tay, B. Panda, M.J. Tan, Fresh and hardened properties of 3D printable cementitious materials for building and construction, Arch. Civ. Mech. Eng. 18 (2018) 311–319. https://doi.org/10.1016/j.acme.2017.02.008.

[31] X. Qian, X. Zhou, B. Mu, Z. Li, Fiber alignment and property direction dependency of FRC extrudate, Cem. Concr. Res. 33 (2003) 1575–1581.

[32] Z. Li, B. Mu, Innovations forum: Application of extrusion for manufacture of short fiber reinforced cementitious composite, J. Mater. Civ. Eng. 10 (1998) 2–4. https://doi.org/10.1061/(ASCE)0899-1561(1998)10:1(2).

[33] Z. Hou, X. Tian, J. Zhang, D. Li, 3D printed continuous fibre reinforced composite corrugated structure, Compos. Struct. 184 (2018) 1005–1010. https://doi.org/10.1016/j.compstruct.2017.10.080.

[34] S.P. Shah, Y. Shao, Extrusion processing of fiber-reinforced cement-matrix composites, Process. Des. Perform. Compos. Mater. 52 (1994) 205–210.

[35] L. Ferrara, N. Ozyurt, M. di Prisco, High mechanical performance of fibre reinforced cementitious composites: the role of “casting-flow induced” fibre orientation, Mater. Struct. 44 (2011) 109–128. https://doi.org/10.1617/s11527-010-9613-9.

[36] X. Zhou, Z. Li, Characterization of rheology of fresh fiber reinforced cementitious composites through ram extrusion, Mater. Struct. 38 (2005) 17–24. https://doi.org/10.1007/BF02480570.

[37] S.-T. Kang, J.-K. Kim, Numerical simulation of the variation of fiber orientation distribution during flow molding of ultra high performance cementitious composites (UHPCC), Cem. Concr. Compos. 34 (2012) 208–217.

[38] H. Huang, X. Gao, L. Li, H. Wang, Improvement effect of steel fiber orientation control on mechanical performance of UHPC, Constr. Build. Mater. 188 (2018) 709–721. https://doi.org/10.1016/j.conbuildmat.2018.08.146.

[39] S.T. Kang, B.Y. Lee, J.-K. Kim, Y.Y. Kim, The effect of fibre distribution characteristics on the flexural strength of steel fibre-reinforced ultra high strength concrete, Constr. Build. Mater. 25 (2011) 2450–2457. https://doi.org/10.1016/j.conbuildmat.2010.11.057.

[40] R. Zerbino, J.M. Tobes, M.E. Bossio, G. Giaccio, On the orientation of fibres in structural members fabricated with self compacting fibre reinforced concrete, Cem. Concr. Compos. 34 (2012) 191–200. https://doi.org/10.1016/j.cemconcomp.2011.09.005.

[41] I. da Silva Brito, D. Alan Strauss Rambo, S. Martini, R. Pícolo Salvador, M. Fabrízio de Menezes Freitas, Flexural behavior of HPFRCC: Enhancing post-crack strength and toughness by magnetic alignment of the reinforcement, Constr. Build. Mater. 269 (2021) 121265. https://doi.org/10.1016/j.conbuildmat.2020.121265.

[42] B. Pan, K. Qian, H. Xie, A. Asundi, Two-dimensional digital image correlation for in-plane displacement and strain measurement: a review, Meas. Sci. Technol. 20 (2009) 062001. https://doi.org/10.1088/0957-0233/20/6/062001.

[43] S. Roux, J. Réthoré, F. Hild, Digital image correlation and fracture: an advanced technique for estimating stress intensity factors of 2D and 3D cracks, J. Phys. Appl. Phys. 42 (2009) 214004. https://doi.org/10.1088/0022-3727/42/21/214004.

[44] S.G. Shah, J.M. Chandra Kishen, Fracture Properties of Concrete–Concrete Interfaces Using Digital Image Correlation, Exp. Mech. 51 (2011) 303–313. https://doi.org/10.1007/s11340-010-9358-y.

[45] D.G. Aggelis, S. Verbruggen, E. Tsangouri, T. Tysmans, D. Van Hemelrijck, Characterization of mechanical performance of concrete beams with external reinforcement by acoustic emission and digital image correlation, Constr. Build. Mater. 47 (2013) 1037–1045. https://doi.org/10.1016/j.conbuildmat.2013.06.005.

[46] S. Rouchier, G. Foray, N. Godin, M. Woloszyn, J.-J. Roux, Damage monitoring in fibre reinforced mortar by combined digital image correlation and acoustic emission, Constr. Build. Mater. 38 (2013) 371–380. https://doi.org/10.1016/j.conbuildmat.2012.07.106.

[47] S.Y. Alam, J. Saliba, A. Loukili, Fracture examination in concrete through combined digital image correlation and acoustic emission techniques, Constr. Build. Mater. 69 (2014) 232–242. https://doi.org/10.1016/j.conbuildmat.2014.07.044.

[48] K. Yu, L. Li, J. Yu, J. Xiao, J. Ye, Y. Wang, Feasibility of using ultra-high ductility cementitious composites for concrete structures without steel rebar, Eng. Struct. 170 (2018) 11–20. https://doi.org/10.1016/j.engstruct.2018.05.037.

[49] M.C. Jenkins, A.S. Brand, T.T. Painter, S.T. Sherry, A Preliminary Digital Image Correlation Study of the AnisotropicMechanical Properties of a 3D-Printed Mortar, 6th Int. Conf. Civ. Struct. Transp. Eng. (2021). https://doi.org/10.11159/iccste21.146.

[50] Y. Niu, H. Huang, J. Zhang, W. Jin, J. Wei, Q. Yu, Development of the strain field along the crack in ultra-high-performance fiber-reinforced concrete (UHPFRC) under bending by digital image correlation technique, Cem. Concr. Res. 125 (2019) 105821. https://doi.org/10.1016/j.cemconres.2019.105821.

[51] R. Alarrak, B. Jeon, A.S. Brand, Fracture properties of extruded fiber-reinforced mortar with preferentially aligned fibers, Constr. Build. Mater. 403 (2023) 133022. https://doi.org/10.1016/j.conbuildmat.2023.133022.

[52] C1609/C1609M − 19a, Standard test method for flexural performance of fiber-reinforced concrete (Using beam with third-point loading), ASTM International, 2019. https://doi.org/10.1520/C1609_C1609M-19A.

[53] J. Roesler, G. Paulino, C. Gaedicke, A. Bordelon, K. Park, Fracture Behavior of Functionally Graded Concrete Materials for Rigid Pavements, Transp. Res. Rec. J. Transp. Res. Board. 2037 (2007) 40–49. https://doi.org/10.3141/2037-04.

[54] H. Schreier, J.-J. Orteu, M.A. Sutton, Image Correlation for Shape, Motion and Deformation Measurements: Basic Concepts,Theory and Applications, Springer US, Boston, MA, 2009. https://doi.org/10.1007/978-0-387-78747-3.

[55] B. Rehder, K. Banh, N. Neithalath, Fracture behavior of pervious concretes: The effects of pore structure and fibers, Eng. Fract. Mech. 118 (2014) 1–16. https://doi.org/10.1016/j.engfracmech.2014.01.015.

[56] M. Maalej, V.C. Li, Flexural/Tensile-Strength Ratio in Engineered Cementitious Composites, J. Mater. Civ. Eng. 6 (1994) 513–528. https://doi.org/10.1061/(ASCE)0899-1561(1994)6:4(513).

[57] I.H. Yang, C. Joh, B.-S. Kim, Structural behavior of ultra high performance concrete beams subjected to bending, Eng. Struct. 32 (2010) 3478–3487. https://doi.org/10.1016/j.engstruct.2010.07.017.

[58] E.A. Zimmermann, M.E. Launey, R.O. Ritchie, The significance of crack-resistance curves to the mixed-mode fracture toughness of human cortical bone, Biomaterials. 31 (2010) 5297–5305. https://doi.org/10.1016/j.biomaterials.2010.03.056.

[59] A. Akram, The Overview of Fracture Mechanics Models for Concrete, Archit. Civ. Eng. Environ. 14 (2021) 47–57. https://doi.org/10.21307/acee-2021-005.

Chapter 5. Size Effect of Fracture Properties of Extruded Fiber-Reinforced Mortar with Preferentially Aligned Fibers[3]

Abstract

This research investigates the fracture properties of polyvinyl alcohol fiber-reinforced concrete (FRC), employing the size effect method (SEM) to analyze and compare the impacts of conventional casting (CV) and pump-driven extrusion (EB) techniques. The investigation revealed that, consistent with previous findings, the inclusion of fibers improves ductility and post-peak behavior in concrete. Notably, through SEM analysis, this investigation presented the role of fiber reinforcement by demonstrating that fiber alignment, as facilitated by the EB technique, markedly enhances FRC's fracture properties, including total fracture energy. This enhancement is primarily due to the fibers' enhanced crack-bridging capabilities in EB specimens, which contribute to greater ductility and toughness. Additionally, the study revealed that while the random addition of fibers in CV specimens did not consistently improve – and may even reduce – fracture properties, the precise alignment of fibers *via* the EB method substantially enhanced these characteristics. The findings shed light on the crucial interaction between fiber orientation, casting technique, and specimen size, offering critical insights for the design and implementation of FRC in structural applications.

Keywords: Fiber-reinforced concrete, Fracture, Size-effect, Extrusion, Fiber alignment.

[3] **R. Alarrak**, A. Al-Rufaydah, A.S. Brand, Size Effect of Fracture Properties of Extruded Fiber-Reinforced Mortar with Preferentially Aligned Fibers, In Preparation. (2024).

5.1. Introduction

5.1.1. Background and Motivation

The field of civil engineering has witnessed a growing interest in Fiber-reinforced concrete (FRC) owing to its superior mechanical properties, which notably include enhanced resistance to cracking and increased toughness. The performance of FRC is significantly influenced by the type and amount of fibers incorporated in the mixture [1,2]. However, traditional methods of mixing and casting have been inadequate in ensuring the uniform distribution of fibers, often resulting in a random orientation that reduces the material's effectiveness [3]. This limitation has led to the adoption of extrusion-based casting techniques, which offer a marked improvement in fiber alignment within FRC structures. By aligning fibers in parallel with the flow of concrete and along tensile stress lines, these methods significantly enhance the material's mechanical characteristics [4–6]. The phenomenon of size effect plays a pivotal role in the fracture behavior of extruded FRC, making it a focal point of this research. The study aims to provide a detailed examination of existing literature on the influence of size effect on the fracture properties of extruded FRC, employing polyvinyl alcohol (PVA) fibers, with a special emphasis on fracture energy and the size of the process zone. It also aims to draw a comparison with the properties of conventionally cast FRC to underline the benefits of fiber alignment achieved through pump extrusion.

5.1.2. Previous Research on Fiber Alignment

Since the early 1970s, the alignment of fibers within FRC has been a focal point of research due to its substantial influence on the material's mechanical properties [7–9]. The ability to control and optimize fiber orientation is recognized as a crucial factor in enhancing the performance of FRC, prompting a wide range of studies and innovations [3,10–12]. Various techniques have been

developed to orient fibers effectively, including the use of magnetic fields to align steel fibers [10,13–16], and the adaptation of casting processes that orient fibers during the consolidation process as the concrete settles and flows [3,17–21]. Among the innovative techniques, extrusion-based methods have emerged as particularly effective in achieving precise fiber alignment [22–35], employing techniques, such as additive manufacturing, to ensure fibers are positioned optimally for maximum tensile strength. Early investigations into extruded FRC in the 1990s and early 2000s, although scarce, revealed the potential for such methods to induce strain-hardening behaviors in FRC fibers [7,23,24,30,36]. However, only a limited number of studies have delved into how extrusion techniques specifically affect fiber alignment within cementitious composites [32,29,35].

5.1.3. Nozzle Design for Pump Extrusion-Based FRC

The role of nozzle design in enhancing the extrusion-based additive manufacturing of FRC has gained prominence in recent research. Innovations in this area aim to refine fiber alignment during the extrusion process, addressing the critical challenge of optimizing mechanical properties. Ma *et al*. [33] demonstrated the potential of using 3D printing technologies to extrude basalt fiber-reinforced cementitious materials, achieving fiber alignment along the print direction by employing a nozzle with a diameter smaller than the length of the fibers. Despite the success in aligning fibers, the study identified limitations such as the presence of weak interfaces and voids within layers of circular beads [28,31,33]. In an effort to address these shortcomings, Ye *et al*. [28] experimented with a rectangular-shaped nozzle while extruding FRC that included polyethylene fibers. This adjustment yielded a more consistent fiber orientation but also revealed a drawback which is an increase in fiber content, leading to a more twisted fiber arrangement.

A promising solution to these challenges is the combination of flow-induced casting with pump extrusion through a specifically designed nozzle conveyor system. This technique is composed to leverage rheological advantages by aligning fibers more effectively post-extrusion [19,37,38]. Employing a nozzle conveyor system that transitions from pump pressure to extrusion can mitigate the issue of fiber twisting caused by the rotation of the pump shaft, facilitating better fiber alignment and, consequently, enhancing the mechanical performance of FRC [3,28,39].

5.1.4. Size Effect Method

The phenomenon of size effect presents significant challenges in the design and analysis of quasi-brittle materials, such as concrete. Unlike purely brittle materials, where fracture propagation occurs suddenly upon reaching the critical stress intensity factor, or ductile materials that exhibit significant plastic deformation before failure, concrete can show a transition from ductile to brittle failure as the size of the structure or its components increases [40,41]. This dual nature necessitates a nuanced approach to predict failure, one that goes beyond traditional strength theories [42,43]. The size effect is particularly relevant because it highlights how the strength of concrete structures decreases more significantly with size than traditional scaling laws would predict. This phenomenon is largely attributed to the presence of the Fracture Process Zone (FPZ), a region, around the crack tip, experiencing substantial deformation before the occurrence of total failure [44–46]. The FPZ introduces a characteristic material length that must be considered in structural design and analysis, affecting the distribution of stress and the rate of energy release during fracture.

Incorporating fracture mechanics and understanding the size effect are essential for the accurate prediction of structural strength and failure in concrete structures. This understanding bridges the gap between plasticity, which describes the material behavior at smaller scales or under

ductile failure conditions, and Linear Elastic Fracture Mechanics (LEFM), which applies to larger scales or under brittle failure conditions [42,43]. The transition between these behaviors, dictated by the size and characteristics of the FPZ, underscores the importance of the size effect in ensuring the safety, reliability, and efficiency of concrete structures. By accounting for the size effect in the design and assessment of concrete structures, engineers can better predict potential failures, enhancing the safety and longevity of critical infrastructure. Bažant's comprehensive review on the subject emphasizes the necessity of this approach, showcasing the complex interplay between material properties, structural size, and failure mechanisms in concrete engineering [43].

The FPZ is a critical source of the size effect, deeply embedded in the material's inherent quasi-brittleness and influenced by its heterogeneity. The size of aggregate particles within concrete plays a pivotal role, impacting not only the material's mechanical properties but also its brittleness and specific fracture parameters [47]. Several studies has shown that the fracture energy of concrete is affected by the maximum size of the aggregate [48–52]. Nonetheless, contradictory findings were reported by several studies which conducted additional research on this topic and found that aggregate size had non-monotonic impacts on fracture mechanics parameters [53–57].

The complexity and variability found in the literature regarding the influence of aggregate size on fracture properties underscore the importance of comprehensively understanding these interactions. Such an understanding is vital for accurately predicting size effects and refining concrete design techniques. In response to this need, the Size Effect Method (SEM), presented in RILEM [58,59], was developed to quantify these challenges [60]. SEM introduces a new size effect model that accounts for the heterogeneity size, making it possible to determine size-independent fracture properties. SEM's innovative framework enhances the ability to quantify and

account for size effect in quasi-brittle materials, offering a more accurate and reliable basis for the design and analysis of concrete structures.

5.1.5. Size Effect for Fracture in FRC

The study of the size effect is crucial in the realm of concrete and FRC, particularly because the mechanical behaviors of materials can shift notably with variations in structural dimensions. This phenomenon directly influences the load-bearing capacity and fracture resistance of structures, underscoring the importance of size effect comprehension for the safety and dependability of civil infrastructure [61]. Exploring the size effect not only aids in developing more accurate design standards tailored for specific needs but also in predicting how structures respond under different loading conditions. Moreover, it contributes to the broader understanding of material behavior mechanisms, leading to advancements in material science and structural engineering [62].

The size effect's role in modifying the mechanical properties of FRC and its impact on fracture behavior has gained extensive investigation. A study by Daneshfar *et al.* [63] examined how specimen size affects the fracture energy of macro-synthetic FRC, revealing that fracture toughness and critical stress intensity parameters improve with an increase in specimen dimensions. This study also found that while thickness and fiber dosage significantly impact fracture energy, the interaction between them does not. Similarly, Xu *et al.* [64] explored the influence of specimen size and steel fiber content on fracture parameters through an evaluation of single-edge notched beams varying in size and steel fiber concentrations. Their findings highlighted a positive correlation between fiber content and fracture energy, although the study's focus on steel-fiber-reinforced high-strength concrete limits the generalizability of the results to other concrete types or fiber materials.

A study on size effect by Li *et al.* [65], focused on the effect of crack-parallel stress on FRC's fracture properties, demonstrating how it significantly affects fracture energy and the fracture process zone (FPZ) size. This study indicated that fiber reinforcement could mitigate the impact of crack-parallel stress, thereby enhancing ductility. However, its limitation lies in its exclusive concentration on crack-parallel stress without considering other fracture behavior factors. Another study by Zhang *et al.* [66], adopted a mesoscale modeling approach to analyze the size effect on steel FRC's fracture properties, developing a three-dimensional model that accounts for the random distribution of fibers. Their model, which simulates the flexural responses of notched steel FRC beams of varying sizes, closely matched experimental data, effectively capturing the fracture behavior of steel FRC beams under bending. These studies collectively contribute to a deeper knowledge of the size effect in FRC and highlight the need for further research to fully understand its implications on fracture behavior and structural integrity.

5.1.6. Research Objective

This study is centered on a detailed investigation into the size effects on fracture properties within FRC, utilizing the SEM to specifically examine fracture energy and the size of the FPZ. The research focuses on extruded FRC that incorporates PVA fibers, drawing a comparison with the properties of conventionally cast FRC to underline the significance of fiber alignment achieved through pump extrusion techniques. The novelty of this research lies in its comprehensive quantification of the fracture properties of extruded FRC across varying specimen sizes, providing crucial insights for industrial applications where larger specimens are utilized. Through this approach, the study aims to highlight the potential improvements in mechanical performance and structural integrity that can be achieved with optimized fiber alignment in extruded FRC, offering a substantial contribution to the field of civil engineering and material science.

5.2. Experimental Methodology

5.2.1. Theoretical Background

The SEM provides a size- and shape-independent approach for determining fracture parameters of concrete structures, which are important for structural design and assessment. This method's significance lies in its direct assessment of concrete's quasi-brittle nature and the complexities of the FPZ [41,43]. SEM accurately predicts structural behavior across different scales by integrating the size effect, thus enabling the extrapolation of results from smaller specimens to real-life structures. This scalability is invaluable in structural design and assessment, where full-scale testing is often impractical. By providing reliable fracture parameters that genuinely reflect the material's behavior under varied conditions, SEM enhances the safety, durability, and economic efficiency of concrete infrastructure, leading to more refined design codes and optimized construction practices.

By utilizing geometrically similar notched specimens across different sizes for three-point bending tests, SEM facilitates a straightforward determination of key fracture characteristics [67]. To comply with SEM's requirements, specimens were cast in three sizes, all maintaining consistent dimensions in terms of width (b), span-to-depth ratio (S/d), length-to-depth ratio (L/d), and notch-to-depth ratio (a_o/d), as detailed in Table 5.1. This approach allows for the examination of the energy dissipation at the point of failure, taking into account both the specimen size and the width of the fracture process zone. Consequently, SEM enables the calculation of critical fracture parameters, including the strain energy release rate (G_{IC}), the effective length of the FPZ (c_f), and the Mode I critical stress intensity factor (K_{IC}). Additionally, the total fracture energy (G_F) is derived following the methodology introduced by Hillerborg [68,69]. These parameters play a

pivotal role in evaluating the structural integrity and performance of concrete elements, offering a comprehensive framework for understanding the mechanics of fracture within concrete materials.

Table 5.1: Dimensions of the Beam Specimens Used for the Size Effect Model

Specimen Size	$L\ (mm)$	$S\ (mm)$	$b\ (mm)$	$d\ (mm)$	$a_o\ (mm)$	L/d	S/d	a_o/d
Small	280	240	80	60	20	4.67	4	0.33
Medium	700	600	80	150	50	4.67	4	0.33
Large	1120	960	80	240	80	4.67	4	0.33

Single-edge notched beams (SENB) were cast. All SENB specimens were subjected to a three-point monotonic loading, conducted at a consistent displacement rate of 0.1 mm/min, using the test setup shown in Figure 5.1. The primary objective in testing each beam was to determine its first peak load (P_j). To refine this measurement, the first peak load value was adjusted to obtain the corrected peak load (P_j^0) using Equation 1, where for specimen j, the variables were defined based on the span length (S), the length of the specimen (L), the mass of the specimen (m), and the acceleration due to gravity (g).

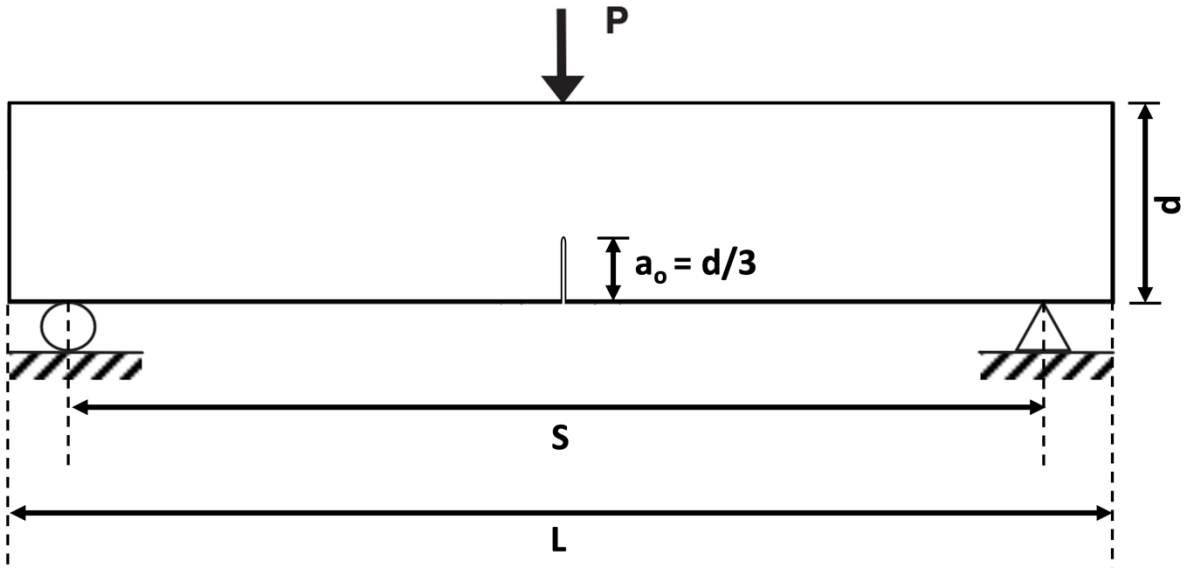

Figure 5.1: Test Setup of Three-point Bending Beam Specimen

$$P_j^0 = P_j + \frac{2S_j - L_j}{2S_j} m_j g \tag{1}$$

Following the determination of P_j^0, a linear regression analysis was conducted using Equation 3. The ordinates (Y_j) and the abscissae (X_j) are defined in Equation 3 and Equation 4, respectively, where b_j is the width of the specimen and d_j is the depth of the specimen.

$$Y = AX + C \tag{2}$$

$$Y_j = \left(\frac{b_j d_j}{P_j^0}\right)^2 \tag{3}$$

$$X_j = d_j \tag{4}$$

To further analyze the fracture mechanics, the geometric factor (g_1) and the non-dimensional energy release rate (g_2) were computed using Equation 5 and Equation 6, respectively. These calculations were based on the notch-to-depth ratio (α), a significant factor in evaluating the specimen's fracture properties. Subsequently, the critical fracture properties, including G_{IC}, K_{IC}, c_f, and $CTOD_C$, were computed employing Equations 7 to 10, respectively, with E denoting the elastic modulus.

$$g_1(\alpha) = \frac{1.99 - \alpha(1-\alpha)[2.15 - 3.93(\alpha) + 2.70(\alpha)^2]}{\sqrt{\pi}[1 + 2(\alpha)][1 - (\alpha)]^{\frac{3}{2}}} \tag{5}$$

$$g_2(\alpha) = \left(\frac{S}{d}\right)^2 \pi\alpha[1.5\ g_1(\alpha)]^2 \tag{6}$$

$$G_{IC} = \frac{g_2(\alpha)}{EA} \tag{7}$$

$$K_{IC} = \sqrt{G_{IC}E} \tag{8}$$

$$c_f = \frac{g_2(\alpha)}{g_2'(\alpha)}\frac{C}{A} \tag{9}$$

$$CTOD_C = \sqrt{\frac{32G_{IC}c_f}{\pi E}} \tag{10}$$

Adopting Hillerborg's methodology [68,69], the total fracture energy (G_F) is defined as the ratio of the total work done (W_T) to the area of concrete fracture $(d - a_o)b$. The W_T itself is derived from the sum of the area under the load versus mid-span deflection curve (W_r) and the product of the equivalent self-weight force (P_w) multiplied by the deflection value at failure (δ_f), as detailed in Equation 13. To ensure consistency across tested samples, a relative fracture energy parameter ($G_{F,10}$) was applied at a 10 mm deflection (δ_f = 10 mm).

$$G_F = \frac{W_T}{(d - a_o)b} = \frac{W_r + 2P_w\delta_f}{(d - a_o)b} = \frac{W_r + \frac{W_o S}{L}\delta_f}{(d - a_o)b} \tag{13}$$

5.2.2. Mix Design and Properties

For this comparative analysis, two mortar mixtures were prepared with varying PVA fiber dosages, 0 % for a baseline comparison and 1 % by volume, reflecting a pragmatic choice for real-world engineering applications [70]. The inclusion of PVA fibers was investigated through two different casting methods: the conventional casting technique as defined by ASTM C192 and an innovative extrusion-based casting approach. To provide a comprehensive understanding of the

fibers' impact, a plain concrete mixture without fibers was also prepared, serving as the control group. Given the constraints imposed by the extrusion pump, particularly regarding aggregate size, the mixtures were limited to fine aggregate with a maximum size of 4.75 mm and a fineness modulus of 2.6. This choice ensures compatibility with the extrusion process while still aiming to investigate the potential benefits of fiber inclusion effectively [4,5].

Each set of mixtures was uniquely identified to facilitate easy reference and analysis. The identification codes were formulated to reflect the casting method (CV = conventional casting and EB = extrusion-based casting), the fiber volume percentage (1 %), and the specimen size (L = Large, M = Medium, and S = Small). Specimens of plain concrete were labeled as PC. Detailed information on the mixture proportions and the properties of the PVA fibers are systematically presented in Table 5.2 and Table 5.3, respectively, with Figure 5.2 showing the PVA fibers. The properties of the PVA fibers were specified by the manufacturer.

Table 5.2: Concrete Mixture Proportions

Mixture ID	**PC**	**CV1%**	**EB1%**
Type I cement (kg/m^3)	688	688	688
Fine aggregate (kg/m^3)	1042	1042	1042
Water to cement ratio	0.40	0.40	0.40
PVA fiber volume	0%	1%	1%

Table 5.3: Properties of PVA Fibers

Length (mm)	19
Filament diameter (mm)	0.2
Specific gravity	1.3
Tensile strength (MPa)	1,000
Flexural strength (MPa)	29,000

Figure 5.2: PVA Fibers

To evaluate the compressive strength of the materials, tests were conducted in line with ASTM C39 standards, focusing exclusively on specimens casted through conventional casting. Following a 28-day period of moist curing, three cylindrical specimens from each mixture group, each with dimensions of 4 inches (100 mm) in diameter and 8 inches (200 mm) in height, underwent compressive strength testing. The outcomes of these tests, accompanied by relevant statistical analyses, are documented in Table 5.4.

Table 5.4: Compressive Strength Results

	Compressive strength (MPa)	**Mean (MPa)**	**Standard deviation (MPa)**	**Coefficient of variation (%)**
PC_1	50.1	49.7	0.67	1.34
PC_2	50.0			
PC_3	48.9			
1%_1	50.6	48.3	2.04	4.23
1%_2	46.8			
1%_3	47.4			

5.2.3. Testing Program and Sample Preparation

In the scope of this research, a comprehensive testing program was developed, comprising the preparation and testing of twenty-seven beam specimens. This set included nine plain concrete

specimens (PC), nine produced *via* extrusion-based casting method (EB), and nine produced *via* conventional casting method (CV). These specimens were cast in three distinct sizes, as outlined in Table 5.1, to explore size effects thoroughly. The largest beams were created using wooden forms, whereas the medium and small beams were formed in steel molds, ensuring precision and consistency in dimensions. Following a 27-day period of moist curing, each beam was precisely notched at mid-span, employing a one-third depth saw-cut in preparation for subsequent fracture testing.

The development and implementation of the EB method were key aspects of this study, utilizing an electric pump capable of exerting pressures up to 2.1 MPa. This system, characterized by a continuous cavity rotor-stator mechanism, facilitated the smooth transition of the mortar mix from a material hopper through a drive shaft and eventually to a dispensing head. A custom-designed nozzle, depicted in Figure 5.3, created from 3D-printed polyethylene terephthalate and featuring a 45-degree angled tilt, was crucial in promoting the desired fiber alignment within the extruded beams. This nozzle's design was meticulously designed to ensure fiber alignment within the mold's confines, preventing any extraneous dispersion of fibers [4,5].

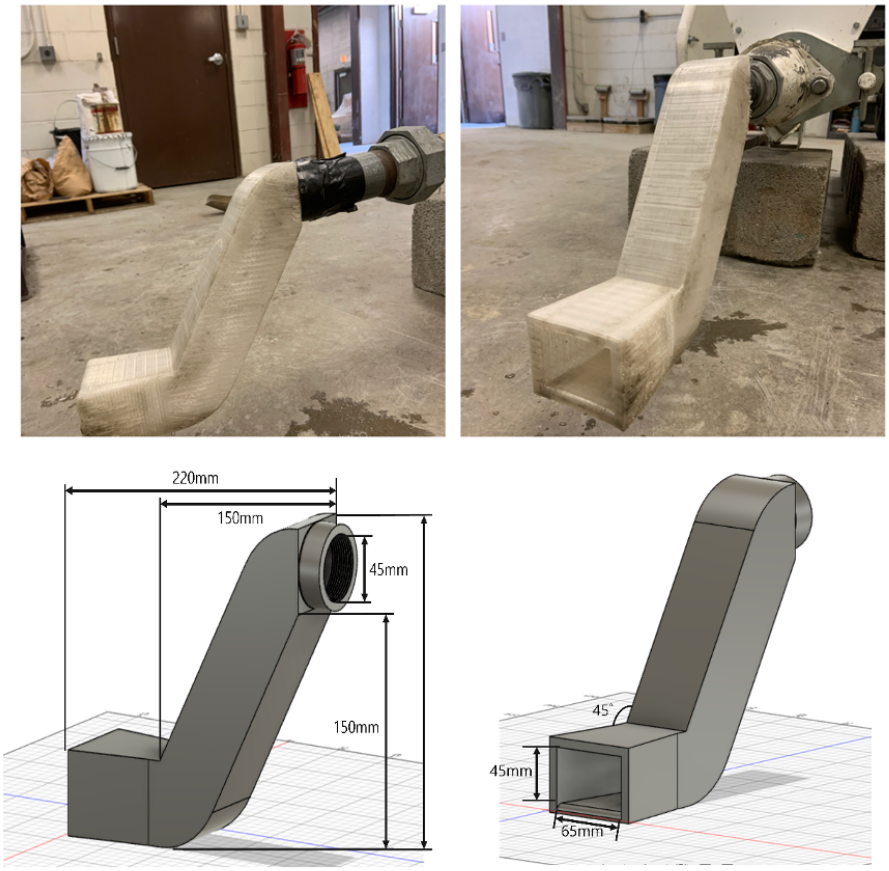

Figure 5.3: Extrusion-based Method's Nozzle Design

Both EB and CV specimen batches were mixed and cast concurrently to maintain consistency in comparison. For the EB group, the FRC mixture was extruded into molds in a controlled manner, forming a three-layered structure within each beam without the application of additional consolidation methods. In contrast, the casting of CV and PC specimens followed ASTM C192 standards, ensuring the validity and reliability of comparative analyses.

Fracture testing was performed using an MTS Insight 150 SL electromechanical universal testing machine, equipped with a crosshead, that measure the mid-span deflection accurately. This meticulous approach to sample preparation and testing underpins the study's aim to provide a nuanced understanding of the size effects and mechanical properties of FRC, comparing the outcomes of conventional and extrusion-based casting methodologies.

5.3. Test Results and Discussion

5.3.1. Peak Load and Total Fracture Energy

The results of peak loads (P) and the fracture energy at a 10 mm deflection ($G_{F,10}$) across all specimens are presented in Table 5.5. According to the analysis, which utilized a one-tailed two-sample t-test with a 95 % confidence interval, the peak loads between plain concrete (PC), conventionally-cast (CV), and extrusion-based (EB) specimens did not exhibit significant variance. This finding aligns with existing literature [4,11,70], suggesting that the incorporation of polymer fibers into the concrete matrix does not inherently enhance peak strength.

Table 5.5: Peak Load and Relative Fracture Energy Values for All Specimens

Sample	$\boldsymbol{P}$ $(\boldsymbol{N})$	$\boldsymbol{G_{F,10}}$ $(\boldsymbol{N/m})$
PC_S_1	913	87
PC_S_2	1160	109
PC_S_3	859	64
Mean	977	87
SD	160	23
CV1%_S_1	1013	1123
CV1%_S_2	990	1098
CV1%_S_3	848	860
Mean	950	1027
SD	89	145
EB1%_S_1	868	2058
EB1%_S_2	967	2038
EB1%_S_3	1105	1939
Mean	980	2012
SD	119	64
PC_M_1	2037	93
PC_M_2	2217	256
PC_M_3	1943	154
Mean	2066	168
SD	139	82
CV1%_M_1	2088	1380
CV1%_M_2	2335	1247
CV1%_M_3	1926	1228
Mean	2116	1285
SD	206	83
EB1%_M_1	2235	1766
EB1%_M_2	2173	1906
EB1%_M_3	2087	1928
Mean	2165	1867
SD	74	88
PC_L_1	2559	145
PC_L_2	3448	256
PC_L_3	2779	113
Mean	2929	171
SD	463	75
CV1%_L_1	2748	1205
CV1%_L_2	2595	1485
CV1%_L_3	3134	1800
Mean	2826	1497
SD	278	298
EB1%_L_1	3485	1990
EB1%_L_2	2827	2164
EB1%_L_3	2952	1739
Mean	3088	1964
SD	349	214

However, a notable differentiation emerged in the context of fracture energy, particularly with the $G_{F,10}$ property. The introduction of fibers into the concrete matrix universally increased fracture energy, a result attributed to the fibers' capacity to bridge cracks effectively, thus necessitating greater energy for crack propagation [4,60,67]. This reinforcing action by the fibers leads to enhanced mid-span deflection values at failure, underlining the fibers' crucial role in enhancing concrete's ductility.

The impact of fiber orientation on fracture energy was profoundly evident. As shown in the comparison in Figure 5.4, EB1% specimens demonstrated significantly higher $G_{F,10}$ values compared to their CV1% counterparts. This improvement can be observed also in Figure 5.5 for small specimens, Figure 5.6 for medium specimens, and Figure 5.7 for large specimens, where EB1% specimens had greater areas under the load–deflection curves compared to the CV1% specimens. This difference was consistent across all specimen sizes, attributed to the EB method's effectiveness in aligning fibers parallel to the flow of concrete and consequently, parallel to the tensile stresses. Such alignment enhances the fibers' ability to bridge and inhibit crack propagation more efficiently than the randomly oriented fibers in CV specimens.

The magnitude of improvement in fracture energy offered by the EB casting method varied with specimen size, showing a pronounced benefit in smaller specimens. Specifically, the EB method yielded a $G_{F,10}$ increase of approximately 96 % in small specimens, 45 % in medium specimens, and 31 % in large specimens compared to CV specimens with the same fiber volume. This scale-dependent effect suggests that in smaller specimens, the condensed arrangement of fibers along the beam's depth amplifies the beneficial impact of fiber alignment. Conversely, in larger specimens, the distributed nature of fibers, along the depth of a specimen, reduces the relative advantage of alignment.

These findings underscore the significant role of casting method and specimen size in influencing the fracture energy of FRC. While the extrusion-based casting method markedly enhances the material's fracture energy through improved fiber alignment, the extent of improvement is controlled by the specimen's dimensions. These results not only affirm the critical influence of fiber orientation on FRC's mechanical properties but also highlight the nuanced interplay between casting technique and specimen size, offering valuable insights for the design and implementation of FRC in structural applications.

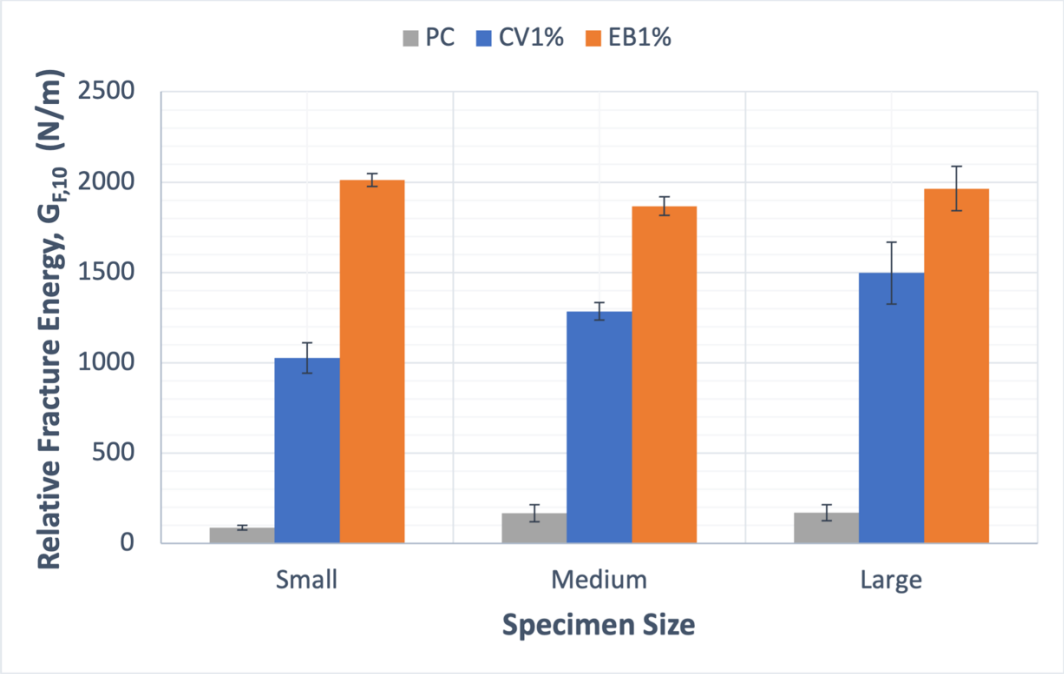

Figure 5.4: Relative Fracture Energy Comparison

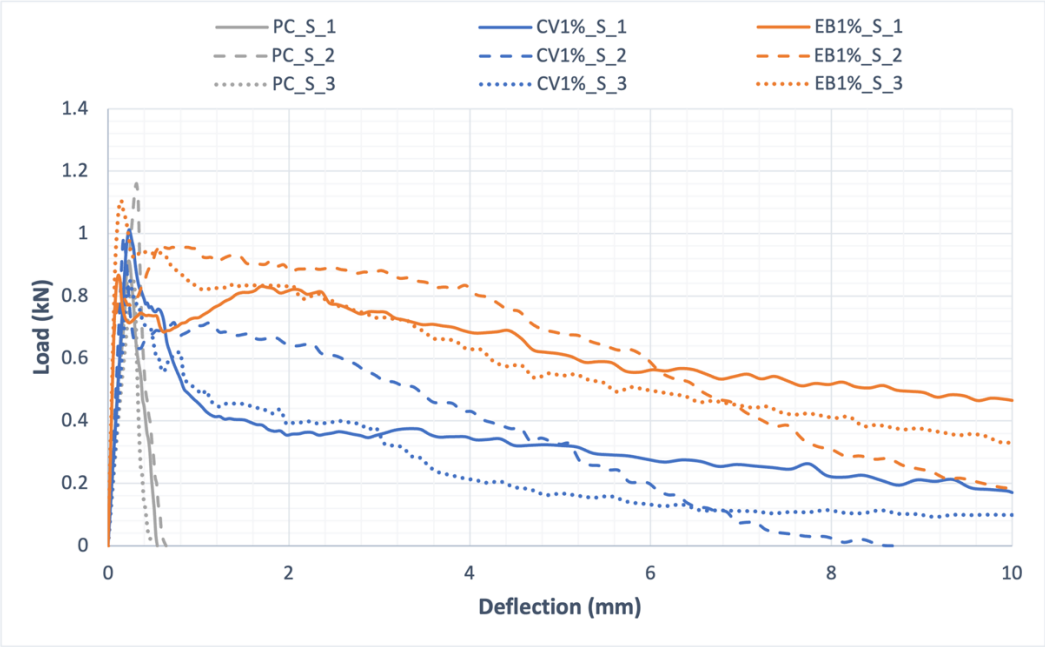

Figure 5.5: Load-deflection Curve for Small-Size Specimens

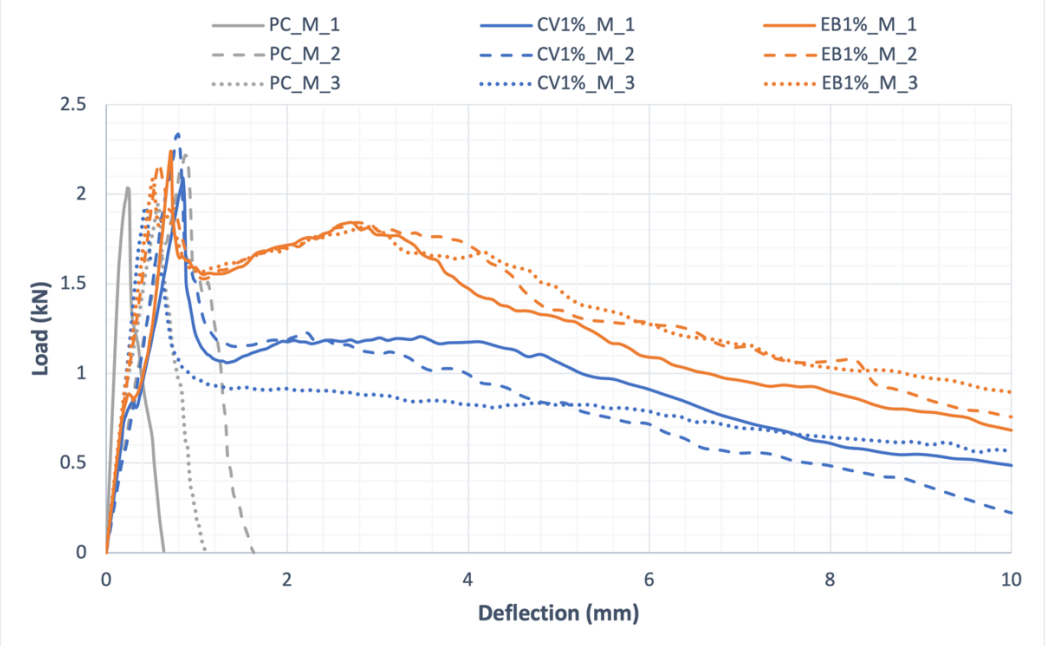

Figure 5.6: Load-deflection Curve for Medium-Size Specimens

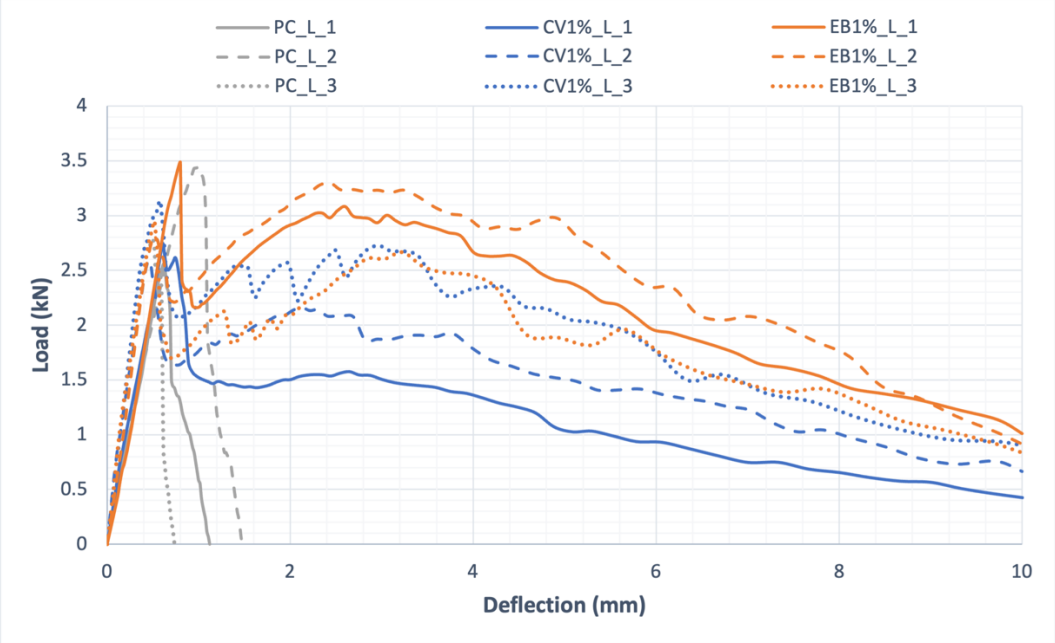

Figure 5.7: Load-deflection Curve for Large-Size Specimens

5.3.2. SEM Fracture Properties

The examination of major fracture parameters through the SEM unveiled nuanced insights into the impact of fiber reinforcement and orientation on the fracture properties of concrete. Parameters such as K_{IC}, $CTOD_C$, G_{IC}, and c_f for PC, CV1%, and EB1% specimens are outlined in Table 5.6. Regression analyses for these three specimen categories – PC, CV1%, and EB1% – are visually presented in Figure 5.8, Figure 5.9, and Figure 5.10, respectively.

The comparative analysis between CV1% and PC specimens revealed an interesting observation which indicated that the incorporation of fibers into the concrete matrix might not inherently enhance fracture properties. In fact, PC specimens exhibited slightly higher values across all measured fracture parameters. This suggests that fibers, when randomly oriented, may adversely impact certain fracture properties. Fibers aligned perpendicular to tensile stresses could introduce void-like disruptions within the concrete matrix, potentially compromising performance.

This observation aligns with findings from previous research [67], indicating that the orientation of fibers plays a pivotal role in their effectiveness as reinforcement.

Conversely, the strategic orientation of fibers using the extrusion-based method appears to significantly improve the concrete's fracture properties. Notably, the length of the fracture process zone (c_f) was larger in EB1% specimens, indicating that fibers aligned with tensile stresses enhance crack bridging capabilities. An extended FPZ suggests more efficient energy dissipation during crack propagation, attributed to the action of well-oriented fibers. Remarkably, the EB1% method yielded a 39 % improvement in c_f values compared to CV1% specimens, underscoring the importance of fiber orientation.

The outcome revealed a critical distinction in FRC. While random addition of fibers may not necessarily improve or could even reduce fracture properties, aligning fibers in the direction of tensile stresses significantly enhances these properties. Hence, the method of fiber integration and orientation emerges as a key determinant in leveraging the full potential of FRC in improving structural fracture resistance.

Table 5.6: Fracture Parameters of PC and FRC Specimens Using Size-Effect Method

Sample	A (mm^3/N^2)	C (mm^4/N^2)	K_{IC} $(MPa\sqrt{m})$	$CTOD_C$ (mm)	G_{IC} (N/m)	c_f (mm)
PC	0.0790	19.774	0.746	0.0150	16.92	43.01
CV1%	0.0847	19.307	0.721	0.0138	15.78	39.16
EB1%	0.0583	20.275	0.868	0.0206	22.93	59.75

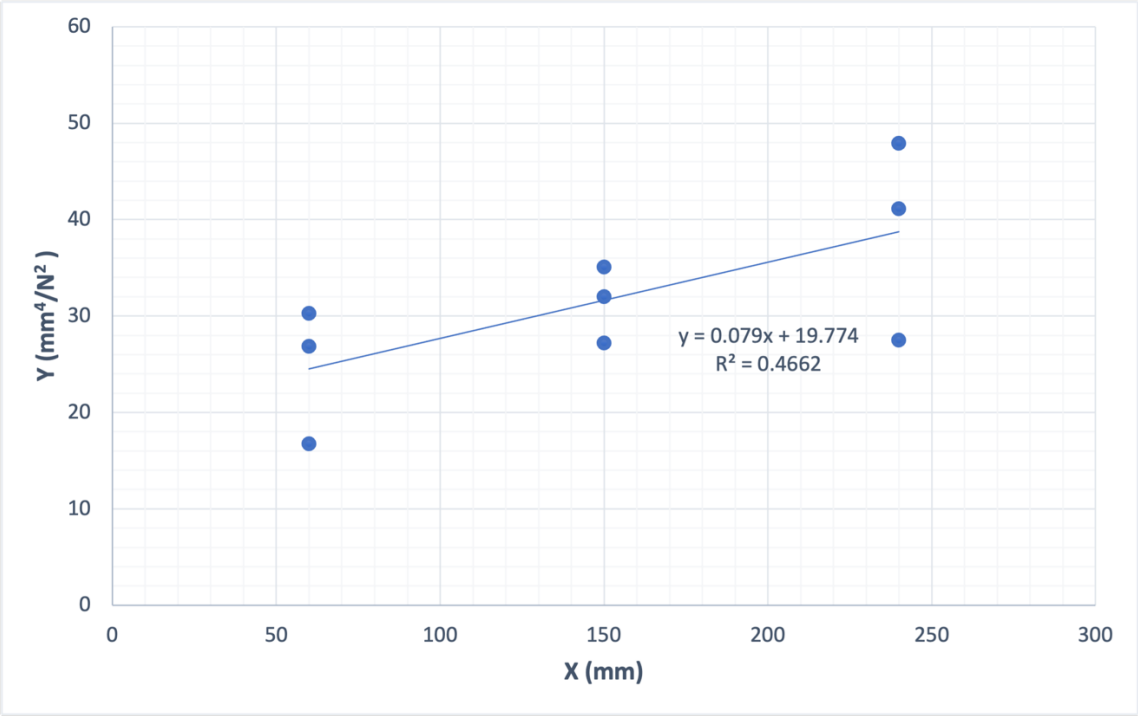

Figure 5.8: Size-effect Regression for Variables X and Y for PC Specimens

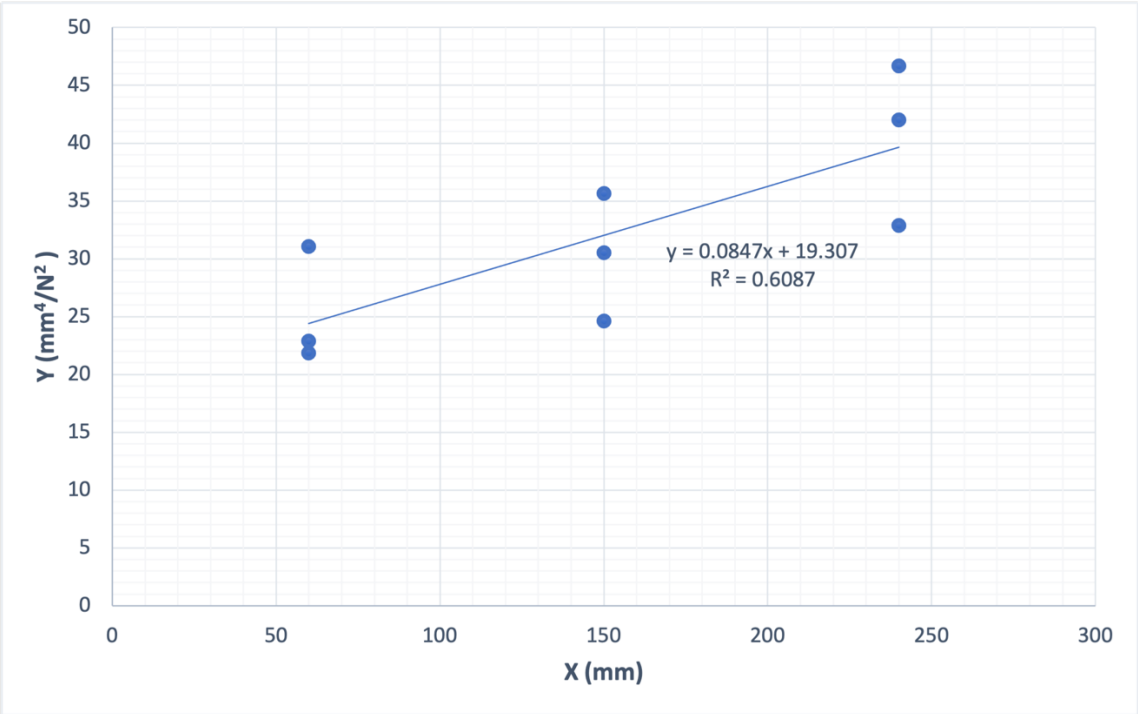

Figure 5.9: Size-effect Regression for Variables X and Y for CV1% Specimens

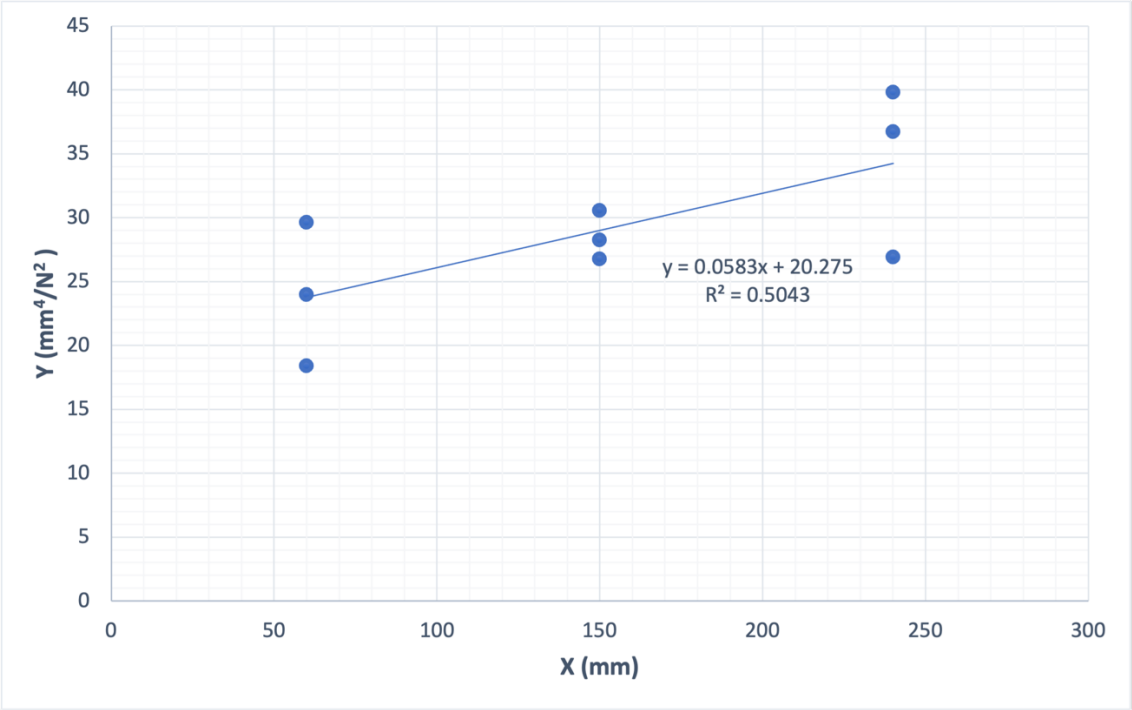

Figure 5.10: Size-effect Regression for Variables X and Y for EB1% Specimens

5.4. Conclusion

This study evaluated the fracture properties of PVA FRC, employing the SEM to compare the efficacy of extrusion-based (EB) and conventional (CV) casting methods. Through thorough experimentation and analysis, the research revealed pivotal insights into how casting techniques and fiber orientation influence the mechanical dynamics of FRC. The principal findings of this investigation can be summarized as follows:

1. Even though the integration of PVA fibers into the concrete matrix did not lead to an increase in peak load, a notable enhancement in post-peak behavior was observed, suggesting improved energy absorption capabilities.
2. The degree of improvement in fracture energy attributable to the EB casting method is depending on the specimen size. There was a marked increase in $G_{F,10}$ for EB

specimens, with improvements of approximately 96 %, 45 %, and 31 % in small, medium, and large specimens, respectively, when compared to CV specimens.

3. The EB casting method notably improved c_f values by 39 % compared to the CV method, underscoring the critical role of fiber orientation in enhancing the mechanical properties of FRC.
4. The random incorporation of fibers, as seen in CV specimens, did not invariably enhance, and in some instances, could potentially degrade fracture properties. In contrast, the strategic alignment of fibers in the desired direction through the EB method significantly improved these properties.

The findings from this research highlight the significant benefits of employing an extrusion-based casting method for optimizing the fracture properties of FRC. By facilitating superior fiber alignment, this approach not only enhances the mechanical integrity of the material but also opens new pathways for innovation in construction materials and methodologies. The study's insights into the interaction between fiber orientation, casting technique, and specimen size provide invaluable guidance for the design and application of FRC in structural endeavors, paving the way for advancements in the field of civil engineering and construction technology.

5.4.1. Limitation and Future Work

The research demonstrated the considerable promise of extrusion-based casting in enhancing the mechanical properties of FRC. However, several limitations were encountered during the study, which opens avenues for future investigations. A key limitation was the dependency on a pump mechanism that restricted the length of fibers to 20 mm, resulting in the exclusive use of 19 mm synthetic fibers. This restriction suggests questions regarding the potential

performance of FRC with longer fibers, which could further influence the material's fracture properties and mechanical behavior.

Moreover, the necessity to employ mixtures devoid of coarse aggregate, due to the extrusion pump's limitations, represents another significant constraint. The absence of coarse aggregate might not fully capture the complex interactions and fiber orientation effects present in typical concrete mixtures used in construction projects. Despite these challenges, the insights gleaned from experiments using mortar-based formulations provide a valuable foundation for understanding the fracture properties of FRC, especially given the current technological constraints in 3D printing and construction material formulation that often limit material choices to finer aggregates.

Future research endeavors should aim to address these limitations by exploring the feasibility of incorporating longer fibers and coarse aggregates within the extrusion process. Such advancements could involve the development of new extrusion pump designs or modified casting techniques capable of handling a wider range of materials without compromising fiber alignment and distribution.

5.5. Authorship Contribution Statement

The authors confirm their contributions to the paper as follows: Rashed Alarrak: Writing – review & editing, Writing – original draft, Visualization, Validation, Methodology, Investigation, Formal analysis, Data curation, Conceptualization. Abdullah Al-Rufaydah: Investigation. Alexander S. Brand: Writing – review & editing, Supervision, Methodology, Conceptualization.

5.6. References

[1] A. Bentur, S. Mindess, Fibre reinforced cementitious composites, 2nd ed, Taylor & Francis, London ; New York, 2007.

[2] R.F. Zollo, Fiber-reinforced concrete: an overview after 30 years of development, Cem. Concr. Compos. 19 (1997) 107–122. https://doi.org/10.1016/S0958-9465(96)00046-7.

[3] L. Ferrara, N. Ozyurt, M. di Prisco, High mechanical performance of fibre reinforced cementitious composites: the role of "casting-flow induced" fibre orientation, Mater. Struct. 44 (2011) 109–128. https://doi.org/10.1617/s11527-010-9613-9.

[4] R. Alarrak, B. Jeon, A.S. Brand, Fracture properties of extruded fiber-reinforced mortar with preferentially aligned fibers, Constr. Build. Mater. 403 (2023) 133022. https://doi.org/10.1016/j.conbuildmat.2023.133022.

[5] R. Alarrak, B. Jeon, A.S. Brand, Flexural toughness of extruded fiber-reinforced mortar with preferentially aligned fibers, Constr. Build. Mater. 407 (2023) 133528. https://doi.org/10.1016/j.conbuildmat.2023.133528.

[6] R. Alarrak, A.S. Brand, Mechanical Performance of Extruded Functionally Graded Fiber-Reinforced Mortar with Targeted Fiber Injection, Rev. (2024).

[7] Y. Akkaya, J. Picka, S.P. Shah, Spatial distribution of aligned short fibers in cement composites, J. Mater. Civ. Eng. 12 (2000) 272–279.

[8] A.E. Naaman, H.W. Reinhardt, Characterization of high performance fiber reinforced cement composites—HPFRCC, in: High Perform. Fiber Reinf. Cem. Compos., 1996: pp. 1–24.

[9] S.P. Shah, C. Ouyang, Mechanical behavior of fiber-reinforced cement-based composites, J. Am. Ceram. Soc. 74 (1991) 2727–2953.

[10] A. Abrishambaf, M. Pimentel, S. Nunes, Influence of fibre orientation on the tensile behaviour of ultra-high performance fibre reinforced cementitious composites, Cem. Concr. Res. 97 (2017) 28–40. https://doi.org/10.1016/j.cemconres.2017.03.007.

[11] A. Enfedaque, M.G. Alberti, J.C. Gálvez, Influence of Fiber Distribution and Orientation in the Fracture Behavior of Polyolefin Fiber-Reinforced Concrete, Materials 12 (2019) 220. https://doi.org/10.3390/ma12020220.

[12] C. Xie, M. Cao, M. Khan, H. Yin, J. Guan, Review on different testing methods and factors affecting fracture properties of fiber reinforced cementitious composites, Constr. Build. Mater. 273 (2021) 121766. https://doi.org/10.1016/j.conbuildmat.2020.121766.

[13] R. Mu, Y. Xue, L. Qing, H. Li, Y. Zhao, J. Zhou, J. Su, Preparation and mechanical performance of annularly aligned steel fiber reinforced cement-based composite pipes, Constr. Build. Mater. 211 (2019) 167–173. https://doi.org/10.1016/j.conbuildmat.2019.03.146.

[14] R. Mu, H. Li, L. Qing, J. Lin, Q. Zhao, Aligning steel fibers in cement mortar using electro-magnetic field, Constr. Build. Mater. 131 (2017) 309–316. https://doi.org/10.1016/j.conbuildmat.2016.11.081.

[15] L. Liu, J. Xu, Y. Wang, T. Yin, H. Chu, Electrical and piezoresistive properties of steel fiber cement-based composites aligned by a magnetic field, J. Wuhan Univ. Technol.-Mater Sci Ed 37 (2022) 229–240. https://doi.org/10.1007/s11595-022-2522-2.

[16] P. Kheml, K. Carrera, K. Künzel, V. Papež, R. Sovják, Summary of findings on magnetic orientation of fibers in cement composites, Mater. Today Proc. 58 (2022) 1104–1107. https://doi.org/10.1016/j.matpr.2022.01.201.

[17] L. Ferrara, M. Di Prisco, M.G.L. Lamperti, Identification of the stress-crack opening behavior of HPFRCC: the role of flow-induced fiber orientation, in: Proc. Fram., 2010: pp. 1541–1550.

[18] S.-T. Kang, J.-K. Kim, Investigation on the flexural behavior of UHPCC considering the effect of fiber orientation distribution, Constr. Build. Mater. 28 (2012) 57–65. https://doi.org/10.1016/j.conbuildmat.2011.07.003.

[19] S.-T. Kang, J.-K. Kim, Numerical simulation of the variation of fiber orientation distribution during flow molding of Ultra High Performance Cementitious Composites (UHPCC), Cem. Concr. Compos. 34 (2012) 208–217. https://doi.org/10.1016/j.cemconcomp.2011.09.015.

[20] L. Ferrara, N. Tregger, S.P. Shah, Flow-induced fiber orientation in SCSFRC: monitoring and prediction, in: Des. Prod. Place. Self-Consol. Concr., Springer, 2010: pp. 417–428.

[21] A.C. Bordelon, J.R. Roesler, Spatial distribution of synthetic fibers in concrete with X-ray computed tomography, Cem. Concr. Compos. 53 (2014) 35–43. https://doi.org/10.1016/j.cemconcomp.2014.04.007.

[22] X. Sun, J. Zhou, Q. Wang, J. Shi, H. Wang, PVA fibre reinforced high-strength cementitious composite for 3D printing: Mechanical properties and durability, Addit. Manuf. 49 (2022) 102500. https://doi.org/10.1016/j.addma.2021.102500.

[23] Y. Shao, S. Marikunte, S.P. Shah, Extruded fiber-reinforced composites, Concr. Int. 17 (1995) 48–53.

[24] Z. Li, B. Mu, T.P. Chang, C.-T. Hsu, Prediction of overall tension behavior of short fiber-reinforced composites, Int. J. Solids Struct. 36 (1999) 4071–4087.

[25] H. Takashima, K. Miyagai, T. Hashida, V.C. Li, A design approach for the mechanical properties of polypropylene discontinuous fiber reinforced cementitious composites by extrusion molding, Eng. Fract. Mech. 70 (2003) 853–870. https://doi.org/10.1016/S0013-7944(02)00154-6.

[26] X. Zhou, Z. Li, Characterizing rheology of fresh short fiber reinforced cementitious composite through capillary extrusion, J. Mater. Civ. Eng. 17 (2005) 28–35.

[27] Y. Zhang, F. Aslani, Development of fibre reinforced engineered cementitious composite using polyvinyl alcohol fibre and activated carbon powder for 3D concrete printing, Constr. Build. Mater. 303 (2021) 124453. https://doi.org/10.1016/j.conbuildmat.2021.124453.

[28] J. Ye, C. Cui, J. Yu, K. Yu, F. Dong, Effect of polyethylene fiber content on workability and mechanical-anisotropic properties of 3D printed ultra-high ductile concrete, Constr. Build. Mater. 281 (2021) 122586. https://doi.org/10.1016/j.conbuildmat.2021.122586.

[29] M. Sugavaneswaran, G. Arumaikkannu, Modelling for randomly oriented multi material additive manufacturing component and its fabrication, Mater. Des. 1980-2015 54 (2014) 779–785. https://doi.org/10.1016/j.matdes.2013.08.102.

[30] H. Stang, V.C. Li, Extrusion of ECC-material, in: Proc High Perform. Fiber Reinf. Cem. Compos., 1999: pp. 203–212.

[31] S.C. Paul, Y.W.D. Tay, B. Panda, M.J. Tan, Fresh and hardened properties of 3D printable cementitious materials for building and construction, Arch. Civ. Mech. Eng. 18 (2018) 311–319. https://doi.org/10.1016/j.acme.2017.02.008.

[32] X. Qian, X. Zhou, B. Mu, Z. Li, Fiber alignment and property direction dependency of FRC extrudate, Cem. Concr. Res. 33 (2003) 1575–1581.

[33] G. Ma, Z. Li, L. Wang, F. Wang, J. Sanjayan, Mechanical anisotropy of aligned fiber reinforced composite for extrusion-based 3D printing, Constr. Build. Mater. 202 (2019) 770–783. https://doi.org/10.1016/j.conbuildmat.2019.01.008.

[34] Z. Li, B. Mu, Innovations forum: Application of extrusion for manufacture of short fiber reinforced cementitious composite, J. Mater. Civ. Eng. 10 (1998) 2–4. https://doi.org/10.1061/(ASCE)0899-1561(1998)10:1(2).

[35] Z. Hou, X. Tian, J. Zhang, D. Li, 3D printed continuous fibre reinforced composite corrugated structure, Compos. Struct. 184 (2018) 1005–1010. https://doi.org/10.1016/j.compstruct.2017.10.080.

[36] S.P. Shah, Y. Shao, Extrusion processing of fiber-reinforced cement-matrix composites, Process. Des. Perform. Compos. Mater. 52 (1994) 205–210.

[37] L. Ferrara, N. Ozyurt, M. di Prisco, High mechanical performance of fibre reinforced cementitious composites: the role of “casting-flow induced” fibre orientation, Mater. Struct. 44 (2011) 109–128. https://doi.org/10.1617/s11527-010-9613-9.

[38] X. Zhou, Z. Li, Characterization of rheology of fresh fiber reinforced cementitious composites through ram extrusion, Mater. Struct. 38 (2005) 17–24. https://doi.org/10.1061/(ASCE)0899-1561(2005)17:1(28).

[39] S.-T. Kang, J.-K. Kim, Numerical simulation of the variation of fiber orientation distribution during flow molding of ultra high performance cementitious composites (UHPCC), Cem. Concr. Compos. 34 (2012) 208–217.

[40] S.P. Shah, S.E. Swartz, C. Ouyang, Fracture mechanics of concrete : applications of fracture mechanics to concrete, rock and other quasi-brittle materials, Wiley, New York, 1995.

[41] Z.P. Bažant, J. Planas, Fracture and Size Effect in Concrete and Other Quasibrittle Materials, 1st ed., Routledge, 2019. https://doi.org/10.1201/9780203756799.

[42] Z.P. Bažant, Size effect, Int. J. Solids Struct. 37 (n.d.) 69–80.

[43] Z.P. Bažant, Size effect on structural strength: a review, Arch. Appl. Mech. 69 (1999) 703–725. https://doi.org/10.1007/s004190050252.

[44] S.Y. Alam, J. Saliba, A. Loukili, Fracture examination in concrete through combined digital image correlation and acoustic emission techniques, Constr. Build. Mater. 69 (2014) 232–242. https://doi.org/10.1016/j.conbuildmat.2014.07.044.

[45] Z.P. Bažant, P.A. Pfeiffer, Determination of Fracture Energy from Size Effect and Brittleness Number, ACI Mater. J. 84 (1987). https://doi.org/10.14359/2526.

[46] Z.P. Bažant, M.T. Kazemi, Size Effect in Fracture of Ceramics and Its Use To Determine Fracture Energy and Effective Process Zone Length, J. Am. Ceram. Soc. 73 (1990) 1841–1853. https://doi.org/10.1111/j.1151-2916.1990.tb05233.x.

[47] R. Gettu, H. Saldívar, M.T. Kazemi, Implications of the size effect method for analyzing the fracture of concrete, Int. J. Solids Struct. 35 (1998) 4121–4132. https://doi.org/10.1016/S0020-7683(97)00305-3.

[48] P. Nallathambi, B.L. Karihaloo, B.S. Heaton, Various size effects in fracture of concrete, Cem. Concr. Res. 15 (1985) 117–126. https://doi.org/10.1016/0008-8846(85)90016-X.

[49] A. Hillerborg, A model for fracture analysis, Div. Build. Mater. LTH Lund Univ. 3005 (1978) 8.

[50] M.A.T. Canan Tasdemir Nicholas Mills, Ben I.G. Barr, and Frank D. Lydon, Combined Effects of Silica Fume, Aggregate Type, and Size on Post-Peak Response of Concrete in Bending, ACI Mater. J. 96 (1999). https://doi.org/10.14359/431.

[51] H. Mihashi, N. Nomura, S. Niiseki, Influence of aggregate size on fracture process zone of concrete detected with three dimensional acoustic emission technique, 21 (n.d.).

[52] K. Otsuka, H. Date, Fracture process zone in concrete tension specimen, Eng. Fract. Mech. 65 (2000) 111–131. https://doi.org/10.1016/S0013-7944(99)00111-3.

[53] H. Kleinschrodt, H. Winkler, The influence of the maximum aggregate size and the size of specimen on fracture mechanics parameters, Fract. Toughness Fract. Energy Concr. (1986) 391–402.

[54] P.E. Petersson, Fracture energy of concrete: Practical performance and experimental results, Cem. Concr. Res. 10 (1980) 91–101. https://doi.org/10.1016/0008-8846(80)90055-1.

[55] S. Wolinski, D.A. Hordijk, H.W. Reinhardt, H.A.W. Cornelissen, Influence of aggregate size on fracture mechanics parameters of concrete, Int. J. Cem. Compos. Lightweight Concr. 9 (1987) 95–103. https://doi.org/10.1016/0262-5075(87)90025-X.

[56] B.I.G. Barr, E.B.D. Hasso, V.J. Weiss, Effect of specimen and aggregate sizes upon the fracture characteristics of concrete, Int. J. Cem. Compos. Lightweight Concr. 8 (1986) 109–119. https://doi.org/10.1016/0262-5075(86)90006-0.

[57] Ph. Regnault, E. Brühwiler, Holographic interferometry for the determination of fracture process zone in concrete, Spec. Issue Fract. Damage Concr. Rock 35 (1990) 29–38. https://doi.org/10.1016/0013-7944(90)90180-O.

[58] RILEM Committee, Size-effect method for determining fracture energy and process zone size of concrete, Mater. Struct. 23 (1990) 461–465.

[59] Z.P. Bažant, M.T. Kazemi, Determination of fracture energy, process zone longth and brittleness number from size effect, with application to rock and conerete, Int. J. Fract. 44 (1990) 111–131. https://doi.org/10.1007/BF00047063.

[60] M.T. Kazemi, H. Golsorkhtabar, M.H.A. Beygi, M. Gholamitabar, Fracture properties of steel fiber reinforced high strength concrete using work of fracture and size effect methods, Constr. Build. Mater. 142 (2017) 482–489. https://doi.org/10.1016/j.conbuildmat.2017.03.089.

[61] W.-H. Zhang, D.-G. Lu, J. Qin, S. Thöns, M.H. Faber, Value of information analysis in civil and infrastructure engineering: a review, J. Infrastruct. Preserv. Resil. 2 (2021) 16. https://doi.org/10.1186/s43065-021-00027-0.

[62] A. Lampropoulos, D. Nicolaides, S. Paschalis, O. Tsioulou, Experimental and Numerical Investigation on the Size Effect of Ultrahigh-Performance Fibre-Reinforced Concrete (UHFRC), Materials 14 (2021) 5714. https://doi.org/10.3390/ma14195714.

[63] M. Daneshfar, A. Hassani, M.R.M. Aliha, T. Sadowski, Assessment of the Specimen Size Effect on the Fracture Energy of Macro-Synthetic-Fiber-Reinforced Concrete, Materials 16 (2023) 673. https://doi.org/10.3390/ma16020673.

[64] P. Xu, J. Ma, Y. Ding, M. Zhang, Influences of Steel Fiber Content on Size Effect of the Fracture Energy of High-Strength Concrete, KSCE J. Civ. Eng. 25 (2021) 948–959. https://doi.org/10.1007/s12205-021-0141-7.

[65] L. Li, B. Wang, H. Xu, H.T. Nguyen, Z.P. Bažant, M.H. Hubler, Crack-Parallel Stress Effect on Fracture of Fiber-Reinforced Concrete Revealed by Gap Tests, J. Eng. Mech. 150 (2024) 04024011. https://doi.org/10.1061/JENMDT.EMENG-7531.

[66] J. Zhang, X. Liu, Z. Wu, H. Yu, Q. Fang, Fracture properties of steel fiber reinforced concrete: Size effect study via mesoscale modelling approach, Eng. Fract. Mech. 260 (2022) 108193. https://doi.org/10.1016/j.engfracmech.2021.108193.

[67] M. Ghasemi, M.R. Ghasemi, S.R. Mousavi, Studying the fracture parameters and size effect of steel fiber-reinforced self-compacting concrete, Constr. Build. Mater. 201 (2019) 447–460. https://doi.org/10.1016/j.conbuildmat.2018.12.172.

[68] A. Hillerborg, The theoretical basis of a method to determine the fracture energy GF of concrete, Mater. Struct. 18 (1985) 291–296. https://doi.org/10.1007/BF02472919.

[69] RILEM Draft Recommendation(50-FMC), Determination of the Fracture Energy of Mortar and Concrete by Means of Three-Point Bend Tests on Notched Beames, Mater. Struct. 18 (1985) 285–290.

[70] J. Roesler, G. Paulino, C. Gaedicke, A. Bordelon, K. Park, Fracture Behavior of Functionally Graded Concrete Materials for Rigid Pavements, Transp. Res. Rec. J. Transp. Res. Board 2037 (2007) 40–49. https://doi.org/10.3141/2037-04.

Chapter 6. Mechanical Performance of Extruded Functionally Graded Fiber-Reinforced Mortar with Targeted Fiber Injection[4]

Abstract

This research investigated the mechanical performance of Functionally Graded Fiber-Reinforced Concrete (FG-FRC) produced via extrusion with a targeted fiber injection. Flexural toughness was assessed using a modified ASTM C1609, and fracture properties were analyzed through implementation of the two-parameter fracture model. The study introduced an innovative targeted fiber injection technique using a conveyor system, tailored for the integration of high-stiffness steel fibers into the mortar prior to extrusion. This method permits the use of fibers in more extrusion systems, since the fibers cannot jam in the pump. The research utilized digital image correlation to observe the full displacement field, allowing for an in-depth examination of crack propagation and strain localization. Additionally, X-ray computed tomography was employed to analyze fiber dosage and distribution within the FG-FRC layers. Results indicated that the targeted fiber injection method facilitated effective fiber distribution within FG-FRC layers, leading to enhanced mechanical performance through fiber dosage's optimization.

Keywords: Fiber-reinforced concrete, Flexural, Fracture, Digital image correlation, Extrusion, Injection, Fiber alignment, X-ray computed tomography, Crack propagation, Strain localization.

[4] **R. Alarrak**, A.S. Brand, Mechanical Performance of Extruded Functionally Graded Fiber-Reinforced Mortar with Targeted Fiber Injection, In Review. (2024).

6.1. Introduction

Conventional concrete, being inherently brittle, offers limited resistance to applied loads, whether dynamic or static, due to its weakness in the tensile and flexural properties. This limitation has historically been mitigated through the use of reinforcement methods such as rebar or fibers. These methods have provided essential support, improving the material's strength against cracking and enhancing its load-bearing capacity. Nevertheless, a more advanced solution is emerging in the form of Functionally Graded Fiber-Reinforced Concrete (FG-FRC). This material offers an improvement in combating concrete's natural weaknesses in tension and flexure. FG-FRC not only substantially enhances load resistance and structural durability but also introduces an unparalleled combination of strength, toughness, and durability [1]. This makes FG-FRC an ideal choice for a wide range of applications, including long-span bridges, seismic-resistant structures, and super high-rise buildings [2–4]. To optimize the mechanical properties of FG-FRC, extensive research has focused on integrating fibers into its matrix. Among these, steel fibers are often preferred due to their processing ease, cost-effectiveness, and minimal water use, thereby ensuring structural integrity, environmental sustainability, and economy [5].

6.1.1. Mechanical Performance of FG-FRC

Previous research on FG-FRC offers tailored mechanical properties through variations in fiber content, distribution, and orientation within a single concrete element [6,7]. Researchers have explored effects such as fiber content or type on mechanical behavior of FG-FRC with notable increases in bending performance and energy absorption due to addition of steel fibers into its matrix [8–11]. Additional research has been useful in demonstrating the beneficial impacts of fiber distribution optimization on tensile strength and fracture toughness [12,13]. Furthermore, FG-FRC mixes with steel fiber-reinforced concrete (SFRC) as the bottom layer demonstrate notably

superior tensile strength [14,15]. One study by Jiang *et al.* focused on assessing FG-FRC's long-term performance, particularly in cold regions, which demonstrated that the combination of anti-freezing polycarboxylate superplasticizer, steel fiber, and polypropylene fiber, resulted in improved FG-FRC durability in cold climates [12]. Despite these advancements, a gap remains in the comprehensive understanding of FG-FRC. Key areas such as optimizing fiber dosage, distribution, and orientation still require further investigation to fully unlock the potential of this innovative material.

6.1.2. Fiber Injection Techniques

The injection of fibers into concrete or mortar matrices as explored in previous research has gained attention as a method to enhance mechanical properties. This approach involves direct incorporation of fibers into the material, improving dispersion and interlocking with the matrix, leading to enhanced performance [16,17]. The fibers have the potential to be included into the anhydrous mix beforehand, included during the concrete mixing process, or inserted into the mortar or concrete just before it is deposited. Most of the studies have introduced fibers into the concrete during the mixing process [3,18–22]. Ahmed *et al.* demonstrated a device designed to include various types of fibers into the mortar of an extrusion-based 3D concrete printing facility before to the printing process, addressing possible compatibility challenges, such as introducing high stiffness and long steel fibers; however, the printing process of that study resulted in randomly oriented fibers [23]. Conveyor systems and pneumatic injection have streamlined the process, by continuously injecting fibers as the mixture advances, and providing precise control over dosage and distribution, respectively. While previous research has emphasized the potential of fiber reinforcement, within these novel techniques, promising not only improved mechanical properties but also efficient, reliable, and consistent fiber integration [24,25].

6.1.3. Fiber Alignment

Fiber alignment within concrete or mortar matrices significantly impacts material mechanical behavior. Understanding influencing factors is crucial for optimizing fiber-reinforced materials [26,27]. The alignment of steel fibers has been achieved by the use of magnetic fields [18,28–32], and the orientation of fibers during the consolidation process as fresh concrete flows has been facilitated through the development of improved casting processes [33–38]. Extrusion-based technologies have shown potential in attaining enhanced fiber alignment, as indicated by recent studies [21,22,39–52]. These techniques leverage additive manufacturing processes to place fibers aligned to the desired direction to have most effective tensile resistance.

6.1.4. Additive Manufacturing Techniques

By leveraging technologies such additive manufacturing, the construction industry has explored a transition from traditional manual methods to automated processes [23,53−61]. Previous research on additive manufacturing techniques for fiber-reinforced concrete has drawn notable attention. Ning *et al.* aimed to evaluate the impact of carbon fiber content and length on the mechanical properties of thermoplastic matrix carbon fiber-reinforced plastic composites fabricated using fused deposition modeling, revealing significant improvements while stressing the importance of parameter optimization and material compatibility [53]. In contrast, Blok *et al.* explored fused filament fabrication in 3D printing fiber-reinforced thermoplastic composites, distinguishing between short and continuous fiber feedstocks [54]. Their findings highlighted the substantial performance gains achieved with continuous carbon fibers but noted design limitations, while short carbon microfibers showed better printability with modest enhancements in mechanical properties [62,63]. These studies collectively emphasize additive manufacturing's

transformative potential in the fiber-reinforced concrete industry, emphasizing the need for ongoing optimization and scalability solutions.

6.1.5. X-ray Computed Tomography

X-ray computed tomography (XCT), as explored in previous studies to examine fibers in concrete, represents a non-destructive imaging technique widely employed for investigating the intricate internal structure of concrete and mortar, encompassing the distribution and orientation of fibers [64,65]. The research conducted by Xue *et al.* employed XCT to scrutinize the influence of various fiber types and dosages on the internal configuration and mechanical attributes of cement-tailings matrix composites [66]. Furthermore, correlative relationships between porosity, grayscale value, and mechanical performance surfaced, underlining the role of essential structural integrity. Nevertheless, XCT may have limitations when discerning extremely fine fibers, and the resolution of the technique can potentially affect the precision of fiber characterization [67,68].

6.1.6. Digital Image Correlation

Digital image correlation (DIC) is a non-contact optical technique that enables the measurement of deformation and displacement in materials subjected to external loads. It is a powerful tool for studying crack propagation and strain localization in materials, including fiber-reinforced concrete [20–22,69,70]. DIC can successfully yield calculated strain maps, allowing for the prediction of crack locations and observation of microcrack initiation. One notable benefit of is its capacity to provide high-resolution, comprehensive surface displacement and strain data. This capability is typically difficult to achieve through conventional strain gauge measurements [71–77,45,61]. DIC has also proven effective in visualizing and quantifying crack patterns and strain distribution [78,79].

6.1.7. Research Objective

This review of literature establishes a framework for this study that introduces a novel targeted fiber injection technique, which employs a conveyor system designed for integrating high-stiffness steel fibers into mortar directly at the nozzle just before extrusion. This approach is a significant leap forward in construction technology, especially for extrusion-based systems, since it adeptly solves the common issue of fiber-induced jamming in pumps, augers, and the constricted sections of piping or hosing, which has been a longstanding challenge in the use of fibers in extrusion processes of cementitious materials.

The study focuses on the mechanical performance of FG-FRC, particularly its flexural toughness and fracture properties, following the successful injection of targeted steel fibers. It details the innovative approach of developing a targeted fiber injection technique tailored to infuse high-stiffness steel fibers into the extruded mortar. This method does not complicate the logistics by requiring multiple concrete mixes to be mixed at the same time, thereby offering a more streamlined and efficient construction method.

The research encompasses various aspects of material properties, fiber incorporation methods, alignment, imaging techniques, and additive manufacturing. These diverse aspects of research contribute to this study understanding of how to enhance the mechanical performance of FG-FRC and provide valuable insights and directions for future investigations in this field.

6.2. Experimental Methodology

6.2.1. Theoretical Background

6.2.1.1. Flexural Properties

The methodology for assessing flexural toughness in this study was inspired by the ASTM C1609 standard [80]. Nonetheless, the necessity to adapt the specimen fabrication process prompted certain deviations from the standard. The test samples were reshaped into rectangular beams measuring 700 mm by 80 mm by 150 mm with a testing span of 600 mm. These adjustments were made to align with the bending configurations of prior research by the authors [21,22], enhancing the ability to compare mechanical properties affected by the employment of a pump extrusion technique.

Each beam sample underwent a third-point monotonic load application until reaching a net deflection of L/75, where L represents the length of the specimen, using a displacement rate of 0.1 mm/min. The load-deflection curve obtained from the bending test was categorized into two distinct behaviors, including softening and hardening. The softening behavior in the load-deflection curve was divided into five stages, as shown in Figure 6.1. These stages range from the onset to the first peak deflection ($\delta_1 = \delta_P$) and include net deflections at L/600, L/300, L/150, and L/75. Within this context, the phases are sequentially termed: the 1st stage (up to the first peak load), the 2nd stage (up to L/600 net deflection), the 3rd stage (up to L/300 net deflection), the 4th stage (up to L/150 net deflection), and the 5th stage (up to L/75 net deflection). The 1st stage indicates the material's peak flexural strength, or modulus of rupture, while the 2nd stage reflects the residual flexural strength immediately post-peak, providing insight into the material's performance post-peak stress. The 3rd, 4th, and 5th stages are indicative of the residual flexural

strength at increasing net deflections, serving as essential indicators for evaluating the material's residual flexural toughness. On the other hand, the hardening behavior in the load-deflection curve was divided into six stages, which has one more stage than softening behavior in the load-deflection curve, including the maximum peak load stage that corresponds to the maximum peak deflection (δ_P), as shown in Figure 6.2.

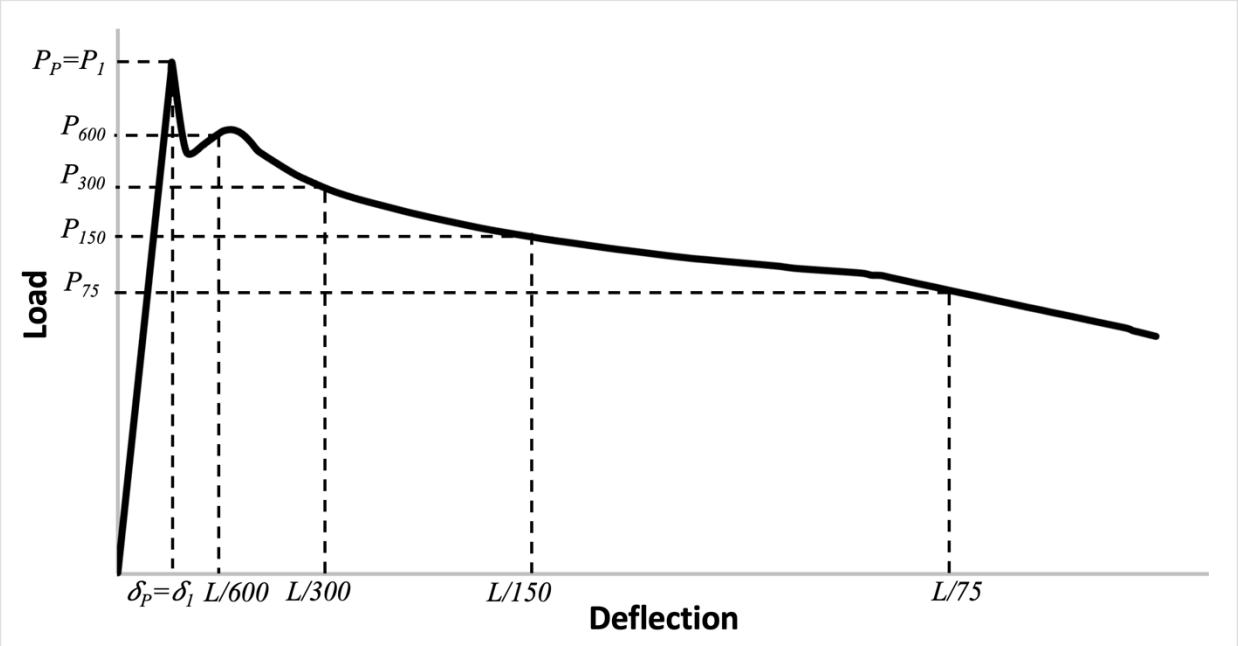

Figure 6.1: Five Stages of Load-deflection Curve for Softening Behavior (adapted from ASTM C1609)

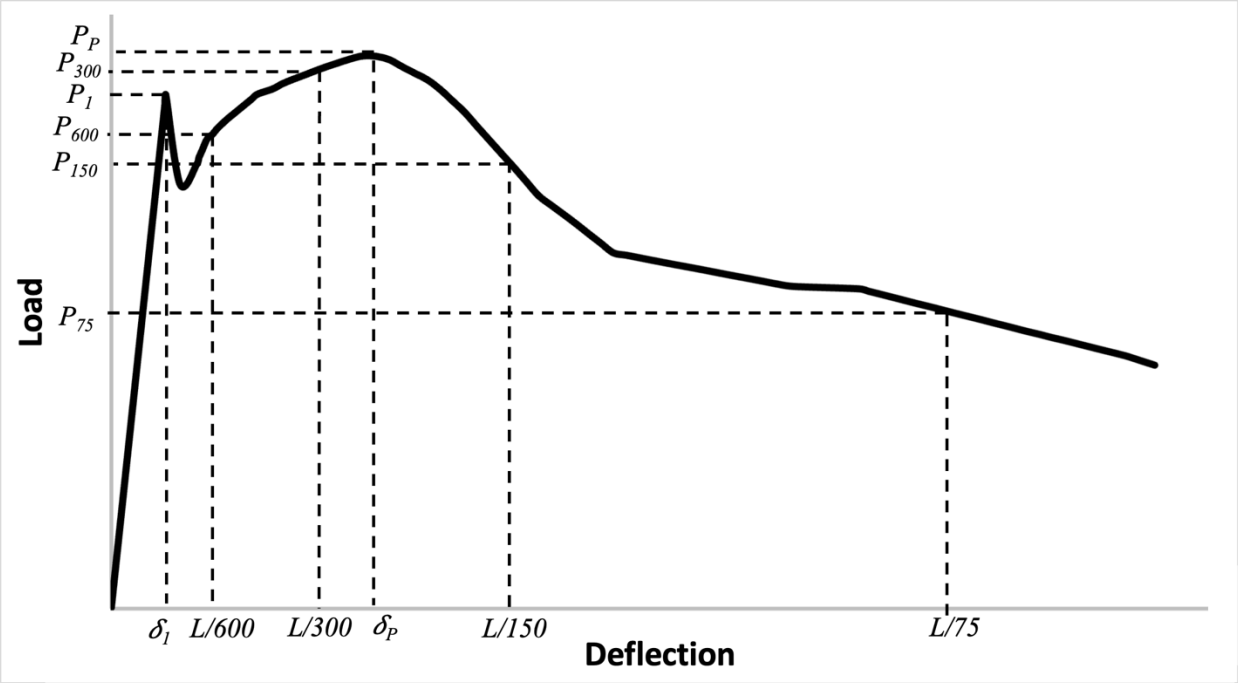

Figure 6.2: Five Stages of Load-deflection Curve for Hardening Behavior (adapted from ASTM C1609)

The investigation determined several flexural properties including the peak strength (f_P), residual strengths at various net deflections ($f_{600}, f_{300}, f_{150}, f_{75}$), flexural toughness indices for selected deflections (T_{300}, T_{150}, T_{75}), and equivalent flexural strength ratios at specific deflections ($R_{T,300}, R_{T,150}, R_{T,75}$). In the case of hardening behavior, the first peak strength (f_1) was differentiated from the maximum peak strength (f_P). Peak strength along with residual strengths (f), were computed using Equation 1, where P is the corresponding load, L is the span length, b is the width of the specimen, and d is the depth of the specimen. Flexural toughness parameters (T_x) were determined by quantifying the total area under the load-deflection curve up to the corresponding net deflections. The equivalent flexural strength ratios were calculated using Equation 2, where x is the corresponding net deflection, T_x is the flexural toughness corresponding to that net deflection, b is the width of the specimen, and d is the depth of the specimen.

$$f = \frac{PL}{bd^2} \quad (1)$$

$$R_{T,x} = \frac{x \cdot T_x}{f_1 bd^2} \cdot 100\% \quad (2)$$

6.2.1.2. Fracture Properties

Single-edge notched beams (SENB) were fabricated to evaluate fracture characteristics in accordance with the two-parameter fracture model (TPFM) [81,82]. The total fracture energy was calculated following the approach introduced by Hillerborg [83,84]. Utilizing these integrative fracture tests, the Mode I critical stress intensity factor (K_{IC}), the critical crack tip opening displacement ($CTOD_C$), the strain energy release rate (G_{IC}), and the total fracture energy (G_F) were computed through three-point bend tests. The test configuration was detailed for extruded fiber-reinforced mortar beams in a previous study by the authors [22].

Each beam specimen underwent a single cycle of loading and unloading, using a displacement rate of 0.1 mm/min, to obtain K_{IC}, $CTOD_C$, and G_{IC} based on the loading and unloading compliances. Upon reaching the first peak load and then decreasing to around 95 % of that first peak load, the specimen was unloaded. Subsequently, the specimen was reloaded to until failure. The loading compliance (C_i) was established as the inverse of the slope found on the initial loading curve, while the unloading compliance (C_u) was similarly obtained from the inverse of the slope of the unloading curve. The critical effective crack length (a_c) was then calculated by setting the modulus of elasticity derived from the loading compliance (E_i) equal to the modulus of elasticity from the unloading compliance (E_u). These elastic moduli are detailed in Equation 3 for the loading phase and Equation 4 for the unloading phase, where S is the span length, a_o is the initial notch depth, b is the width of the specimen, d is the depth of the specimen, α_o is the initial

notch depth ratio, α_c is the critical notch depth ratio, and $g_2(\alpha)$ is the geometric factor of opening displacement defined in Equation 5.

$$E_i = \frac{6Sa_o g_2(\alpha_o)}{C_i bd^2} \tag{3}$$

$$E_u = \frac{6Sa_c g_2(\alpha_c)}{C_u bd^2} \tag{4}$$

$$g_2(\alpha) = 0.76 - 2.28\alpha + 3.87\alpha^2 - 2.04\alpha^3 + \frac{0.66}{(1-\alpha)^2} \tag{5}$$

The critical stress intensity factor, designated as K_{IC}, was calculated by Equation 6, where P_1 is the first peak load, W_o is the self-weight of the specimen, L is the length of the specimen, and $g_1(\alpha)$ is the geometric function defined in Equation 7. The values of $CTOD_C$ and G_{IC} were determined using Equations 8 and 9, respectively.

$$K_{IC} = 3\left(P_1 + \frac{0.5W_o S}{L}\right)\frac{S\sqrt{\pi a_c}}{2bd^2} g_1\left(\frac{a_c}{d}\right) \tag{6}$$

$$g_1(\alpha) = \frac{1.99 - \alpha(1-\alpha)[2.15 - 3.93(\alpha) + 2.70(\alpha)^2]}{\sqrt{\pi}[1 + 2(\alpha)][1 - (\alpha)]^{\frac{3}{2}}} \tag{7}$$

$$CTOD_C = \frac{6Sa_c g_2\left(\frac{a_c}{d}\right)}{Ebd^2}\left(P_1 + \frac{0.5W_o S}{L}\right)\left[\left(1 - \left(\frac{a_c}{a_o}\right)\right)^2 + \left(1.081 - 1.149\left(\frac{a_c}{d}\right)\right)\left(\left(\frac{a_c}{a_o}\right) - \left(\frac{a_c}{a_o}\right)^2\right)\right]^{\frac{1}{2}} \tag{8}$$

$$G_{IC} = \frac{K_{IC}^2}{E} \tag{9}$$

Following the methodology formulated by Hillerborg [83], the total fracture energy (G_F) is defined as the ratio of the quotient of the total energy absorbed during fracture (W_T) to the concrete fracture area (*i.e.*, $(d - a_o)b$). The total energy (W_T) is determined by summing the area

under the load-CMOD curve (W_r) to the equivalent self-weight force (P_w) multiplied by the CMOD value at failure (δ_f), as shown in Equation 10.

$$G_F = \frac{W_T}{(d - a_o)b} = \frac{W_r + 2P_w\delta_f}{(d - a_o)b} = \frac{W_r + \frac{W_o S}{L}\delta_f}{(d - a_o)b} \quad (10)$$

6.2.2. Mix Design and Properties

For this study, a single mortar mixture was prepared, and steel fibers were incorporated at three different volumetric dosages: 0 %, 0.5 %, and 1 % by volume. These specific dosages were chosen because they fall within a practical range that could be realistically applied in actual construction field [85]. Each FG-FRC specimen was extruded using an electric pump. Owing to the size limitations imposed by the extrusion pump on the aggregate used, only fine aggregate with a maximum size of 4.75 mm and a fineness modulus of 2.6 was incorporated into the mixtures.

Each specimen in the study was composed of three layers of mortar mix, each with different fiber dosages, creating functionally graded mixtures. Table 6.1 details the specific proportions of each mortar mix, and Table 6.2 outlines the fiber properties as specified by the manufacturer. A notable feature of the steel fibers used in this study, as depicted in Figure 6.3, is their 3D hooked ends. These data are crucial for understanding the behavior and performance of the fibers within the mortar mixtures, particularly in how they contribute to the overall structural integrity and characteristics of the specimens.

Table 6.1: Concrete Mixture Proportions

Mixture ID	**0%**	**0.5%**	**1%**
Type I cement (kg/m^3)	688	688	688
Fine aggregate (kg/m^3)	1042	1042	1042
Water to cement ratio	0.40	0.40	0.40
Steel fiber volume	0%	0.5%	1%

Table 6.2: Properties of Steel Fibers

Length (mm)	**30**
Filament diameter (mm)	0.38
Aspect ratio	80
Specific gravity	7.8
Tensile strength (MPa)	3,070

Figure 6.3: Steel Fibers

The compressive strength of the specimens was measured according to the ASTM C39 standard. Following a 28-day period of moist curing, three cylindrical samples from each mixture were selected for testing. These cylinders each had dimensions of 4 inches (100 mm) in diameter

and 8 inches (200 mm) in height. The results of these compressive strength tests, accompanied by the relevant statistical analysis, are presented in Table 6.3.

Table 6.3: Compressive Strength Results

Fiber dosage	Compressive strength (MPa)	Mean (MPa)	Standard deviation (MPa)	Coefficient of variation (%)
0%	42.6 42.0 41.2	41.9	0.70	1.68
0.5%	39.1 40.4 38.4	39.3	1.02	2.58
1%	41.3 38.8 40.6	40.2	1.29	3.21

6.2.3. Testing Program and Sample Preparation

In this study, a total of thirty beam specimens were prepared, divided among five different functionally graded mixtures. Each mixture contributed six beams to the sample set. Of these, three specimens per mixture were allocated each for flexural and fracture testing. The experimental setups for these tests are illustrated in Figure 6.4 for the four-point bending tests, assessing flexural properties, and Figure 6.5 for the three-point bending tests, assessing fracture properties. Each beam was cast with dimensions of 700 mm in length, 150 mm in height, and 80 mm in width, and was tested over a span of 600 mm. For the beams subjected to fracture testing, each beam had a notch saw-cut to one-third of its depth at the mid-span, resulting in an initial notch depth (a_o) of 50 mm. This feature was essential for accurately simulating and studying fracture behaviors under the test conditions.

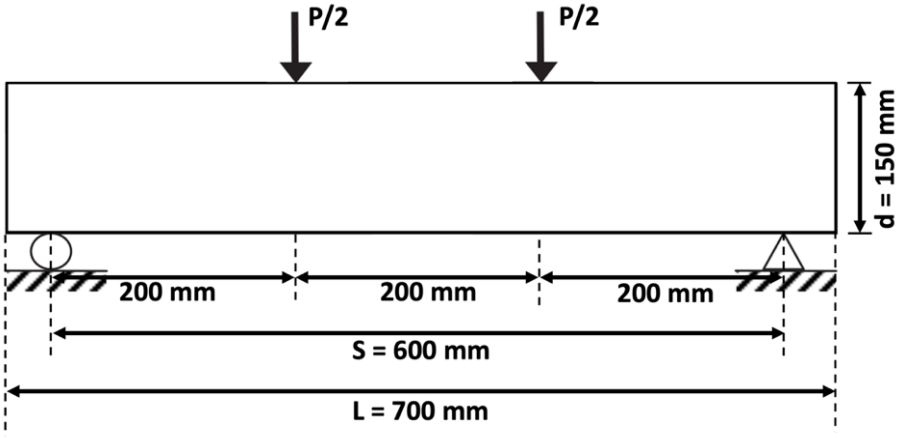

Figure 6.4: Test Setup of Four-point Bending Beam Specimen

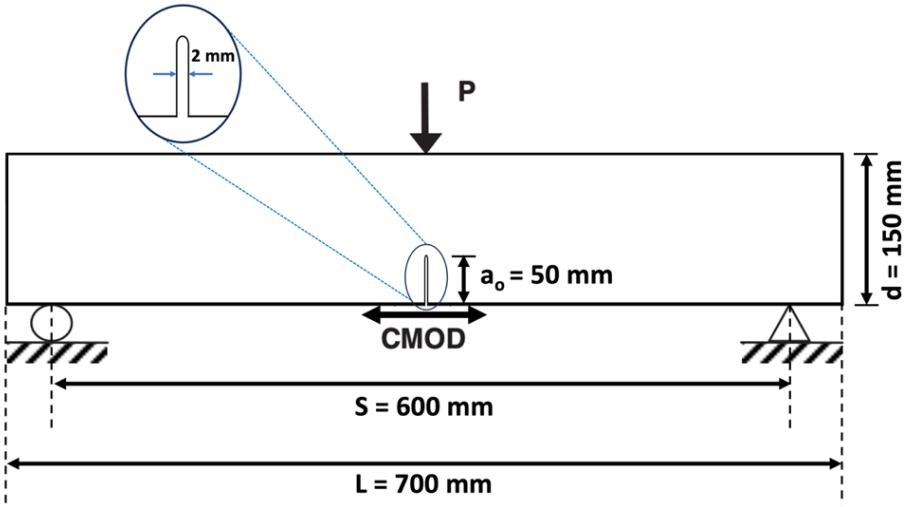

Figure 6.5: Test Setup of Three-point Bending Beam Specimen

The beam specimens in this study were cast using an innovative targeted fiber injection method, as depicted in Figure 6.6. This method involved the use of an electric pump capable of delivering high pressure, reaching up to 2.1 MPa. Within the system, a driving shaft positioned in a material hopper was responsible for feeding the mortar into a continuous cavity rotor-stator pump unit. This unit then conveyed the mix to a dispensing head, to which a PVC pipe, with a diameter of 2 inches, was attached at a 45-degree downward angle. This orientation was crucial for ensuring proper alignment of the fibers during the extrusion process.

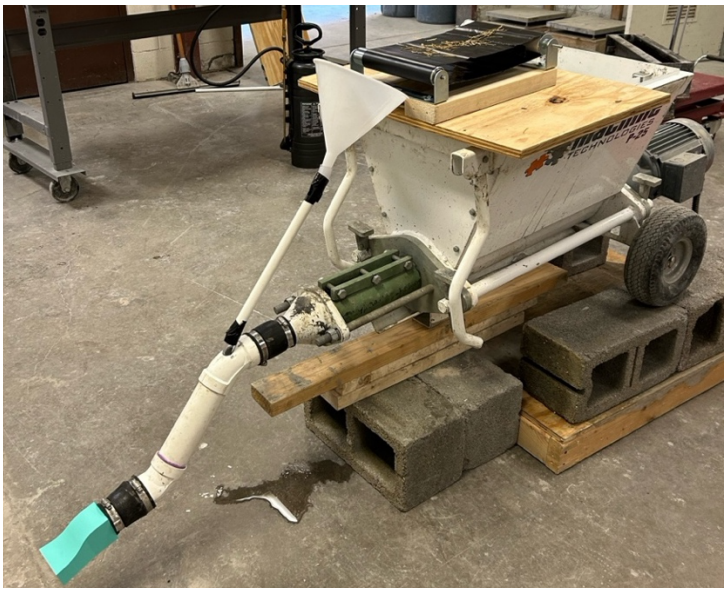

Figure 6.6: Targeted Fiber Injection Method's Setup

The PVC pipe led to a rectangular 3D printed nozzle, shown in Figure 6.7, crafted from polyethylene terephthalate (PET), which was specifically designed to match the dimensions of the mold frame. This design consideration was vital to prevent the fibers from protruding beyond the free surface of the extruded material.

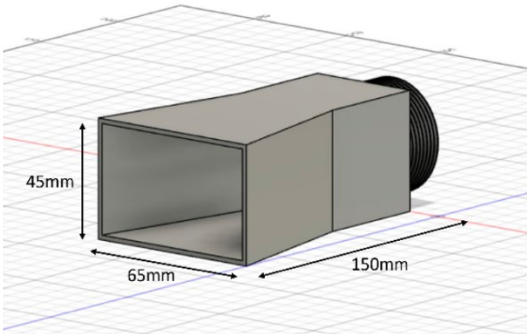

Figure 6.7: Extrusion-based Method's Nozzle Design

For the introduction of fibers, the system utilized a conveyor belt mechanism. This belt deposited the fibers into a funnel, which then channeled them through another PVC pipe directly into the extrusion stage. At this point, the fibers were integrated with the mortar, aligning and moving with the flow direction of the material. This extrusion fiber integration is a key aspect of

the process, ensuring uniform distribution and orientation of fibers within the mortar mix. The mechanics of this extrusion-based fiber injection process is detailed in a schematic representation shown in Figure 6.8. This schematic provides a clear visual understanding of how the fibers are introduced and incorporated into the mortar, highlighting the system's efficiency in maintaining the quality and consistency of the FG-FRC beams.

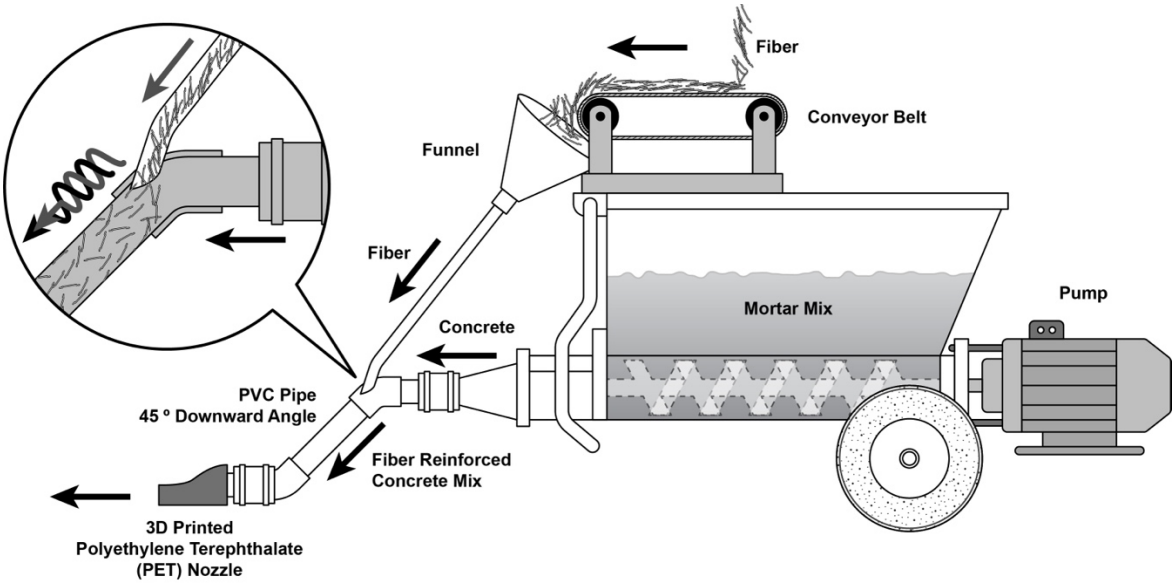

Figure 6.8: Schematic of Extrusion-based Fiber Injection Process

The FG-FRC beams were extruded into the mold by moving the pump along the length of the beam mold, which successfully resulted in the formation of three distinct layers of mortar within each beam. To effectively differentiate among the FG-FRC mixtures, shown in Figure 6.9, a unique identification label was assigned to each. A critical aspect of this process was the precise control over the geometry of the layers and the interfaces between them, which was achieved through a careful timing strategy. A new layer of fresh mortar was added approximately 30 minutes after the application of the previous layer. This interval was carefully chosen, drawing on insights from other studies [86], which detailed the setting and hardening characteristics of the mortar. This method was notable for its avoidance of any additional consolidation techniques. By relying on

the extrusion process and the controlled timing of layer application, the methodology ensured that the layers adhered to each other while maintaining their distinct boundaries and properties. This approach was critical for achieving the desired structural and material characteristics in the final FG-FRC beams.

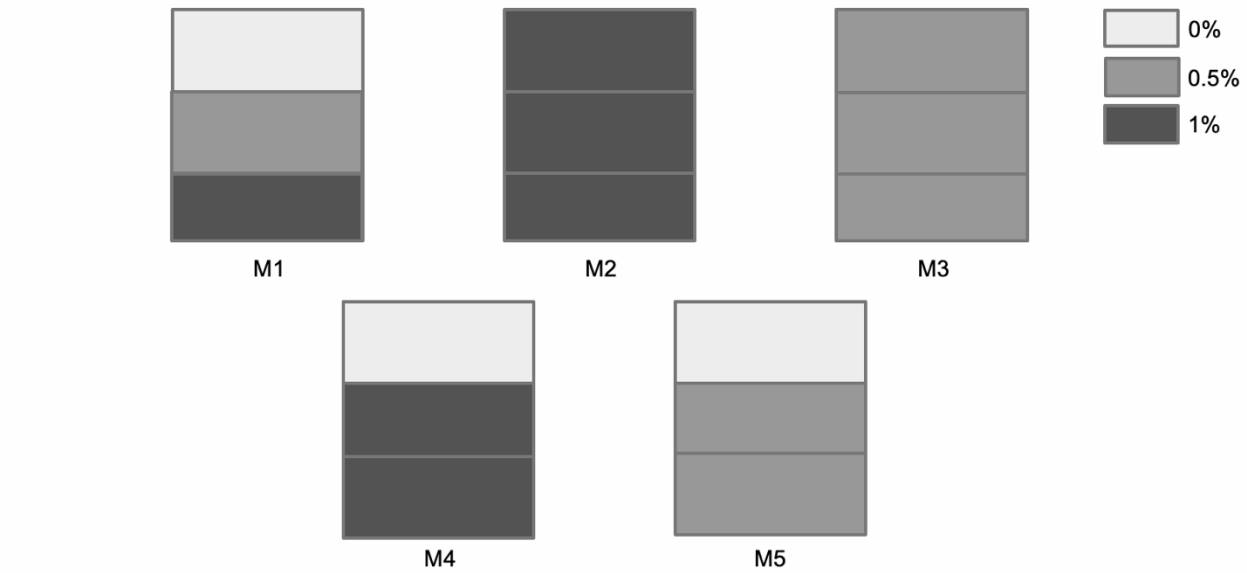

Figure 6.9: FG-FRC Mix Designs

The flexural and fracture properties of the specimens were evaluated using an MTS Insight 150 SL electromechanical universal testing machine. In the flexural tests, a linear variable differential transducer (LVDT) was utilized to measure the mid-span deflection (δ), featuring a deflection measuring capacity of up to 6 mm. The LVDT was strategically positioned to make contact with a steel piece attached to the top of the beam, a setup that is clearly illustrated in Figure 6.10. For the fracture tests, a clip gauge was employed to accurately measure the crack mouth opening displacement (CMOD), having a maximum CMOD measurement capacity of 8 mm. To facilitate this measurement, knife edges were installed beneath the notch to securely hold the clip gauge in place, as demonstrated in Figure 6.11. All tests, both flexural and fracture, were carried

out at a consistent displacement rate of 0.1 mm/min. This standardization of the testing rate was essential for ensuring the reliability and comparability of the results across all specimens.

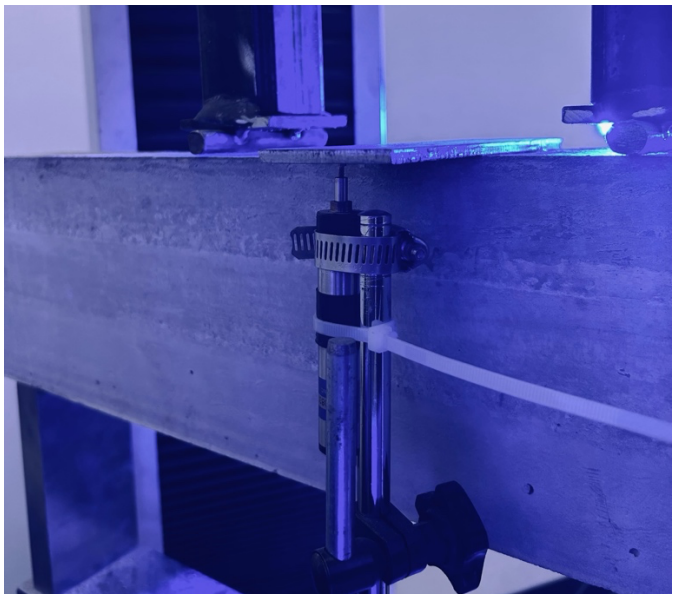

Figure 6.10: LVDT Installation on Beam Specimen

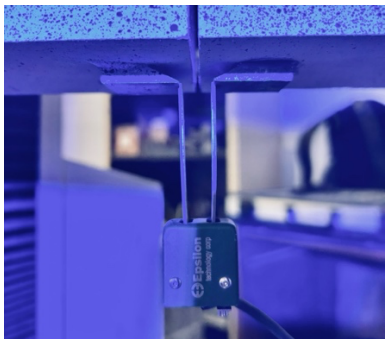

Figure 6.11: Clip Gauge Attached to the Knife Edges

6.2.4. Digital Image Correlation

In this study, DIC analysis was facilitated by painting the specimen surfaces with a random speckle pattern using black and white spray paint, as shown in Figure 6.12. Two digital cameras, positioned on a tripod in front of the testing machine (Figure 6.13), captured images at a frequency of 0.1 Hz. The working distance, the distance between the DIC system and the specimen, was maintained at 724 mm, while the sliding distance, the distance separating the two cameras, was

400 mm. This setup yielded a field of view of 420 mm x 320 mm x 320 mm and a pixel size of 53 µm. 2D image correlation analysis was executed using the GOM™ software, which applies a normalized cross-correlation function to match deformed image subsets with corresponding subsets from a reference image, thus calculating displacement and strain fields.

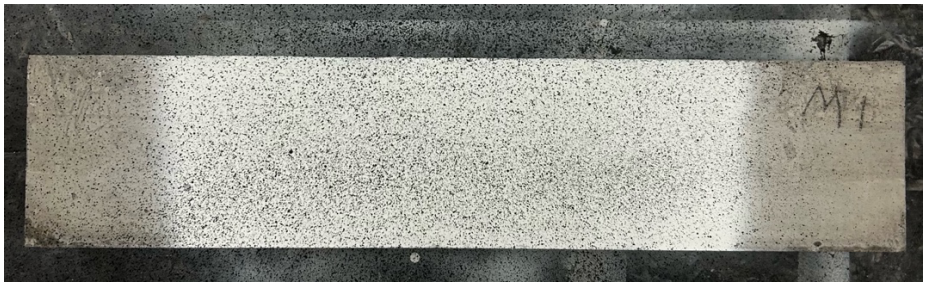

Figure 6.12: Beam Specimen Painted for DIC

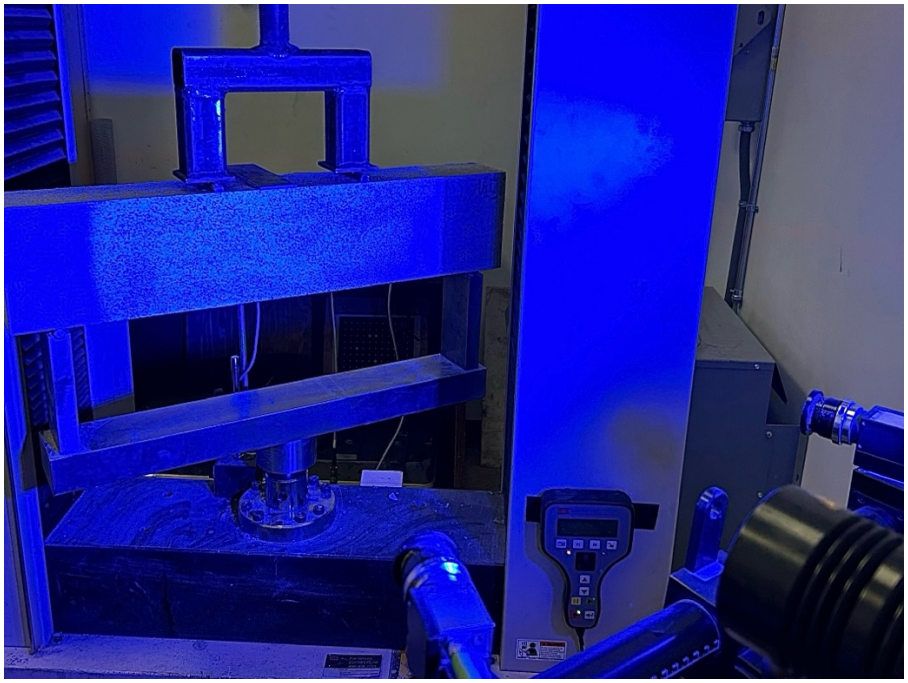

Figure 6.13: Two Digital Cameras Used in DIC

DIC played a crucial role in monitoring the surface deformation of the specimens. It included setting up a coordinate system with X, Y, and Z axes and creating a surface component on the beam surface with distinct patterns for tracking. Additionally, a projected point component, aligned in the Y-direction, was placed atop the middle of the beam surface for deflection data

collection, and an extensometer component, aligned in the X-direction, was placed at the notch base for CMOD data collection.

For flexural test measurements, DIC data was combined with data from the MTS and LVDT systems. The accuracy of DIC in measuring displacement was validated by the close correlation between load-deflection curves from both DIC and LVDT data, as seen in Figure 6.14. While the LVDT measured mid-span deflection, DIC was essential for monitoring post-peak deflection, which was beyond the LVDT's range.

Similarly, in assessing fracture characteristics, DIC data was used alongside MTS and clip gauge data. The systems were synchronized, ensuring accurate correlation between bending test data and DIC imagery. As illustrated with a specimen example in Figure 6.15, the load-CMOD curves from both DIC and clip gauge data were closely correlated, confirming DIC's effectiveness in displacement measurement. Here, DIC was vital for monitoring post-peak CMOD, which exceeded the clip gauge opening capacity.

The DIC system's ability to analyze speckle pattern movements and simultaneously monitor strain profiles along the beam's depth, CMOD, and deflection was crucial. It was particularly instrumental in determining if the FG-FRC specimens exhibited localized strains due to manufacturing errors or poor bonding at the layers' interfaces, enabling a thorough investigation of the crack propagation process.

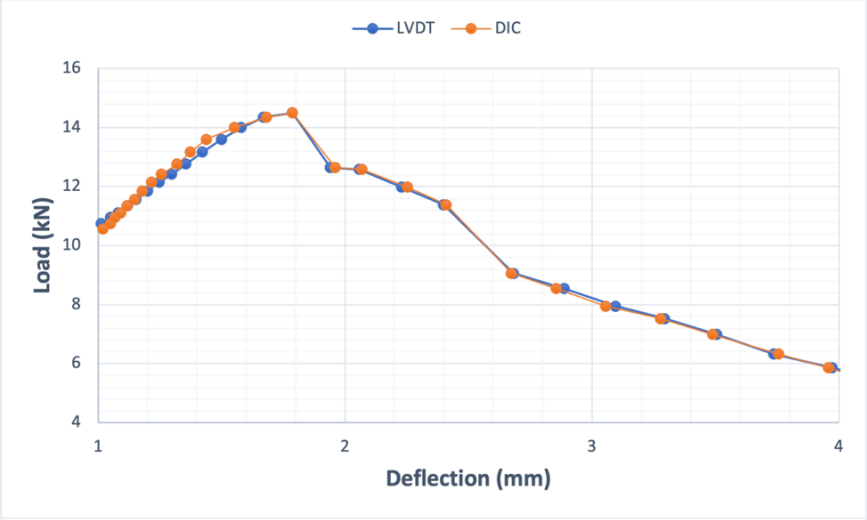

Figure 6.14: Load-deflection Curves for DIC and LVDT

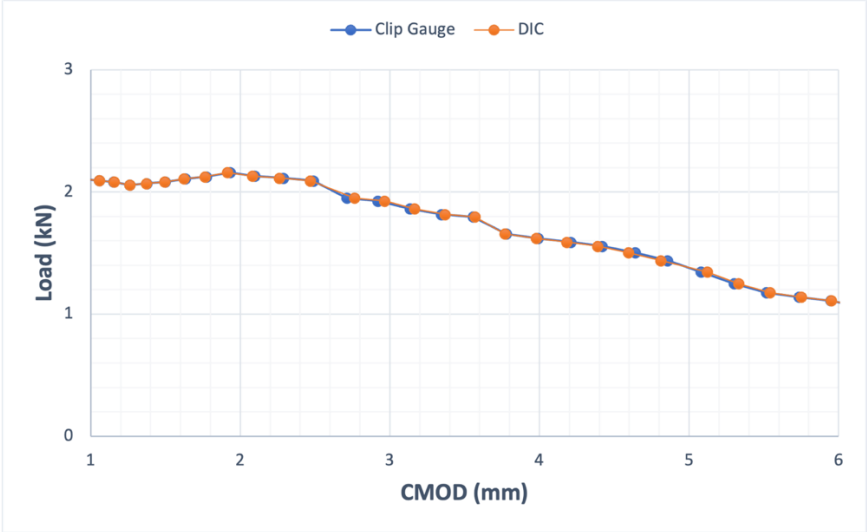

Figure 6.15: Load-CMOD Curves for DIC and Clip Gauge

6.2.5. X-ray Computed Tomography

In this study, the initial hypothesis suggested that the extrusion process would align fibers parallel to tensile stresses, potentially enhancing the mechanical properties of the concrete. Additionally, it was assumed that a specific fiber dosage would be present in each layer of the composite. To test these hypotheses, a thorough examination of fractured specimens was

conducted using XCT to ascertain and confirm the fiber dosage and orientation within each layer of the FG-FRC mixtures.

The XCT system used in this research was a Toshiba Aquilion CT scanner. This setup enables two-dimensional, three-dimensional, and multiplanar reconstructions, offering a comprehensive view of the material's internal structure. The images produced by this scanner are both rapid and detailed, with an average scanning time ranging between 10 to 20 seconds. For optimal imaging, the CT scanner was calibrated to operate at a tube voltage of 120 kV and a tube current of 300 mA. Each scan conducted by this scanner simultaneously captures 64 slices, each with a thickness of 0.5 mm, in a single revolution lasting 350 milliseconds. The XCT analysis utilized Horos™ software, which is tailored for the straightforward visualization of CT data. This software enables the analysis of three 2D views of the scanned specimens: top, front, and cross-sectional views (illustrated in Figure 6.16). For uniformity in analysis, the top view was consistently used to investigate fiber dosage and orientation. This approach allowed for a comprehensive evaluation of the original hypotheses.

To differentiate the fibers within the concrete matrix, grayscale settings were adjusted. All FG-FRC mix designs, comprising three layers with varying fiber dosages, were examined. For each FG-FRC layer, three 1 mm thin sections located at different depths were analyzed. These sections, illustrated in Figure 6.17 using the M1 mixture as an example, provided a top view of the beam specimens. The dimensions of these specimens were 600 mm in length, 80 mm in width, and 1 mm in thickness.

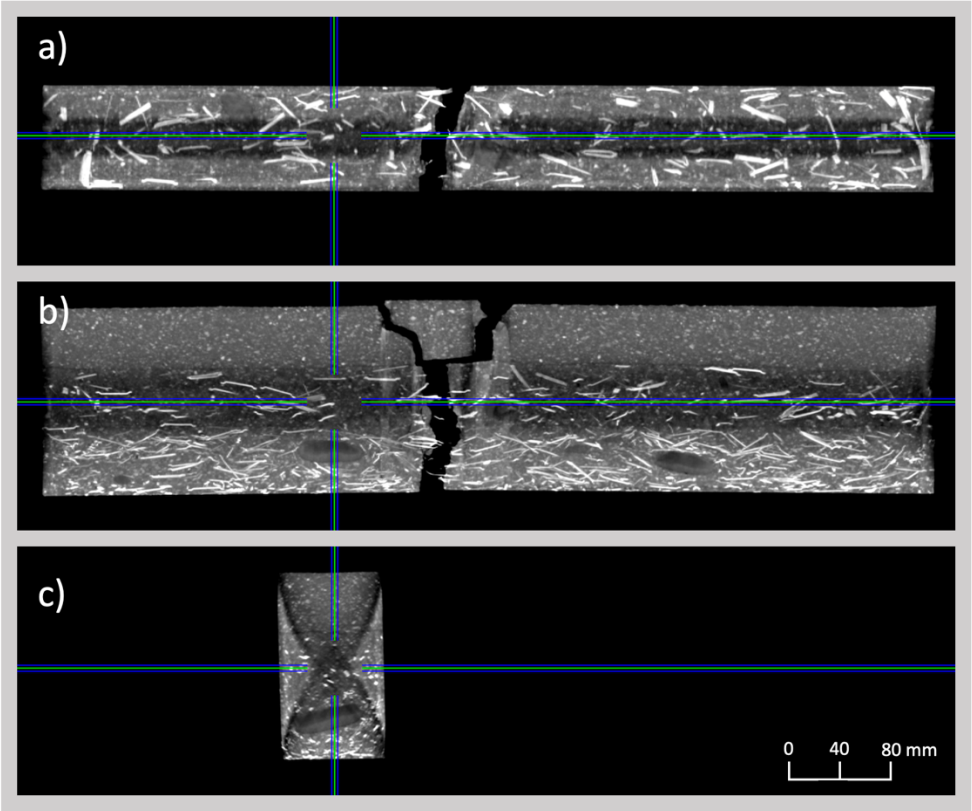

Figure 6.16: XCT Analysis Views: a) Top, b) Front, and c) Cross-sectional

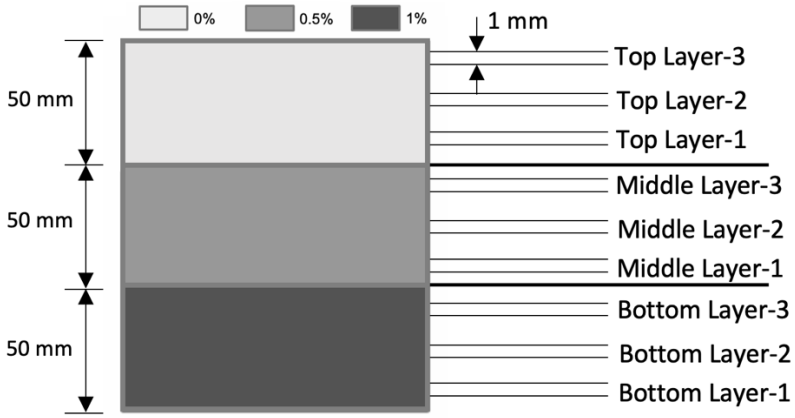

Figure 6.17: XCT Layer Analysis Sections

A MATLAB code incorporating an image processing algorithm was developed to analyze and quantify the orientation of fibers within a concrete matrix. The algorithm processes a digital image of the concrete, where fibers appear as red thin lines against a solid black background. The code initially segments the fibers from the background using color thresholding techniques,

leveraging the distinct red color of the fibers. After segmenting and isolating the fibers, the code labels each fiber and calculates its orientation relative to the horizontal axis, which corresponds to the length of the specimen. For intersecting fibers, an average of the angles is computed. The algorithm's output includes a visual representation of the concrete matrix, with the orientation angles of each fiber annotated on the image.

6.3. Test Results and Discussion

6.3.1. Fiber Dosage and Orientation

The analysis of fiber count, percentage by volume, and orientation angles across the three layers of FG-FRC specimens is presented in Table 6.4. A notable observation is the higher fiber count in the lower section of each FG-FRC specimen, attributed to gravity and the weight of the overlying layer causing some fibers to sink. Moreover, a consistent fiber count was observed across the specimens. A minimal number of fibers were found in the 0 % layers due to casting errors, but the quantity was negligible. The fiber count averages ranged between 56 and 63 in the 0.5 % fiber layers and 96 to 120 in the 1 % fiber layers, validating the successful implementation of the desired fiber dosage in each layer, with nearly double the fibers in 1 % layers compared to 0.5 % layers.

Given that both the volume of the slices and the fibers can be calculated based on their dimensions, it becomes feasible to ascertain the fiber content percentage in each layer, as shown in Table 6.4. This calculation allows for a comparative analysis with the proposed fiber content. Notably, in the 0 % fiber layers, the average fiber content percentage aligned with the designed 0 %, confirming the accuracy of the targeted fiber dosage. In the 0.5 % layers, the average fiber content percentage was approximately 0.4 %, marginally lower than the designed dosage of 0.5

%. Similarly, for the 1 % layers, the average was around 0.8 %, slightly less than the intended 1 %. This discrepancy, though present, is acceptable considering the possibility that some fibers might not be visible or detectable in the XCT images. Therefore, it is reasonable to affirm that the fiber dosages discerned from the XCT images corroborate the proposed fiber dosages in the design.

Figure 6.18 through Figure 6.22 illustrate the fiber orientation angles for M1, M2, M3, M4, and M5 specimens in the three layers, respectively. The data indicated that the majority of fibers were aligned along the beam length. The average fiber orientation angles were between 2° and 3° in the 0.5 % fiber layers and 2° and 7° in the 1 % fiber layers. This comparative analysis confirmed the initial hypothesis, demonstrating that the extrusion process effectively aligned fibers parallel to the tensile stresses, a factor potentially enhancing the mechanical performance of FRC.

*Table 6.4: Fiber Count and Orientation of FG-FRC Specimens**

Fiber dosage/	**M1**			**M2**			**M3**			**M4**			**M5**		
Sample	#	%	θ	#	%	θ	#	%	θ	#	%	θ	#	%	θ
0% in Top Layer	2	0	8°	-	-	-	-	-	-	6	0	2°	2	0	2°
Mean	2	0	8°	-	-	-	-	-	-	6	0	2°	2	0	2°
0.5% in Top Layer	-	-	-	-	-	-	52	0.4	6°	-	-	-	-	-	-
0.5% in Middle Layer	63	0.5	3°	-	-	-	58	0.4	1°	-	-	-	53	0.4	1°
0.5% in Bottom Layer	-	-	-	-	-	-	64	0.5	3°	-	-	-	58	0.4	5°
Mean	63	0.5	3°	-	-	-	61	0.4	3°	-	-	-	56	0.4	2°
1% in Top Layer	-	-	-	89	0.6	2°	-	-	-	-	-	-	-	-	-
1% in Middle Layer	-	-	-	98	0.7	4°	-	-	-	95	0.7	3°	-	-	-
1% in Bottom Layer	120	0.9	7°	101	0.7	0°	-	-	-	126	0.9	9°	-	-	-
Mean	120	0.9	7°	96	0.7	2°	-	-	-	111	0.8	4°	-	-	-

* # represents the fiber count, % represents the fiber percentage, and θ represents the fiber orientation angle.

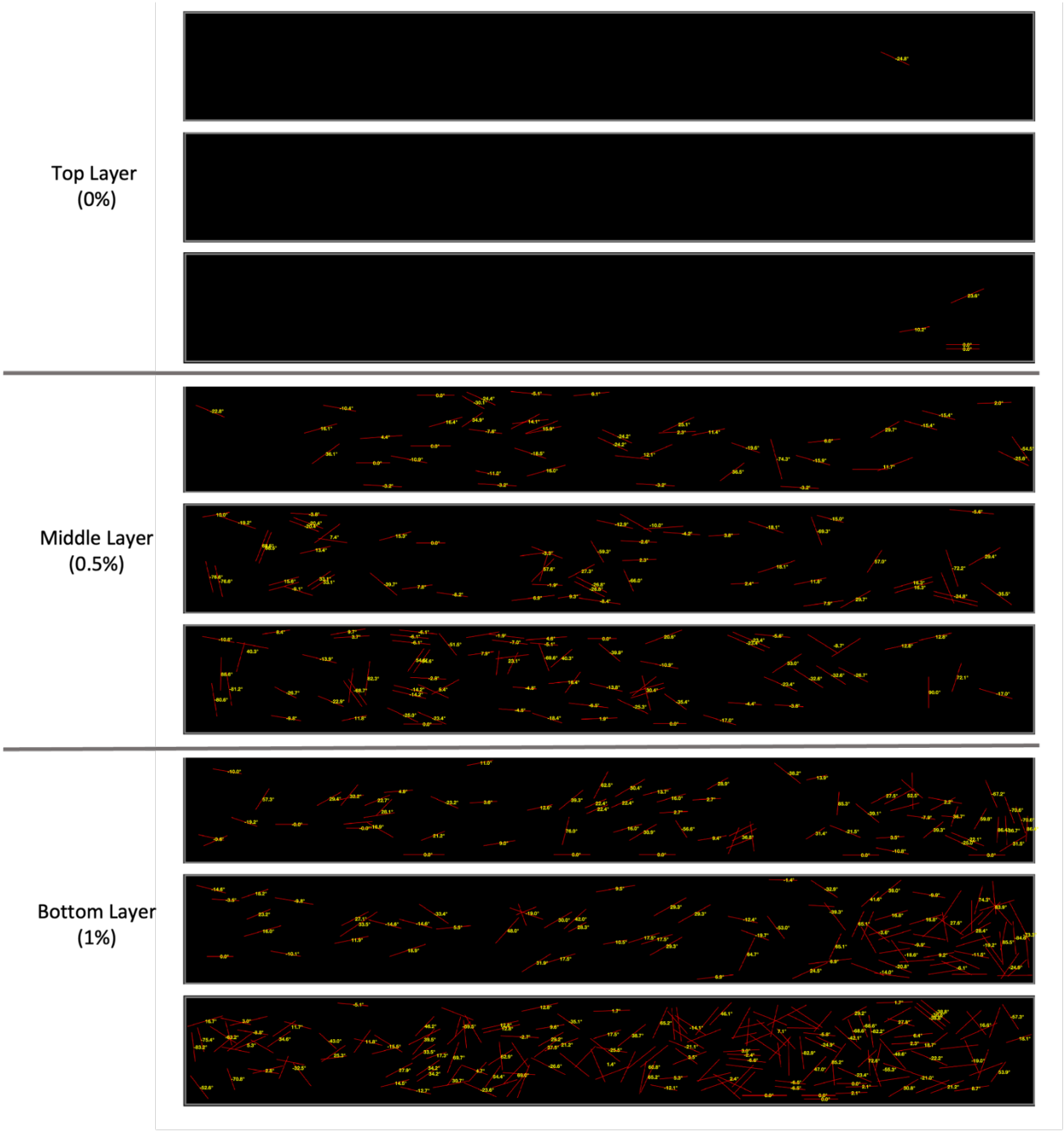

Figure 6.18: Fiber Orientation Angle for M1 Specimen

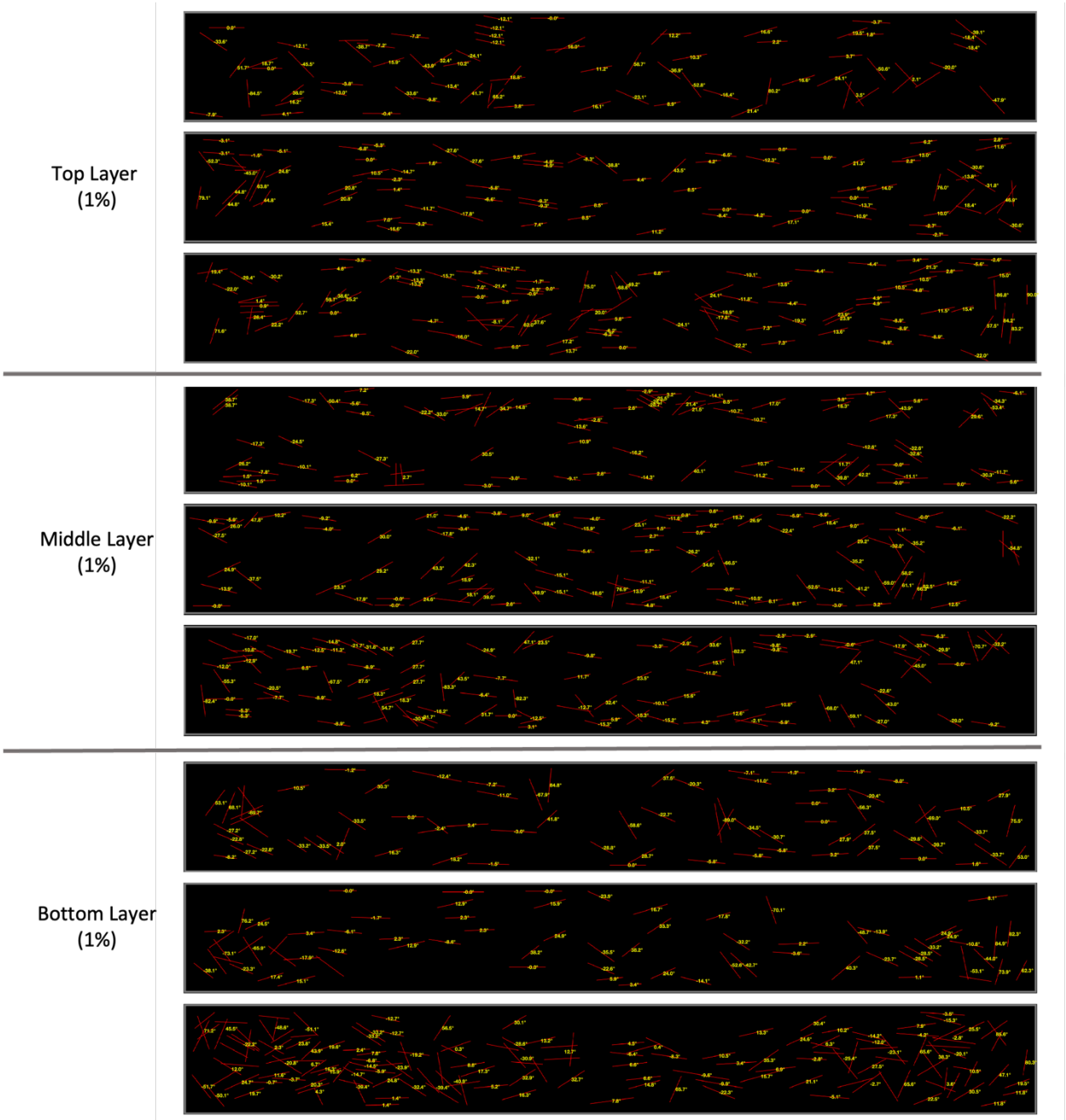

Figure 6.19: Fiber Orientation Angle for M2 Specimen

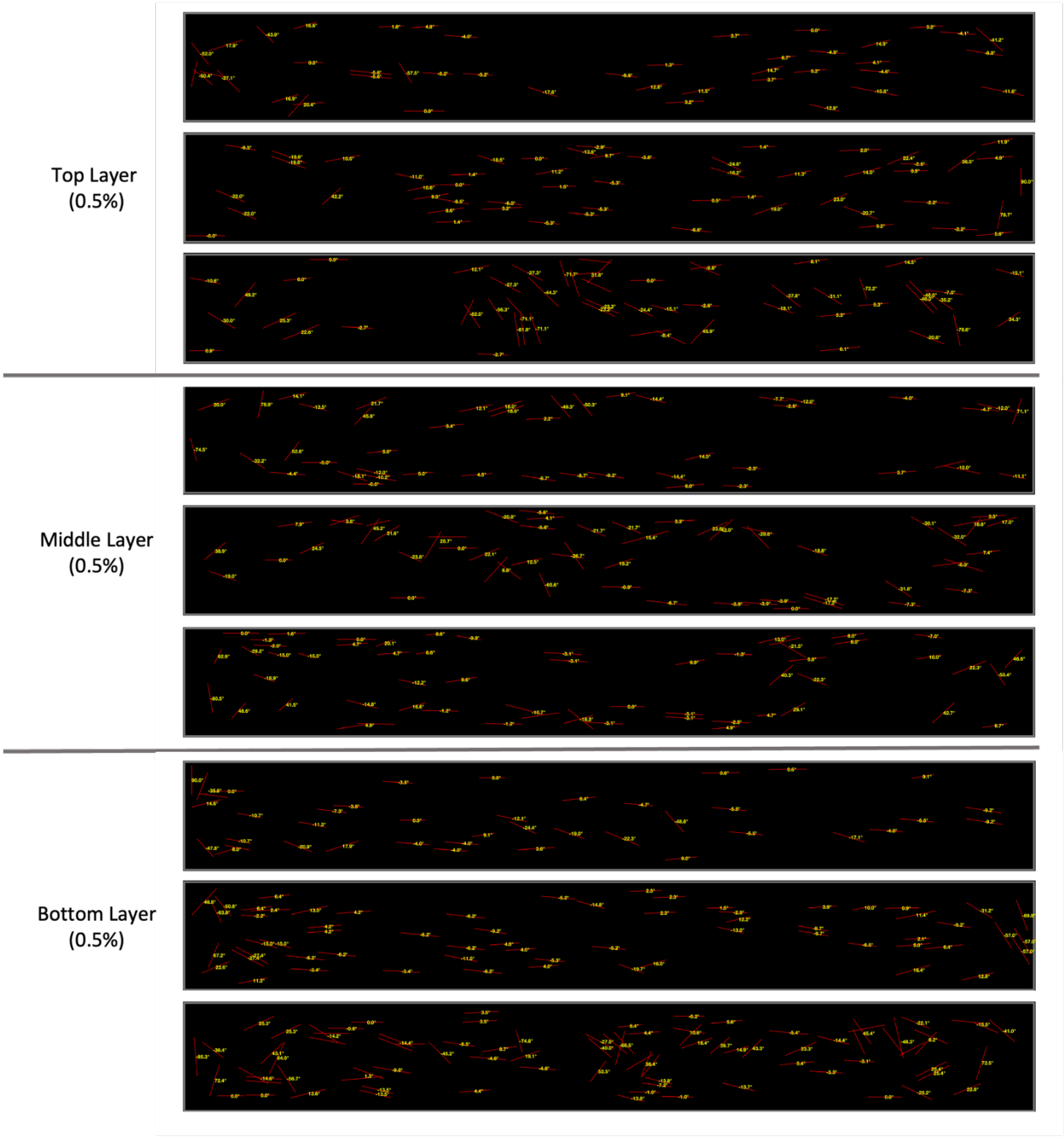

Figure 6.20: Fiber Orientation Angle for M3 Specimen

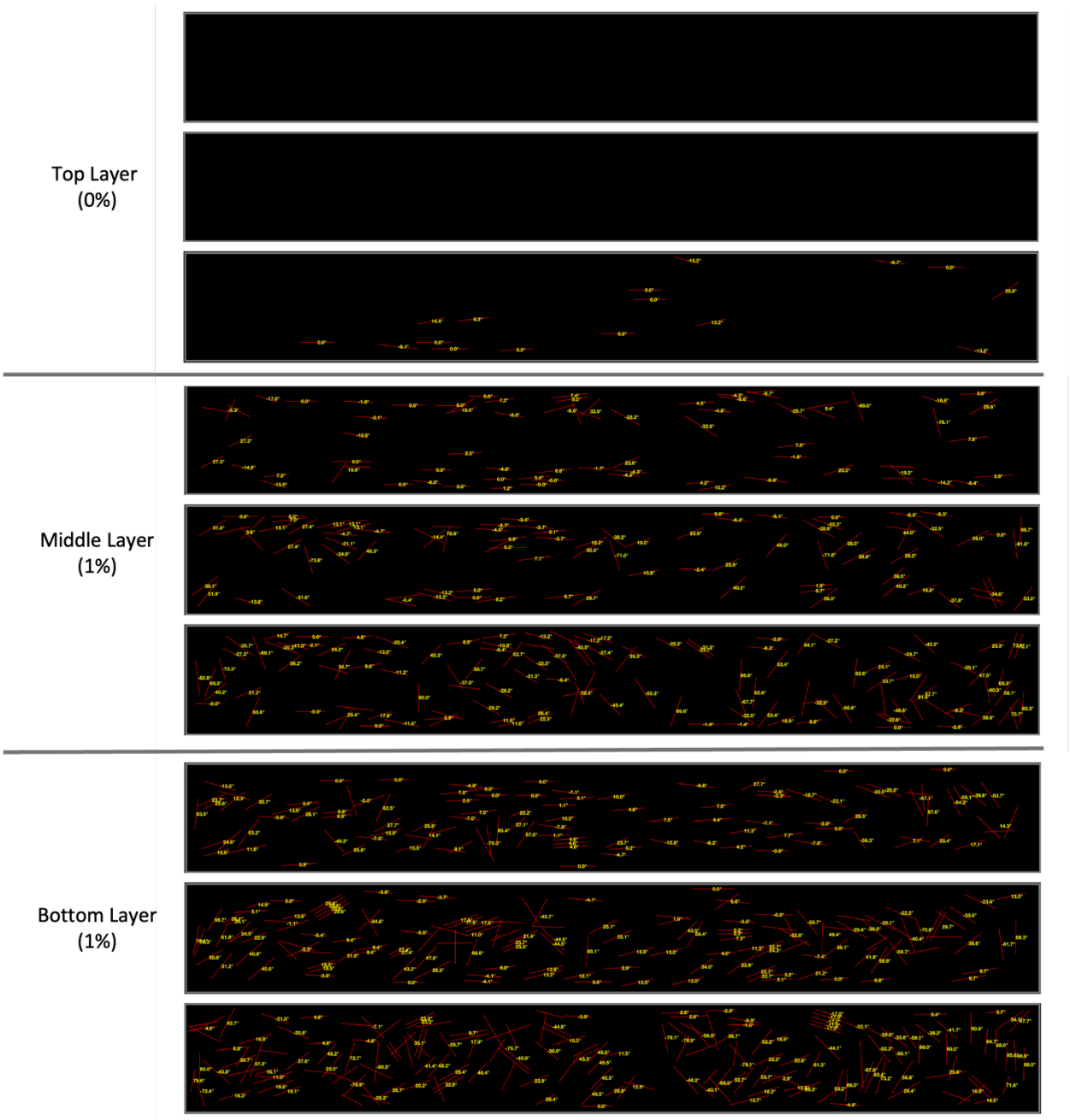

Figure 6.21: Fiber Orientation Angle for M4 Specimen

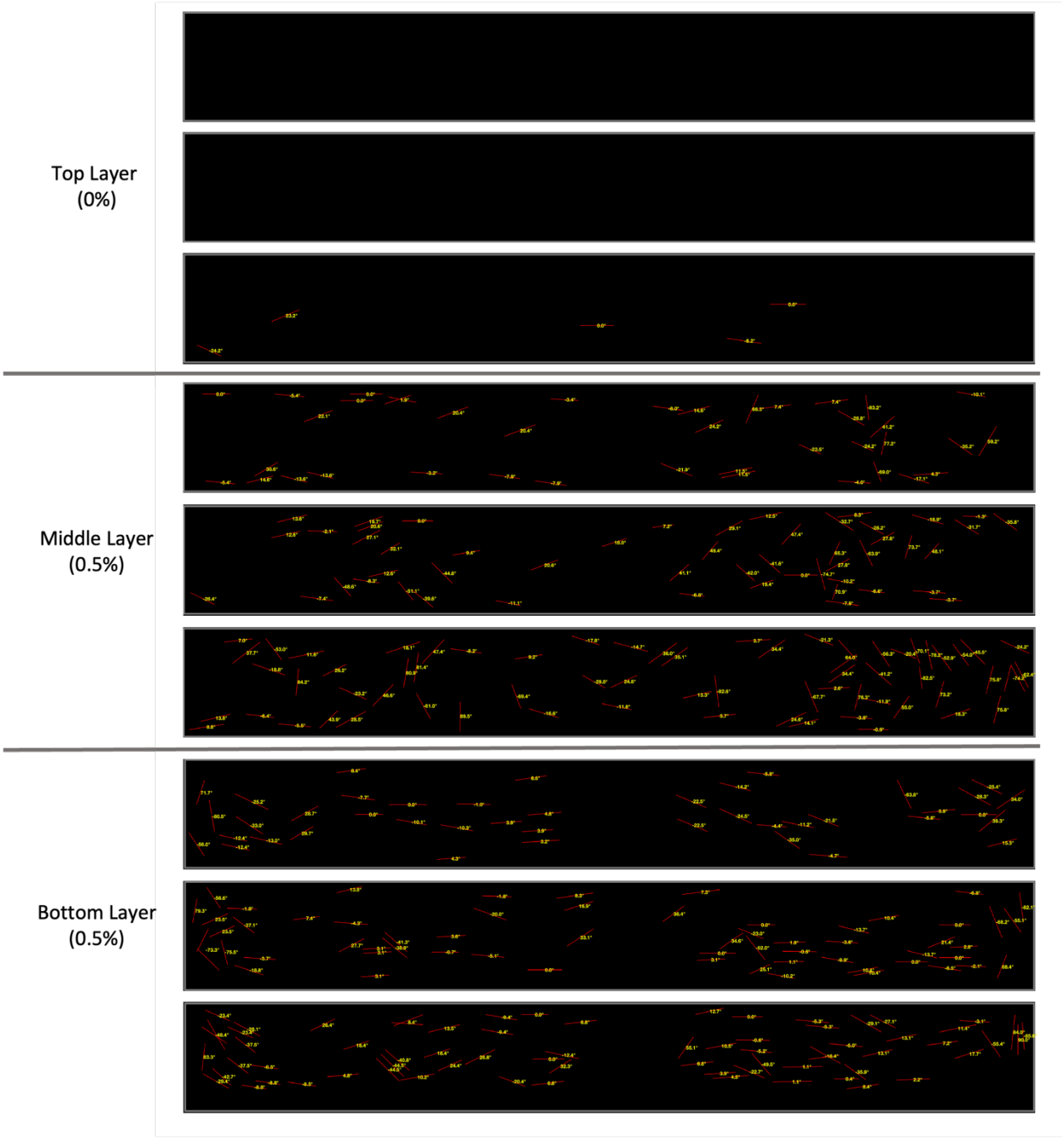

Figure 6.22: Fiber Orientation Angle for M5 Specimen

6.3.2. Flexural Properties

The outcomes of the flexural tests, including initial and peak loads (P_1, P_P), flexural strengths (f_1, f_P), and residual strengths at various deflections (f_{600}, f_{300}, f_{150}, f_{75}), are detailed in Table 6.5. Additionally, assessments of flexural toughness and the equivalent flexural strength

ratios for the specimens are presented in Table 6.6. A statistical approach, specifically a one-tailed two-sample t-test with a 95 % confidence interval, was employed to analyze the effects of different fiber dosages in each layer of the FG-FRC mixtures. This method allowed for a robust comparison across the various mixtures, providing insights into how modifications in fiber content within each layer impact the overall flexural performance of the concrete.

Table 6.5: Flexural Properties of FG-FRC Specimens

Sample	$\boldsymbol{P_1}$ $(\boldsymbol{N})$	$\boldsymbol{P_P}$ $(\boldsymbol{N})$	$\boldsymbol{f_1}$ $(\boldsymbol{MPa})$	$\boldsymbol{f_P}$ $(\boldsymbol{MPa})$	$\boldsymbol{f_{600}}$ $(\boldsymbol{MPa})$	$\boldsymbol{f_{300}}$ $(\boldsymbol{MPa})$	$\boldsymbol{f_{150}}$ $(\boldsymbol{MPa})$	$\boldsymbol{f_{75}}$ $(\boldsymbol{MPa})$
M1_1	13747	20204	4.60	6.75	4.75	6.50	4.50	0.80
M1_2	13692	18867	4.55	6.30	5.40	6.15	2.50	0.55
M1_3	12150	12804	4.05	4.25	4.10	4.20	1.40	0.20
Mean	13196	17292	4.40	5.75	4.75	5.60	2.80	0.50
M2_1	11505	18439	3.85	6.15	5.15	6.10	3.85	1.15
M2_2	11570	16050	3.85	5.35	4.55	4.80	2.65	1.10
M2_3	16353	23239	5.45	7.75	5.45	7.15	4.50	1.50
Mean	13143	19243	4.40	6.40	5.05	6.00	3.70	1.25
M3_1	11955	11955	4.00	4.00	3.30	3.00	1.15	0.10
M3_2	13452	15653	4.50	5.20	3.95	4.95	3.15	1.40
M3_3	10389	11517	3.45	3.85	3.15	3.70	1.80	0.55
Mean	11932	13042	4.00	4.35	3.45	3.90	2.05	0.70
M4_1	14723	18207	4.90	6.05	4.75	6.05	3.65	0.85
M4_2	9267	13881	3.10	4.65	4.10	4.60	1.60	0.25
M4_3	12290	16915	4.10	5.65	4.70	5.05	2.35	0.15
Mean	12093	16334	4.05	5.45	4.5	5.25	2.55	0.40
M5_1	11533	14525	3.85	4.85	3.25	4.50	1.90	0.50
M5_2	11540	11540	3.85	3.85	3.15	1.75	0.80	0.20
M5_3	10306	14499	3.45	4.85	4.40	3.00	1.25	0.15
Mean	11126	13521	3.70	4.50	3.60	3.10	1.30	0.30

Table 6.6: Flexural Toughness Properties of FG-FRC Specimens

Sample	T_{300} (J)	T_{150} (J)	T_{75} (J)	$R_{T,300}$ (%)	$R_{T,150}$ (%)	$R_{T,75}$ (%)
M1_1	25	61	87	91	111	79
M1_2	29	51	67	104	94	62
M1_3	22	38	45	89	78	47
Mean	25	50	66	95	94	62
M2_1	29	61	83	128	132	90
M2_2	25	49	68	108	106	73
M2_3	32	73	103	99	111	79
Mean	29	61	84	112	116	81
M3_1	19	30	36	80	63	38
M3_2	24	49	73	90	92	68
M3_3	19	34	45	92	83	54
Mean	21	38	51	88	79	53
M4_1	28	55	74	97	94	63
M4_2	24	40	49	130	108	66
M4_3	27	59	61	111	119	62
Mean	27	51	61	112	107	64
M5_1	20	40	53	87	86	58
M5_2	16	23	28	69	50	30
M5_3	22	34	40	107	83	49
Mean	19	32	40	88	73	45

The study examined the impact of fiber dosage in the bottom layer of FG-FRC, which is crucial since this layer primarily experiences tensile stresses. For this analysis, M1 specimens, with a 1 % fiber dosage, were compared to M5 specimens, which contained a 0.5 % fiber dosage. The load-deflection curves for these specimens are displayed in Figure 6.23. Statistically significant differences were observed between M1 and M5 in terms of initial load (P_1) and initial flexural strength (f_1). This finding indicates that increasing the steel fiber dosage in the bottom layer leads to enhanced peak load capacity, corroborating the results of previous studies [8,13,87]. Furthermore, the means of residual strengths at lower deflections (f_{600} and f_{300}) also showed significant differences between M1 and M5. This suggests that a higher fiber content in the bottom layer is more effective in controlling the drop in load post-peak, likely due to a greater number of

fibers available to bridge cracks. However, this increase in fiber content did not show a significant impact on the residual strengths at higher deflections (f_{150} and f_{75}).

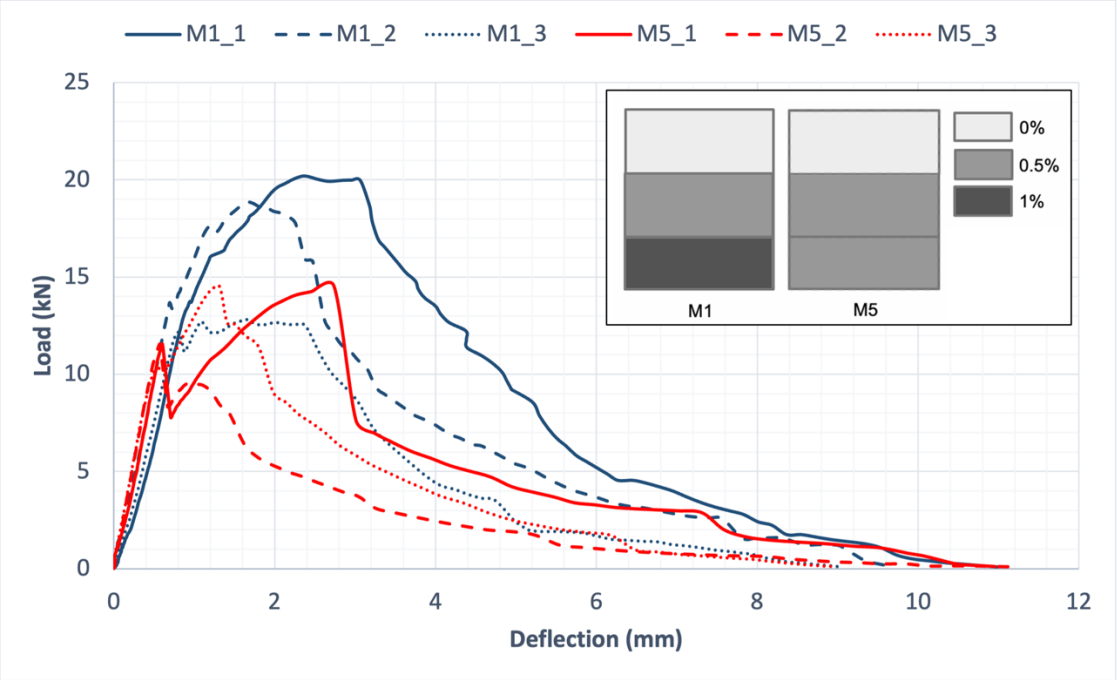

Figure 6.23: Load-deflection Curve for M1 and M5 Specimens

When examining the flexural toughness properties (T_{300}, T_{150}, and T_{75}), M1 specimens demonstrated statistically higher values than M5, with a 95 % confidence level. This enhancement aligns with findings from previous studies [13,87] and supports the notion that incorporating fibers in the tension-experiencing bottom layer substantially boosts the flexural toughness of FRC.

A detailed analysis of the areas under the load-deflection curves reveals notable differences. M1 specimens exhibited a wider coverage area under the load-deflection curves compared to M5, as evident in Figure 6.23. Additionally, all M1 specimens showed a hardening behavior, whereas an M5 specimen (M5_2) exhibited softening. This difference suggests that adding fibers to the bottom layer considerably improves the flexural energy absorption of the FRC specimens.

The equivalent flexural strength ratios ($R_{T,300}$, $R_{T,150}$, and $R_{T,75}$) further underscore this point. As shown in Figure 6.24, M1 specimens had higher ratios than M5, indicating better maintenance of strength post-cracking, which is a crucial aspect of FRC performance. The increase in fiber content from 0.5 % to 1 % in the bottom layer enhanced these ratios by 8 %, 29 %, and 38 %, respectively, suggesting that higher fiber content significantly improves the ductility of FRC specimens.

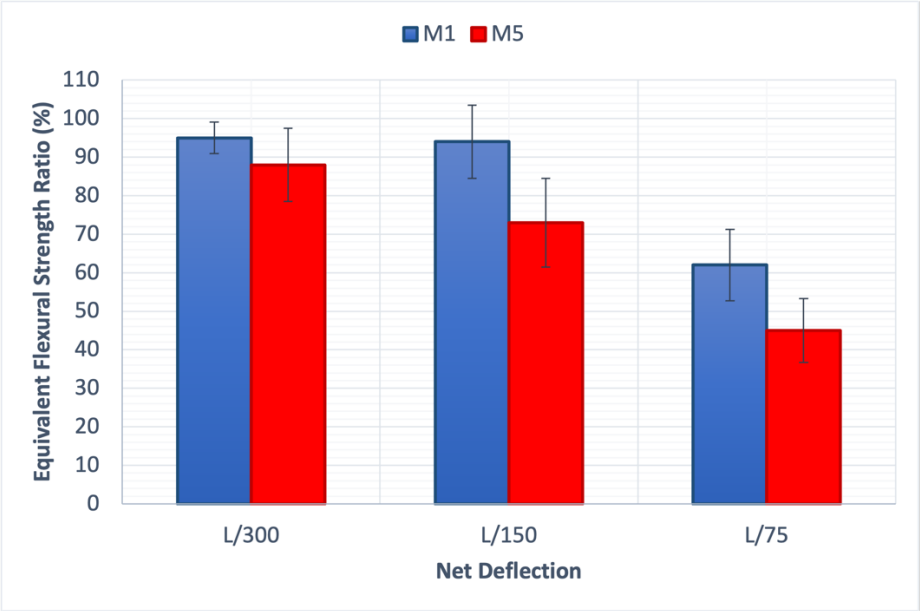

Figure 6.24: Equivalent Flexural Strength Ratio Comparison for M1 and M5 Specimens

The study also investigated the impact of varying fiber dosages in the middle layer of FG-FRC specimens, a region typically near the neutral axis where stress is minimal. This involved a comparative analysis between M1 specimens (with a 0.5 % fiber dosage) and M4 specimens (with a 1 % fiber dosage). The corresponding load-deflection curves are presented in Figure 6.25. Statistical analysis revealed that the differences in initial load (P_1) and initial flexural strength (f_1) between M1 and M4 were insignificant. This outcome suggests that increasing the steel fiber content in the middle layer does not contribute to enhanced peak strength, aligning with the findings of previous studies [8,13,88]. Additionally, the analysis of residual strengths at various

net deflections (f_{600}, f_{300}, f_{150}, f_{75}) showed no significant improvement when increasing fiber content in the middle layer. Therefore, this indicates that additional fibers in this layer do not substantially affect the residual strength of FRC at different deflection levels.

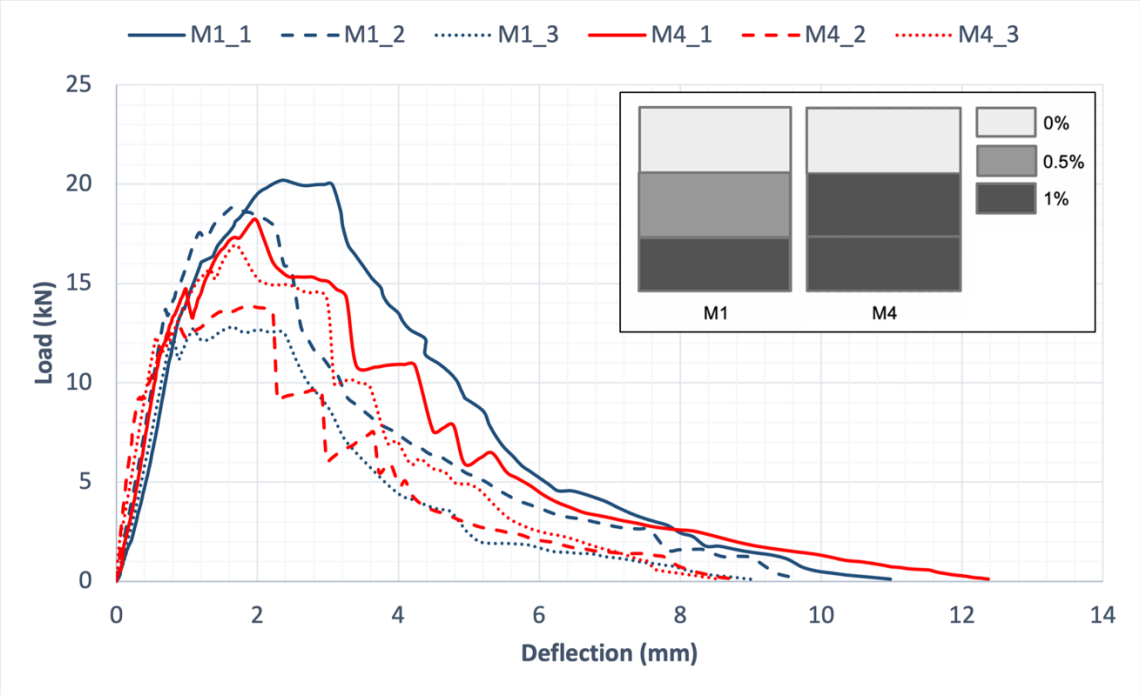

Figure 6.25: Load-deflection Curve for M1 and M4 Specimens

Regarding the flexural toughness properties (T_{300}, T_{150}, and T_{75}), the study found no marked differences in the means for M1 compared to M4 specimens, confirming the hypothesis that adding fibers in the middle layer, close to the neutral axis, does not significantly improve the flexural toughness of FRC. This is evidenced in Figure 6.25, where the load-deflection curves for M1 and M4 exhibit similar areas.

However, when examining the equivalent flexural strength ratios ($R_{T,300}$, $R_{T,150}$, and $R_{T,75}$), as shown in Figure 6.26, a slight increase is observed for the M4 specimens over M1, particularly at L/300 and L/150 net deflections. This indicates that a higher fiber dosage in the middle layer could contribute to maintaining a greater proportion of FRC strength post-cracking.

Specifically, increasing the fiber content from 0.5 % to 1 % in the middle layer of FRC improved these equivalent flexural strength ratios by 18 %, 14 %, and 3 %, respectively. This finding suggests that while the addition of fibers in the middle layer may not significantly enhance peak strength or residual strengths, it could contribute to a modest improvement in the overall ductility and toughness of the material.

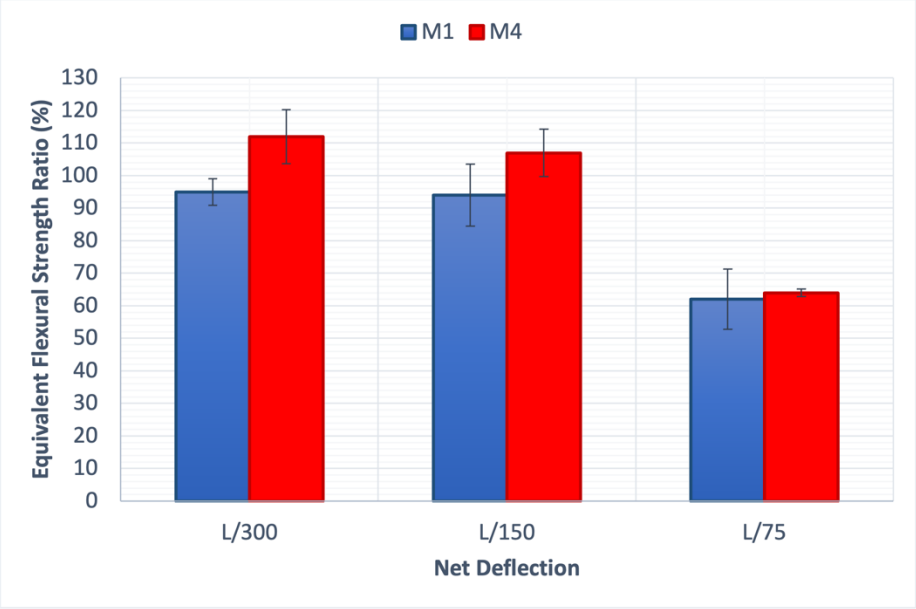

Figure 6.26: Equivalent Flexural Strength Ratio Comparison for M1 and M4 Specimens

The study explored the influence of fiber dosage in the top layer of FG-FRC specimens, a section primarily subjected to compressive stresses. Two comparison was made in this layer with two fiber dosages (0.5 % and 1 %). This was assessed by comparing M2 specimens (with 1 % fiber dosage) to M4 (with no fibers) and M3 specimens (with 0.5 % fiber dosage) to M5 (with no fibers).

When it comes to the studying the effect of the 1 % fiber content in the top layer, the load-deflection curves for both M2 and M4 specimens are shown in Figure 6.27. The statistical analysis between M2 and M4 indicated no significant difference in initial load (P_1) and initial flexural strength (f_1), suggesting that adding 1 % steel fibers to the top layer does not enhance the peak

strength, in line with previous research [6,8,13]. Additionally, there were no significant differences in the residual strengths at lower and middle deflections (f_{600}, f_{300}, and f_{150}) between these specimens. However, a notable difference was observed in the residual strength at higher deflections (f_{75}), indicating that steel fibers in the top layer contribute significantly to the residual strength at higher deflections, which is consistent with previous studies [6].

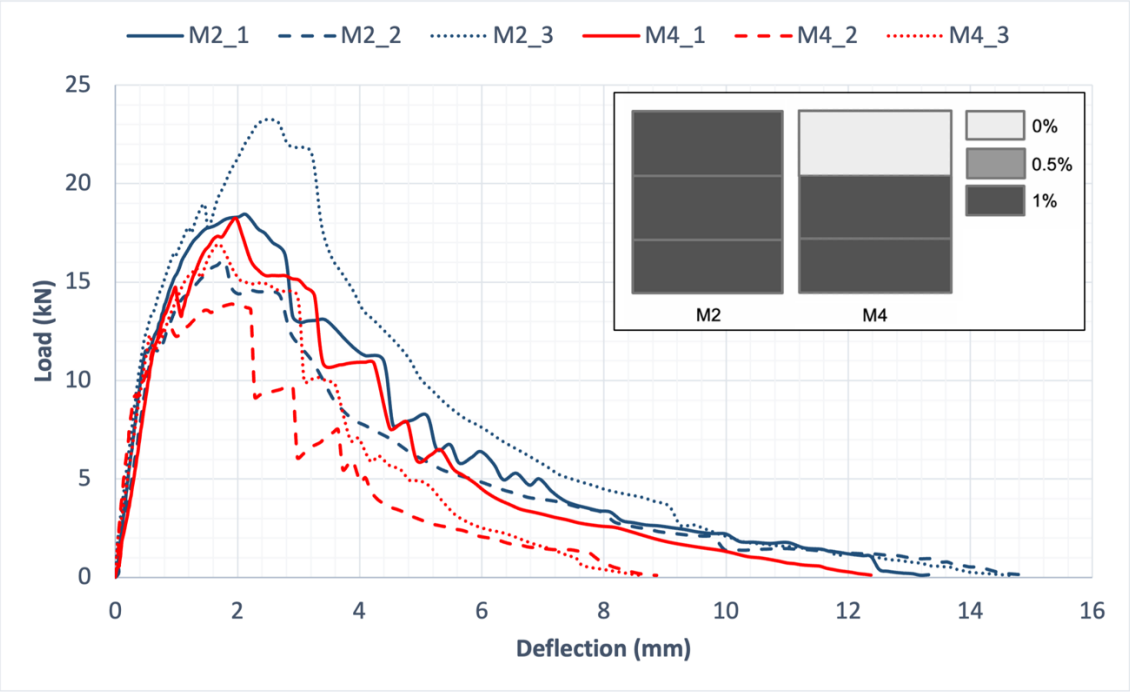

Figure 6.27: Load-deflection Curve for M2 and M4 Specimens

In terms of flexural toughness (T_{300} and T_{150}), no significant improvement was seen with the addition of fibers in the top layer. Nonetheless, a significant increase was observed in the toughness at higher deflections (T_{75}), supporting the idea that fibers in the top layer enhance the material's flexural toughness at these higher stress levels, aligning with the findings of previous studies [6,8]. The equivalent flexural strength ratios ($R_{T,300}$, $R_{T,150}$, and $R_{T,75}$) for M2 compared to M4, as shown in Figure 6.28, illustrate that increasing the fiber content to 1 % in the top layer

improves these ratios by 0 %, 8 %, and 27 %, respectively. This suggests that such an increase in fiber content primarily enhances FRC's flexural properties at higher net deflections.

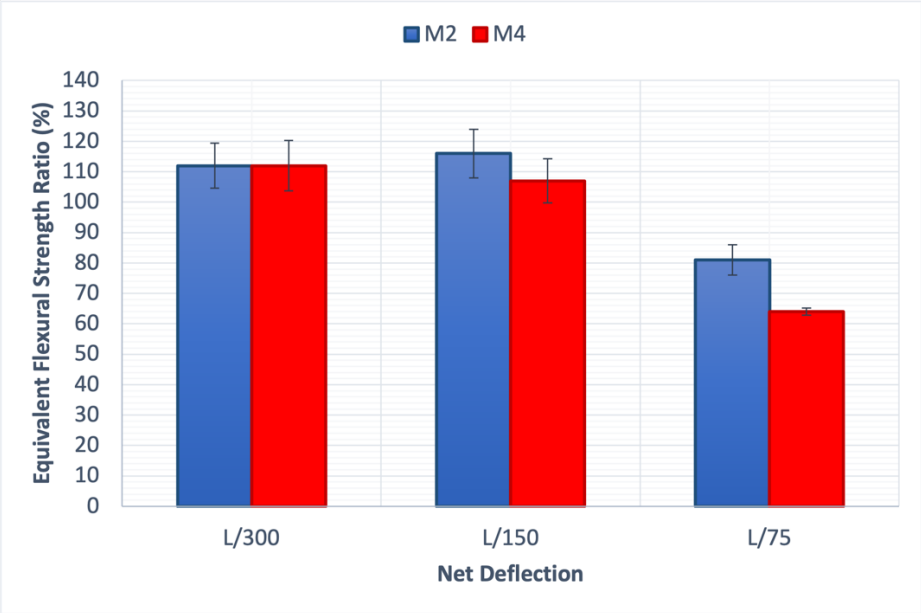

Figure 6.28: Equivalent Flexural Strength Ratio Comparison for M2 and M4 Specimens

When it comes to the studying the effect of the 0.5 % fiber content in the top layer, the load-deflection curves for both M3 and M5 specimens are shown in Figure 6.29. The addition of 0.5 % fiber content did not significantly impact the mean values of (P_1) and (f_1), nor did it significantly improve any of the residual strengths (f_{600}, f_{300}, f_{150}, and f_{75}). This outcome indicates that a 0.5 % fiber dosage in the top layer does not substantially enhance the flexural strengths of FRC.

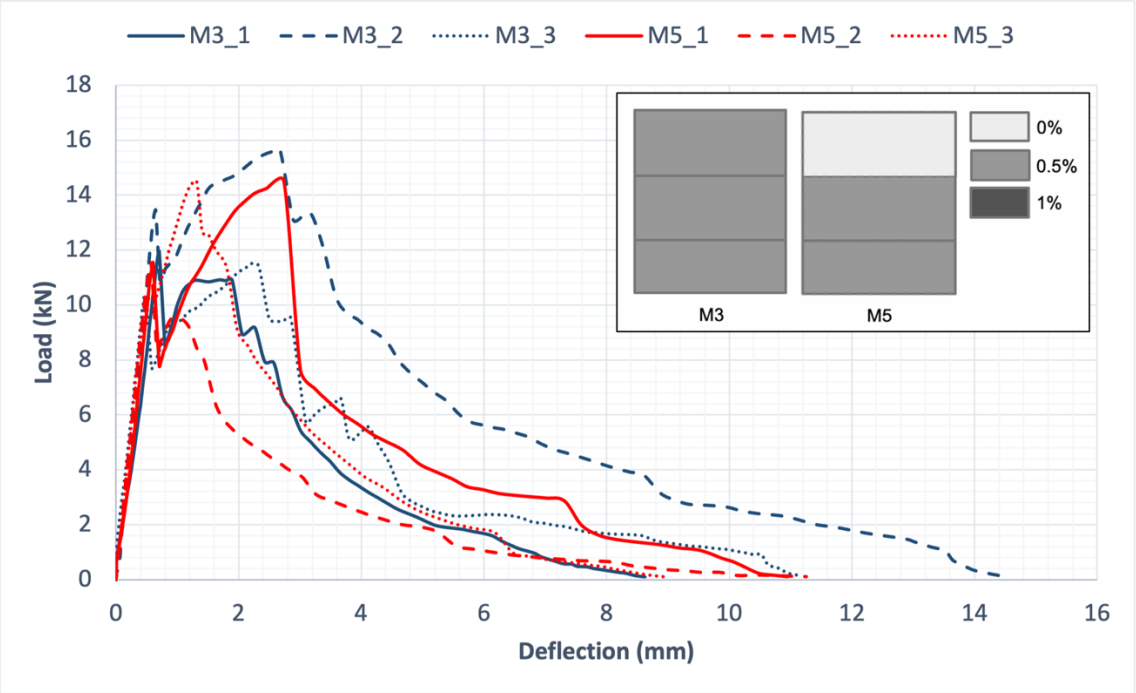

Figure 6.29: Load-deflection Curve for M3 and M5 Specimens

In terms of flexural toughness (T_{300}, T_{150}, and T_{75}), no significant improvement was observed with the 0.5 % addition of fibers in the top layer. The equivalent flexural strength ratios for M3 and M5, as depicted in Figure 6.30, show modest improvements with 0.5 % fiber content, particularly at higher net deflections. The equivalent flexural strength ratios ($R_{T,300}$, $R_{T,150}$, and $R_{T,75}$) improved by 0 %, 8 %, and 18 %, respectively. However, these improvements are less pronounced compared to the 1 % fiber dosage scenario.

In summary, the addition of steel fibers in the top layer of FG-FRC demonstrates a significant impact mainly at higher deflection levels, enhancing residual strength and flexural toughness. While the improvement is more marked with a 1 % fiber dosage, even a 0.5 % increase leads to some enhancement in the material's flexural properties, although to a lesser extent.

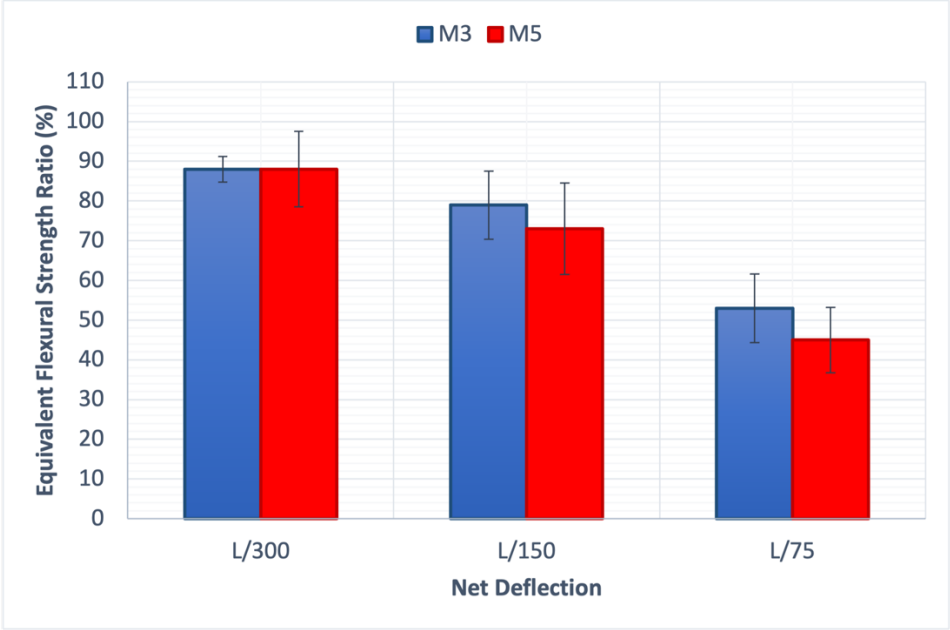

Figure 6.30: Equivalent Flexural Strength Ratio Comparison for M3 and M5 Specimens

The study further delved into the impact of homogenous FG-FRC specimens with uniform fiber dosages across all layers, by comparing M2 (with a consistent 1 % fiber content in each layer) to M3 (with a uniform 0.5 % fiber content in each layer). The load-deflection curves of these specimens are illustrated in Figure 6.31. A significant difference was observed in the residual strengths at various deflections (f_{600}, f_{300}, f_{150}, and f_{75}) between M2 and M3. This finding indicates that FG-FRC sections with a uniform 1 % fiber content exhibit more efficient improvement in residual strengths than those with a 0.5 % fiber content, which is consistent with the findings of previous studies [13,87].

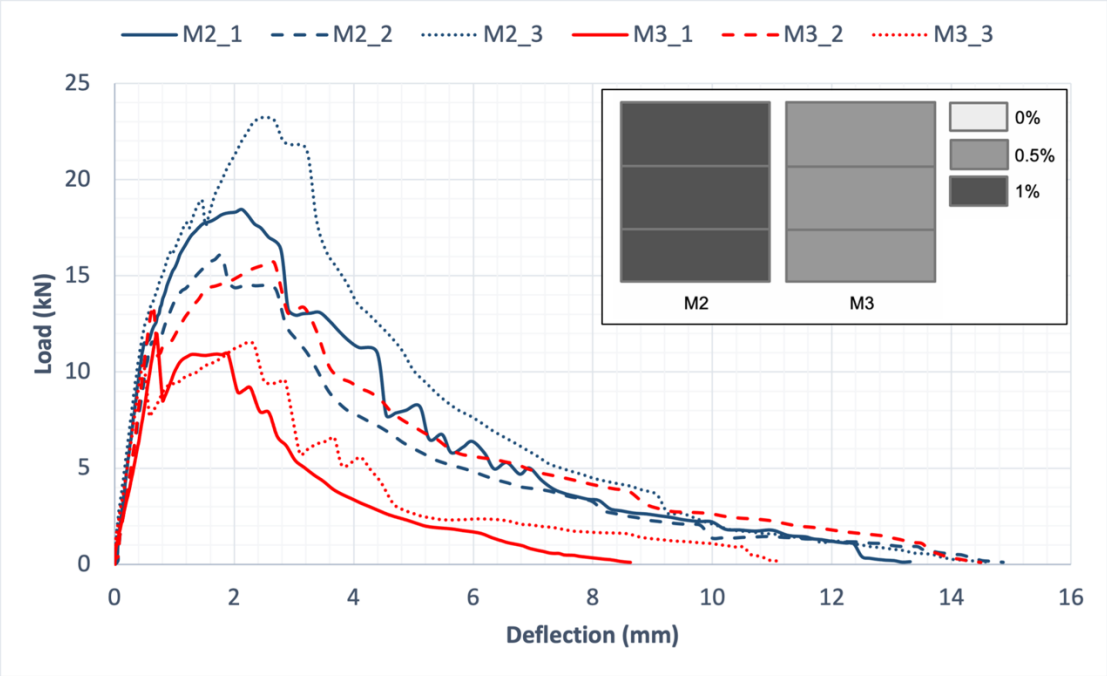

Figure 6.31: Load-deflection Curve for M2 and M3 Specimens

Consistent with the findings on residual strengths, increasing the fiber content uniformly from 0.5 % to 1 % in all layers resulted in a substantial improvement in the flexural toughness properties (T_{300}, T_{150}, and T_{75}). The load-deflection curves further support this, with the M2 specimens showing a larger area under the curve compared to M3 (Figure 6.31). This expanded area suggests a greater capacity for energy absorption and a higher resistance to crack propagation in the specimens with higher fiber content. This enhancement points to a direct correlation between the amount of fiber content and the flexural toughness of the FG-FRC specimens.

The equivalent flexural strength ratios ($R_{T,300}$, $R_{T,150}$, and $R_{T,75}$) for both M2 and M3, as depicted in Figure 6.32, were markedly higher in M2 specimens. This indicates that a uniform increase in fiber content from 0.5 % to 1 % across all layers of FRC significantly enhances these ratios by 27 %, 47 %, and 53 %, respectively. This improvement in the equivalent flexural strength ratios demonstrates that a higher and consistent fiber dosage across the FRC section not only

maintains a greater proportion of the material's strength post-cracking but also implies improved ductility and toughness of the FRC.

In summary, the study clearly illustrates that a homogenous increase in fiber dosage within FRC sections significantly enhances both the residual strengths and flexural toughness properties. The consistent and higher fiber content across all layers contributes to an overall improvement in the structural integrity and performance of FRC, particularly under conditions of high stress and deflection.

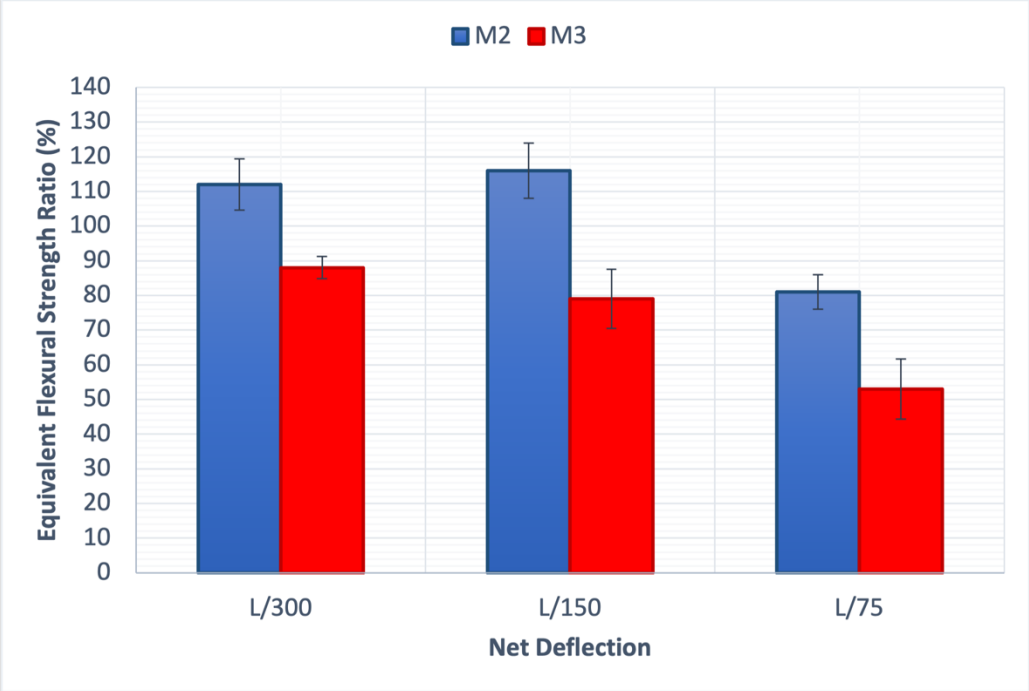

Figure 6.32: Equivalent Flexural Strength Ratio Comparison for M2 and M3 Specimens

6.3.3. Fracture Properties

In the examination of fracture properties of FG-FRC specimens, this study applied the TPFM to determine critical parameters such as initial and peak loads (P_1, P_P), critical stress intensity factor (K_{IC}), crack tip opening displacement ($CTOD_C$), and strain energy release rate

(G_{IC}). The findings from these measurements are detailed in Table 6.7, while the results pertaining to total fracture energy (G_F) and the CMOD at failure ($CMOD_f$) are presented in Table 6.8.

A key aspect of the study was to assess the impact of varying fiber dosages in different layers of the FG-FRC specimens. To achieve this, a comparative analysis was conducted across various FG-FRC mixtures. This analysis employed a one-tailed two-sample t-test with a 95 % confidence interval, providing a statistically robust method to understand the influence of fiber content on fracture properties. An important consideration in this comparison was the presence of a notch in the specimens, equating to one-third of their depth and corresponding to the depth of the first layer. Due to this feature, the first layer was excluded from the comparative analysis. This approach ensured that the focus remained on the layers of the specimens where the fiber dosage variation could have a more pronounced effect on the fracture properties.

Table 6.7: Fracture Properties of FG-FRC Specimens

Sample	$\boldsymbol{P_1}$ $(\boldsymbol{N})$	$\boldsymbol{P_P}$ $(\boldsymbol{N})$	$\boldsymbol{K_{IC}}$ $\left(\boldsymbol{MPa\sqrt{m}}\right)$	$\boldsymbol{CTOD_C}$ $(\boldsymbol{mm})$	$\boldsymbol{G_{IC}}$ $(\boldsymbol{N/m})$
M1_1	3506	3506	0.782	0.0103	79.6
M1_2	4084	4084	1.338	0.0499	108.4
M1_3	3209	3692	1.225	0.0457	81.7
Mean	3600	3761	1.115	0.0353	89.9
M2_1	2954	4427	1.069	0.0279	57.2
M2_2	3983	4788	1.074	0.0372	103.9
M2_3	3121	5060	1.011	0.0240	49.2
Mean	3353	4758	1.051	0.0297	70.1
M3_1	2351	2950	0.781	0.0155	55.0
M3_2	3204	3247	1.051	0.0346	67.9
M3_3	2563	2962	0.927	0.0289	46.7
Mean	2706	3053	0.920	0.0263	56.5
M4_1	2705	3212	1.007	0.0386	67.6
M4_2	4279	4279	1.918	0.0751	186.0
M4_3	4386	4909	1.423	0.0394	108.6
Mean	3790	4133	1.449	0.0510	120.7
M5_1	3121	3643	0.91	0.0161	37.0
M5_2	3727	4367	1.167	0.0251	60.6
M5_3	2858	2858	1.073	0.0303	54.1
Mean	3235	3623	1.050	0.0238	50.6

Table 6.8: Total Fracture Energy Results of FG-FRC Specimens

Sample	$\boldsymbol{CMOD_f}$ $(\boldsymbol{mm})$	$\boldsymbol{G_F}$ $(\boldsymbol{N/m})$
M1_1	19	3060
M1_2	19	2742
M1_3	12	2053
Mean	17	2618
M2_1	23	4805
M2_2	24	5160
M2_3	24	5594
Mean	24	5186
M3_1	26	5469
M3_2	21	2973
M3_3	25	3535
Mean	24	3992
M4_1	24	5255
M4_2	18	3426
M4_3	15	4039
Mean	19	4240
M5_1	12	1875
M5_2	16	3069
M5_3	24	3249
Mean	17	2731

The analysis of the effect of fiber dosage in the bottom layer of FG-FRC specimens involved a comparison between M1 specimens (with 0.5 % fiber content) and M4 specimens (with 1 % fiber content). The statistical analysis showed that the mean peak load (P_1) was not significantly different between M1 and M4 specimens. This finding suggests that increasing steel fiber content from 0.5 % to 1 % in the bottom layer does not lead to an improvement in peak load capacity, which aligns with the results of other studies [85], indicating a limited effect of increased fiber dosage on peak load in this specific layer. Furthermore, the means of K_{IC}, $CTOD_C$, and G_{IC} were also found to be statistically similar between M1 and M4. This indicates that increasing the fiber dosage from 0.5 % to 1 % does not significantly impact these specific fracture properties.

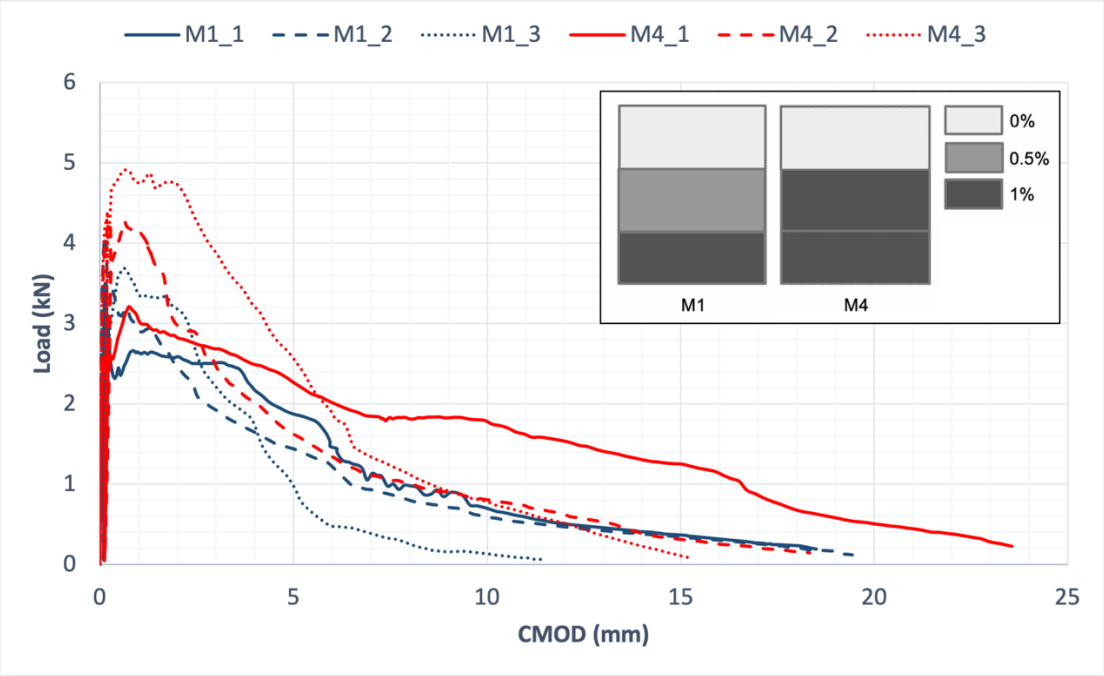

Figure 6.33: Load-CMOD Curve for M1 and M4 Specimens

A closer examination of the load-CMOD curves, shown in Figure 6.33, revealed notable differences in the behavior of the specimens. M4 specimens, with a higher fiber dosage, generally exhibited a hardening behavior, except for one specimen (M4_2). In contrast, most M1 specimens, with lower fiber dosage, displayed softening behavior, except for M1_3 specimen. This observation suggests that increasing fiber content in the bottom layer enhances the fracture energy absorption of the FRC, primarily through a crack bridging mechanism. The comparison of total fracture energy (G_F) between M1 and M4, as shown in Figure 6.34, reinforces this conclusion. The results indicated a 38 % increase in total fracture energy when the fiber content in the bottom layer was increased from 0.5 % to 1 %. This increase in fracture energy can be attributed to improved ductility due to higher fiber content, which enhances the material's ability to absorb and dissipate energy during fracture.

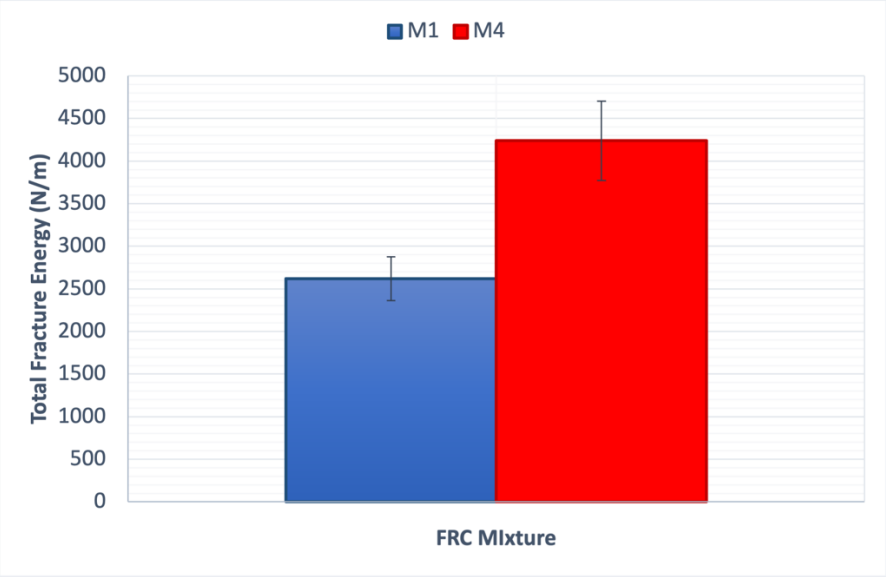

Figure 6.34: Total Fracture Energy Comparison for M1 and M4 Specimens

The study explored the effect of fiber dosage in the top layer of FG-FRC specimens. Two comparison was made in this layer with two fiber dosages (0.5 % and 1 %). This was assessed by comparing M2 specimens (with 1 % fiber dosage) to M4 (with no fibers) and M3 specimens (with 0.5 % fiber dosage) to M5 (with no fibers). The findings from these comparisons provide insights into how fiber content in the top layer influences the fracture properties of FRC.

Considering the M2 to M4 comparison, the analysis of load-CMOD curves, as shown in Figure 6.35, indicates that increasing steel fiber content in the top layer to 1 % does not lead to a significant improvement in the peak load (P_1) for M2 compared to M4, which aligns with the results of previous studies [85,89]. Additionally, the means of K_{IC}, $CTOD_C$, and G_{IC} were statistically similar between M2 and M4, suggesting that a 1 % increase in fiber content does not significantly enhance these fracture properties. This aligns with the results of previous research [85].

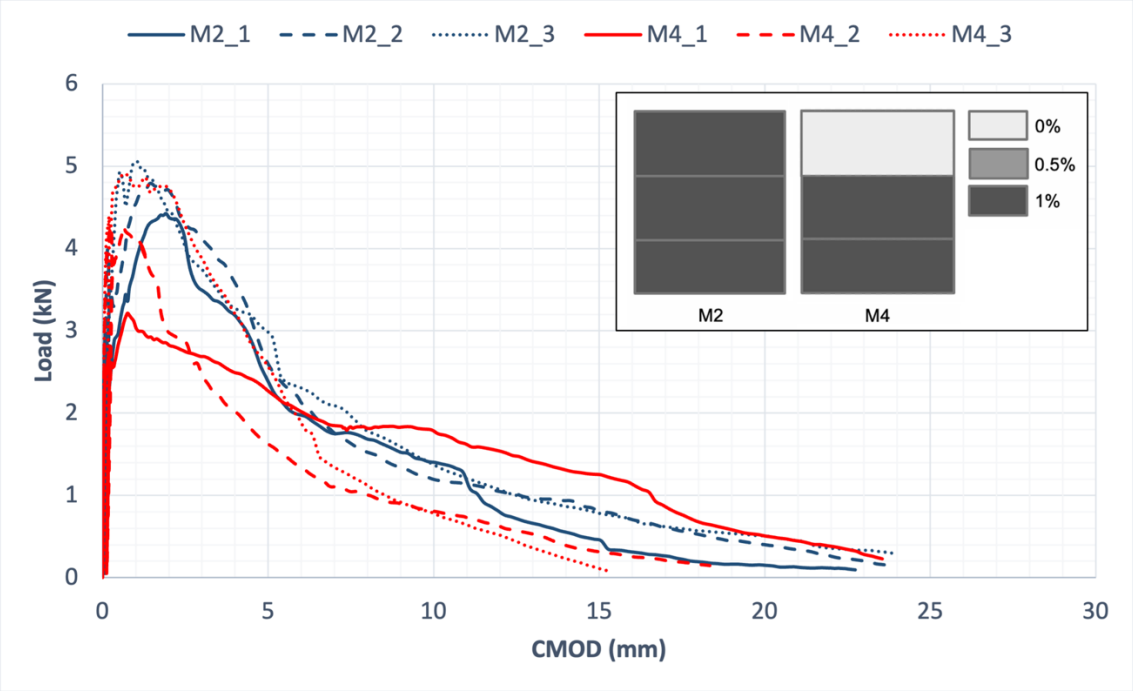

Figure 6.35: Load-CMOD Curve for M2 and M4 Specimens

However, a notable difference was observed in the behavior of the specimens (Figure 6.35). All M2 specimens exhibited a hardening behavior, whereas M4 included a specimen (M4_2) that showed softening behavior. This suggests that adding fibers in the top layer contributes to a more consistent hardening behavior in FRC. Furthermore, the CMOD values at failure were significantly higher for M2, indicating effective crack bridging by the fibers. The comparison of total fracture energy (G_F) between M2 and M4, as shown in Figure 6.36, reveals a 22 % increase in G_F for the M2 specimens. This improvement is attributed to the added fibers in the top layer, enhancing the material's ability to absorb and dissipate energy during fracture.

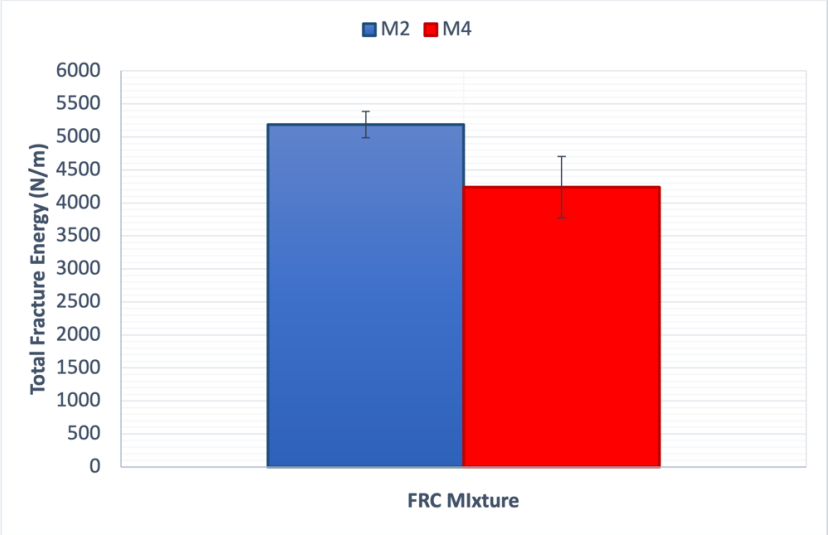

Figure 6.36: Total Fracture Energy Comparison for M2 and M4 Specimens

Considering the M3 to M5 comparison, the analysis of load-CMOD curves, as shown in Figure 6.37. Similar to the 1 % fiber content scenario, the increase in fiber content to 0.5 % in the top layer did not significantly affect the P_1, K_{IC}, $CTOD_C$, and G_{IC}. However, M3 specimens reached higher CMOD values at failure than M5, demonstrating the fibers' role in crack bridging and maintaining higher deformation capacity.

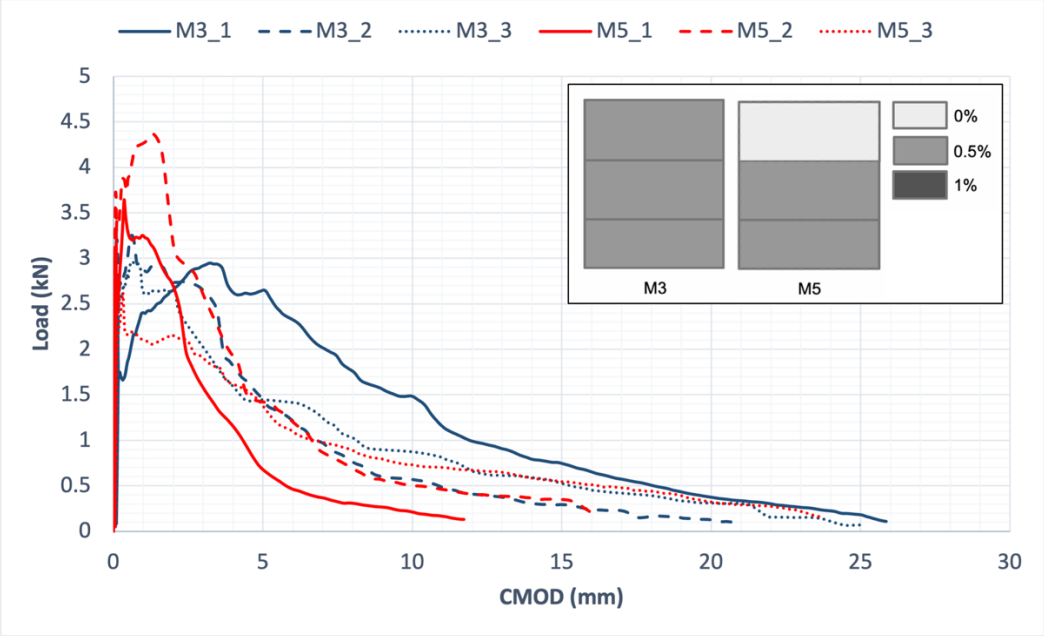

Figure 6.37: Load-CMOD Curve for M3 and M5 Specimens

When it comes to the post-peak behavior, all M3 specimens exhibited a hardening behavior, in contrast to one softening behavior observed in M5 (M5_3). This indicates that even a 0.5 % fiber content in the top layer promotes hardening behavior in FRC. The total fracture energy comparison, as presented in Figure 6.38, shows a 46 % increase in G_F for M3 specimens over M5. This significant enhancement in fracture energy with 0.5 % fiber content highlights the effectiveness of fibers in increasing the energy absorption capacity of FRC.

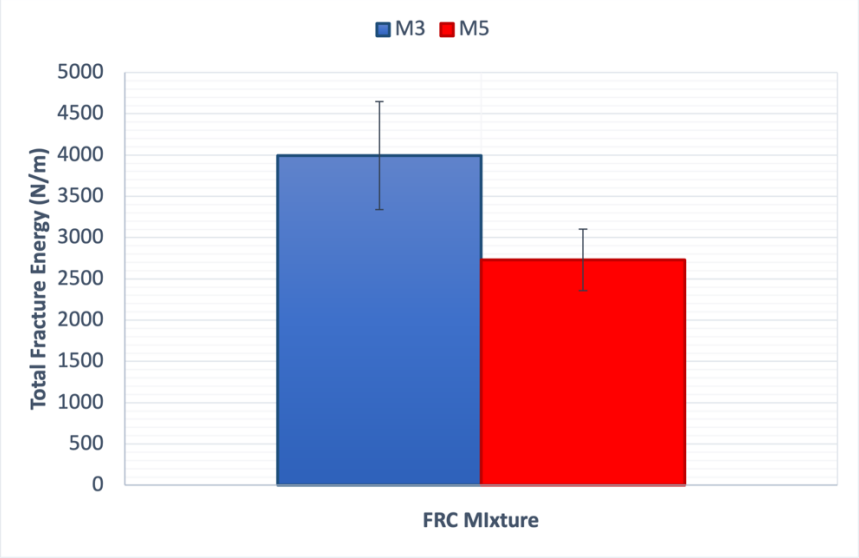

Figure 6.38: Total Fracture Energy Comparison for M3 and M5 Specimens

To study the effect of a homogenous 0.5 % and 1 % fiber dosage FG-FRC sections, M2 specimens (with a uniform 1 % fiber content across all layers) was compared to M3 specimens (with a uniform 0.5 % fiber content across all layers). The load-CMOD curves for both M2 and M3 specimens are shown in Figure 6.39. A significant difference was observed between M2 and M3 specimens in terms of mean P_1 and K_{IC}, which aligns with the results of previous research [90]. The results indicate that increasing the steel fiber content uniformly from 0.5 % to 1 % across the FRC layers leads to improvements in both the peak load capacity and resistance to crack initiation. However, no significant differences were found between M2 and M3 in the means of

$CTOD_C$ and G_{IC}. This suggests that while higher fiber content improves peak load and crack initiation resistance, it does not markedly impact the behavior of FRC specimens in terms of $CTOD_C$ and G_{IC}.

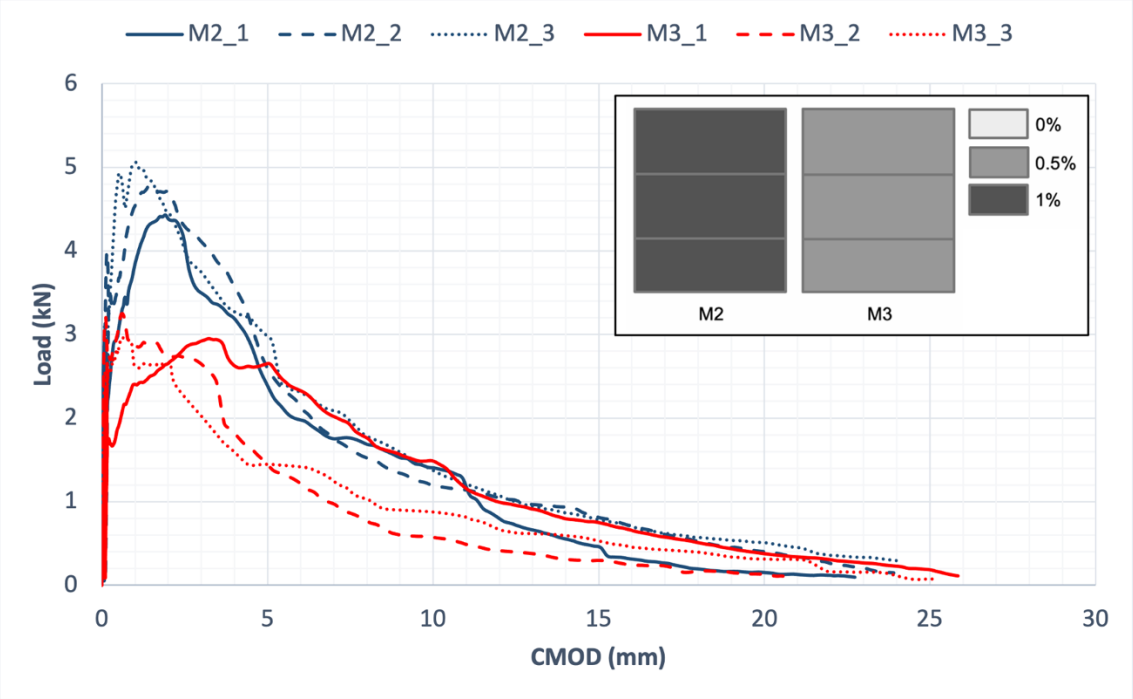

Figure 6.39: Load-CMOD Curve for M2 and M3 Specimens

A closer examination of the load-CMOD curves, particularly the areas beneath these curves (Figure 6.39), revealed that M2 specimens exhibited a broader coverage compared to M3. Despite both sets of specimens showing hardening behavior, the larger area under the curves for M2 implies greater fracture energy absorption. This can be attributed to the increased fiber content enhancing the material's ability to absorb and dissipate energy during fracture through a more effective crack bridging mechanism. The comparison of total fracture energy between M2 and M3, as shown in Figure 6.40, underscores this observation. There was a 30 % improvement in total fracture energy (G_F) when increasing the fiber content from 0.5 % to 1 % in the FRC. This

significant increase in G_F with higher fiber content underlines the effectiveness of fibers in boosting the energy absorption and ductility of FRC.

In conclusion, the study demonstrates that a uniform increase in fiber dosage within FRC significantly enhances key structural properties such as peak load, resistance to crack initiation, and total fracture energy. The findings indicate that higher and consistent fiber content across all layers of FRC contributes to an overall improvement in the fracture behavior, reinforcing the material's capacity to withstand higher stress and deformation.

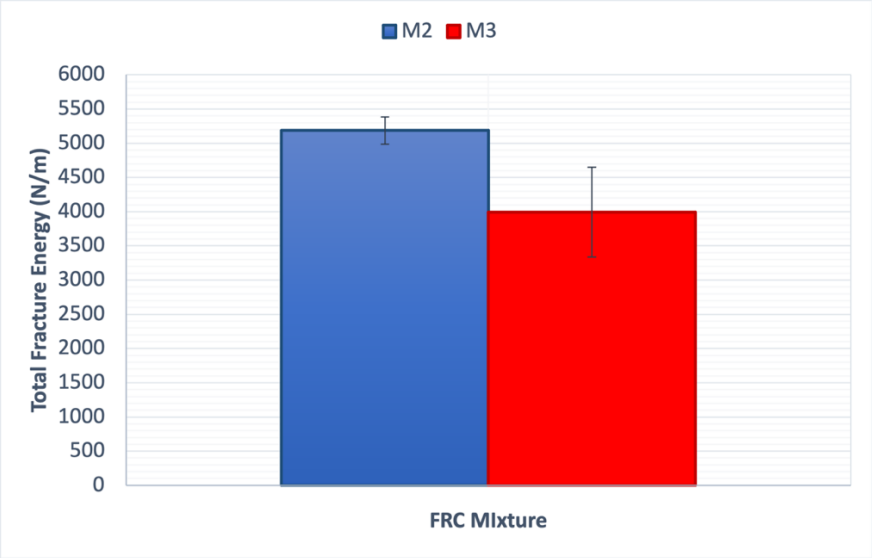

Figure 6.40: Total Fracture Energy Comparison for M2 and M3 Specimens

6.3.4. Crack Propagation and Strain Localization

In the field of FG-FRC, understanding the dynamics of crack propagation and strain localization is crucial for enhancing the performance of FRC structures. The behavior of cracks and strain under stress not only influences the structural integrity of FRC but also provides insights into optimizing fiber dosage, distribution, and alignment for improved performance. The process of crack propagation in FRC is significantly influenced by how the fibers are integrated within the concrete matrix. Proper alignment of fibers, especially parallel to the direction of tensile stresses,

and their proximity to the crack initiation sites are vital. In cases where fibers are well-aligned or optimally positioned near potential crack initiation spots, they effectively bridge and deflect the cracks, thereby impeding their further propagation. In addition to crack propagation, strain localization is a significant concern, particularly in beams cast using extrusion-based methods. The layering technique inherent in this method could potentially introduce weak points at the interfaces between layers, which might become preferential paths for crack propagation. Understanding and mitigating this strain localization is essential for ensuring the structural efficacy and longevity of FG-FRC components.

The use of DIC as a primary investigative tool in this study provides a detailed and precise analysis of both crack propagation and strain localization phenomena in FG-FRC beams. Through this analysis, the study aimed to contribute to the development of more robust, durable, and reliable FRC structures, capable of withstanding various stress conditions while minimizing the risk of failure.

The crack propagation process was investigated. During the flexural testing of FG-FRC beams, two critical stages were closely examined to understand crack propagation: the initial stage (1^{st} stage) at peak load, and a later stage (4^{th} stage) where the crack has fully developed and reached the top of the beam. Figure 6.41 illustrates the critical crack lengths for FG-FRC specimens at the initial stage of testing.

It was observed that all FG-FRC specimens developed multiple cracks initiating from the beam's bottom, which can influence its flexural performance [91]. In bending scenarios, the bottom of the beam undergoes tension, making it a common site for crack initiation. The multiplicity of cracks points to the fibers' role in redistributing stress more evenly across the beam, reducing the possibility of catastrophic failure [92]. The presence of multiple cracks also suggests that the fibers

within these specimens were well-distributed and aligned, which is evidence to the efficiency of the targeted fiber injection process used in casting the FG-FRC beams.

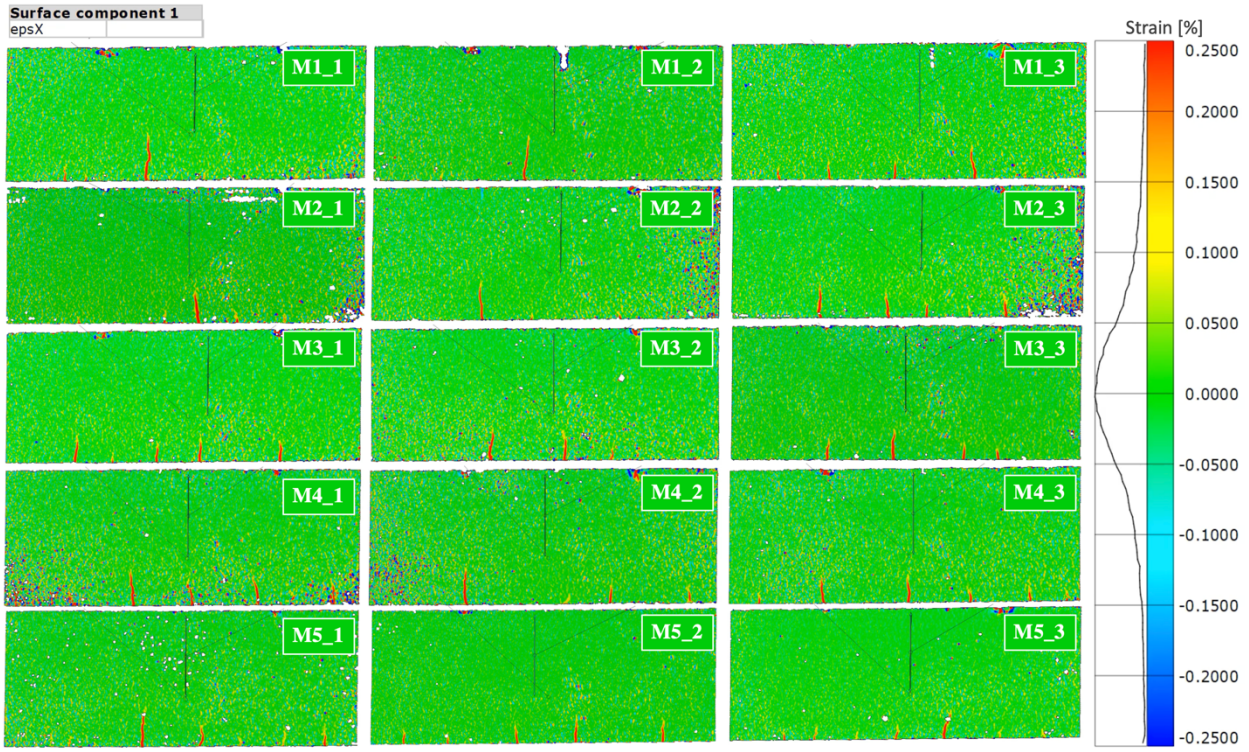

Figure 6.41: Full Strain Field (x-axis) at the 1st Stage FG-FRC Specimens (the contour legend indicates the concentration of each strain level)

The detailed examination of crack propagation in FG-FRC specimens provides significant insights into how cracks evolve and affect the overall performance. Figure 6.42 showcases the crack propagation during the 4th stage of testing for FG-FRC specimens. A key observation is that although all specimens began with multiple cracks at the bottom of the beam, not all these cracks continued to propagate through the entire depth of the beam. This variance in crack propagation patterns across different specimens is crucial for understanding the relationship between crack behavior and the flexural toughness of FRC.

By correlating these observations with the flexural toughness data presented in Table 6.6, a clear pattern emerges that specimens exhibiting multiple cracks that continued to propagate throughout the beam displayed higher levels of flexural toughness. For instance, the M1_1

specimen, with four cracks that propagated, showed the highest toughness among the M1 series. Similarly, the M2_3 specimen, with fully propagated cracks, had the highest toughness in the M2 series. This trend underscores the critical role of crack behavior in determining the flexural resilience of FRC specimens.

The presence of deflected cracks, which can prevent the development of a crack and potentially initiate new ones, highlights the influence of fiber distribution within the FG-FRC specimens. Fibers, by bridging and deflecting cracks, contribute to a more complex crack network. As cracks are deflected or bridges due to the presence and orientation of fibers, the surface area of the cracks increases, leading to greater energy absorption. These phenomenon directly contributes to the enhanced toughness of the material [93,94]. They demonstrate how the strategic distribution and alignment of fibers within concrete can significantly improve its capacity to withstand stress and mitigate the propagation of cracks, thereby enhancing the overall durability and reliability of FRC structures.

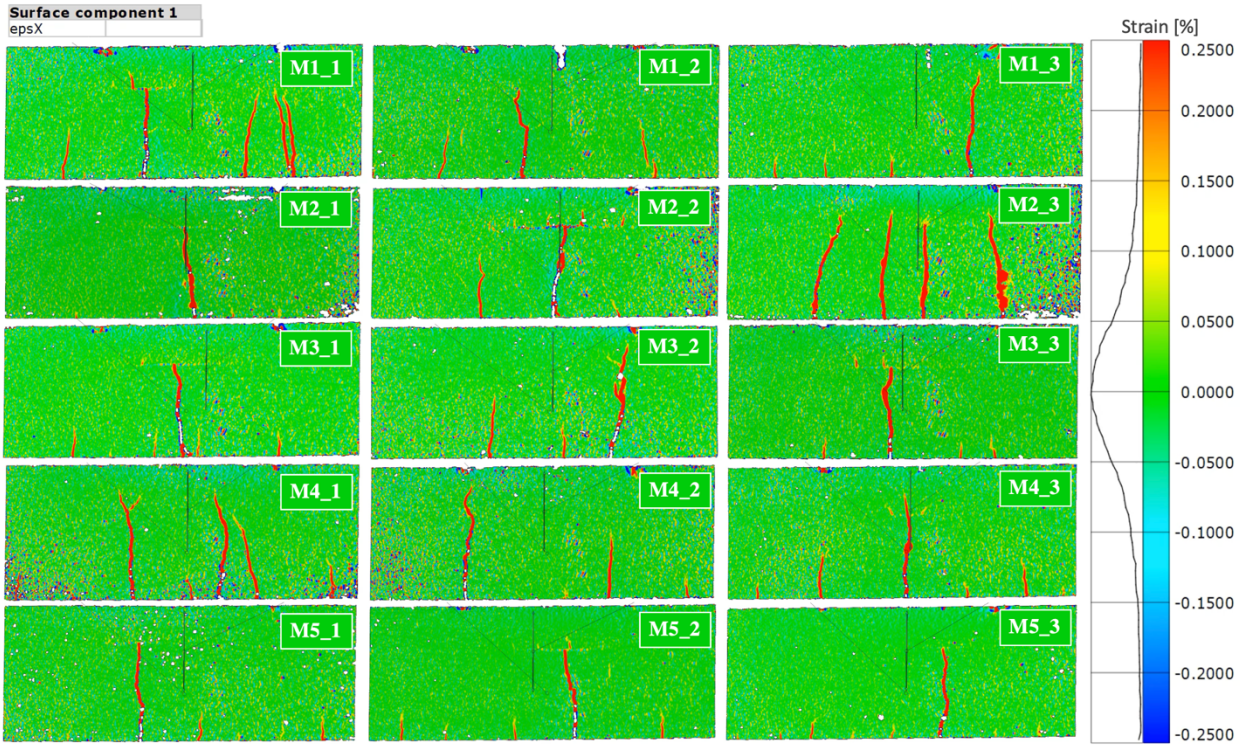

Figure 6.42: Full Strain Field (x-axis) at the 4th Stage for FG-FRC Specimens (the contour legend indicates the concentration of each strain level)

The investigation into strain localization, particularly at the interfaces between layers in FG-FRC specimens, offers crucial insights into the structural behavior of these materials. The analysis focused on two crucial stages of the testing process: the initial stage (1st stage) and a later stage where significant crack propagation occurs (4th stage). Notably, during the 1st stage, no pronounced localized strains were detected at the layer interfaces in any of the FG-FRC specimens, as shown in Figure 6.43. This observation suggests that at the onset of loading, the layer interfaces were sufficiently bonded to distribute the stresses uniformly.

However, the scenario was changed during the 4th stage of testing. Figure 6.44 reveals the emergence of localized strains, extending horizontally along the interfaces between layers in all FG-FRC specimens. This development points to potential issues in material consistency and

bonding strength at the interfaces in FG-FRC specimens. Inadequate interlayer bonding could hinder effective load transfer, potentially leading to delamination and increased strain at the interfaces [61].

An interesting observation was made in the case of the M2_3 specimen. Despite the presence of localized strains, these did not extend horizontally along the layer interfaces. The unique aspect of the M2_3 specimen was its higher number of initiated cracks that propagated through to the top layer, coupled with its superior flexural toughness compared to other specimens. This suggests a correlation between the initiation and propagation of multiple cracks from the beam's bottom and the redistribution of strain within the beam, thereby minimizing strain concentration at the layer interfaces.

The presence of multiple cracks initiating from the bottom appears to play a significant role in mitigating strain localization at the layer interfaces. This observation underscores the importance of crack distribution and propagation patterns in influencing the structural integrity and performance of FRC. However, this phenomenon necessitates further investigation to fully understand its implications on the material behavior and to explore potential strategies for enhancing interlayer bonding and overall material performance in extrusion-based FG-FRC.

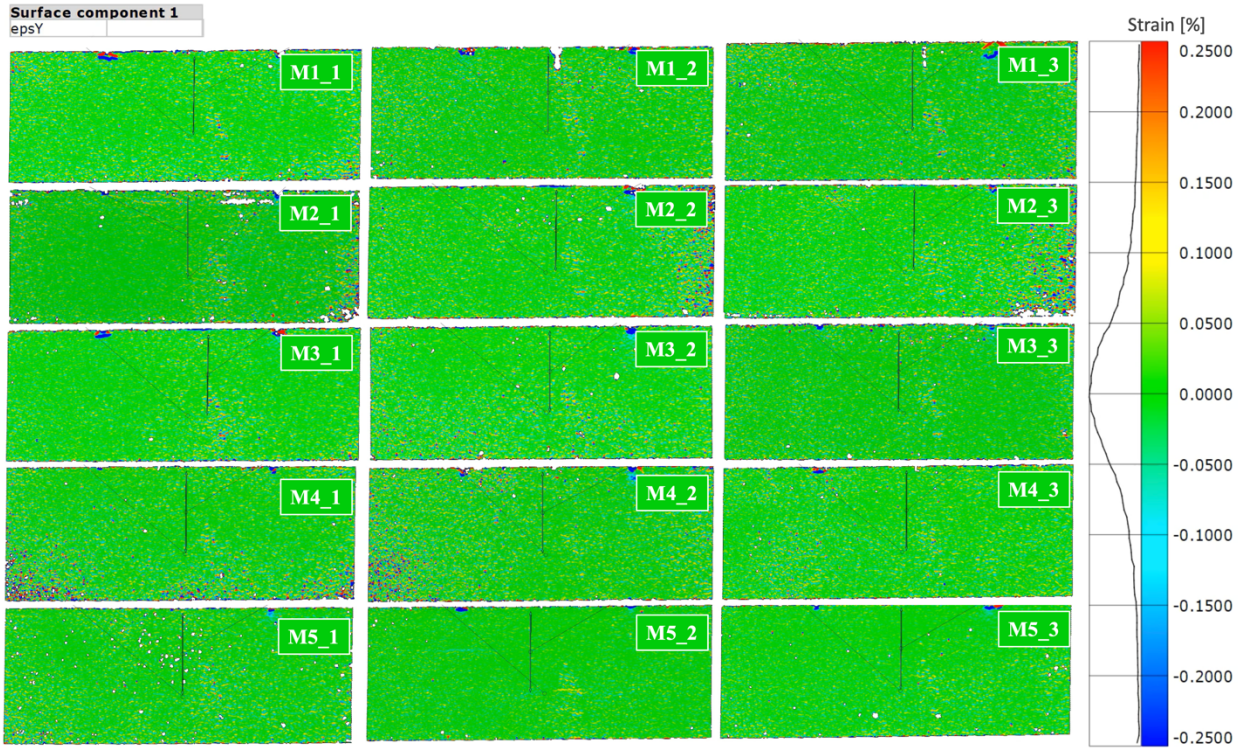

Figure 6.43: Full Strain Field (y-axis) at the 1st Stage for FG-FRC Specimens (the contour legend indicates the concentration of each strain level)

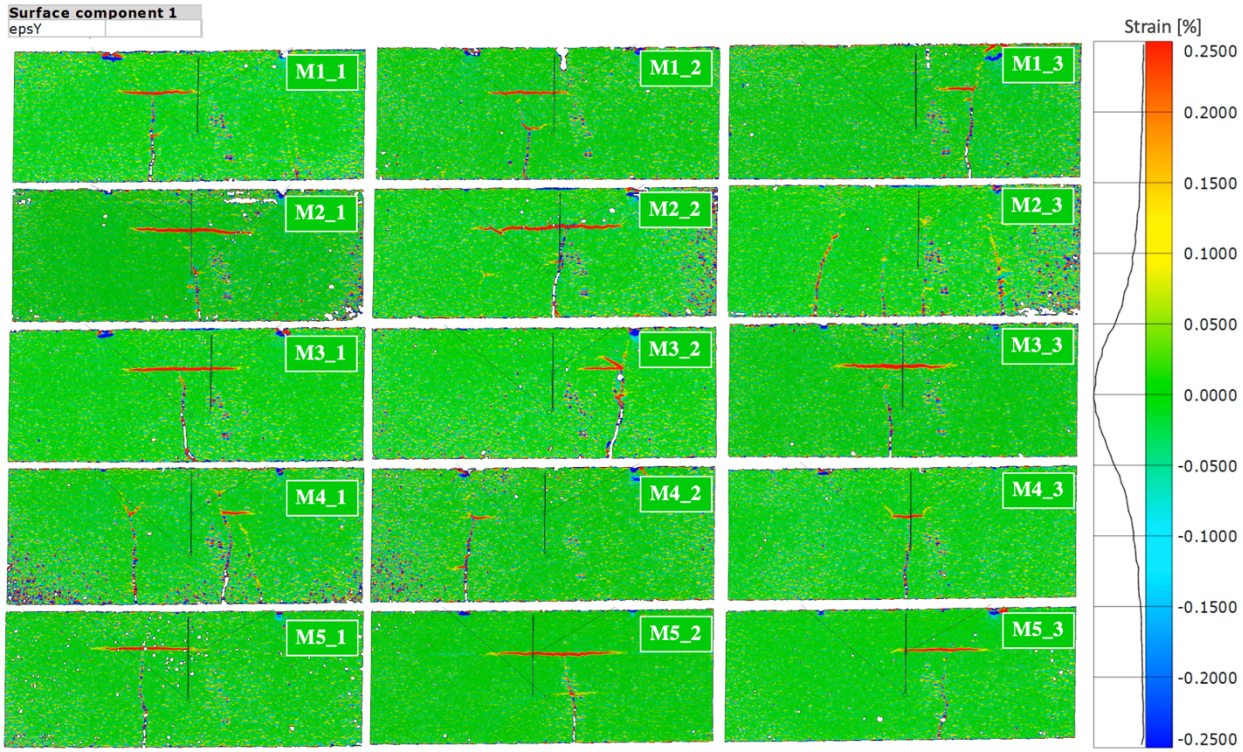

Figure 6.44: Full Strain Field (y-axis) at the 4th Stage for FG-FRC (the contour legend indicates the concentration of each strain level)

6.4. Conclusion

This comprehensive study on the flexural and fracture properties of FG-FRC with targeted fiber injection marks a significant advancement in the understanding of extruded FRC behavior and performance. The research successfully demonstrated that strategic fiber distribution plays a crucial role in enhancing the structural integrity and resilience of FG-FRC.

The use of XCT proved instrumental in verifying the hypotheses regarding fiber alignment and dosage within the concrete matrix. Through XCT, the study was able to visualize and quantify the orientation and distribution of fibers, which are critical factors in determining the mechanical properties of FG-FRC. The MATLAB-based image processing algorithm further enhanced this analysis by enabling precise segmentation and orientation measurement of individual fibers. This comprehensive approach, combining advanced XCT techniques with sophisticated image analysis, has conclusively demonstrated that the unique casting method employed in this study resulted in the desired alignment and distribution of fibers. The successful determination of fiber dosage and orientation is an evidence to the potential of XCT in advancing material science and engineering, offering new approaches for optimizing the design and performance of fiber-reinforced composites.

The investigation into the flexural properties of FG-FRC revealed that varying fiber dosages across different layers significantly impact the material's toughness and strength. Higher fiber dosages, particularly in layers experiencing tensile stresses and uniformly across the section, significantly enhanced both the residual strengths and flexural toughness of FRC, contributing to improved material ductility and energy absorption capabilities. This outcome underscores the importance of fiber placement in relation to the stress distribution within the concrete.

Regarding fracture properties, the application of the TPFM provided insightful observations on the influence of fiber content on critical stress intensity factor, crack tip opening displacement, and strain energy release rate. The study illustrated that while increasing fiber content in different layers of FRC does not always significantly improve peak load or fracture properties, it substantially enhances the material's fracture energy absorption. This is particularly evident in specimens with higher fiber content, which exhibit better crack bridging capabilities, leading to improved ductility and energy absorption, especially in sections experiencing tensile stresses.

The crack propagation and strain localization analysis, facilitated by DIC, offered vital insights into the dynamics of FG-FRC under stress. The findings indicated that well-distributed and aligned fibers contribute to a complex network of cracks that absorb more energy, thereby enhancing the material's toughness. Furthermore, the presence of localized strains at the layer interfaces during later stages of testing pointed to potential areas for improvement in material consistency and bonding strength.

6.4.1. Limitation and Future Work

This study, while revealing the benefits of the pump extrusion method combined with fiber injection for enhancing FRC, also uncovers areas that necessitate further exploration and optimization. One of the primary limitations encountered was the constraint imposed by the extrusion pump, which required mixtures without coarse aggregate. This necessity led to a focus on mortar-based experiments. Despite this, the insights derived are still highly relevant to FRC's mechanical properties, particularly under the current industry limitations in 3D printing materials that often rely on mortar. It not only points to a broader application in the construction industry

but also underscores the need for future research to integrate and assess the impact of coarse aggregate on fiber orientation and overall concrete performance.

Another significant area highlighted by this study is the need for a more extensive exploration of diverse fiber types and dosages. The research, in its current scope, was limited to certain fiber types and proportions, suggesting a potential avenue for future investigations to expand upon. Delving into a wider range of fibers and their respective proportions will provide a more comprehensive understanding of their effects on the structural and mechanical properties of FRC.

In summary, this study serves as a foundational step in demonstrating the positive impact of fiber reinforcement in FG-FRC, while also paving the way for future research. The potential advancements in optimizing fiber dosage, distribution, and alignment offer exciting prospects for the development of more robust, efficient, and durable construction materials. Further development of this research trajectory is essential for pushing the boundaries of current construction material technologies and for realizing the full potential of FG-FRC in modern construction practices.

6.5. Authorship Contribution Statement

The authors confirm their contributions to the paper as follows: Rashed Alarrak: Writing – review & editing, Writing – original draft, Visualization, Validation, Methodology, Investigation, Formal analysis, Data curation, Conceptualization. Alexander S. Brand: Writing – review & editing, Supervision, Methodology, Conceptualization.

6.6. References

[1] N. San Ha, S.S. Marundrury, T.M. Pham, E. Pournasiri, F. Shi, H. Hao, Effect of grounded blast furnace slag and rice husk ash on performance of ultra-high-performance concrete (UHPC) subjected to impact loading, Constr. Build. Mater. 329 (2022) 127213. https://doi.org/10.1016/j.conbuildmat.2022.127213.

[2] J. Liu, C. Wu, J. Li, Z. Liu, S. Xu, K. Liu, Y. Su, J. Fang, G. Chen, Projectile impact resistance of fibre-reinforced geopolymer-based ultra-high performance concrete (G-UHPC), Constr. Build. Mater. 290 (2021) 123189. https://doi.org/10.1016/j.conbuildmat.2021.123189.

[3] K. Habel, M. Viviani, E. Denarié, E. Brühwiler, Development of the mechanical properties of an Ultra-High Performance Fiber Reinforced Concrete (UHPFRC), Cem. Concr. Res. 36 (2006) 1362–1370. https://doi.org/10.1016/j.cemconres.2006.03.009.

[4] A. Tafraoui, G. Escadeillas, T. Vidal, Durability of the Ultra High Performances Concrete containing metakaolin, Constr. Build. Mater. 112 (2016) 980–987. https://doi.org/10.1016/j.conbuildmat.2016.02.169.

[5] D. Lai, C. Demartino, Y. Xiao, High-strain rate compressive behavior of Fiber-Reinforced Rubberized Concrete, Constr. Build. Mater. 319 (2022) 125739. https://doi.org/10.1016/j.conbuildmat.2021.125739.

[6] X. Liu, M. Yan, I. Galobardes, K. Sikora, Assessing the potential of functionally graded concrete using fibre reinforced and recycled aggregate concrete, Constr. Build. Mater. 171 (2018) 793–801. https://doi.org/10.1016/j.conbuildmat.2018.03.202.

[7] A. Cascardi, F. Longo, F. Micelli, M.A. Aiello, Compressive strength of confined column with Fiber Reinforced Mortar (FRM): New design-oriented-models, Constr. Build. Mater. 156 (2017) 387–401. https://doi.org/10.1016/j.conbuildmat.2017.09.004.

[8] B. Shen, M. Hubler, G.H. Paulino, L.J. Struble, Functionally-graded fiber-reinforced cement composite: Processing, microstructure, and properties, Cem. Concr. Compos. 30 (2008) 663–673. https://doi.org/10.1016/j.cemconcomp.2008.02.002.

[9] V.M. Luan, B.P. Trinh, D.Q. Viet, H.T. Phuoc, Effect of the height of reinforced concrete layer on the mechanical properties of functionally graded concrete incorporating fly ash and polypropylene fiber, J. Sci. Technol. Civ. Eng. STCE - NUCE 15 (2021) 30–43. https://doi.org/10.31814/stce.nuce2021-15(3)-03.

[10] M. Mastali, M. Ghasemi Naghibdehi, M. Naghipour, S.M. Rabiee, Experimental assessment of functionally graded reinforced concrete (FGRC) slabs under drop weight and projectile impacts, Constr. Build. Mater. 95 (2015) 296–311. https://doi.org/10.1016/j.conbuildmat.2015.07.153.

[11] K. Park, G.H. Paulino, J. Roesler, Cohesive fracture model for functionally graded fiber reinforced concrete, Cem. Concr. Res. 40 (2010) 956–965. https://doi.org/10.1016/j.cemconres.2010.02.004.

[12] Z. Jiang, S. Jin, W. Xu, Durability Investigation of Fiber-Reinforced Functionally Graded Concretes in Cold Regions, Appl. Sci. 12 (2022) 6651. https://doi.org/10.3390/app12136651.

[13] Sabireen, F. Butt, A. Ahmad, K. Ullah, O. Zaid, H. Ahmed Shah, T. Kamal, Mechanical performance of fiber-reinforced concrete and functionally graded concrete with natural and recycled aggregates, Ain Shams Eng. J. 14 (2023) 102121. https://doi.org/10.1016/j.asej.2023.102121.

[14] M. Nematzadeh, S. Fallah-Valukolaee, Experimental and analytical investigation on structural behavior of two-layer fiber-reinforced concrete beams reinforced with steel and GFRP rebars, Constr. Build. Mater. 273 (2021) 121933. https://doi.org/10.1016/j.conbuildmat.2020.121933.

[15] C. Zhao, Z. Wang, Z. Zhu, Q. Guo, X. Wu, R. Zhao, Research on different types of fiber reinforced concrete in recent years: An overview, Constr. Build. Mater. 365 (2023) 130075. https://doi.org/10.1016/j.conbuildmat.2022.130075.

[16] W. Meng, K.H. Khayat, Mechanical properties of ultra-high-performance concrete enhanced with graphite nanoplatelets and carbon nanofibers, Compos. Part B Eng. 107 (2016) 113–122. https://doi.org/10.1016/j.compositesb.2016.09.069.

[17] L. Tzounis, S. Debnath, S. Rooj, D. Fischer, E. Mäder, A. Das, M. Stamm, G. Heinrich, High performance natural rubber composites with a hierarchical reinforcement structure of carbon nanotube modified natural fibers, Mater. Des. 58 (2014) 1–11. https://doi.org/10.1016/j.matdes.2014.01.071.

[18] R. Mu, Y. Xue, L. Qing, H. Li, Y. Zhao, J. Zhou, J. Su, Preparation and mechanical performance of annularly aligned steel fiber reinforced cement-based composite pipes, Constr. Build. Mater. 211 (2019) 167–173. https://doi.org/10.1016/j.conbuildmat.2019.03.146.

[19] R. Mu, H. Li, L. Qing, J. Lin, Q. Zhao, Aligning steel fibers in cement mortar using electro-magnetic field, Constr. Build. Mater. 131 (2017) 309–316. https://doi.org/10.1016/j.conbuildmat.2016.11.081.

[20] G.W. Melenka, J.P. Carey, Evaluation of fiber reinforced cement using digital image correlation, PLOS ONE 10 (2015) e0128644. https://doi.org/10.1371/journal.pone.0128644.

[21] R. Alarrak, B. Jeon, A.S. Brand, Flexural toughness of extruded fiber-reinforced mortar with preferentially aligned fibers, Constr. Build. Mater. 407 (2023) 133528. https://doi.org/10.1016/j.conbuildmat.2023.133528.

[22] R. Alarrak, B. Jeon, A.S. Brand, Fracture properties of extruded fiber-reinforced mortar with preferentially aligned fibers, Constr. Build. Mater. 403 (2023) 133022. https://doi.org/10.1016/j.conbuildmat.2023.133022.

[23] Z.Y. Ahmed, F.P. Bos, M.C.A.J. Van Brunschot, T.A.M. Salet, On-demand additive manufacturing of functionally graded concrete, Virtual Phys. Prototyp. 15 (2020) 194–210. https://doi.org/10.1080/17452759.2019.1709009.

[24] M.P. Iniya, K. Nirmalkumar, A review on fiber reinforced concrete using sisal fiber, IOP Conf. Ser. Mater. Sci. Eng. 1055 (2021) 012027. https://doi.org/10.1088/1757-899X/1055/1/012027.

[25] P.O. Awoyera, O.L. Odutuga, J.U. Effiong, A. De Jesus Silvera Sarmiento, S.J. Mortazavi, J.W. Hu, Development of fibre-reinforced cementitious mortar with mineral wool and coconut Fibre, Materials 15 (2022) 4520. https://doi.org/10.3390/ma15134520.

[26] C.-P. Fung, Manufacturing process optimization for wear property of fiber-reinforced polybutylene terephthalate composites with grey relational analysis, Wear 254 (2003) 298–306. https://doi.org/10.1016/S0043-1648(03)00013-9.

[27] K. Palanikumar, L. Karunamoorthy, R. Karthikeyan, Assessment of factors influencing surface roughness on the machining of glass fiber-reinforced polymer composites, Mater. Des. 27 (2006) 862–871. https://doi.org/10.1016/j.matdes.2005.03.011.

[28] R. Mu, H. Li, L. Qing, J. Lin, Q. Zhao, Aligning steel fibers in cement mortar using electro-magnetic field, Constr. Build. Mater. 131 (2017) 309–316. https://doi.org/10.1016/j.conbuildmat.2016.11.081.

[29] L. Liu, J. Xu, Y. Wang, T. Yin, H. Chu, Electrical and piezoresistive properties of steel fiber cement-based composites aligned by a magnetic field, J. Wuhan Univ. Technol.-Mater Sci Ed 37 (2022) 229–240. https://doi.org/10.1007/s11595-022-2522-2.

[30] P. Kheml, K. Carrera, K. Künzel, V. Papež, R. Sovják, Summary of findings on magnetic orientation of fibers in cement composites, Mater. Today Proc. 58 (2022) 1104–1107. https://doi.org/10.1016/j.matpr.2022.01.201.

[31] A. Abrishambaf, M. Pimentel, S. Nunes, Influence of fibre orientation on the tensile behaviour of ultra-high performance fibre reinforced cementitious composites, Cem. Concr. Res. 97 (2017) 28–40. https://doi.org/10.1016/j.cemconres.2017.03.007.

[32] H. Huang, X. Gao, L. Teng, Fiber alignment and its effect on mechanical properties of UHPC: An overview, Constr. Build. Mater. 296 (2021) 123741. https://doi.org/10.1016/j.conbuildmat.2021.123741.

[33] L. Ferrara, M. Di Prisco, M.G.L. Lamperti, Identification of the stress-crack opening behavior of HPFRCC: the role of flow-induced fiber orientation, in: Proc. Fram., 2010: pp. 1541–1550.

[34] L. Ferrara, N. Ozyurt, M. di Prisco, High mechanical performance of fibre reinforced cementitious composites: the role of “casting-flow induced” fibre orientation, Mater. Struct. 44 (2011) 109–128. https://doi.org/10.1617/s11527-010-9613-9.

[35] S.-T. Kang, J.-K. Kim, Investigation on the flexural behavior of UHPCC considering the effect of fiber orientation distribution, Constr. Build. Mater. 28 (2012) 57–65. https://doi.org/10.1016/j.conbuildmat.2011.07.003.

[36] S.-T. Kang, J.-K. Kim, Numerical simulation of the variation of fiber orientation distribution during flow molding of Ultra High Performance Cementitious Composites (UHPCC), Cem. Concr. Compos. 34 (2012) 208–217. https://doi.org/10.1016/j.cemconcomp.2011.09.015.

[37] L. Ferrara, N. Tregger, S.P. Shah, Flow-induced fiber orientation in SCSFRC: monitoring and prediction, in: Des. Prod. Place. Self-Consol. Concr., Springer, 2010: pp. 417–428.

[38] A.C. Bordelon, J.R. Roesler, Spatial distribution of synthetic fibers in concrete with X-ray computed tomography, Cem. Concr. Compos. 53 (2014) 35–43. https://doi.org/10.1016/j.cemconcomp.2014.04.007.

[39] X. Sun, J. Zhou, Q. Wang, J. Shi, H. Wang, PVA fibre reinforced high-strength cementitious composite for 3D printing: Mechanical properties and durability, Addit. Manuf. 49 (2022) 102500. https://doi.org/10.1016/j.addma.2021.102500.

[40] Y. Shao, S. Marikunte, S.P. Shah, Extruded fiber-reinforced composites, Concr. Int. 17 (1995) 48–53.

[41] Z. Li, B. Mu, T.P. Chang, C.-T. Hsu, Prediction of overall tension behavior of short fiber-reinforced composites, Int. J. Solids Struct. 36 (1999) 4071–4087.

[42] H. Takashima, K. Miyagai, T. Hashida, V.C. Li, A design approach for the mechanical properties of polypropylene discontinuous fiber reinforced cementitious composites by extrusion molding, Eng. Fract. Mech. 70 (2003) 853–870. https://doi.org/10.1016/S0013-7944(02)00154-6.

[43] X. Zhou, Z. Li, Characterizing rheology of fresh short fiber reinforced cementitious composite through capillary extrusion, J. Mater. Civ. Eng. 17 (2005) 28–35.

[44] Y. Zhang, F. Aslani, Development of fibre reinforced engineered cementitious composite using polyvinyl alcohol fibre and activated carbon powder for 3D concrete printing, Constr. Build. Mater. 303 (2021) 124453. https://doi.org/10.1016/j.conbuildmat.2021.124453.

[45] J. Ye, C. Cui, J. Yu, K. Yu, F. Dong, Effect of polyethylene fiber content on workability and mechanical-anisotropic properties of 3D printed ultra-high ductile concrete, Constr. Build. Mater. 281 (2021) 122586. https://doi.org/10.1016/j.conbuildmat.2021.122586.

[46] M. Sugavaneswaran, G. Arumaikkannu, Modelling for randomly oriented multi material additive manufacturing component and its fabrication, Mater. Des. 1980-2015 54 (2014) 779–785. https://doi.org/10.1016/j.matdes.2013.08.102.

[47] H. Stang, V.C. Li, Extrusion of ECC-material, in: Proc High Perform. Fiber Reinf. Cem. Compos., 1999: pp. 203–212.

[48] S.C. Paul, Y.W.D. Tay, B. Panda, M.J. Tan, Fresh and hardened properties of 3D printable cementitious materials for building and construction, Arch. Civ. Mech. Eng. 18 (2018) 311–319. https://doi.org/10.1016/j.acme.2017.02.008.

[49] X. Qian, X. Zhou, B. Mu, Z. Li, Fiber alignment and property direction dependency of FRC extrudate, Cem. Concr. Res. 33 (2003) 1575–1581.

[50] G. Ma, Z. Li, L. Wang, F. Wang, J. Sanjayan, Mechanical anisotropy of aligned fiber reinforced composite for extrusion-based 3D printing, Constr. Build. Mater. 202 (2019) 770–783. https://doi.org/10.1016/j.conbuildmat.2019.01.008.

[51] Z. Li, B. Mu, Innovations forum: Application of extrusion for manufacture of short fiber reinforced cementitious composite, J. Mater. Civ. Eng. 10 (1998) 2–4. https://doi.org/10.1061/(ASCE)0899-1561(1998)10:1(2).

[52] Z. Hou, X. Tian, J. Zhang, D. Li, 3D printed continuous fibre reinforced composite corrugated structure, Compos. Struct. 184 (2018) 1005–1010. https://doi.org/10.1016/j.compstruct.2017.10.080.

[53] F. Ning, W. Cong, J. Qiu, J. Wei, S. Wang, Additive manufacturing of carbon fiber reinforced thermoplastic composites using fused deposition modeling, Compos. Part B Eng. 80 (2015) 369–378. https://doi.org/10.1016/j.compositesb.2015.06.013.

[54] L.G. Blok, M.L. Longana, H. Yu, B.K.S. Woods, An investigation into 3D printing of fibre reinforced thermoplastic composites, Addit. Manuf. 22 (2018) 176–186. https://doi.org/10.1016/j.addma.2018.04.039.

[55] L. Gebhard, J. Mata-Falcón, A. Anton, B. Dillenburger, W. Kaufmann, Structural behaviour of 3D printed concrete beams with various reinforcement strategies, Eng. Struct. 240 (2021) 112380. https://doi.org/10.1016/j.engstruct.2021.112380.

[56] L. Wang, F. Aslani, Structural performance of reinforced concrete beams with 3D printed cement-based sensor embedded and self-sensing cementitious composites, Eng. Struct. 275 (2023) 115266. https://doi.org/10.1016/j.engstruct.2022.115266.

[57] Z. Hou, X. Tian, J. Zhang, D. Li, 3D printed continuous fibre reinforced composite corrugated structure, Compos. Struct. 184 (2018) 1005–1010. https://doi.org/10.1016/j.compstruct.2017.10.080.

[58] G. Ma, Z. Li, L. Wang, F. Wang, J. Sanjayan, Mechanical anisotropy of aligned fiber reinforced composite for extrusion-based 3D printing, Constr. Build. Mater. 202 (2019) 770–783. https://doi.org/10.1016/j.conbuildmat.2019.01.008.

[59] J. Ye, C. Cui, J. Yu, K. Yu, F. Dong, Effect of polyethylene fiber content on workability and mechanical-anisotropic properties of 3D printed ultra-high ductile concrete, Constr. Build. Mater. 281 (2021) 122586. https://doi.org/10.1016/j.conbuildmat.2021.122586.

[60] C. Tang, J. Liu, W. Hao, Y. Wei, Flexural properties of 3D printed graded lattice reinforced cementitious composites using digital image correlation, Mater. Des. 227 (2023) 111734. https://doi.org/10.1016/j.matdes.2023.111734.

[61] M.C. Jenkins, A.S. Brand, T.T. Painter, S.T. Sherry, A Preliminary Digital Image Correlation Study of the AnisotropicMechanical Properties of a 3D-Printed Mortar, 6th Int. Conf. Civ. Struct. Transp. Eng. (2021). https://doi.org/10.11159/iccste21.146.

[62] F. Inam, D.W.Y. Wong, M. Kuwata, T. Peijs, Multiscale hybrid micro-nanocomposites based on carbon nanotubes and carbon fibers, J. Nanomater. 2010 (2010) 1–12. https://doi.org/10.1155/2010/453420.

[63] T. Carlson, Multifunctional composite materials: design, manufacture and experimental characterisation, Luleå University of Technology, Luleå, 2013.

[64] J.S. Popovics, NDE techniques for concrete and masonry structures, Prog. Struct. Eng. Mater. 5 (2003) 49–59. https://doi.org/10.1002/pse.146.

[65] E. Maire, P.J. Withers, Quantitative X-ray tomography, Int. Mater. Rev. 59 (2014) 1–43. https://doi.org/10.1179/1743280413Y.0000000023.

[66] G. Xue, E. Yilmaz, W. Song, S. Cao, Analysis of internal structure behavior of fiber reinforced cement-tailings matrix composites through X-ray computed tomography, Compos. Part B Eng. 175 (2019) 107091. https://doi.org/10.1016/j.compositesb.2019.107091.

[67] P.J. Withers, C. Bouman, S. Carmignato, V. Cnudde, D. Grimaldi, C.K. Hagen, E. Maire, M. Manley, A. Du Plessis, S.R. Stock, X-ray computed tomography, Nat. Rev. Methods Primer 1 (2021) 18. https://doi.org/10.1038/s43586-021-00015-4.

[68] M. Wevers, B. Nicolaï, P. Verboven, S. Rudy, S. Roels, E. Verstrynge, S. Lomov, G. Kerckhofs, B. Van Meerbeek, A. Mavridou, L. Bergmans, P. Lambrechts, J. Soete, S. Claes, H. Claes, Applications of CT for non-destructive testing and materials characterization, in: Ind. X-Ray Comput. Tomogr., 2018: pp. 267–331. https://doi.org/10.1007/978-3-319-59573-3_8.

[69] B.S. Sindu, A. Thirumalaiselvi, S. Sasmal, Investigations on fracture related properties of strain hardened concrete using digital image correlation and acoustic emission techniques, Eur. J. Environ. Civ. Eng. 26 (2022) 6807–6829. https://doi.org/10.1080/19648189.2021.1962411.

[70] N. Hasheminejad, C. Vuye, A. Margaritis, B. Ribbens, G. Jacobs, J. Blom, W. Van Den Bergh, J. Dirckx, S. Vanlanduit, Investigation of Crack Propagation and Healing of Asphalt Concrete Using Digital Image Correlation, Appl. Sci. 9 (2019) 2459. https://doi.org/10.3390/app9122459.

[71] B. Pan, K. Qian, H. Xie, A. Asundi, Two-dimensional digital image correlation for in-plane displacement and strain measurement: a review, Meas. Sci. Technol. 20 (2009) 062001. https://doi.org/10.1088/0957-0233/20/6/062001.

[72] S. Roux, J. Réthoré, F. Hild, Digital image correlation and fracture: an advanced technique for estimating stress intensity factors of 2D and 3D cracks, J. Phys. Appl. Phys. 42 (2009) 214004. https://doi.org/10.1088/0022-3727/42/21/214004.

[73] S.G. Shah, J.M. Chandra Kishen, Fracture Properties of Concrete–Concrete Interfaces Using Digital Image Correlation, Exp. Mech. 51 (2011) 303–313. https://doi.org/10.1007/s11340-010-9358-y.

[74] D.G. Aggelis, S. Verbruggen, E. Tsangouri, T. Tysmans, D. Van Hemelrijck, Characterization of mechanical performance of concrete beams with external reinforcement by acoustic emission and digital image correlation, Constr. Build. Mater. 47 (2013) 1037–1045. https://doi.org/10.1016/j.conbuildmat.2013.06.005.

[75] S. Rouchier, G. Foray, N. Godin, M. Woloszyn, J.-J. Roux, Damage monitoring in fibre reinforced mortar by combined digital image correlation and acoustic emission, Constr. Build. Mater. 38 (2013) 371–380. https://doi.org/10.1016/j.conbuildmat.2012.07.106.

[76] S.Y. Alam, J. Saliba, A. Loukili, Fracture examination in concrete through combined digital image correlation and acoustic emission techniques, Constr. Build. Mater. 69 (2014) 232–242. https://doi.org/10.1016/j.conbuildmat.2014.07.044.

[77] K. Yu, L. Li, J. Yu, J. Xiao, J. Ye, Y. Wang, Feasibility of using ultra-high ductility cementitious composites for concrete structures without steel rebar, Eng. Struct. 170 (2018) 11–20. https://doi.org/10.1016/j.engstruct.2018.05.037.

[78] C.G. Berrocal, I. Fernandez, M.F. Bado, J.R. Casas, R. Rempling, Assessment and visualization of performance indicators of reinforced concrete beams by distributed optical fibre sensing, Struct. Health Monit. 20 (2021) 3309–3326. https://doi.org/10.1177/1475921720984431.

[79] A. Teramoto, M. Watanabe, R. Murakami, T. Ohkubo, Visualization of internal crack growth due to alkali–silica reaction using digital image correlation, Constr. Build. Mater. 190 (2018) 851–860. https://doi.org/10.1016/j.conbuildmat.2018.09.168.

[80] C1609/C1609M − 19a, Standard test method for flexural performance of fiber-reinforced concrete (Using beam with third-point loading), ASTM International, 2019. https://doi.org/10.1520/C1609_C1609M-19A.

[81] Y. Jenq, S.P. Shah, Two parameter fracture model for concrete, J. Eng. Mech. 111 (1985) 1227–1241. https://doi.org/10.1061/(ASCE)0733-9399(1985)111:10(1227).

[82] RILEM Committee, Determination of fracture parameters (KIC and CTODC) of plain concrete using three-point bend tests, Mater. Struct. 23 (1990) 457–760. https://doi.org/10.1007/BF02472029.

[83] A. Hillerborg, The theoretical basis of a method to determine the fracture energy GF of concrete, Mater. Struct. 18 (1985) 291–296. https://doi.org/10.1007/BF02472919.

[84] Determination of the fracture energy of mortar and concrete by means of three-point bend tests on notched beams, Mater. Struct. 18 (1985) 287–290. https://doi.org/10.1007/BF02472918.

[85] J. Roesler, G. Paulino, C. Gaedicke, A. Bordelon, K. Park, Fracture Behavior of Functionally Graded Concrete Materials for Rigid Pavements, Transp. Res. Rec. J. Transp. Res. Board 2037 (2007) 40–49. https://doi.org/10.3141/2037-04.

[86] G. Torelli, M.G. Fernández, J.M. Lees, Functionally graded concrete: Design objectives, production techniques and analysis methods for layered and continuously graded elements, Constr. Build. Mater. 242 (2020) 118040. https://doi.org/10.1016/j.conbuildmat.2020.118040.

[87] W. Abbass, M.I. Khan, S. Mourad, Evaluation of mechanical properties of steel fiber reinforced concrete with different strengths of concrete, Constr. Build. Mater. 168 (2018) 556–569. https://doi.org/10.1016/j.conbuildmat.2018.02.164.

[88] Q. Li, S. Xu, Experimental investigation and analysis on flexural performance of functionally graded composite beam crack-controlled by ultrahigh toughness cementitious composites, Sci. China Ser. E Technol. Sci. 52 (2009) 1648–1664. https://doi.org/10.1007/s11431-009-0161-x.

[89] A.A. Elakhras, M.H. Seleem, H.E.M. Sallam, Real fracture toughness of FRC and FGC: size and boundary effects, Arch. Civ. Mech. Eng. 22 (2022) 99. https://doi.org/10.1007/s43452-022-00424-6.

[90] P. Zhang, C. Wang, Z. Gao, F. Wang, A review on fracture properties of steel fiber reinforced concrete, J. Build. Eng. 67 (2023) 105975. https://doi.org/10.1016/j.jobe.2023.105975.

[91] M. Maalej, V.C. Li, Flexural/Tensile-Strength Ratio in Engineered Cementitious Composites, J. Mater. Civ. Eng. 6 (1994) 513–528. https://doi.org/10.1061/(ASCE)0899-1561(1994)6:4(513).

[92] I.H. Yang, C. Joh, B.-S. Kim, Structural behavior of ultra high performance concrete beams subjected to bending, Eng. Struct. 32 (2010) 3478–3487. https://doi.org/10.1016/j.engstruct.2010.07.017.

[93] E.A. Zimmermann, M.E. Launey, R.O. Ritchie, The significance of crack-resistance curves to the mixed-mode fracture toughness of human cortical bone, Biomaterials 31 (2010) 5297–5305. https://doi.org/10.1016/j.biomaterials.2010.03.056.

[94] A. Akram, The overview of fracture mechanics models for concrete, Archit. Civ. Eng. Environ. 14 (2021) 47–57. https://doi.org/10.21307/acee-2021-005.

Chapter 7. Flexural Models Exploration for Functionally Graded Steel Fiber-Reinforced Mortar Considering Fiber Dosage and Orientation[5]

Abstract

This research critically examined the performance of three flexural models, ER 465, fib linear, and fib rigid-plastic, on functionally graded fiber-reinforced concrete (FG-FRC) specimens, emphasizing their predictability against actual experimental outcomes from three-point bending tests on notched beams as per EN 14651. Focused on discerning the tensile behavior of different FRC material classes at both Serviceability Limit State and Ultimate Limit State, the study investigated the impact of two pivotal factors: fiber dosage and orientation within the FG-FRC layers. Recognizing a significant gap in existing models, which assume material homogeneity and often yield conservative outcomes, this research introduces a functionally graded factor. This novel factor accounts for the FG-FRC's complexity, characterized by variable fiber dosages across its layers, thus refining the predictive accuracy of the models. By incorporating this factor, the modified flexural models have reflected the complex relationship between fiber content and layer distribution more accurately, thereby improving their precision and practical application in the engineering of FG-FRC structures.

Keywords: Fiber-reinforced concrete, Functionally graded, Flexural, Model, Extrusion, Injection, Fiber alignment, X-ray computed tomography.

[5] **R. Alarrak**, C. L. Roberts-Wollmann, A.S. Brand, Flexural Models Exploration for Functionally Graded Steel Fiber-Reinforced Mortar Considering Fiber Dosage and Orientation, In Preparation. (2024).

7.1. Introduction

Due to its constructability and resistance to compression, concrete is widely used in construction to execute structural design shapes and frames. Despite its widespread use, concrete's inherent brittleness and limited tensile strength present significant challenges to its structural performance [1–3]. Traditionally, these limitations have been mitigated through reinforcement techniques, notably rebar. Yet, a more advanced solution has been proposed in the form of Fiber Reinforced Concrete (FRC), which involves the addition of micro-reinforcements such steel, synthetic, and organic fibers, intending to enhance the tensile strength and overall structural performance of the concrete [4,5]. With the increasing application of FRC, there is a growing need for precise predictions of its flexural behavior, prompting research into various flexural modeling techniques. Several models have laid the groundwork for a deeper understanding of FRC's mechanical behavior [6–9], complemented by studies like those of Blanco *et al*. [10], which delve into European codes and guidelines for FRC structural design, shedding light on constitutive models.

Laying the foundation for a comprehensive exploration, this literature review provides an overview of previous research in the domain of flexural models, specifically focusing on the Evaluation Report (ER-465) [11], the fib Linear Model (fib-L), and the fib Rigid-Plastic Model (fib-RP) [12]. The application of these models is examined in the context of experimental data obtained through three-point bending tests, conforming to EN 14651 standard. These models offer insights into FRC's behavior, addressing the critical need for reliable predictive tools in engineering applications.

7.1.1. Innovation of Functionally Graded FRC

Within the realm of FRC, the emergence of Functionally Graded Fiber-Reinforced Concrete (FG-FRC) marks a significant leap forward in addressing the inherent limitations of traditional concrete. FG-FRC represents an innovative advancement, offering a superior blend of load-bearing capacity, structural durability, and a balance of strength and toughness. This innovative material is particularly suited for demanding construction projects such as long-span bridges, buildings designed to withstand seismic activity, and towering skyscrapers, due to its enhanced performance characteristics [13−16]. FG-FRC distinguishes itself by allowing for strategic placement and distribution of fibers within the concrete matrix, specifically targeting areas under tensile stress. This targeted reinforcement approach ensures that fibers are utilized where they are most needed, optimizing the material's mechanical properties [17]. Among various fibers, steel fibers are frequently chosen for their ease of integration, cost efficiency, and eco-friendly attributes, such as reduced water requirements. These advantages contribute to FG-FRC's appeal, merging enhanced structural performance with environmental sustainability [18].

7.1.2. Fiber Injection Techniques and Alignment

Fibers can be incorporated into the dry mortar before mixing, introduced during the mixing phase, or added to the mortar or concrete immediately before placement. Historically, the mixing stage has been the preferred moment for fiber addition, as documented by numerous studies [14,19–23]. However, Ahmed *et al.* introduced a specialized device designed for the inclusion of various fiber types into the mortar used in extrusion-based 3D concrete printing, aiming to mitigate compatibility issues such as incorporating high-stiffness and long steel fibers. This process, however, resulted in fibers being oriented randomly within the mixture [24].

Central to this research is a novel targeted fiber injection technique that directly integrates high-stiffness steel fibers into mortar at the point of extrusion. This method represents a significant advancement in permitting the use of fibers in more extrusion systems, since the fibers, by this method, are prevented cannot from blocking pumps, augers, or narrowing passages within pipes or hoses, ensuring a smoother integration process. Extrusion-based technologies are recognized for their ability to improve fiber alignment, a critical factor in optimizing the structural performance of concrete, as recent studies have demonstrated [22,23,25–38]. Therefore, by integrating this targeted fiber injection method with extrusion technologies, the process achieves superior fiber dispersion and orientation within the concrete matrix [17]. This integration not only ensures a uniform distribution of fibers but also enhances their alignment, significantly boosting the mechanical properties of the concrete. Such advancements in fiber injection and extrusion techniques are pivotal in advancing the development of high-performance concrete materials, offering improved durability and structural integrity.

7.1.3. Flexural Models in FRC

The exploration of flexural models such as ER-465, fib-L, and fib-RP has significantly contributed to understanding the behavior of FRC under various loading conditions. Zhong *et al.* [39] investigated the potential of substituting traditional steel reinforcement with steel fibers in high-strength concrete. Their theoretical analysis, aimed at assessing ductility and toughness, highlighted a strong correlation between predicted and actual flexural strengths, illuminating aspects of FRC's performance. Nonetheless, these models showed sensitivity to variations in fiber content and distribution, underscoring some limitations in their predictive capability.

Khalel and Khan [40] tackled the challenge of selecting appropriate fiber materials for reinforced cementitious composites. They introduced the Khan Khalel model, which predicts compressive and flexural strengths based on critical fiber parameters, facilitating optimal fiber selection in construction projects. The study found that the incorporation of steel and plastic fibers affected compressive strength inversely with increasing fiber length. Despite the model's high predictability, with errors below 6 % for compressive strength and 15 % for flexural strength, its limitations include overlooking fibers' plastic behavior and focusing solely on linear elastic behavior. Furthermore, Ayub *et al.* [41] contributed to this field by developing a flexural capacity model for polyvinyl alcohol (PVA) and basalt FRC beams, employing equivalent stress block parameters. Validated through experimental testing and finite element analysis, the models accurately predicted the load-bearing capacity of FRC beams with up to 3 % fiber volume fraction, without using reinforcing bars. The analytical models proved effective for predicting FRC's flexural behavior, though their applicability was mainly demonstrated on rectangular beam sections, pointing to the necessity for broader exploration.

7.1.3.1. fib Rigid-Plastic Model

The fib-RP model has been utilized to examine the impact of fiber content, aspect ratio, and distribution on FRC's flexural strength and stiffness. Enfedaque *et al.* [42] compared the fib-RP Model with a trilinear approach, revealing significant differences in their ability to replicate the flexural characteristics of Polymer FRC. The trilinear approach was found to more accurately predict peak loads and model the unloading process, challenging the fib Model Code 2010 (MC 2010) models' applicability for polymer FRC. Moreover, Conforti *et al.* [43] explored the effect of various macrofibers on the flexural performance of concrete beams, finding that fibers positively influenced bending behavior at serviceability and ultimate limit states, in line with MC 2010

recommendations, without compromising ductility. However, the study called for further research on different fiber types to overcome potential predictive limitations regarding crack localization.

7.1.3.2. fib Linear Model

Buttignol *et al.* [44] used the fib-L Model for a comprehensive design analysis of concrete beams reinforced with steel fibers, adhering to fib MC 2010 guidelines. Their findings affirmed the conservativeness of MC 2010 design rules and validated the Rule of Mixture for predicting flexural strength across various FRC compositions. Nevertheless, they recommended adopting finite element models for a more in-depth analysis due to limitations in linear statistical analysis. In addition, Aidarov *et al.* [45] investigated the effects of low temperatures on the flexural strength of macro-synthetic FRC, noting an improvement in flexural strength, especially in post-cracking behavior, with decreasing temperature. Their study underscores the importance of considering temperature effects in design procedures and calls for further research to establish comprehensive temperature-flexural strength relationships.

7.1.3.3. ER-465 Model

The ER-465 Model, specifically designed for Dramix steel fibers, is notable for its specialized application in the field of steel FRC. Despite its limited use, the model presents a valuable tool for studies incorporating Dramix steel fibers. A prime example of ability in usage is found in the work of Marcalíková *et al*. [46], which focused on examining the mechanical properties of concrete enhanced with Dramix fibers. Their research aimed to evaluate the impact of different fiber dosages on flexural behavior. The research, which included a range of tests, offers valuable insights into dosage effects on flexural strength predictions using the ER-465 model.

7.1.4. Prediction of FRC's Flexural Strength

Understanding and applying flexural models to FRC is crucial in connecting theoretical principles with practical outcomes in structural engineering. Models such as ER-465, fib-L, and fib-RP, as outlined in the MC 2010, offer in-depth insights into FRC's behavior under flexural stress. These models provide a comprehensive understanding of FRC's flexural behavior by delving into complex relationships among parameters such as residual flexural tensile strength, crack mouth opening displacement (CMOD), and the stress-crack width relationship (σ-w), providing a nuanced understanding of how FRC behaves under load.

The value of these flexural models lies in their efficiency and cost-effectiveness, enabling engineers to refine mix designs, ensuring compliance with industry standards, and advancing research and development efforts in the realm of FRC. Incorporating validated flexural models into design practices aligns with industry norms and coding standards, ensuring construction projects comply with recognized best practices. As the construction industry continues to embrace FRC for its superior mechanical properties, the significance of flexural models in predicting FRC flexural strength becomes paramount, driving advancements in research, design methodologies, and practical applications.

The reliability of these models to experimental data from standardized tests, such as the three-point bending tests following EN 14651, provides empirical validation to their applicability in real-world scenarios. The adoption of these flexural models facilitates an informed and optimized design process, enhancing the competitiveness, usability, and versatility of FRC in construction. As highlighted by Danish *et al.* [47] the utilization of flexural models empowers engineers to tailor FRC structures to specific project requirements, ensuring an optimal balance between material efficiency and structural performance. Overall, the theoretical importance

coupled with empirical underscores the critical importance of flexural models in advancing modern construction methodologies. They are instrumental in fostering the development of durable, efficient, and optimized structural elements, marking a significant stride towards innovative and resilient construction practices.

7.1.5. Research Objective

This literature review lays the groundwork for notable research that offers the potential of exploring the efficacy of three different flexural models – ER-465, fib-L, and fib-RP – when applied to extruded FG-FRC. The innovation of this research lies in its application of established flexural models to predict the flexural strength of FRC sections under a novel context. The FG-FRC sections were cast using an advanced targeted fiber injection technique, utilizing a conveyor system for the direct integration of high-stiffness steel fibers into mortar at the nozzle just prior to extrusion. This method represents a significant advancement in construction technology, particularly for extrusion-based systems, by effectively addressing and overcoming the traditional challenges associated with fiber reinforcement, such as clogging in pumps, augers, and pipes, which has historically limited fiber use in extrusion processes.

The research is distinguished by its focus on two primary variables, namely the orientation and dosage of fibers, and their impact on the accurate prediction of FRC's flexural strength. The underlying hypothesis suggests that the extrusion-based casting method inherently aligns fibers with the concrete flow direction, thereby optimizing fiber orientation parallel to tensile stress lines. This strategic alignment is anticipated to significantly enhance the mechanical performance of FRC. Moreover, the study examines FG-FRC specimens across five different mix designs, each varying in fiber dosage within the layers, to assess the influence of these configurations on the material's flexural strength.

This study also introduces a novel factor, the functionally graded factor (K_{FG}), to the established flexural models. K_{FG} is designed to accurately reflect the variations in fiber dosage and distribution across the layers of FG-FRC sections, which are pivotal in influencing the composite's structural behavior and material performance. Traditional flexural models, designed for homogeneous FRC sections, assume a uniform fiber distribution throughout the material. The emergence of FG-FRC, however, presents a complexity unaddressed by these models. Therefore, the K_{FG} factor aims to bridge this gap by providing a systematic approach to account for the effects of functionally graded fiber distribution within the analytical framework of flexural models. It is founded on a thorough analysis that assesses the impact of fiber dosage variations, ultimately leading to a marked improvement in the predictability of the models.

7.2. Experimental Methodology

7.2.1. Flexural Properties

The evaluation of flexural toughness in this investigation was inspired by the EN 14651 standard, with modifications to accommodate the unique aspects of specimen preparation introduced by this study [48]. The samples were formed into rectangular beams, each measuring 700 mm in length, 80 mm in width, and 150 mm in height, with a testing span of 600 mm and a notch depth of 50 mm. The setup for the three-point bending tests is depicted in Figure 7.1. This adjustment ensures consistency with the three-point bending test setups used in earlier studies [17,22,23], allowing for a more direct comparison of mechanical properties influenced by the use of pump extrusion in specimen fabrication.

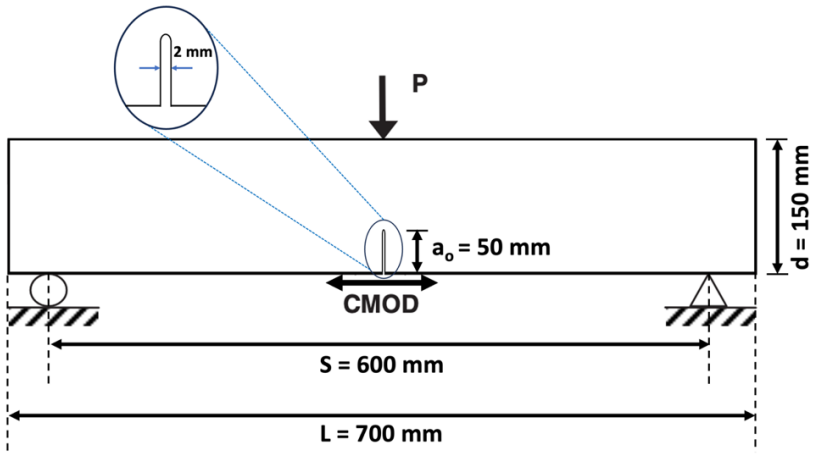

Figure 7.1: Test Setup of Three-point Bending Beam Specimen [17]

For the testing procedure, each beam was subjected to a monotonic load applied at a three-point configuration until a crack mouth opening displacement (CMOD) of 4 mm was achieved. The resulting load-CMOD curve was segmented into five distinct stages, as illustrated in Figure 7.2. These stages represent critical points from the initial load application to the limit of proportionality, and the residual loads at CMOD values of 0.5 mm, 1.5 mm, 2.5 mm, and 3.5 mm.

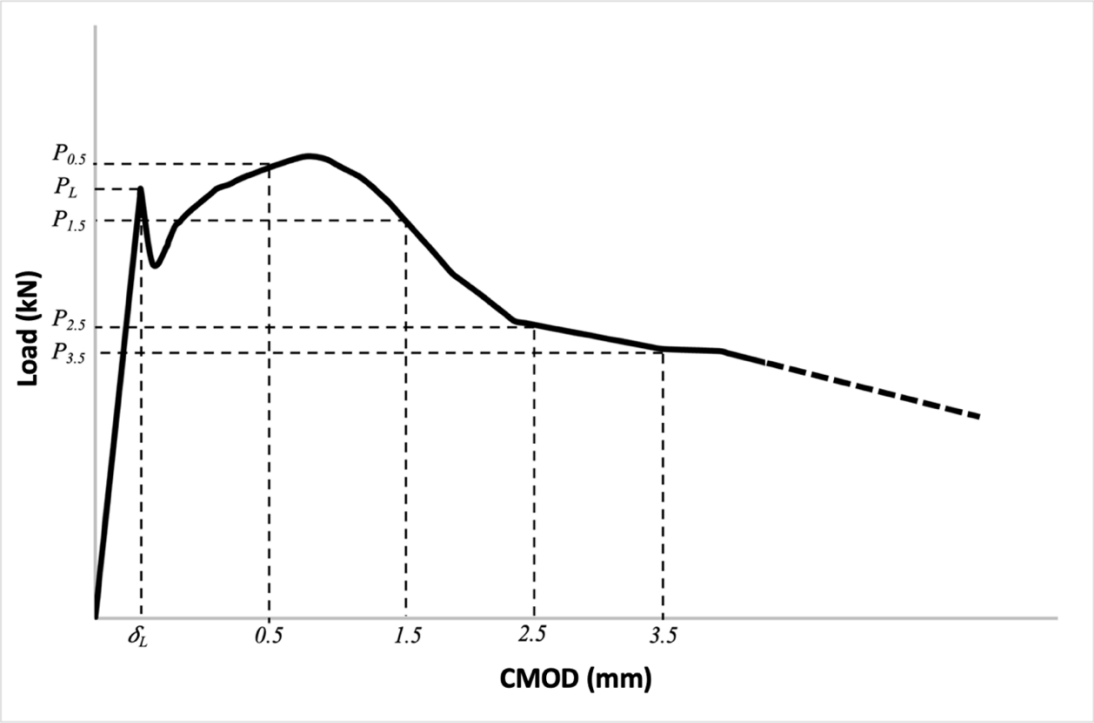

Figure 7.2: Five Stages of Load-CMOD Curve (adapted from EN 14651)

The investigation into the flexural properties of FG-FRC included the assessment of several critical properties, such as the limit of proportionality strength (f_L), residual strengths at various CMODs denoted as ($f_{0.5}, f_{1.5}, f_{2.5}, f_{3.5}$), the flexural toughness at a CMOD of 4 mm (T_4), and the equivalent flexural strength ratio at a CMOD of 4 mm ($R_{T,4}$). Limit of proportionality strength along with residual strengths (f), were computed using Equation 1, where P is the corresponding load, L is the span length, b is the width of the specimen, and d_{sp} is the distance between the tip of the notch and the top of the specimen.

Flexural toughness parameters (T_x) were determined by calculating the area under the load-CMOD curve up to the specified CMOD. This quantification provides a measure of the energy absorbed by the specimen until a given CMOD, offering insights into the material's ductility and energy dissipation capabilities. The equivalent flexural strength ratios were calculated using Equation 2, where x is the corresponding CMOD, T_x is the flexural toughness corresponding to that CMOD, and b is the width of the specimen.

$$f = \frac{3PL}{2bd_{sp}^2} \tag{1}$$

$$R_{T,x} = \frac{x \cdot T_x}{f_L b d_{sp}^2} \cdot 100\% \tag{2}$$

7.2.2. Theoretical Background of Flexural Models

The utilization of three distinct flexural models, ER-465, fib-L, and fib-RP, forms the foundation of this study's theoretical framework. These models are instrumental in predicting the flexural behavior of FRC, offering a range of analytical approaches to understand how FRC sections respond under varying loading conditions. By comparing the outcomes predicted by these

models with actual experimental data, the study aims to assess their predictability and applicability in the context of FRC.

7.2.2.1. ER-465 Model

The ER-465 model is specifically tailored for the design of FRC members that incorporate Dramix steel fibers, emphasizing its application for both strength and serviceability design considerations [11]. This model is distinguished by its focus on steel FRC members, offering a set of design provisions that are uniquely applicable to constructions utilizing Dramix steel fibers. Within the ER-465 framework, there are three distinct FRC flexural models designed to accommodate various structural scenarios. These models can incorporate conventional steel rebar on both the tension and compression sides, with FRC in tension and conventional concrete in compression. Given the focus of this study on FRC without the inclusion of steel rebars, the analysis concentrates on the behavior of FRC under stress and strain as per the specifications of the constitutive models provided by the ER-465.

For the purpose of analysis, the ER-465 model stipulates that the concrete compressive strain in material non-linear analysis is limited to a compressive strain of 0.003. The concrete stress (f_c) in compression is represented by Hognestad's parabolic model, shown in Figure 7.3 and represented in Equation 3, where f_c' is the maximum concrete compressive stress, ε_c is concrete compressive strain, and ε_c' is the concrete strain corresponds to f_c', which is set to 0.002.

$$f_c = f_c' \left[2\frac{\varepsilon_c}{\varepsilon_c'} - \left(\frac{\varepsilon_c}{\varepsilon_c'}\right)^2 \right] \tag{3}$$

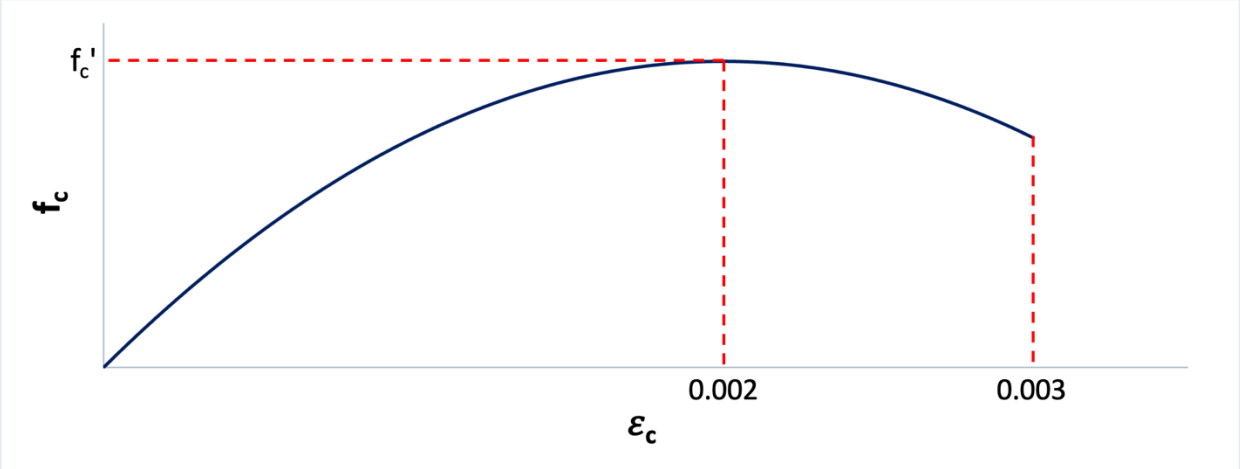

Figure 7.3: Stress-strain Relationship for Concrete in Compression (adapted from ER-465)

In the ER-465 model, the behavior FRC under tensile stress is modeled to account for material non-linearity, reflecting the complex interaction between the concrete matrix and embedded steel fibers. This is particularly important for understanding how FRC performs under tensile loads, which significantly influence the structural integrity and serviceability of FRC elements. The constitutive model for FRC under tension is depicted in Figure 7.4, where f_{ns} represents the nominal axial tensile strength at a strain of 0.0001 (serviceability), and f_{nu} represents the nominal axial tensile strength at the strain limit of 0.025 (ultimate).

The value of f_{ns} is determined based on the ratio of residual strengths ($f_{3.5}/f_{0.5}$). It is calculated using Equation 4 for $f_{3.5}/f_{0.5} < 0.7$ or using Equation 5 for $f_{3.5}/f_{0.5} \geq 0.7$, where K_o is the fiber orientation factor, which would be determined later in this research, K_s is the size factor equal to $0.68 + 0.31bd_{sp}$, and K_c is the structural use factor which is set to 1.0 for all cases, indicating a standard application across different structural uses. The calculation of f_{nu}, involves Equation 6, where a conversion factor (α_c) is used. This conversion factor is derived from Table 7.1, which provides specific values based on the composition and characteristics of the FRC being analyzed.

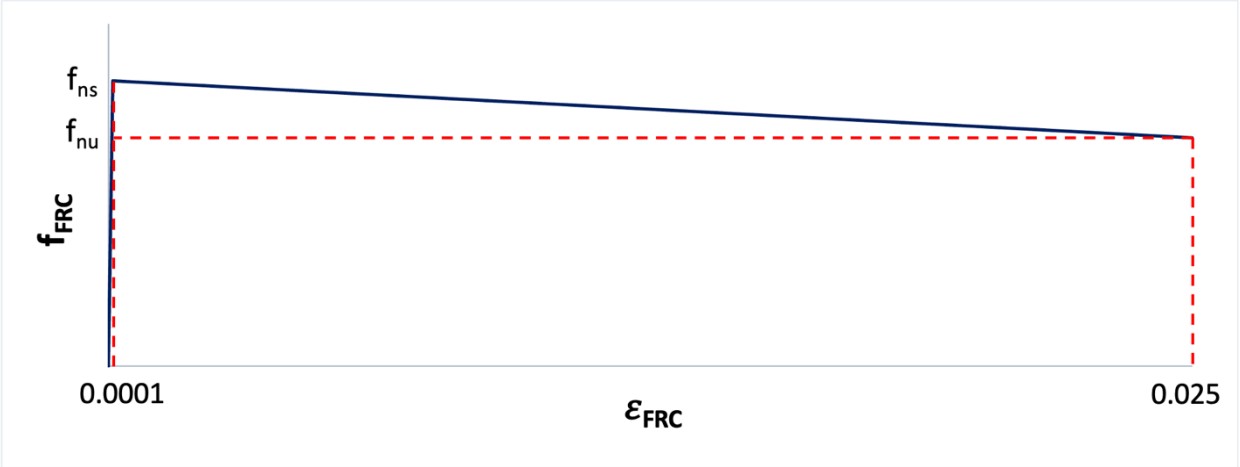

Figure 7.4: Stress-strain Relationship for FRC in Tension (adapted from ER 465)

$$f_{ns} = 0.37K_oK_sK_cf_{3.5} \quad (4)$$

$$f_{ns} = 0.40K_oK_sK_cf_{0.5} \quad (5)$$

$$f_{nu} = \alpha_cK_oK_sK_cf_{3.5} \quad (6)$$

Table 7.1: Conversion Factor (α_c)

α_c Value	Conditions
0.37	$f_{3.5}/f_{0.5} < 0.7$
0.25 + ($f_{3.5}/f_{0.5}$ - 0.7)/3	$0.7 \leq f_{3.5}/f_{0.5} \leq 1.0$
0.35 + 0.9($f_{3.5}/f_{0.5}$ - 1.0)/5	$1.0 \leq f_{r4}/f_{r1} \leq 1.5$
0.44	$1.5 \leq f_{3.5}/f_{0.5}$

The transition from Flexural Model I to Flexural Model III within the ER-465 framework highlights the adaptability required in modeling the behavior of FRC under flexural loading conditions. This shift acknowledges the limitations encountered when applying Model I assumptions to the real-world performance of FRC, particularly regarding the tensile strain capacity of the material. Flexural Model III, shown in Figure 7.5, is recommended by ER-465 for

scenarios where the tensile strain in FRC exceeds the predetermined limit of 0.025, a common occurrence due to the relatively low tensile stress capacity of FRC compared to its compressive strength. This model is designed to more accurately reflect the behavior of FRC under flexural stress by setting the maximum tensile strain limit to 0.025 and limiting the concrete compressive strain at 0.003. Such parameters ensure that the model accounts for the FRC's probability to fail in tension prior to experiencing crushing failure in compression [11].

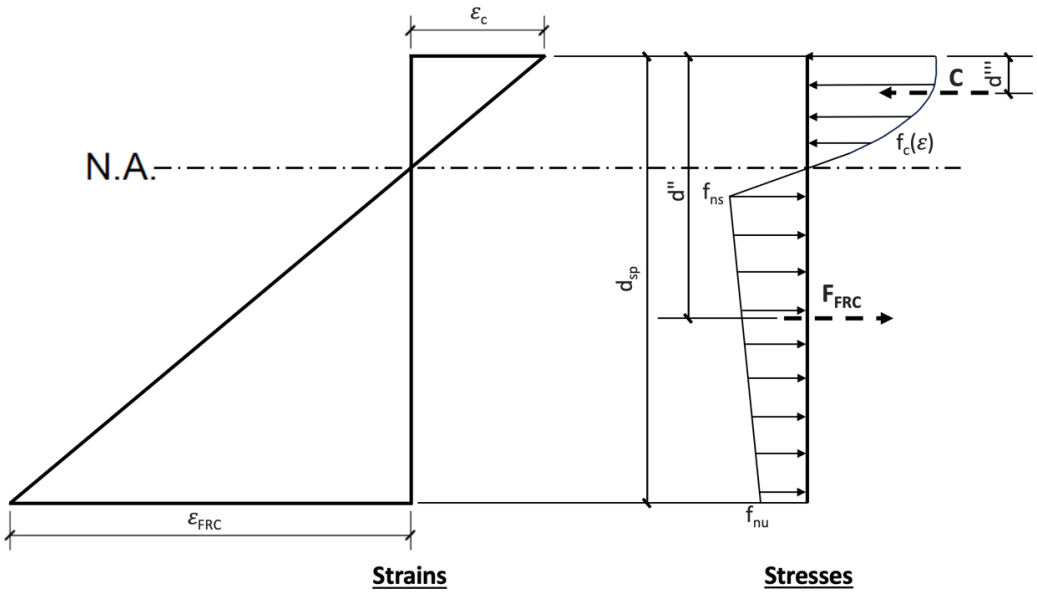

Figure 7.5: ER-465 Flexural Model III (adapted from ER 465)

The foundation of Flexural Model III lies in Equation 7, an equation defining the relationships for individual constituents within the cross-section, where ϕ is the strength reduction factor for bending sue to FRC which is equal to 0.80. This equation considers dimensional parameters (d_{sp}, d'', d'''), crucial in determining the depth and centroid of the compressive stress block within the FRC section. These parameters help in accurately locating the neutral axis and the distribution of compressive stresses across the concrete cross-section.

$$\phi M_n = \phi_{FRC} F_{FRC}(d'' - d''') \tag{7}$$

In order to guarantee its applicability, Flexural Model III sets out particular requirements. A maximum tensile strain in FRC of 0.025, acknowledging the enhanced tensile capacity FRC offers due to fiber reinforcement. Besides, a maximum compressive strain in concrete of 0.003, ensuring that the concrete's behavior in compression remains within acceptable and predictable limits. The model emphasizes strain compatibility between the concrete compressive strain (ε_c) and FRC tensile strain (ε_{FRC}), a critical aspect ensuring that the theoretical model aligns with the actual behavior of FRC under bending stresses. This strain compatibility is essential for accurately modeling the stress distribution across the FRC section, particularly under conditions where the FRC is expected to exhibit significant tensile strength.

By incorporating these parameters and requirements, Flexural Model III offers a detailed methodology for assessing the flexural performance of FRC. It acknowledges the unique contributions of fibers to tensile strength and the interaction between the concrete matrix and the fibers under load. The model is designed to provide a comprehensive understanding of how FRC sections respond to bending forces, facilitating the prediction of their flexural capacity with a higher degree of accuracy.

7.2.2.2. fib Linear Model

The fib-L model, embedded within the MC 2010, serves as a fundamental framework for understanding the flexural behavior FRC [12]. This model operates under a stress-crack width constitutive law, which defines the relationship between stress and crack width during flexural loading [10]. This model is particularly useful for assessing FRC's performance across different states of loading, specifically focusing on the serviceability limit state (SLS) and ultimate limit state (ULS).

The serviceability residual tensile strength (f_{Fts}) represents the strength of FRC post-cracking, specifically for cracks that are significant for SLS considerations. This value corresponds to CMOD of 0.5 mm [12]. The calculation of f_{Fts}, presented in Equation 8, is crucial for ensuring that the FRC can maintain its integrity and functionality under normal service conditions, preventing excessive cracking or deformation that could compromise its usability.

The ultimate residual tensile strength (f_{Ftu}) is derived from a more detailed analysis, considering the linear-elastic distribution of stresses up to the ULS. This parameter is associated with the ultimate CMOD (w_u), which is determined based on the structural ductility requirements. The calculation of f_{Ftu}, presented in Equation 9, is essential for understanding the maximum tensile capacity of FRC, ensuring that the material can withstand extreme loading conditions without catastrophic failure.

The ultimate crack width (w_u), is a function of the strain at ULS (ε_{Fu}) and the structural characteristic length (l_{cs}), as presented in Equation 10. For the purposes of this model, ε_{Fu} is assumed to be 2 %, reflecting the strain when the neutral axis crosses the cross-section. The value of l_{cs} can be approximated as the beam depth, facilitating a simplified analysis under the assumption of plane sections. This calculation is vital for determining the maximum allowable crack width under ULS conditions, guiding the design and analysis of FRC structures to ensure adequate ductility and resistance to fracture.

$$f_{Fts} = 0.45 f_{0.5} \tag{8}$$

$$f_{Ftu} = f_{Fts} - \frac{w_u}{CMOD_3}(0.45 f_{0.5} - 0.5 f_{2.5} + 0.2 f_{0.5}) \geq 0 \tag{9}$$

$$w_u = \min\left(l_{cs}\, \varepsilon_{Fu}, 2.5\ mm\right) \tag{10}$$

Furthermore, the fib-L model, as depicted in Figure 7.6 and specified within the MC 2010, showcases an adaptable approach to modeling the flexural behavior of FRC. This model's capacity to describe both the load-descending (softening) behavior typical of many FRC materials after initial cracking and the potential for a load-ascending (hardening) response under certain conditions is a crucial aspect of its application. The softening curve represents the typical reduction in load-carrying capacity of FRC following the formation of a crack, indicating a decrease in material stiffness and strength as the crack width increases. This behavior is characteristic of materials where the post-cracking strength is less than the peak strength, a common scenario in many FRC compositions. Conversely, the possibility of a load-ascending behavior, or post-crack hardening, introduces a significant dynamic to FRC analysis. Post-crack hardening occurs when the FRC, after initial cracking, exhibits an increase in strength with further deformation or crack widening. This phenomenon is attributed to the distribution of fibers within the concrete matrix, which bridge the cracks and provide additional tensile capacity beyond the initial crack formation [49]. The fib-L acknowledgment of this behavior aligns with the advanced performance characteristics observed in certain types of FRC, particularly those with high fiber content or specialized fiber materials that engage effectively during the post-cracking phase.

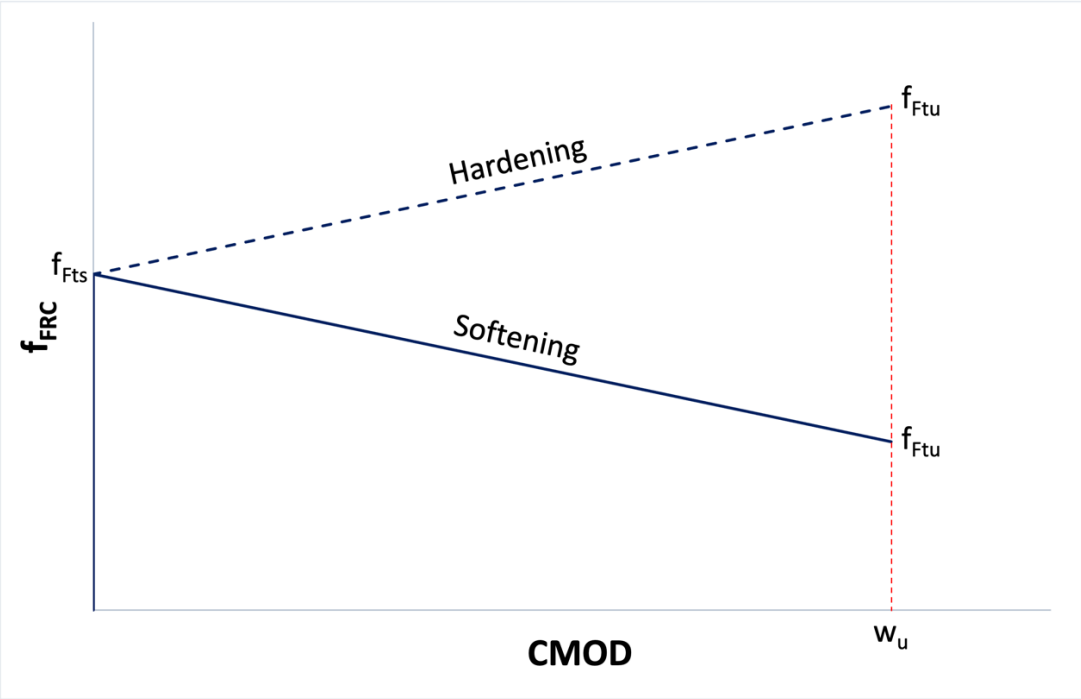

Figure 7.6: fib Linear Model (adapted from MC 2010)

7.2.2.3. fib Rigid Plastic Model

The fib-RP model presents an alternative approach to analyzing the flexural behavior of FRC within the framework of MC 2010. Distinct from the linear-elastic model, this model simplifies the analysis by focusing on a singular parameter, the ultimate residual tensile strength (f_{Ftu}), to predict the structural response of FRC at the ULS. The core of the fib-RP is the assumption of rotational equilibrium at ULS, which simplifies the stress distribution analysis across the cross-section of the FRC element. As shown in Figure 7.7, by concentrating the compressive stress at the top fiber of the cross-section and uniformly distributing the tensile post-cracking residual stress across the critical cross-section, the model provides a clear and straightforward method for evaluating FRC's capacity to withstand bending moments under extreme loading conditions.

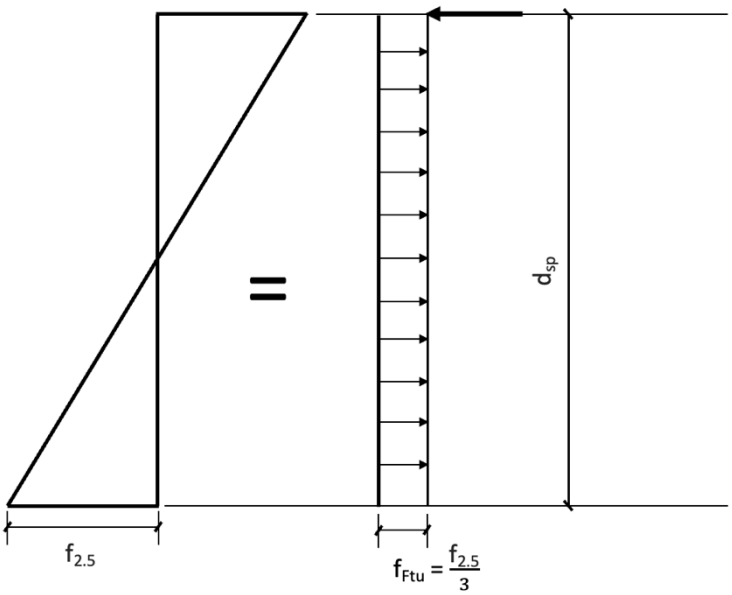

Figure 7.7: Residual Tensile Strength Computation in fib Rigid-plastic Model (adapted from MC 2010)

This model is based on the assumption that stress remains constant from the moment cracking initiates until it reaches the ultimate crack width limit value, denoted as (w_u), which corresponds to a CMOD of 2.5 mm. This limit represents a critical point in the analysis, linking the applied load directly to the ultimate residual tensile strength at CMOD. As shown in Figure 7.8, the ultimate residual tensile strength (f_{Ftu}) corresponds to the applied load when the CMOD equals w_u. The specific equation used to calculate f_{Ftu}, presented in Equation 11, is formulated based on the principles of rotational equilibrium at ULS.

$$f_{Ftu} = \frac{f_{2.5}}{3} \tag{11}$$

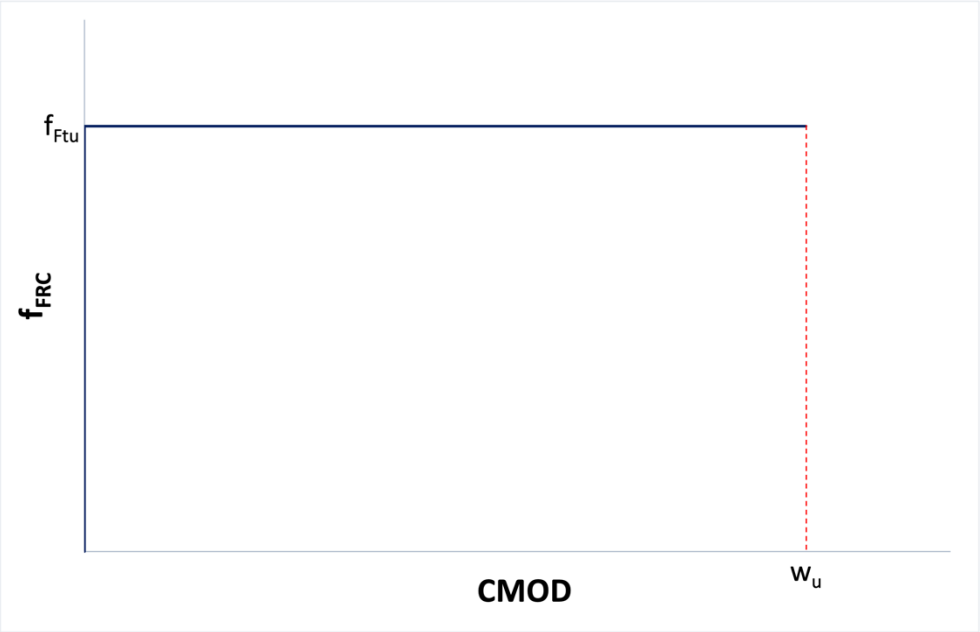

Figure 7.8: fib Rigid-plastic Model (adapted from MC 2010)

7.2.3. Theoretical Background of Flexural Models FRC Classifications

The classification of FRC is a critical aspect of its use in structural applications, reflecting the need for specific design parameters that account for its unique material properties, especially in tension. Unlike ordinary concrete, whose classification typically revolves around compressive strength, workability, or exposure classes, FRC introduces the residual post-cracking tensile strength as a principal design consideration, due to the significant influence of fibers on this property.

As direct uniaxial tensile tests are challenging to perform due to the difficulties in preparing specimens and applying loads without inducing secondary stresses, bending tests on notched beams have become the standard method for evaluating FRC's tensile behavior. Bending tests offer insights into the material's flexural performance, including its post-cracking behavior. These tests typically involve notched beams to ensure crack initiation at a predetermined location, facilitating the observation and measurement of crack propagation and the material's response to increasing

loads. The relationship between the material's behavior in uniaxial tension and its response in bending tests is complex. Materials that exhibit softening behavior in uniaxial tension might display hardening behavior in bending tests [50,51]. This phenomenon occurs because cracks can form and propagate in a stable manner under bending loads, even as the applied load increases, leading to flexure hardening behavior.

The classification system for FRC, structured around the EN 14651 standard, uses the results from bending tests on notched prisms to determine key performance indicators, specifically the post-cracking tensile strength at designated CMODs [48]. FRC Classification is based on two key parameters which are SLS and ULS. The post-cracking residual strength at a CMOD of 0.5 mm, denoted as ($f_{0.5k}$), characterizes the material's behavior under service conditions, ensuring it can withstand typical loads without excessive cracking or deformation. The classification also considers the post-cracking residual strength at a CMOD of 2.5 mm, denoted as ($f_{2.5k}$), indicative of the material's capacity to resist ultimate loads leading to failure. Instead of using $f_{2.5k}$ directly, the classification system emphasizes the ratio $f_{2.5k}/f_{0.5k}$, providing insight into the material's ductility and strength beyond initial cracking. Under these assumptions, FRC materials are classified using two parameters including a numerical value representing the $f_{0.5k}$ class, with specified strength values ranging from 1.0 to 8.0 MPa, and a letter denoting the ratio ($f_{2.5k}/f_{0.5k}$), categorized from 'a' to 'e' as presented in Table 7.2, which gives an indication of the material's performance from initial cracking to a more advanced post-cracking stage.

Table 7.2: FRC Material Classification

Letter	Conditions	Behavior
a	$0.5 \leq f_{2.5k}/f_{0.5k} \leq 0.7$	Softening
b	$0.7 \leq f_{2.5k}/f_{0.5k} \leq 0.9$	Softening
c	$0.9 \leq f_{2.5k}/f_{0.5k} \leq 1.1$	Softening
d	$1.1 \leq f_{2.5k}/f_{0.5k} \leq 1.3$	Hardening
e	$1.3 \leq f_{2.5k}/f_{0.5k}$	Hardening

According to MC 2010, the potential for fiber reinforcement to replace traditional rebars or welded mesh, even partially, in structural members at the ULS is depending upon satisfying specific criteria shown in Equation 12 and Equation 13, where f_{Lk} is the characteristic value of the nominal strength, corresponding to the limit of proportionality strength [12].

$$f_{0.5k}/f_{Lk} > 0.4 \tag{12}$$

$$f_{2.5k}/f_{0.5k} > 0.5 \tag{13}$$

7.2.4. Mix Design and Properties

This study, in consistent with a previous study [17], involved the preparation of a single mortar mixture and the incorporation of steel fiber at three different concentrations of 0 %, 0.5 %, and 1 % by volume. These concentrations were selected based on their practical applicability in real-world construction scenarios, as supported by reference [52]. The production of each FG-FRC specimen was carried out using an electric pump, which necessitated the use of fine aggregate with a maximum size limit of 4.75 mm and a fineness modulus of 2.6, due to the extrusion pump's limitations on aggregate size.

The experimental setup for the study included the composition of each specimen from three layers of mortar, with each layer containing a distinct fiber dosage, thus creating functionally graded mixtures. To facilitate differentiation among these mixtures, as depicted in Figure 7.9, a unique identification label was assigned to each. The compositions of the mortar mixes and the properties of the Dramix steel fibers used are detailed in Table 7.3 and Table 7.4, respectively. The properties of the Dramix steel fibers, shown in Figure 7.10, were provided by the manufacturer.

Table 7.3: Concrete Mixture Proportions [17]

Mixture ID	**0%**	**0.5%**	**1%**
Type I cement (kg/m^3)	688	688	688
Fine aggregate (kg/m^3)	1042	1042	1042
Water to cement ratio	0.40	0.40	0.40
Steel fiber volume	0%	0.5%	1%

Table 7.4: Properties of Steel Fibers [17]

Length (mm)	**30**
Filament diameter (mm)	0.38
Aspect ratio	80
Specific gravity	7.8
Tensile strength (MPa)	3,070

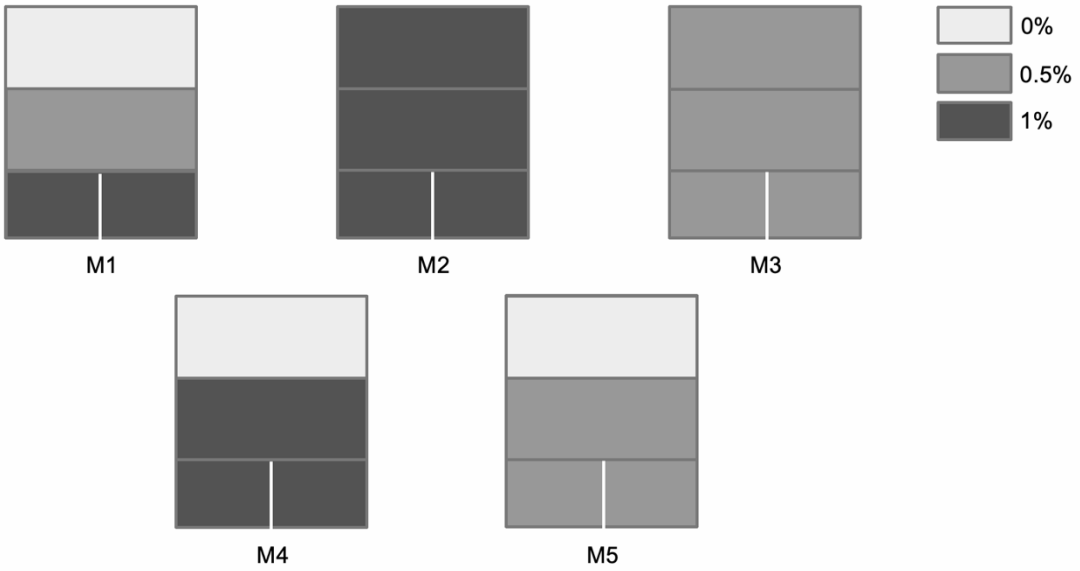

Figure 7.9: FG-FRC Mix Designs

Figure 7.10: Steel Fibers [17]

The compressive strength testing of the specimens adhered to the ASTM C39 standard. After undergoing a moist curing process for 28 days, three cylindrical samples from each mixture were chosen for evaluation. The dimensions of these cylinders were standardized at 4 inches (100 mm) in diameter and 8 inches (200 mm) in height. Table 7.5 shows the outcomes of these compressive strength assessments, along with the statistical analysis.

Table 7.5: Compressive Strength Results [17]

Fiber dosage	Compressive strength (MPa)	Mean (MPa)	Standard deviation (MPa)	Coefficient of variation (%)
0%	42.6 42.0 41.2	41.9	0.70	1.68
0.5%	39.1 40.4 38.4	39.3	1.02	2.58
1%	41.3 38.8 40.6	40.2	1.29	3.21

7.2.5. Testing Program and Sample Preparation

This study described the fabrication of fifteen beam specimens, allocated among five unique functionally graded mixtures, with each contributing three specimens to the research. The casting of these beams employed a novel targeted fiber injection technique, illustrated in the schematic provided in Figure 7.11. This technique utilized an electric pump designed for high-pressure operation, capable of achieving pressures up to 2.1 MPa. The pump unit pushed the mixture towards a dispensing head, which was connected to a PVC pipe. This PVC pipe was positioned at a 45-degree angle downward to ensure the fibers were correctly aligned during the extrusion process. Further details on the targeted fiber injection method are available in the previous study [17].

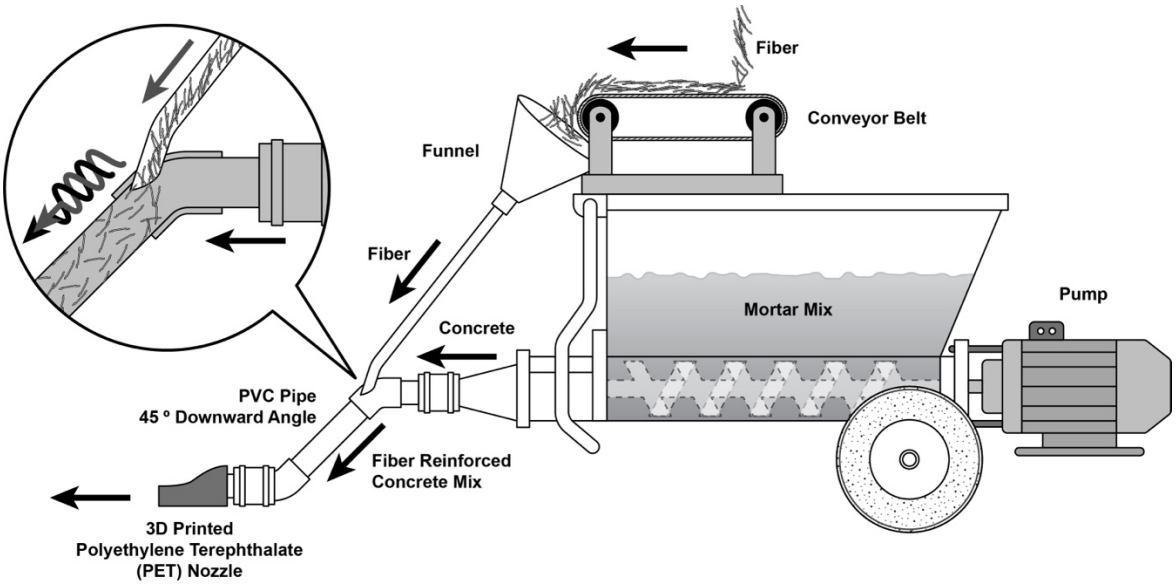

Figure 7.11: Schematic of Extrusion-based Fiber Injection Method [17]

The evaluation of the flexural properties was conducted using an MTS Insight 150 SL electromechanical universal testing machine. For precise measurement of the CMOD, a conventional clip gauge was utilized, boasting a maximum CMOD measurement capacity of 8 mm. The experimental tests proceeded at a uniform displacement rate of 0.1 mm min^{-1}, a standardization critical for the assurance of result reliability and comparability among all specimens.

7.2.6. X-ray Computed Tomography

The initial hypothesis of this study proposed that the extrusion-based casting would orient fibers parallel to the tensile stresses, thereby potentially enhancing the mechanical properties of the concrete. Furthermore, it suggested that a particular fiber dosage would be maintained across each layer of the FG-FRC. To verify these hypotheses, an in-depth analysis of the fractured specimens was performed using X-ray Computed Tomography (XCT) to determine and confirm the fiber dosage and orientation within each layer of FG-FRC [17].

A Toshiba Aquilion CT scanner was employed for the XCT investigations, facilitating two-dimensional, three-dimensional, and multiplanar reconstructions to provide a detailed insight into the material's internal structure. The XCT analysis was conducted using Horos™ software, designed for efficient visualization of CT data. This software facilitated the examination of three 2D perspectives of the scanned specimens: top, front, and cross-sectional views, with the latter being depicted in Figure 7.12. Further details on the XCT analysis of the FG-FRC layers were documented in earlier research [17].

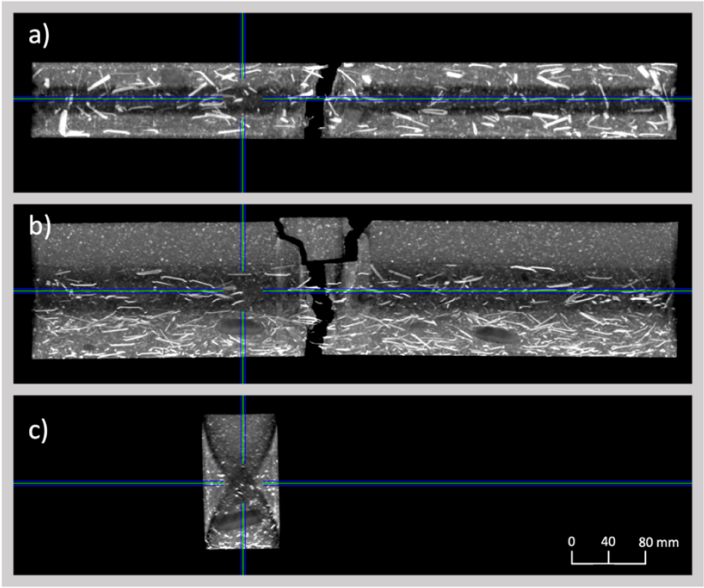

Figure 7.12: XCT Analysis Views: a) Top, b) Front, and c) Cross-sectional [17]

7.3. Test Results and Discussion

7.3.1. Fiber Orientation Factor

The evaluation of fiber count, volume percentage, and orientation angles within the three layers of the FG-FRC specimens is detailed in Table 7.6. Importantly, for the layers without fiber (0 % fiber), the average fiber content percentage was consistent with the intended 0 %, validating the precision of the targeted fiber dosage. In the layers designed for 0.5 % fiber content, the

observed average was approximately 0.4 %, slightly below the targeted 0.5 %. Likewise, the layers intended for 1 % fiber content showed an average of around 0.8 %, marginally below the 1 % purpose. While these variations exist, they are deemed acceptable, acknowledging the probability that some fibers may not be visible or detectable in the XCT scans. Thus, the fiber dosages identified from the XCT images agreed with the planned dosages, supporting the accuracy of the design specifications.

The analysis also revealed that the majority of fibers aligned with the beam length, with average orientation angles ranging from 2° to 3° in the 0.5 % fiber layers and from 2° to 7° in the 1 % fiber layers. This finding validated the initial hypothesis, indicating that the extrusion process effectively oriented the fibers parallel to tensile stresses. A detailed findings on the XCT analysis of the FG-FRC layers were discussed in previous research [17].

Table 7.6: Fiber Count and Orientation of FG-FRC Specimens [17]*

Fiber dosage/	**M1**			**M2**			**M3**			**M4**			**M5**		
Sample	#	%	θ	#	%	θ	#	%	θ	#	%	θ	#	%	θ
0% in Top Layer	2	0	8°	-	-	-	-	-	-	6	0	2°	2	0	2°
Mean	2	0	8°	-	-	-	-	-	-	6	0	2°	2	0	2°
0.5% in Top Layer	-	-	-	-	-	-	52	0.4	6°	-	-	-	-	-	-
0.5% in Middle Layer	63	0.5	3°	-	-	-	58	0.4	1°	-	-	-	53	0.4	1°
0.5% in Bottom Layer	-	-	-	-	-	-	64	0.5	3°	-	-	-	58	0.4	5°
Mean	63	0.5	3°	-	-	-	61	0.4	3°	-	-	-	56	0.4	2°
1% in Top Layer	-	-	-	89	0.6	2°	-	-	-	-	-	-	-	-	-
1% in Middle Layer	-	-	-	98	0.7	4°	-	-	-	95	0.7	3°	-	-	-
1% in Bottom Layer	120	0.9	7°	101	0.7	0°	-	-	-	126	0.9	9°	-	-	-
Mean	120	0.9	7°	96	0.7	2°	-	-	-	111	0.8	4°	-	-	-

* # represents the fiber count, % represents the fiber percentage, and θ represents the fiber orientation angle.

The key to optimizing the performance of fibers in reinforced composites is to align them parallel to the tensile stress that is created, as mentioned in previous research [53]. A deviation

from this alignment to a random orientation in three-dimensional space represents a significant reduction in performance. This principle aligns with classical composite theory, which suggests that the composite's elastic modulus is influenced by the elastic modulus and volume fraction of both the matrix and the fibers. The fiber orientation factor (K_o) is a critical adjustment variable in this context, with K_o= 1.0 denoting perfect parallel alignment to the tensile stress, K_o= 0 indicating perpendicular alignment, and K_o= 0.5 representing a uniform random orientation in three-dimensional space [54]. Given the observed fiber orientation angles ranging from 2° to 7° across all FG-FRC specimens, a K_o value of 1.0 would be appropriately assumed to all the flexural models. This assumption reflects the optimal fiber alignment within the specimens, suggesting a theoretical maximization of their mechanical efficacy in accordance with the principles of composite material behavior.

7.3.2. Flexural Properties

This research investigated the flexural properties of FG-FRC specimens, specifically examining the impact of differential fiber dosages across the layers on these properties. Such properties are crucial for the development of flexural models. The findings from these evaluations, including the limit of proportionality strength (f_L), and residual strengths at different deflections ($f_{0.5}$, $f_{1.5}$, $f_{2.5}$, $f_{3.5}$), are presented in Table 7.7. Furthermore, analyses concerning flexural toughness (T_4) and the equivalent flexural strength ratio ($R_{T,4}$) at a CMOD of 4 mm are presented in Table 7.8. The load-CMOD curves for the FG-FRC specimens, spanning models M1 to M5, are illustrated in Figure 7.13 through Figure 7.17, respectively.

To analyze the effect of varying fiber dosages across each layer of the FG-FRC mixtures, a statistical methodology was applied, specifically a one-tailed two-sample t-test with a 95 %

confidence interval. A key factor in this analysis was the inclusion of a notch in the specimens, equivalent to one-third of their depth, matching the depth of the first layer. This configuration necessitated the exclusion of the first layer from the comparative analysis to ensure accuracy. Employing this statistical approach facilitated a detailed comparison among the mixtures, shedding light on the influence of alterations in fiber content within each layer on the composite's overall flexural performance.

Table 7.7: Flexural Properties of FG-FRC Specimens

Sample	P_L (N)	f_L (MPa)	$f_{0.5}$ (MPa)	$f_{1.5}$ (MPa)	$f_{2.5}$ (MPa)	$f_{3.5}$ (MPa)
M1_1	3506	3.944	2.754	2.942	2.817	2.762
M1_2	4084	4.248	3.231	2.899	2.188	1.849
M1_3	3209	3.574	4.039	3.711	2.959	2.199
Mean	3600	3.922	3.341	3.184	2.655	2.270
M2_1	2954	3.842	3.992	5.637	5.397	4.367
M2_2	3983	4.436	4.062	5.324	4.792	4.305
M2_3	3447	4.121	5.891	5.789	4.760	4.148
Mean	3461	4.133	4.648	5.583	4.983	4.273
M3_1	2351	3.886	3.144	4.699	4.413	3.681
M3_2	3204	3.678	3.581	3.333	3.131	2.772
M3_3	2596	3.136	3.437	3.188	2.649	2.089
Mean	2717	3.567	3.387	3.740	3.398	2.847
M4_1	2705	3.372	3.575	3.641	3.430	3.242
M4_2	4279	5.064	4.781	4.360	3.431	2.613
M4_3	4256	4.985	5.584	5.521	5.081	4.144
Mean	3747	4.474	4.647	4.507	3.981	3.333
M5_1	3121	3.732	3.862	3.634	2.359	1.577
M5_2	3727	4.366	4.538	4.987	3.338	2.633
M5_3	2858	3.489	2.673	2.543	2.552	2.191
Mean	3235	3.862	3.691	3.721	2.750	2.134

Table 7.8: Flexural Toughness Properties of FG-FRC Specimens

Sample	T_4 (J)	$R_{T,4}$ (%)
M1_1	10.05	47.8
M1_2	9.93	40.5
M1_3	11.3	58.7
Mean	10.43	49.0
M2_1	14.62	82.5
M2_2	16.61	69.5
M2_3	16.52	79.9
Mean	15.92	77.3
M3_1	9.66	68.5
M3_2	10.71	55.7
M3_3	9.38	60.2
Mean	9.92	61.5
M4_1	11.05	68.1
M4_2	12.57	49
M4_3	17.08	66.9
Mean	13.57	61.3
M5_1	9.48	50.6
M5_2	13.02	58.2
M5_3	8.14	47.5
Mean	10.21	52.1

The analysis of the flexural properties of the FG-FRC specimens yielded several key observations. Notably, there was no significant variation in the f_L across the FG-FRC specimens, indicating a consistent initial response to loading. Furthermore, an increase in fiber dosage within the bottom layers, which are subjected to tensile stresses, appeared to enhance the flexural residual strengths at various CMOD values. This enhancement was evident when comparing the M1 specimens, which contained a 0.5 % fiber dosage in their bottom layers, with the M4 specimens, which had a 1 % fiber dosage in their second layers. Despite these differences in residual strengths, there were no notable disparities in flexural toughness between M1 and M4 specimens.

The study also examined the effect of fiber dosage in the top layers of FG-FRC specimens, areas primarily under compressive stresses. In this regard, comparisons were made between

specimens with different fiber dosages: M2 (with a 1 % fiber dosage) was compared to M4 (with no fibers) and M3 (with a 0.5 % fiber dosage) to M5 (also with no fibers). The findings suggested that incorporating a 1 % fiber dosage in the top layers significantly enhances the flexural residual strengths at higher CMOD values. However, a 0.5 % fiber dosage in these layers did not yield a significant change in flexural residual strengths. Regarding the flexural toughness, significant improvements, as measured by the $R_{T,4}$ values, were observed only with the addition of a 1 % fiber dosage in the top layers. These observations underline the nuanced impact of fiber dosage and distribution within different layers of FG-FRC specimens on their flexural properties. Further insights into the specific effects of fiber dosage in each layer are found in previous research [17].

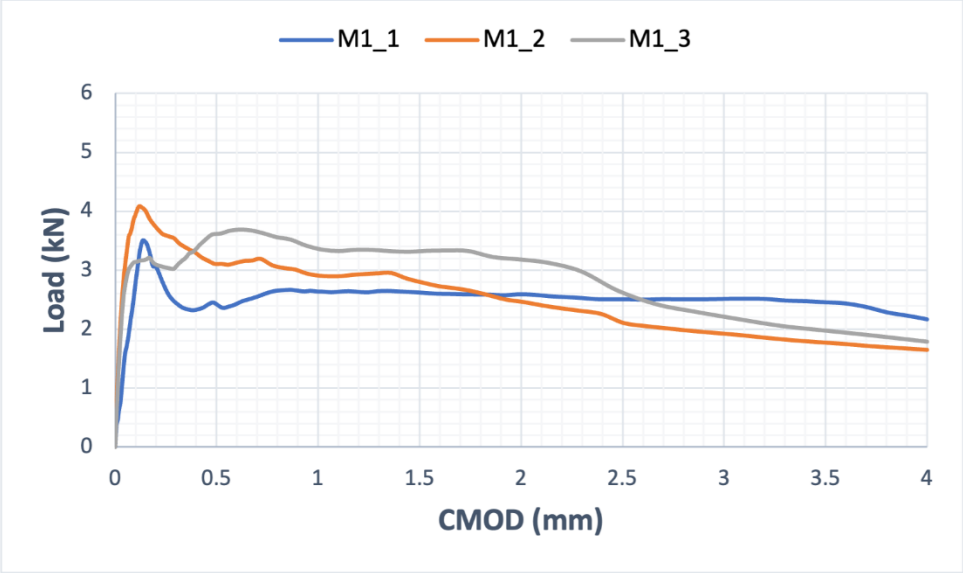

Figure 7.13: Load-CMOD Curve for M1 Specimens

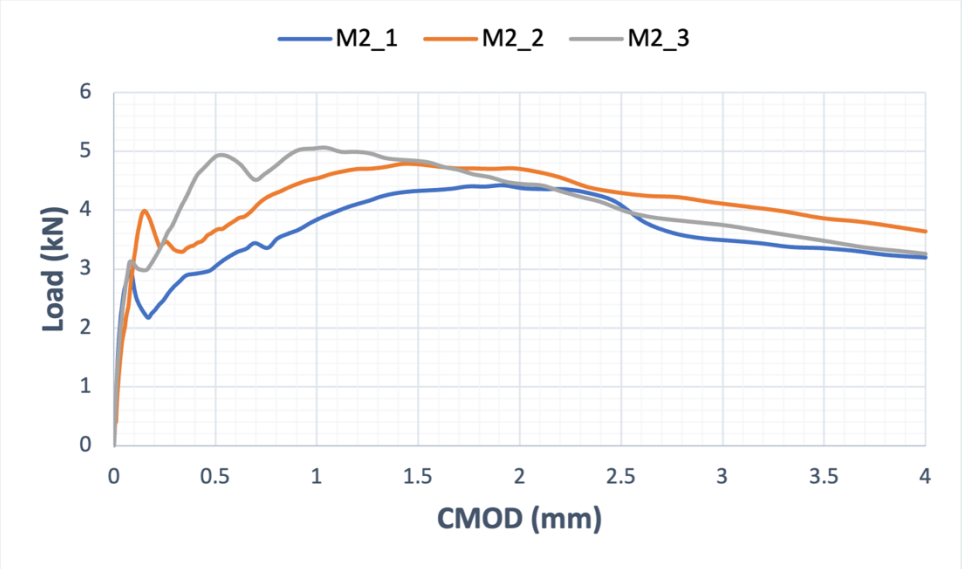

Figure 7.14: Load-CMOD Curve for M2 Specimens

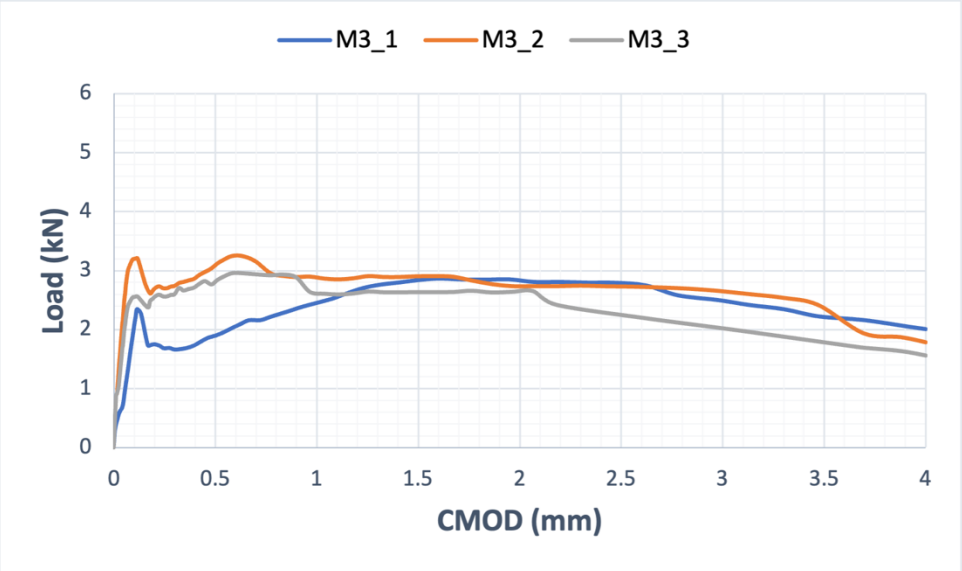

Figure 7.15: Load-CMOD Curve for M3 Specimens

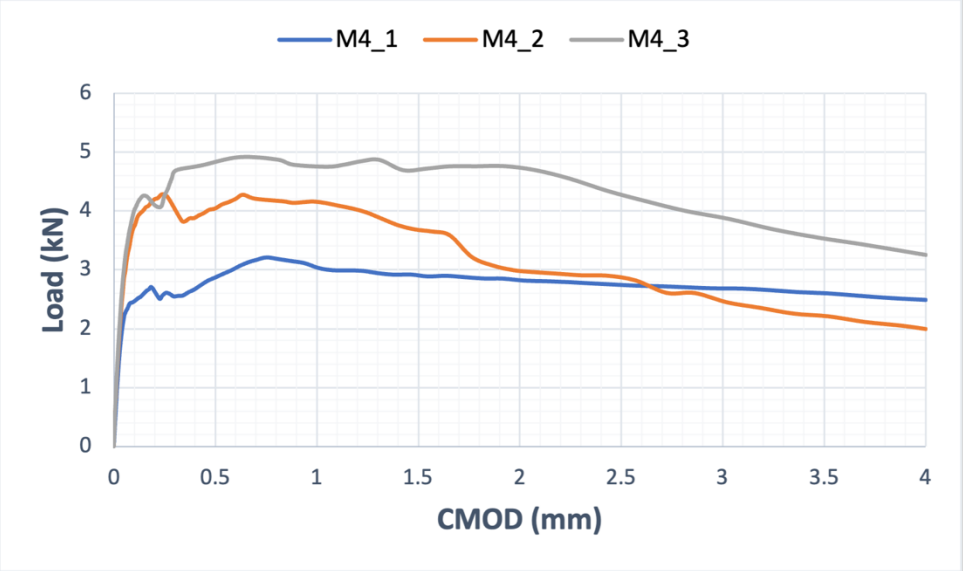

Figure 7.16: Load-CMOD Curve for M4 Specimens

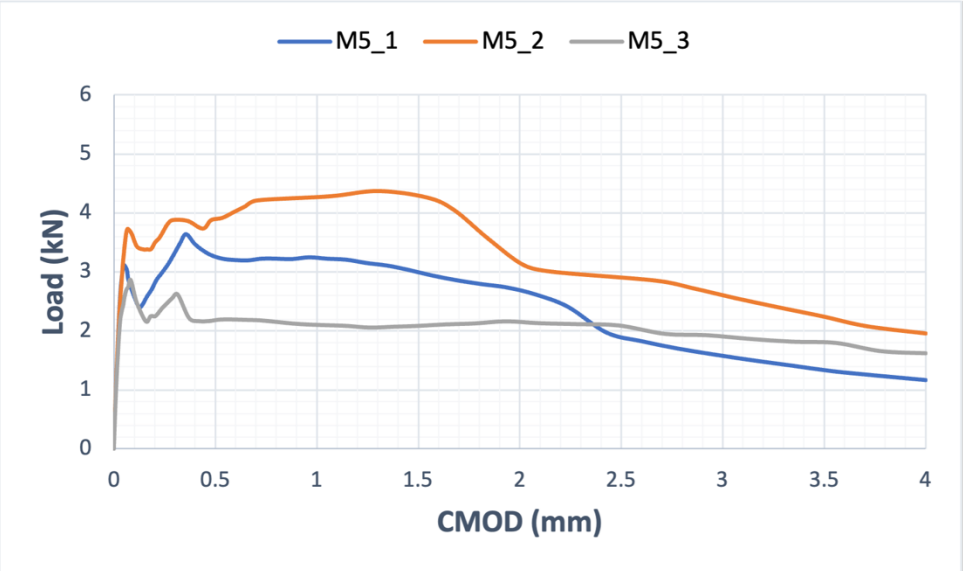

Figure 7.17: Load-CMOD Curve for M5 Specimens

7.3.3. Flexural Models for FRC

Within this study, three flexural models were examined: ER-465, fib-L, and fib-RP. The outcomes regarding the parameters of these models, along with the calculated ultimate moment values for each, are presented in Table 7.9. The ultimate moment, in this context, denotes the

maximum moment that a FRC section can withstand prior to failure. Analyses suggest that the ER-465 model adopts a more conservative stance relative to the fib models, which is attributed to its design consideration for the effects of conventional steel reinforcement, thereby enhancing the section's ultimate moment capacity. Additionally, a significant finding from the study is the potential for a hardening tensile behavior in FRC sections that incorporate fibers across all layers. This phenomenon was particularly observed in the M2_1 specimen, which contained a 1 % fiber dosage in all three layers, and the M3_1 specimen, with a 0.5 % fiber dosage across all layers. Such behavior indicates an improvement in the section's ability to resist increasing tensile forces without immediate failure, a characteristic beneficial for structural applications requiring enhanced durability and resilience.

Furthermore, the research revealed a notable concordance between the ER-465 and fib-L models regarding the tensile behavior prediction of FRC sections. This alignment was consistent across all FRC specimens, indicating that whenever the ER-465 model predicted a softening behavior, the fib-L model reflected a similar trend, and the same held true for predictions of hardening behavior. This consistency underscores the reliability of these models in prediction the tensile performance of FRC, providing valuable insights for the design and analysis of FRC structures.

Table 7.9: Parameter of Flexural Models

Sample/ Model	*ER 465 Model III*			*fib Rigid-plastic*		*fib Linear*		
	f_{ns} (MPa)	f_{nu} (MPa)	M_u $(KN\,mm)$	f_{Ftu} (MPa)	M_u $(KN\,mm)$	f_{Fts} (MPa)	f_{Ftu} (MPa)	M_u $(KN\,mm$
M1_1	0.752	0.661	0.269	0.939	0.376	1.239	0.934	0.414
M1_2	0.467	0.467	0.198	0.729	0.316	1.453	0.617	0.387
M1_3	0.555	0.555	0.219	0.987	0.399	1.817	0.897	0.486
Mean	0.591	0.561	0.229	0.885	0.364	1.503	0.816	0.429
M2_1	1.089	1.093	0.365	1.799	0.622	1.793	1.873	0.666
M2_2	1.109	1.060	0.420	1.597	0.645	1.828	1.632	0.686
M2_3	1.608	0.711	0.370	1.587	0.597	2.651	1.526	0.716
Mean	1.269	0.955	0.385	1.661	0.621	2.091	1.677	0.689
M3_1	0.858	0.956	0.268	1.471	0.401	1.415	1.522	0.434
M3_2	0.978	0.520	0.258	1.044	0.409	1.612	1.008	0.474
M3_3	0.527	0.527	0.192	0.883	0.329	1.547	0.845	0.402
Mean	0.788	0.668	0.239	1.133	0.380	1.525	1.125	0.437
M4_1	0.976	0.706	0.280	1.144	0.413	1.609	1.146	0.470
M4_2	0.660	0.660	0.244	1.144	0.435	2.151	1.065	0.543
M4_3	1.524	0.747	0.376	1.694	0.651	2.513	1.659	0.747
Mean	1.053	0.704	0.300	1.327	0.500	2.091	1.290	0.587
M5_1	0.398	0.398	0.147	0.786	0.296	1.738	0.705	0.395
M5_2	0.665	0.665	0.249	1.113	0.428	2.042	1.038	0.527
M5_3	0.730	0.433	0.192	0.851	0.314	1.203	0.849	0.356
Mean	0.598	0.499	0.196	0.917	0.346	1.661	0.864	0.426

The predictability of each flexural model was assessed through a comparative analysis between the ultimate loads predicted by the models and those obtained from experimental data. The ultimate loads derived from the models are based on the ultimate moments, which represent the maximum moment a section can resist before failure. Conversely, determining the ultimate load from experimental observations, particularly in the context of FRC testing, involves determining the stage at which the material cannot withstand further load increases, a condition marked by phenomena such as fiber pullout or concrete cracking. This critical point is typically identified on the load-CMOD curve as the stage where the load begins to decline while the CMOD

continues to rise, indicating that the material has exceeded its ultimate strength and is undergoing failure.

Table 7.10 provides a crucial evaluation of the predictability of various flexural models by comparing the percent error between the models' predicted ultimate load values (P_{req}) and the actual experimental outcomes (P_{actual}), serving as a measure of each model's accuracy. The analysis underscores the fib-L model as the most predictively accurate, evidenced by its lowest percent error, whereas the ER-465 model exhibited the least predictability, marked by the highest error rates across all FG-FRC mixtures, as depicted in Figure 7.18.

A significant observation from the analysis is the enhanced predictability of all flexural models in FG-FRC mixtures that incorporate uniform fiber dosages throughout their layers. This trend was particularly noticeable in the M2 specimens, which featured a 1 % fiber dosage in all three layers, yielding the smallest percent error among the models. This outcome aligns with the assumptions set by the tested flexural models, which are designed for homogeneous, single-layer FRC. However, the models demonstrated lower predictability in FG-FRC sections lacking fibers in their top layers (M1, M4, and M5), signaling a potential area for model refinement. Specifically, these findings suggest a need for adjustments within the models to reflect the impact of the functionally graded fiber distribution more accurately across the layers of FRC sections.

In summary, the superior accuracy of the fib-L model in predicting the flexural strength of steel FRC sections accentuates its value in the structural design and analysis domain. The overall results not only advocate for the fib-L model as a reliable tool for FRC analysis but also request further model optimization to account for variations in fiber dosages within composite layers. This evolution of flexural models will undoubtedly contribute to more precise and effective design

strategies for FRC structures, enhancing their application and performance in the construction industry.

Table 7.10:Predictability of Flexural Models

Sample/ Model	***Test Data***	***ER-465 Model III***		***fib Rigid-plastic***		***fib Linear***	
	P_{actual} (N)	P_{req} (N)	$Error$ (%)	P_{req} (N)	$Error$ (%)	P_{req} (N)	$Error$ (%)
M1_1	2766	1793	54	2504	10	2762	0
M1_2	2951	1320	124	2104	40	2584	14
M1_3	3692	1460	153	2657	39	3241	14
Mean	3136	1524	110	2422	30	2862	9
M2_1	4447	2433	83	4149	7	4439	0
M2_2	4788	2800	71	4302	11	4570	5
M2_3	5060	2467	105	3981	27	4770	6
Mean	4765	2567	86	4144	15	4593	4
M3_1	2910	1787	63	2670	9	2893	1
M3_2	3247	1720	89	2728	19	3160	3
M3_3	2962	1280	131	2193	35	2679	11
Mean	3040	1596	94	2530	21	2911	5
M4_1	3212	1867	72	2752	17	3130	3
M4_2	4274	1627	163	2899	47	3619	18
M4_3	4980	2507	99	4338	15	4978	0
Mean	4155	2000	111	3330	26	3909	7
M5_1	3644	980	272	1973	85	2633	38
M5_2	4367	1660	163	2850	53	3516	24
M5_3	2616	1280	104	2091	25	2376	10
Mean	3542	1307	180	2305	54	2842	24

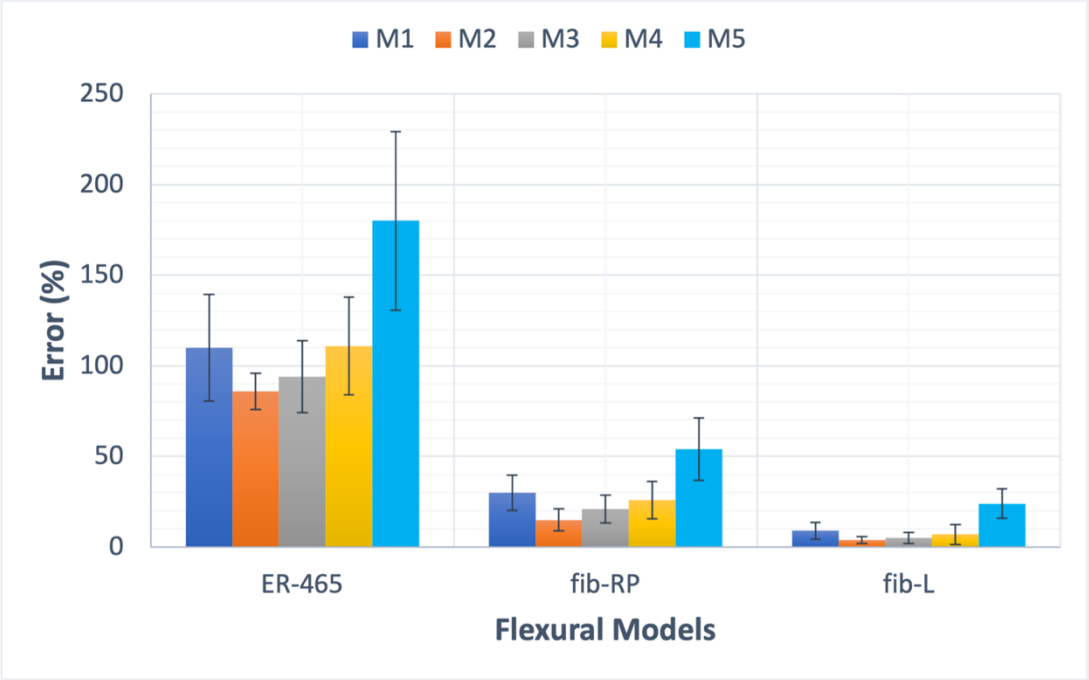

Figure 7.18: Percentage of Error Comparison for Flexural Models

7.3.3.1. ER-465 Flexural Model III Refinement

The ER-465 flexural model, in its evaluation of FG-FRC, exhibited the lowest level of predictability, marked by the highest error rates across all mixtures. This outcome can be primarily attributed to the model's theoretical foundations, which are designed to account for the effects of conventional steel reinforcement, an element which is not presented in the tested specimen's sections. Consequently, the prediction of ER-465 model tends to adopt conservative values compared to the actual experimental data, indicating a need for parameter adjustment to improve its predictive accuracy.

A key variable within the ER-465 model is the size factor (K_s), which is implemental in determining the required and available flexural strength based on the size of the FRC member. For members with a cross-sectional area of 0.023 m² or larger, a K_s value of 1.0 is prescribed. Conversely, for smaller sections, K_s is calculated using the formula $0.68 + 0.31bd_{sp}$, capped at a

maximum value of 1.0. In this study, the cross-sectional area of the FRC sections fell below 0.023 m², which, according to the formula, would typically result in a K_s value of 0.68, a factor that may prove excessively conservative.

In response to this observation, a strategic decision was made to apply the maximum K_s value of 1.0 across all FG-FRC specimens, aiming to achieve a more accurate reflection of strength predictability. As detailed in Table 7.11, the adoption of this approach led to a significant reduction in the percentage error, exceeding 60 % improvement across all FG-FRC mixtures. This outcome, verified by a comparative analysis of predicted ultimate load values and actual experimental data, as illustrated in Figure 7.19, revealed a trend line that closely aligns with observed behaviors. Such adjustments not only underscore the enhanced predictability achieved through the application of the maximum K_s value but also highlight the critical importance of refining model parameters to accurately predict the flexural behavior of FG-FRC specimens. This iterative process of model refinement serves to bridge the gap between theoretical assumptions and empirical data, facilitating more reliable and accurate predictions of FRC structural performance.

Table 7.11:Predictability of ER-465 Model Using Different Values of K_s

Sample/ Model	***Test Data***	***ER-465 Model III (K_s=0.68)***		***ER-465 Model III (K_s=1.0)***	
	$\boldsymbol{P_{actual}}$ $(\boldsymbol{N})$	$\boldsymbol{P_{req}}$ $(\boldsymbol{N})$	$\boldsymbol{Error}$ (%)	$\boldsymbol{P_{req}}$ $(\boldsymbol{N})$	$\boldsymbol{Error}$ (%)
M1_1	2766	1793	54	2613	6
M1_2	2951	1320	124	1920	54
M1_3	3692	1460	153	2127	74
Mean	3136	1524	110	2220	45
M2_1	4447	2433	83	3533	26
M2_2	4788	2800	71	4060	18
M2_3	5060	2467	105	3587	41
Mean	4765	2567	86	3727	28
M3_1	2910	1787	63	2600	12
M3_2	3247	1720	89	2500	30
M3_3	2962	1280	131	1867	59
Mean	3040	1596	94	2322	34
M4_1	3212	1867	72	2707	19
M4_2	4274	1627	163	2367	81
M4_3	4980	2507	99	3640	37
Mean	4155	2000	111	2905	46
M5_1	3644	980	272	1427	155
M5_2	4367	1660	163	2413	81
M5_3	2616	1280	104	1867	40
Mean	3542	1307	180	1902	92

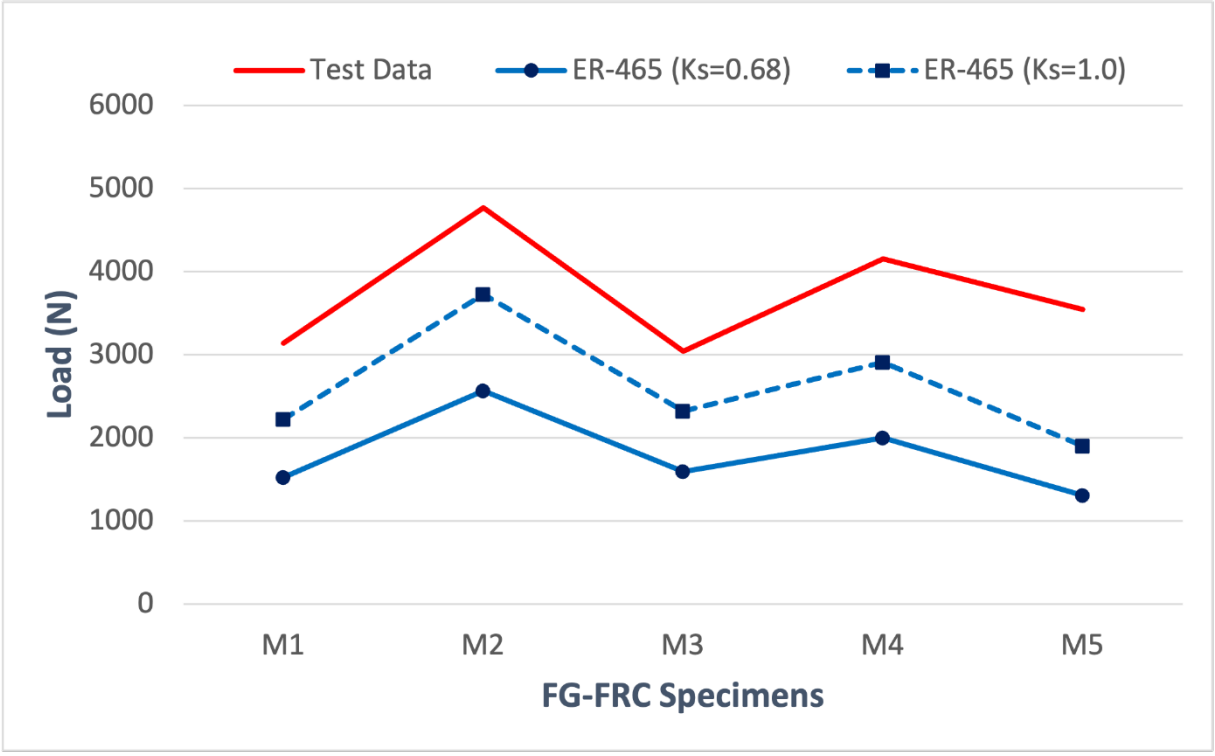

Figure 7.19: Prediction Comparison of ER 465 Model Using Different Values of K_s

7.3.4. Development of Functionally Graded Factor

Given the inherent design of the ER-465, fib-RP, and fib-L flexural models for homogeneous FRC sections, the study's findings highlight the necessity for adjustments to these models to accurately reflect the impact of functionally graded fiber distribution within the layers of FRC sections. Although the fib-L model emerged as a reliable tool for analyzing FG-FRC sections, it, alongside its counterparts, requires further refinement to account for variations in fiber dosages across different composite layers. To address this, the introduction of a new factor, termed the functionally graded factor (K_{FG}), is proposed to account for the effect of having functionally graded layers within FRC sections, thereby enabling the flexural models to offer more accurate predictions for the behavior of FG-FRC structures.

The formulation of the K_{FG} factor is based on the concept of a weighted average that considers both the fiber volume and the layer location (top or bottom). The process of calculating the weighted average involves assigning a weight to each layer's fiber volume, reflecting its contribution to the overall structural behavior. This approach ensures that the varying importance of each layer, based on its position and fiber content, is accurately represented. The calculation of the weighted average then proceeds by multiplying each fiber dosage by its corresponding weight, followed by summing these products. Comparing this weighted average to a simple average yields a ratio (K_{FG}). This ratio illustrates how the actual distribution of fibers within the FG-FRC section diverges from a hypothetical uniform distribution, offering insights into the material's expected performance under flexural loading. Since the FRC tensile behavior calculations, in the flexural models, depend on the residual strengths obtained from the experimental data, the corresponding weight, in the weighted average, was calculated based on the contribution of fiber volume in each layer (bottom or top) to the residual strengths.

The effect of each layer can be seen as a proportion of the total potential increase if both changes happened independently. Although this is a simplification, it will provide a rough estimate of the relative importance of fiber content in each layer on the overall strength. Therefore, from the results in Table 7.7, the examination of mixtures with differing fiber volumes in their bottom layers (1 % in M4 vs. 0.5 % in M1 and M5) indicated that an increase in bottom layer fibers could lead to about 50 % enhancement in overall residual strengths. Conversely, an assessment of top layer fiber content variations (0.5 % in M3 vs. 0 % in M1 and M5) revealed about 27 % increase in overall residual strengths due to the presence of fibers in the top layers.

From this comparative analysis, the relative contribution of fiber content changes in the bottom layer was estimated to be around 65 % towards the overall strength enhancement, whereas

the top layer's contribution was approximated at 35 %. This difference underscores the bottom layer's predominant role in augmenting the structural integrity of FG-FRC sections. Consequently, the functionally graded factor, K_{FG}, is calculated using Equation 14, where V_{fb} and V_{ft} represent the fiber volume in the bottom and top layers, respectively.

$$K_{FG} = \frac{2\left(0.65V_{fb} + 0.35V_{ft}\right)}{V_{fb} + V_{ft}} \tag{14}$$

The K_{FG} introduces a meticulous approach to evaluating the flexural strength of FG-FRC sections, particularly those with a higher fiber volume in their bottom layers. This equation produces a ratio that offers insights into the distribution and significance of different fiber volumes within the composite layers. A K_{FG} value of 1.0 indicates a balanced distribution, where the weighted average aligns with the simple average, suggesting uniform weight across all values. Conversely, a K_{FG} value greater than 1.0 indicates that the weighted average is higher than the simple average, suggesting an uneven distribution that elevates the average due to the uneven emphasis on higher fiber volumes, primarily in the bottom layer. The equation limits the K_{FG} value at 1.3, reflecting the designed scope of its application to FG-FRC sections with such a fiber distribution profile, making ratios below 1.0 inapplicable.

The implementation the K_{FG} factor into the flexural models modifies the calculation of both the serviceability residual tensile strength and the ultimate residual tensile strength. For the ER-465 model, K_{FG} adjustments are applied to Equations 4, 5, and 6. Similarly, in the fib models, K_{FG} is integrated into Equation 8 for the linear model and Equation 11 for the rigid-plastic model. The inclusion of K_{FG} aims to refine these models by accommodating the heterogeneity of fiber distribution across FG-FRC sections.

Subsequent comparative analyses, illustrated through Figure 7.20 to Figure 7.22, show the impact of incorporating K_{FG} into the ER-465, fib-RP, and fib-L models, respectively. Notably, the modified ER-465 model also underwent adjustments for both K_s and K_{FG} to tailor the model more closely to the specifics of FG-FRC sections. The results from these analyses highlight a notable reduction in percentage error across all flexural models after the integration of K_{FG}, with a particularly pronounced improvement observed in FG-FRC mixtures featuring varied fiber dosages across their layers. This enhancement in predictability underscores the value of K_{FG} as a factor in refining the flexural models, ensuring a more accurate representation of FG-FRC sections' performance.

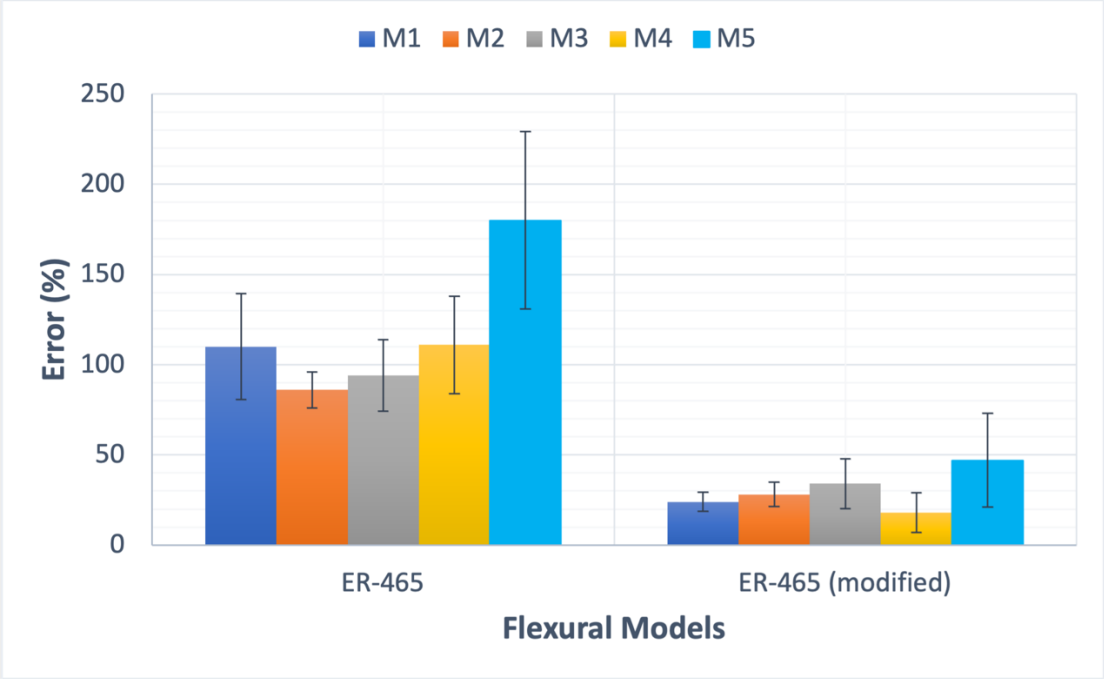

Figure 7.20: Percentage of Error Comparison for ER 465 Flexural Models

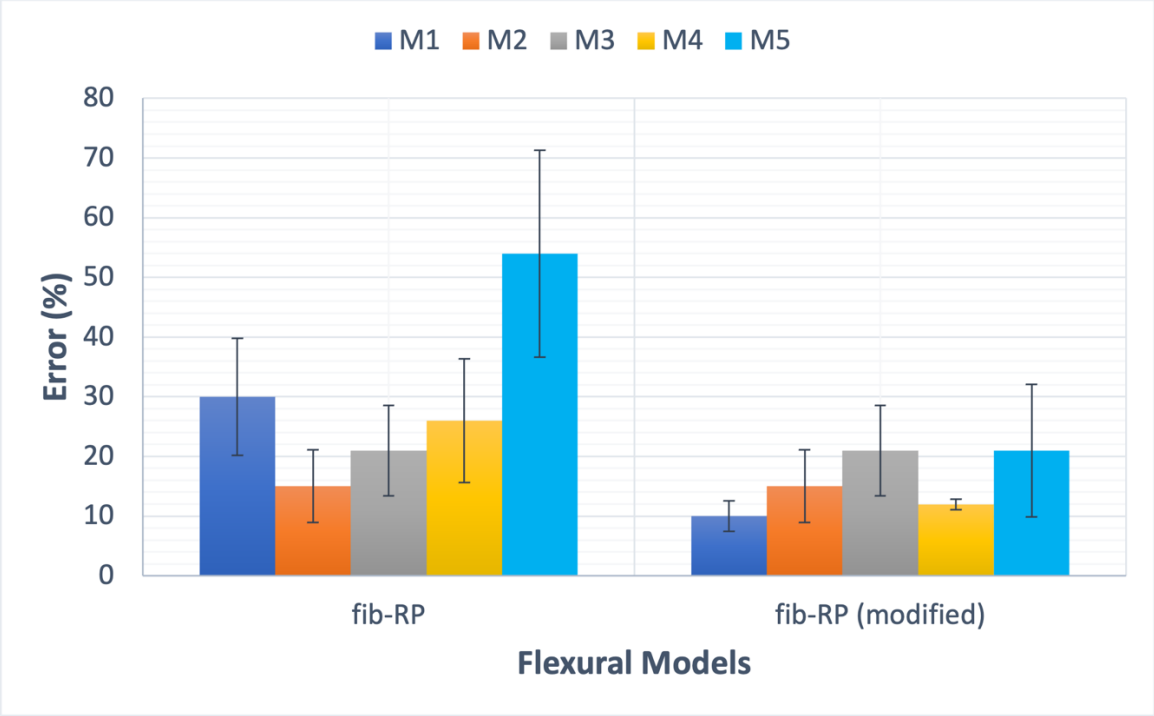

Figure 7.21: Percentage of Error Comparison for fib Rigid-Plastic Flexural Models

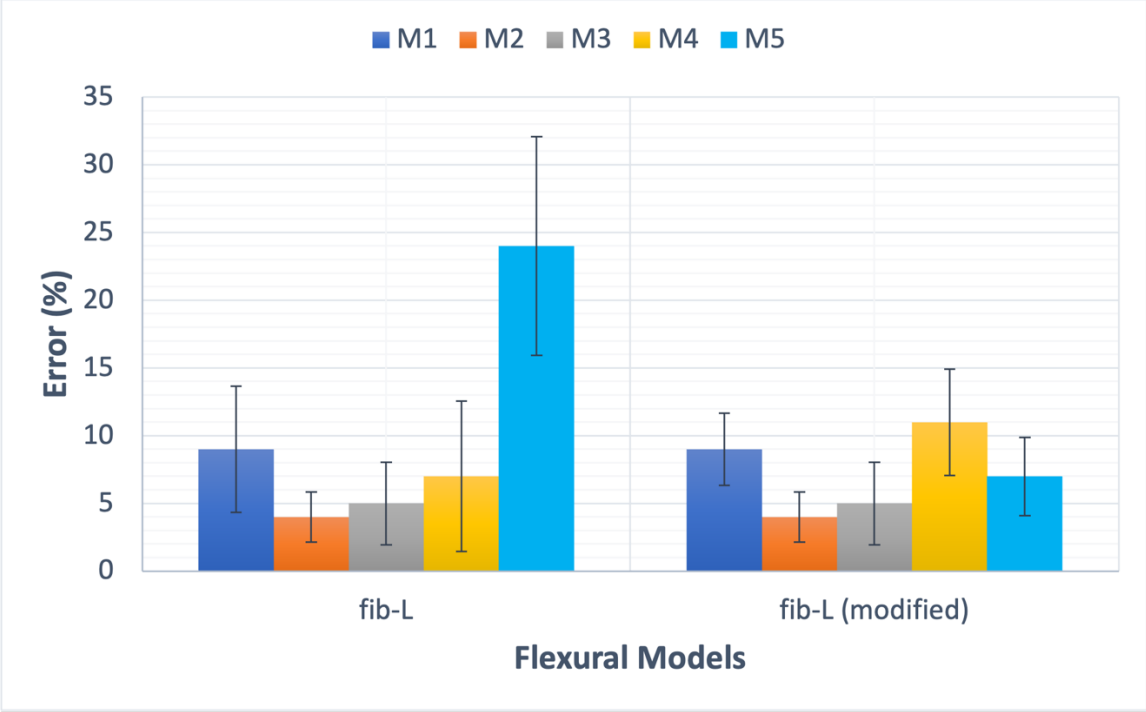

Figure 7.22: Percentage of Error Comparison for fib Linear Flexural Models

7.3.5. FG-FRC Classification

The classification FG-FRC mixtures within this study was determined based on two critical parameters: SLS and ULS, represented by the post-cracking residual strengths $f_{0.5k}$ and $f_{2.5k}$, respectively. These values, which indicates of the material's performance under service conditions and its capacity to withstand ultimate loads prior to failure, were calculated using statistical methods and conservative engineering principles. Specifically, applying a t-score with a 5th percentile ensures that the characteristic values, $f_{0.5k}$ and $f_{2.5k}$, are not exceeded by 95 % of the observed strength population.

The material's classification was derived from analyzing two distinct points on the nominal tensile stress (σ_N)-CMOD curve, which correspond to the SLS and ULS phases, as shown in Figure 7.23. This system offers insights into the ductility and strength of the material post-initial cracking. Table 7.12 shows the FG-FRC material classification results for all mixtures. By meeting Equations 12 and 13 from Section 7.2.3, it appears that all FG-FRC mixtures could potentially replace traditional reinforcement bars in structural elements at the ULS. This improved performance characteristics at ULS, positions FRC as a promising alternative to traditional reinforcement methods, offering the potential for safer, more resilient, and cost-effective construction solutions.

Mixtures with a 1 % fiber dosage in their bottom layer, excluding the first layer which contained a notch, exhibited an $f_{0.5k}$ value of about 3 MPa, similar to those mixtures with a 0.5 % fiber dosage across all layers. Conversely, mixtures lacking fibers in their top layers and containing only a 0.5 % fiber dosage in their bottom layers recorded $f_{0.5k}$ values of about 2 MPa. This suggests that introducing fibers to the top layer and increasing the fiber dosage in the bottom layer enhances the material's service condition behavior.

Furthermore, Figure 7.23 illustrates that all FG-FRC mixtures displayed a softening behavior, with the exception of the M2 mixture, which showed a hardening behavior. This indicates that a 1 % fiber content across all layers ensures the material's hardening capacity against ultimate loads leading to failure. Additionally, comparing the M3 mixture, with a 0.5 % fiber content across all layers, to the M4 mixture, with a 1 % fiber content solely in the bottom layers, it is evident that the M3 exhibited a more pronounced softening behavior. This underscores the benefit of increasing fiber content in the bottom layer, subjected to tensile stresses, for improving the overall performance of FRC sections. The similarity in behavior between M1 and M5 mixtures was expected, given that, excluding the notched layer, they share identical fiber content across their respective layers.

Table 7.12: FG-FRC Material Classification Results

Mixture	Classification	Behavior	Potential Replacement
M1	2-b	Softening	YES
M2	3-e	Hardening	YES
M3	3-a	Softening	YES
M4	3-b	Softening	YES
M5	2-b	Softening	YES

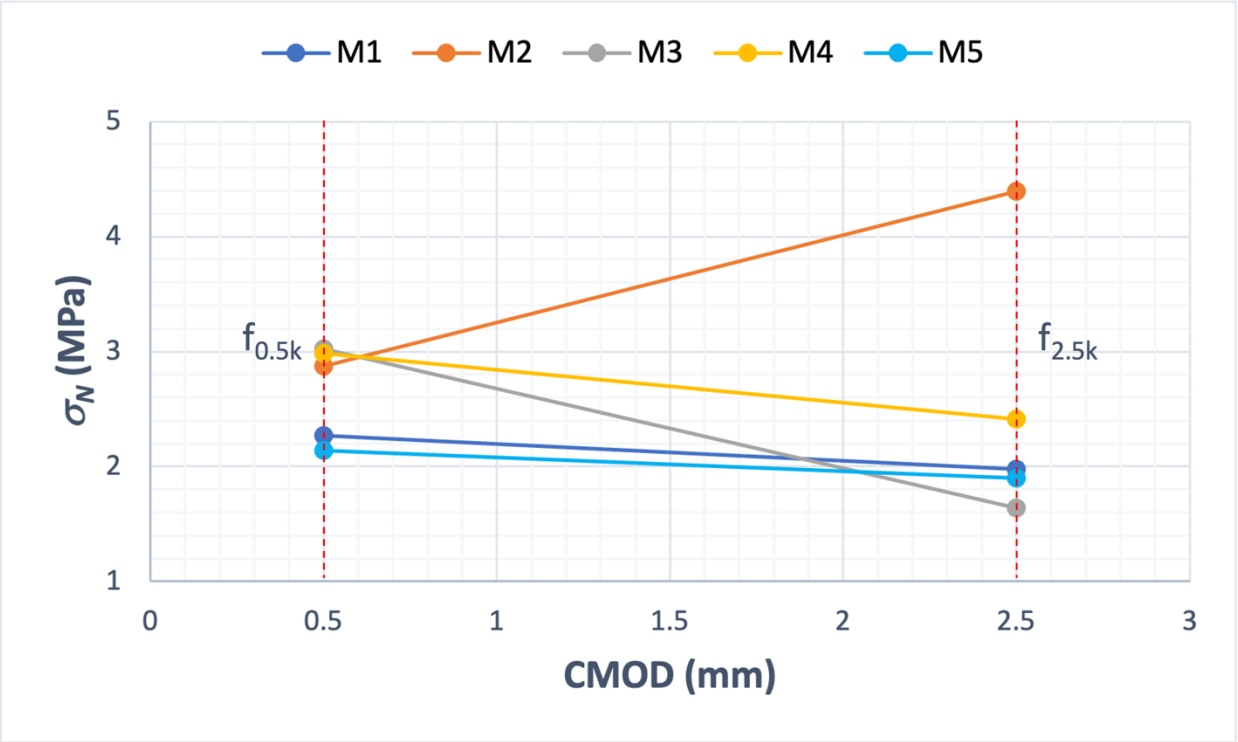

Figure 7.23: FG-FRC Material Classification

7.4. Conclusion

This research delved into the efficacy of three distinct flexural models, ER-465, fib-L, and fib-RP, applied to FG-FRC specimens, with a focus on model predictability and their correlation with actual experimental data derived from three-point bending tests on notched beams. The study's analysis hinged on two primary factors: the fiber dosage and the fiber orientation within the FG-FRC layers. The principal outcomes of this investigation include:

1. The fiber dosages, determined through XCT, corroborated the initially proposed dosages, with a significant proportion of fibers aligning with the direction of concrete flow. This alignment underscored the effectiveness of the targeted fiber injection extrusion technique, leading to the adoption of a fiber orientation factor of 1.0 in the flexural models.

2. Although no significant variance was observed in the f_L across the FG-FRC specimens, an increase in fiber dosage within the bottom layers, which bear tensile stresses, was found to improve the flexural residual strengths at varying CMOD values.
3. The ER-465 model was considered more conservative compared to the fib models, a distinction attributed to its design considerations for the inclusion of conventional steel reinforcement, which in turn, potentially increases the section's ultimate moment capacity.
4. The fib-L model was found as the most accurate in predicting FRC flexural strength, evidenced by the minimal percent error, whereas the ER-465 model was identified as the least accurate, exhibiting the maximum error across all FG-FRC mixtures.
5. The introduction of the K_{FG} factor into flexural models marked a pivotal advancement in accurately predicting the structural behavior of FG-FRC sections, thereby enhancing the reliability and effectiveness of these models in engineering applications.
6. A significant finding of the research is the potential of achieving a hardening tensile behavior in FRC sections that incorporate a 1 % fiber content across all layers.
7. All FG-FRC mixtures have the potential to replace traditional reinforcing bars in structural components at the ULS.
8. The incorporation of fibers into the top layer and the increase of fiber dosage in the bottom layer are strategies that evidently improve the material's performance under SLS.

7.4.1. Limitation and Future Work

This investigation sheds light on the potential advantages of employing diverse flexural models on a novel casting methodology, which integrates a pump extrusion process with fiber

injection to enhance the properties of FRC. However, it also identifies key areas that demand further exploration and refinement. A notable limitation encountered during the study was the extrusion pump's inability to accommodate mixtures containing coarse aggregate, leading to an exclusive focus on mortar-based experiments. This constraint may influence the applicability and accuracy of the flexural prediction models developed, though the findings remain significantly relevant, especially for industries engaged in 3D printing with mortar, reflecting the current technological limitations. The study also underscores the imperative for broader applications within the construction industry and highlights the necessity for future research endeavors to assess the impact of including coarse aggregate on fiber orientation and the overall performance and strength prediction of concrete will be crucial for advancing the field.

Additionally, this research points out the limited exploration of fiber types and dosages as a significant area for future investigation. The study's current scope, confined to specific fiber types and proportions, suggests an expansive opportunity for subsequent research to explore a wider collection of fibers and their dosages. Such investigations are anticipated to enhance the understanding of how different fibers and their respective proportions affect the predictability of flexural models in FRC.

While the integration of the K_{FG} factor significantly improves the accuracy of flexural models for FG-FRC sections, it presents certain limitations that pave the way for future research. One notable limitation is the factor's current calibration, which is primarily based on empirical data from specific FG-FRC configurations. This limitation suggests that the K_{FG} factor might not fully represent the complex interactions and behaviors in FRC sections with highly variable fiber volumes or unconventional layering techniques not examined in the initial study. Future work should focus on extending the applicability of the K_{FG} factor by incorporating a broader range of

FG-FRC configurations and testing conditions. The development of a universal framework for integrating the K_{FG} factor into other predictive models would be invaluable, offering engineers and researchers a versatile tool for designing and analyzing the next generation of fiber-reinforced composites.

In conclusion, this study acts as an essential initial step towards exploring the complexities of flexural models in FG-FRC. It not only reveals the potential benefits and limitations of these models within the context of an innovative casting technique but also sets the stage for future research. The exploration of advancements in strength prediction, through developing constitutive models, presents an exciting prospect for the field of structural and material engineering, promising significant contributions to the development of more reliable and efficient building materials.

7.5. Authorship Contribution Statement

The authors confirm their contributions to the paper as follows: Rashed Alarrak: Writing – review & editing, Writing – original draft, Visualization, Validation, Methodology, Investigation, Formal analysis, Data curation, Conceptualization. Carin L. Roberts-Wollmann: Writing – review & editing, Supervision, Methodology, Conceptualization. Alexander S. Brand: Writing – review & editing, Supervision, Methodology, Conceptualization.

7.6. References

[1] Á. Picazo, M.G. Alberti, A. Enfedaque, J.C. Gálvez, Assessment of the Shear Strength of Steel Fibre-Reinforced Concrete, in: D.A. Hordijk, M. Luković (Eds.), High Tech Concr. Technol. Eng. Meet, Springer International Publishing, Cham, 2018: pp. 405–412. https://doi.org/10.1007/978-3-319-59471-2_49.

[2] P. Kawde, A. Warudkar, Steel fiber reinforced concrete: A review, Int. J. Eng. Sci. Res. Technol. (2017).

[3] B. Li, L. Xu, Y. Shi, Y. Chi, Q. Liu, C. Li, Effects of fiber type, volume fraction and aspect ratio on the flexural and acoustic emission behaviors of steel fiber reinforced concrete, Constr. Build. Mater. 181 (2018) 474–486. https://doi.org/10.1016/j.conbuildmat.2018.06.065.

[4] S. Ragavendra, I.P. Reddy, D.A. Dongre, Fibre Reinforced Concrete- A Case Study, in: Proc. Archit. Eng. Asp. Sustain. Build. Envel., 2017.

[5] B. Miloud, Fibre-reinforced concrete: Past, present and future, 38 (2004) 47–49.

[6] T.S. Lok, J.R. Xiao, Flexural Strength Assessment of Steel Fiber Reinforced Concrete, J. Mater. Civ. Eng. 11 (1999) 188–196. https://doi.org/10.1061/(ASCE)0899-1561(1999)11:3(188).

[7] J.A.O. Barros, J.A. Figueiras, Flexural Behavior of SFRC: Testing and Modeling, J. Mater. Civ. Eng. 11 (1999) 331–339. https://doi.org/10.1061/(ASCE)0899-1561(1999)11:4(331).

[8] Lok Tat-Seng, Pei Jin-Song, Flexural Behavior of Steel Fiber Reinforced Concrete, J. Mater. Civ. Eng. 10 (1998) 86–97. https://doi.org/10.1061/(ASCE)0899-1561(1998)10:2(86).

[9] RILEM TC 162-TDF, Recommendations of RILEM TC 162-TDF: Test and design methods for steel fibre reinforced concrete: bending test, RILEM Publ. SARL 35 (2002) 579–582.

[10] A. Blanco, P. Pujadas, A. De La Fuente, S. Cavalaro, A. Aguado, Application of constitutive models in European codes to RC–FRC, Constr. Build. Mater. 40 (2013) 246–259. https://doi.org/10.1016/j.conbuildmat.2012.09.096.

[11] Bekaert Corporation, Evaluation Report 465, IAPMO UES, 2019.

[12] fib, Model Code 2010, International Federation for Structural Concrete (fib), Lausanne, 2010.

[13] J. Liu, C. Wu, J. Li, Z. Liu, S. Xu, K. Liu, Y. Su, J. Fang, G. Chen, Projectile impact resistance of fibre-reinforced geopolymer-based ultra-high performance concrete (G-UHPC), Constr. Build. Mater. 290 (2021) 123189. https://doi.org/10.1016/j.conbuildmat.2021.123189.

[14] K. Habel, M. Viviani, E. Denarié, E. Brühwiler, Development of the mechanical properties of an Ultra-High Performance Fiber Reinforced Concrete (UHPFRC), Cem. Concr. Res. 36 (2006) 1362–1370. https://doi.org/10.1016/j.cemconres.2006.03.009.

[15] A. Tafraoui, G. Escadeillas, T. Vidal, Durability of the Ultra High Performances Concrete containing metakaolin, Constr. Build. Mater. 112 (2016) 980–987. https://doi.org/10.1016/j.conbuildmat.2016.02.169.

[16] N. San Ha, S.S. Marundrury, T.M. Pham, E. Pournasiri, F. Shi, H. Hao, Effect of grounded blast furnace slag and rice husk ash on performance of ultra-high-performance concrete (UHPC) subjected to impact loading, Constr. Build. Mater. 329 (2022) 127213. https://doi.org/10.1016/j.conbuildmat.2022.127213.

[17] R. Alarrak, A.S. Brand, Mechanical Performance of Extruded Functionally Graded Fiber-Reinforced Mortar with Targeted Fiber Injection, Rev. (2024).

[18] D. Lai, C. Demartino, Y. Xiao, High-strain rate compressive behavior of Fiber-Reinforced Rubberized Concrete, Constr. Build. Mater. 319 (2022) 125739. https://doi.org/10.1016/j.conbuildmat.2021.125739.

[19] R. Mu, Y. Xue, L. Qing, H. Li, Y. Zhao, J. Zhou, J. Su, Preparation and mechanical performance of annularly aligned steel fiber reinforced cement-based composite pipes, Constr. Build. Mater. 211 (2019) 167–173. https://doi.org/10.1016/j.conbuildmat.2019.03.146.

[20] R. Mu, H. Li, L. Qing, J. Lin, Q. Zhao, Aligning steel fibers in cement mortar using electro-magnetic field, Constr. Build. Mater. 131 (2017) 309–316. https://doi.org/10.1016/j.conbuildmat.2016.11.081.

[21] G.W. Melenka, J.P. Carey, Evaluation of fiber reinforced cement using digital image correlation, PLOS ONE 10 (2015) e0128644. https://doi.org/10.1371/journal.pone.0128644.

[22] R. Alarrak, B. Jeon, A.S. Brand, Flexural toughness of extruded fiber-reinforced mortar with preferentially aligned fibers, Constr. Build. Mater. 407 (2023) 133528. https://doi.org/10.1016/j.conbuildmat.2023.133528.

[23] R. Alarrak, B. Jeon, A.S. Brand, Fracture properties of extruded fiber-reinforced mortar with preferentially aligned fibers, Constr. Build. Mater. 403 (2023) 133022. https://doi.org/10.1016/j.conbuildmat.2023.133022.

[24] Z.Y. Ahmed, F.P. Bos, M.C.A.J. Van Brunschot, T.A.M. Salet, On-demand additive manufacturing of functionally graded concrete, Virtual Phys. Prototyp. 15 (2020) 194–210. https://doi.org/10.1080/17452759.2019.1709009.

[25] X. Sun, J. Zhou, Q. Wang, J. Shi, H. Wang, PVA fibre reinforced high-strength cementitious composite for 3D printing: Mechanical properties and durability, Addit. Manuf. 49 (2022) 102500. https://doi.org/10.1016/j.addma.2021.102500.

[26] Y. Shao, S. Marikunte, S.P. Shah, Extruded fiber-reinforced composites, Concr. Int. 17 (1995) 48–53.

[27] Z. Li, B. Mu, T.P. Chang, C.-T. Hsu, Prediction of overall tension behavior of short fiber-reinforced composites, Int. J. Solids Struct. 36 (1999) 4071–4087.

[28] H. Takashima, K. Miyagai, T. Hashida, V.C. Li, A design approach for the mechanical properties of polypropylene discontinuous fiber reinforced cementitious composites by

extrusion molding, Eng. Fract. Mech. 70 (2003) 853–870. https://doi.org/10.1016/S0013-7944(02)00154-6.

[29] X. Zhou, Z. Li, Characterizing rheology of fresh short fiber reinforced cementitious composite through capillary extrusion, J. Mater. Civ. Eng. 17 (2005) 28–35.

[30] Y. Zhang, F. Aslani, Development of fibre reinforced engineered cementitious composite using polyvinyl alcohol fibre and activated carbon powder for 3D concrete printing, Constr. Build. Mater. 303 (2021) 124453. https://doi.org/10.1016/j.conbuildmat.2021.124453.

[31] J. Ye, C. Cui, J. Yu, K. Yu, F. Dong, Effect of polyethylene fiber content on workability and mechanical-anisotropic properties of 3D printed ultra-high ductile concrete, Constr. Build. Mater. 281 (2021) 122586. https://doi.org/10.1016/j.conbuildmat.2021.122586.

[32] M. Sugavaneswaran, G. Arumaikkannu, Modelling for randomly oriented multi material additive manufacturing component and its fabrication, Mater. Des. 1980-2015 54 (2014) 779–785. https://doi.org/10.1016/j.matdes.2013.08.102.

[33] H. Stang, V.C. Li, Extrusion of ECC-material, in: Proc High Perform. Fiber Reinf. Cem. Compos., 1999: pp. 203–212.

[34] S.C. Paul, Y.W.D. Tay, B. Panda, M.J. Tan, Fresh and hardened properties of 3D printable cementitious materials for building and construction, Arch. Civ. Mech. Eng. 18 (2018) 311–319. https://doi.org/10.1016/j.acme.2017.02.008.

[35] X. Qian, X. Zhou, B. Mu, Z. Li, Fiber alignment and property direction dependency of FRC extrudate, Cem. Concr. Res. 33 (2003) 1575–1581.

[36] G. Ma, Z. Li, L. Wang, F. Wang, J. Sanjayan, Mechanical anisotropy of aligned fiber reinforced composite for extrusion-based 3D printing, Constr. Build. Mater. 202 (2019) 770–783. https://doi.org/10.1016/j.conbuildmat.2019.01.008.

[37] Z. Li, B. Mu, Innovations forum: Application of extrusion for manufacture of short fiber reinforced cementitious composite, J. Mater. Civ. Eng. 10 (1998) 2–4. https://doi.org/10.1061/(ASCE)0899-1561(1998)10:1(2).

[38] Z. Hou, X. Tian, J. Zhang, D. Li, 3D printed continuous fibre reinforced composite corrugated structure, Compos. Struct. 184 (2018) 1005–1010. https://doi.org/10.1016/j.compstruct.2017.10.080.

[39] A. Zhong, M. Sofi, E. Lumantarna, Z. Zhou, P. Mendis, Flexural Capacity Prediction Model For Steel Fibre-Reinforced Concrete Beams, Int. J. Concr. Struct. Mater. 15 (2021) 28. https://doi.org/10.1186/s40069-021-00461-0.

[40] H.H.Z. Khalel, M. Khan, Modelling Fibre-Reinforced Concrete for Predicting Optimal Mechanical Properties, Materials 16 (2023) 3700. https://doi.org/10.3390/ma16103700.

[41] T. Ayub, S.U. Khan, N. Shafiq, Flexural Modelling and Finite Element Analysis of FRC Beams Reinforced with PVA and Basalt Fibres and Their Validation, Adv. Civ. Eng. 2018 (2018) 1–18. https://doi.org/10.1155/2018/8060852.

[42] A. Enfedaque, F. Suárez, M.G. Alberti, J.C. Gálvez, Suitability of Constitutive Models of the Structural Concrete Codes When Applied to Polyolefin Fibre Reinforced Concrete, Materials 15 (2022) 2323. https://doi.org/10.3390/ma15062323.

[43] A. Conforti, R. Zerbino, G. Plizzari, Assessing the influence of fibers on the flexural behavior of reinforced concrete beams with different longitudinal reinforcement ratios, Struct. Concr. 22 (2021) 347–360. https://doi.org/10.1002/suco.201900575.

[44] T.E.T. Buttignol, J.F. Fernandes, T.N. Bittencourt, J.L.A.O. Sousa, Design of reinforced concrete beams with steel fibers in the ultimate limit state, Rev. IBRACON Estrut. E Mater. 11 (2018) 997–1024. https://doi.org/10.1590/s1983-41952018000500006.

[45] S. Aidarov, A. Nogales, I. Reynvart, N. Tošić, A. De La Fuente, Effects of Low Temperatures on Flexural Strength of Macro-Synthetic Fiber Reinforced Concrete: Experimental and Numerical Investigation, Materials 15 (2022) 1153. https://doi.org/10.3390/ma15031153.

[46] Z. Marcalíková, L. Procházka, M. Pešata, J. Boháčová, R. Čajka, Comparison of material properties of steel fiber reinforced concrete with two types of steel fiber, IOP Conf. Ser. Mater. Sci. Eng. 549 (2019) 012039. https://doi.org/10.1088/1757-899X/549/1/012039.

[47] A. Danish, M.A. Mosaberpanah, M.U. Salim, M. Amran, R. Fediuk, T. Ozbakkaloglu, M.F. Rashid, Utilization of recycled carbon fiber reinforced polymer in cementitious composites: A critical review, J. Build. Eng. 53 (2022) 104583. https://doi.org/10.1016/j.jobe.2022.104583.

[48] EN 14651, Test method for metallic fibered concrete - Measuring the flexural tensile strength (limit of proportionality (LOP), residual), European Committee for Standardization, 2005.

[49] L. Ferrara, N. Ozyurt, M. Di Prisco, High mechanical performance of fibre reinforced cementitious composites: the role of “casting-flow induced” fibre orientation, Mater. Struct. 44 (2011) 109–128. https://doi.org/10.1617/s11527-010-9613-9.

[50] M. Di Prisco, M. Colombo, FRC Thin Walled Structures: Opportunities and Threats, in: Proc 8th RILEM Int. Symp. BEFIB 2012, RILEM Publications SARL, 2012: pp. 23–49.

[51] M. Di Prisco, G. Plizzari, L. Vandewalle, Fiber Reinforced Concrete in the New fib Model Code, in: 3rd Fib Int. Congr., 2010.

[52] J. Roesler, G. Paulino, C. Gaedicke, A. Bordelon, K. Park, Fracture Behavior of Functionally Graded Concrete Materials for Rigid Pavements, Transp. Res. Rec. J. Transp. Res. Board 2037 (2007) 40–49. https://doi.org/10.3141/2037-04.

[53] B. Mobasher, Mechanics of Fiber and Textile Reinforced Cement Composites, CRC Press, 2012.

[54] W.D. Callister, D.G. Rethwisch, Callister’s Materials science and engineering, 10th edition, Wiley, Hoboken, NJ, 2019.

Chapter 8. Conclusions and Recommendations

8.1. Research Overview

This dissertation embarked on a critical journey to bridge a significant gap in the field of extrusion-based fiber-reinforced concrete (FRC) casting. With a focus on understanding and improving the mechanical behaviors of FRC materials, this research has been pivotal in exploring the influence of fiber alignment and distribution within FRC. The ambition of this work was established through its comprehensive research objectives, aiming to expose the impact of fiber orientation on the mechanical properties of FRC, particularly regarding fracture and flexural behaviors. It delved into the dynamics of crack propagation and strain localization, offering new insights into the material's response under stress.

A cornerstone of this dissertation has been the development of a novel fiber injection technique during the FRC extrusion process, marking a significant step forward in the construction industry's capabilities. Moreover, the pursuit of a comprehensive model for the structural design of extruded FRC, taking into account the crucial aspect of fiber orientation, underlines the dissertation's innovative approach.

Through a meticulously designed series of research tasks, the dissertation has systematically addressed each objective, contributing significantly to the advancement of the FRC casting field. The dissertation consists of five manuscripts, within eight chapters, each contributing novel contributions and advancements to the field of FRC, unfolding detailed narrative from theoretical frameworks to practical applications. The dissertation not only advances academic knowledge but also holds significant implications for the construction industry, demonstrating a profound understanding of the challenges and opportunities in extrusion-based FRC casting.

8.2. Major Findings

Chapters 3 and 4 investigated the fracture and flexural properties of fiber-reinforced mortar, utilizing extrusion-based (EB) and conventional (CV) casting methods with polyvinyl alcohol (PVA) fiber dosages of 0.5 % and 1 %. The hypothesis suggested that the extrusion process would align fibers parallel to tensile stresses, thus enhancing mechanical properties. In Chapter 3, the findings indicated that the EB method significantly improved fracture properties, particularly at higher fiber dosages, due to better fiber alignment. The digital image correlation (DIC) technique highlighted the EB method's effectiveness in achieving crack bridging and deflection, emphasizing the critical role of fiber alignment.

In Chapter 4, the study shifted to the flexural properties of FRC and revealed that the EB method was particularly effective in maintaining residual strength after the peak, attributed to optimal fiber alignment that facilitated stress redistribution. EB specimens exhibited higher deflection at failure and an improved equivalent flexural strength ratio compared to CV specimens. DIC tracking showed that EB specimens developed multiple cracks as opposed to the single large crack observed in CV specimens, further validating the benefits of fiber alignment in enhancing the material's performance.

Chapter 5 explored the impact of casting methods and fiber orientation on the fracture properties of PVA FRC, focusing on the size effect method to compare EB and CV casting. The chapter unveiled a notable size-dependent improvement in fracture energy with the EB method, showcasing increases of approximately 96 %, 45 %, and 31 % for small, medium, and large specimens, respectively, over their CV counterparts Additionally, a 39 % improvement in fracture process zone (FPZ) lengths was observed in the EB specimens, underscoring the significant role of fiber alignment in improving FRC's mechanical properties. Unlike the CV method, where fibers

were randomly incorporated, the EB method's strategic fiber alignment in the desired direction notably enhanced fracture properties.

Chapter 6 explored the role of strategic fiber distribution in enhancing the structural integrity and resilience of functionally-graded FRC (FG-FRC) using strategic steel fiber distribution. It found that varying fiber dosages in layers, experiencing tension, significantly improved FG-FRC's toughness and strength. While increased fiber content did not consistently increase peak loads, it notably improved fracture energy absorption, indicating better crack bridging and ductility under tensile stress. The study X-ray computed tomography (XCT) to quantify fiber orientation and distribution, highlighting their essential role in FG-FRC's mechanical properties. DIC analysis of crack propagation and strain localization revealed that well-distributed and aligned fibers create a complex crack network, enhancing material toughness. This chapter underscores the importance of strategic fiber distribution in advancing FG-FRC's performance.

Chapter 7 investigated the predictability of three flexural models – Evaluation Report (ER-465), fib Linear (fib-L), and fib Rigid-Plastic (fib-RP) – applied to FG-FRC specimens, assessing their correlation with experimental data from three-point bending tests on notched beams. This analysis focused on fiber dosage and orientation within the FG-FRC layers. The ER-465 model was found to be more conservative compared to the predictions by the fib models. Among these, the fib-L model was identified for its accuracy in predicting FRC flexural strength, with minimal error percentage. The introduction of the functionally graded factor (K_{FG}) into the flexural models significantly advanced the accuracy in predicting the structural behavior of FG-FRC sections. This enhancement marked a significant step forward in the models' applicability and reliability for engineering purposes.

8.3. Limitations

Throughout Chapters 3 to 7, research effectively demonstrated the use of the extrusion-based technique for FRC, revealing significant advancements in fiber alignment and material properties. However, a critical limitation was identified concerning the technique's compatibility with aggregate size. Specifically, the requirement for mixtures without coarse aggregate, due to the extrusion pump's limitations, presents a significant challenge. This constraint does not undermine the findings' relevance to FRC mechanical properties but highlights a broader issue in the 3D printing materials industry, which primarily utilizes mortar. Additionally, the research identified a limited exploration of fiber types and dosages, suggesting a valuable direction for future studies.

In Chapter 7, an important limitation related to the functionally-graded factor (K_{FG}) in flexural models for FG-FRC sections was discussed. While the introduction of K_{FG} significantly enhanced model accuracy, its calibration relied on empirical data from specific FG-FRC configurations, indicating a need for broader validation to ensure its general applicability and precision across various FG-FRC configurations.

8.4. Recommendations for Future Work

The research conducted provides a solid foundation for the future of FRC within the construction industry. The findings not only shed light on current limitations but also open doors to innovative advancements. Future research in these areas could revolutionize FRC applications, paving the way for more sustainable, durable, and innovative construction methodologies. Here are key recommendations for advancing FRC technologies:

- **Integration of Coarse Aggregate in FRC Mixtures:** Investigate the feasibility and impact of incorporating coarse aggregate on fiber orientation and the overall performance of FRC. This research could expand the practical applications of FRC in the construction industry, leading to the development of more robust building materials.
- **Exploration of Diverse Fiber Types and Dosages:** Conduct a comprehensive study on a wider range of fiber types and their proportions to understand their effects on the structural and mechanical properties of FRC. This exploration is crucial for optimizing fiber dosage, distribution, and alignment, potentially leading to advancements in the efficiency, durability, and performance of construction materials.
- **Refinement of the Functionally-Graded Factor in Flexural Models:** Enhance the precision and applicability of the K_{FG} factor within flexural models for FG-FRC sections. Future work should aim to extend the K_{FG} factor's relevance by incorporating a wider range of FRC configurations and testing conditions. Developing a universal framework for this factor could significantly enhance predictive modeling capabilities, aiding in the design and analysis of innovative fiber-reinforced composites.
- **Development of a Fully Automated Fiber Injection System:** Develop a fully automated 3D printing system, using the concept discussed in Chapter 6, capable of injecting high stiffness fibers into concrete mixtures. This system should also accommodate the use of coarse aggregate, overcoming a significant hurdle in current 3D printing technologies.

Addressing these recommendations will not only tackle the limitations identified but also significantly contribute to the advancement of construction material technologies, especially in the domain of FRC.